Universidad de Granada

Dinámica Ambiental
UNIVERSIDAD DE GRANADA

DOCTORAL THESIS

Water-wave interaction with mound breakwaters: from the seabed to the armor layer

Author:
Pilar DÍAZ CARRASCO

Supervisors:
Miguel ORTEGA SÁNCHEZ
María CLAVERO GILABERT

Doctoral Programme: Biogeochemical Fluid Dynamics and their Applications

Environmental Fluid Dynamics Research Group

Department of Structural Mechanics and Hydraulic Engineering
University of Granada

November, 2019

Editor: Universidad de Granada. Tesis Doctorales
Autor: Pilar Díaz Carrasco
ISBN: 978-84-1306-425-3
URI: http://hdl.handle.net/10481/59068

A mis padres

Agradecimientos

En primer lugar, quiero agradecer la inestimable ayuda proporcionada por mis directores de tesis, Miguel Ortega y María Clavero. Sin vuestra dirección constante, ayuda profesional y emocional no habría sido posible hacer y terminar la Tesis Doctoral. He aprendido con vosotros, día a día, cómo recorrer el camino del trabajo en grupo. Gracias, Migue, por haberme orientado y por tu paciencia desde mis inicios en la investigación, así como por tus charlas del ser y los espejos, que tantas risas, y algo de sabiduría, nos han proporcionado. María, gracias también por tus ánimos y por haberme ayudado a gestionar y resolver los problemas que se presentan en la realización de la tesis.

Me gustaría señalar mi agradecimiento y dedicar especialmente mi tesis a Miguel Á. Losada. Miguel, ambos sabemos que este trabajo no habría sido posible sin tu ayuda, tu fuente inagotable de ideas y tus cambios de rumbo en los últimos momentos. Me has enseñado el camino de la investigación y me has hecho, espero, evolucionar como investigadora. Gracias también por tu trato y, por encima de todo, gracias por mostrarme tu forma de pensar.

Gracias a todos mis compañeros del Grupo de Dinámica de Flujos Ambientales, los que están y también los que se han ido a otros lugares. Gracias en especial a mis compañeras de laboratorio, María y Mariví, vuestra ayuda en los ensayos y ánimo han hecho posible la realización de este trabajo. Gracias chicas también por las risas y por endulzarme las jornadas de trabajo. Mi rubia (Mariví), a ti tengo que agradecerte de nuevo que me hayas aguantado todo, me hayas ayudado y, como no, los buenos momentos y risas que hemos compartido.

A mi familia, imprescindibles en este proceso. A mis padres, os dedico toda mi tesis. Sabéis de primera mano el recorrido y todas las fases que tiene hacer una tesis, incluso mucho más. Por ello, gracias por todos los consejos y por el apoyo que siempre he tenido de vuestra parte. A mi hermano, Javier, gracias por tus charlas de hermano mayor y por quitarme presión muchas veces.

Gracias a mis amigos de siempre, en especial a mi amiga Clara que ha estado siempre ahí, en todos los buenos y malos momentos. Gracias también a todos los amigos que he encontrado en este camino... Alba, Jose, Laura, Carlos, Sergio...por vuestras alegrías, cervezas tomadas y risas infinitas. Gracias a todos mis compañeros de Rugby, "Bosones y Fermionas", y a mi entrenador de natación Nico, con vosotros no solo descargo tensiones en los entrenamientos sino que además siempre me sacáis una sonrisa. No me olvido de mi prima mayor Elena (8 meses). Eleni, te doy las gracias por escucharme, por tus audios infinitos que hacen que descanse en el trabajo y bueno... porque eres importante para mi.

Y finalmente, por último pero no menos importante, a Julio. Sinceramente, admiro tu forma de ser, tu constancia, tus metas y tu forma de llevar los problemas. Verte y escucharte me ha dado muchas fuerzas y, sobre todo, motivación para afrontar estos últimos momentos complicados de la tesis. Gracias, por estar ahí, por prestarme tu apoyo y por tu cariño... lo dicho... "mala suerte, buena suerte".

Esta investigación se ha desarrollado en el ámbito del Grupo de Dinámica de Flujos Ambientales (Universidad de Granada) y en el de los Proyectos: VIVALDI (BIA2015-65598-P) y PROTOCOL (917PTE0538). He de mencionar a los Catedráticos de Universidad, Paolo Blondeaux y Giovanna Vittori, por acogerme en mi estancia en la Universidad de Génova y darme la oportunidad de conocer otra forma de trabajar. También agradezco al Dr. Thomas Lykke Andersen, por su ayuda en la Universidad de Aalborg y por dejarme sus instalaciones del laboratorio. Finalmente, deseo también mostrar mi gratitud al Ministerio de Educación, Cultura y Deporte por la concesión de la Ayuda predoctoral para la Formación del Profesorado Universitario (FPU14/03570) para la realización de mi Tesis Doctoral.

Resumen

Los diques de abrigo constituyen la principal infraestructura portuaria y costera, tanto por su funcionalidad, como por su coste, complejidad de diseño e impactos socio-económicos y ambientales. Entre sus diferentes tipologías, el "dique en talud" es la más construida en el mundo por su capacidad para disipar la energía del oleaje y su mayor integración en el medio marino. Actualmente, su diseño y verificación se basa en formulaciones experimentales, cuya variable principal es el número de Iribarren, destinadas a calcular la transformación de la energía incidente y, cuando procede, a verificar la estabilidad y el rebase sobre la estructura. Tales formulaciones presentan variabilidad e incertidumbre difíciles de acotar, y que suele ser significativa en el intervalo correspondiente a las condiciones de diseño. A esta incertidumbre hay que añadir los problemas, tanto ambientales como geotécnicos. Como consecuencia, esta tesis se centra en avanzar en el conocimiento de la interacción *dinámica marina–estructura–lecho marino* mediante el análisis teórico y la caracterización del comportamiento hidrodinámico de la tipología dique en talud frente a la acción de oleaje y su interacción con el lecho marino. Este tema es relevante considerando algunos de los principales retos a los que se enfrenta la sociedad: ascenso del nivel del mar e incremento de la regresión costera asociados al calentamiento global.

En la primera parte de la tesis, se lleva a cabo una revisión teórica de los modelos de comportamiento de los suelos cohesivos y no cohesivos que componen el lecho marino, así como los principales modos de fallo geotécnicos que generan problemas estructurales en el dique. Dependiendo del grado de compactación, los suelos no cohesivos o parcialmente cohesivos se comportan según un modelo reológico poro-elástico o poro-elastoplástico. Para los suelos cohesivos, el modelo que mejor se adapta al comportamiento del suelo bajo la acción del oleaje es el modelo visco-elástico. A partir del comportamiento del suelo bajo la acción del oleaje, se identificaron los principales modos de fallo geotécnicos que pueden generar fallos estructurales en el dique. El exceso de presión de poros debido a la acción de oleaje anula las tensiones efectivas del suelo, pudiendo provocar licuefacción y/o fluidificación del lecho. Asimismo, la erosión superficial del lecho, relacionada con la capacidad de transporte de la dinámica litoral, es el modo de fallo más frecuente en las zonas costeras y en las proximidades del dique. Frente a los modos de fallo geotécnicos y sus consecuencias sobre la estructura marítima, se proponen prácticas recomendaciones de diseño y mantenimiento del dique presentadas según la composición del suelo y su contenido de arcilla.

Sin embargo, después de la extensa revisión realizada, se observa que parte de la complejidad para analizar la interacción *dinámica marina–estructura–lecho marino* se debe a que existe aún incertidumbre en el modelado y la caracterización de cada una de las partes por separado. Por ello, dentro de esta primera parte del trabajo se propone una mejora en el modelado de la interacción del régimen oscilatorio del mar con el lecho marino. En concreto, se ha desarrollado un modelo numérico hidrodinámico y de sedimentos que determina el transporte del sedimento cohesivo y no cohesivo bajo la acción combinada del oleaje y las corrientes de marea. En el módulo hidrodinámico se formula las ecuaciones promediadas de cantidad de movimiento de Reynolds y se incorpora el modelo de turbulencia de Menter, que resuelve el problema desde el fondo del lecho hasta la superficie libre, incluidas todas las regiones de la capa límite. Este modelo de turbulencia facilita la descripción de la estructura del flujo dentro de la capa límite y, con ello, el perfil de velocidad y el transporte de sedimentos en toda la columna de agua. En el módulo de transporte de sedimentos se determina la concentración y el transporte para una mezcla de sedimentos cohesivos y no cohesivos. Para validar el modelo, sus predicciones se compararon con mediciones de laboratorio y datos de campo de

otros estudios sobre lechos ondulados en dos estuarios con diferentes condiciones de marea. Asimismo, se aplicó el modelo a la zona de estudio de Punta Umbría (Huelva, España), con diferentes condiciones de oleaje, corrientes de marea y mezcla de sedimentos. Los resultados obtenidos en esta zona de estudio mostraron que, para cuantificar el transporte del sedimento cohesivo y no cohesivo, es necesario modelar adecuadamente la estructura turbulenta de la capa límite.

En el segunda parte de la tesis, se aborda el análisis de la transformación de la energía del oleaje incidente con el dique en talud. Para ello, se investigan los procesos físicos que dominan la transformación de la energía incidente al interaccionar con un dique en talud y su correlación con el tipo de rotura observada. Esta parte del trabajo se apoya en (i) un análisis dimensional de las principales variables que influyen en el comportamiento hidráulico para cada tipo de talud, (ii) en una experimentación numérica de un talud impermeable mediante el modelo numérico IH-2VOF y (iii) en una experimentación física en un canal 2D de un dique en talud permeable homogéneo y permeable con manto de cubos. La aplicación del análisis dimensional y los resultados experimentales muestran que, para el talud impermeable, el producto de la profundidad relativa y el peralte del tren incidente a pie de dique, $(h/L)(H/L)$, delimita la dispersión experimental mejor que el número de Iribarren y localiza la máxima desviación de los coeficientes de energía reflejada, transmitida y la tasa de disipación, (K_R^2, K_T^2, D^*) con respecto a una función sigmoide ajustada. Asimismo, $(h/L)(H/L)$ identifica los dominios de transformación de la energía incidente y la evolución del tipo de rotura. Entre estos dominios de transformación del tren de ondas y su tipo de rotura asociado se encuentran: (i) dominio disipativo, con roturas en voluta débil, (ii) dominio reflejante, con roturas en oscilación, y (iii) transición entre los dos anteriores, con al menos tres tipo de rotura, colapso débil, colapso violento y voluta violenta, y donde la dispersión de los datos experimentales aumenta. En diques permeables, las regiones se ubican en intervalos de valores de $(h/L)(H/L)$ menores y la desviación experimental de los coeficientes de energía en función de $(h/L)(H/L)$ sigue diferentes trayectorias según los valores del diámetro relativo, $D_{50,p}/L$, y del ancho relativo, B^*/L. Seleccionado un valor de $(h/L)(H/L)$ en la región de transición, K_R^2 aumenta al reducir el valor de B^*/L y $D_{50,p}/L$, y el tipo de rotura varía de colapso violento a oscilación. Esta variabilidad en el modo de transformación de la energía y el tipo de rotura puede ocurrir conservando el número de Iribarren.

Una de las grandes ventajas de la aplicación del análisis dimensional es que permite elaborar un espacio experimental del tren de ondas incidente del tipo: $[\ln(h/L), \ln(H_I/L)]$. Este método experimental implementado permite: (1) optimizar el número de ensayos, (2) cumplir la similitud dinámica entre modelo-prototipo, e (3) identificar las regiones de transformación de la energía del oleaje y los tipos de roturas para intervalos de $(h/L)(H_I/L)$.

Se ha dado un paso más con el estudio de las fuentes de disipación en el manto principal del dique en talud. Para ello, se aplica el teorema Π de Buckingham para agrupar apropiadamente las variables adimensionales que permanecen constantes en un experimento. Asimismo, el trabajo se apoya en dos conjuntos de datos obtenidos en la Universidad de Aalborg y en la Universidad de Granada. En concreto, se ensayaron mantos con diferente tipo de pieza, escollera o cubos, y diferentes tamaños de cubos. Se concluye que la disipación de la energía incidente en el manto principal con diferentes tamaños de cubos es relevante en intervalos específicos de $(h/L)(H/L)$, relacionados con el dominio de transición y tipo de rotura, de colapso débil a voluta violenta. Finalmente se demuestra que el número de estabilidad de la pieza y la disipación en el manto están relacionados funcionalmente y su relación depende de h/L, H/L, las características del núcleo y la pendiente del talud. Este resultado es relevante pues cohesiona el diseño del dique, clarifica y complementa el papel del número de Iribarren, y ayuda a reducir la variabilidad y la incertidumbre de las fórmulas habituales de cálculo.

Abstract

Breakwaters are the main port and coastal maritime infrastructure in terms of its functionality, cost, design complexity and social, economical and environmental impacts. Among their typologies, the "mound breakwater" is the most built in the world due to its ability to dissipate the wave energy and its relative low environmental impact. Currently, breakwaters are designed and verified by means of experimental formulas which main variable is the Iribarren's number; furthermore, these formulas are used to calculate the transformation of the incident wave energy and, where appropriate, to verify stability and overtopping over the structure. Such formulas exhibit variability and uncertainty, being particularly relevant in the range of the design conditions. Besides, both environmental and geotechnical problems are frequently added. As a consequence, this thesis focuses on gaining deeper knowledge on the interaction *dynamic marine – structure – seabed* through the theoretical analysis and the characterization of the hydrodynamic performance of mound breakwaters against the wave action and their interaction with the seabed. This topic is relevant considering some of the major challenges that the society is presently facing: sea level rise and coastal regression associated to the global warming.

In the first part of the thesis, a theoretical review of the behavior models for cohesive and non-cohesive soils that arise in the wave-seabed interaction is presented, as well as the main geotechnical failure modes that generate structural problems in breakwaters. Depending on the soil compaction degree, non-cohesive or partially cohesive soils behave according to a pore-elastic or pore-elastoplastic model. For cohesive soils, the best model that suits the behavior of the soil under wave action is the visco-elastic model. From the behavior of the soil under wave action, the main geotechnical failure modes that provoke structural problems in breakwaters were identified. The excess pore pressure due to the wave action cancels the effective stresses of the soil, which can result in liquefaction and/or fluidization of the seabed. Likewise, the surface erosion of the bed, related to the transport capacity of coastal dynamics, is the most frequent failure mode in coastal areas and in the vicinity of the breakwater. To confront the geotechnical failure modes and their consequences on maritime structures, practical recommendations for the design and maintenance of the breakwater, presented according to the composition of the soil and its clay content, are proposed.

Nevertheless, after the extensive review of the literature, it is observed that part of the complexity to analyze the interaction *dynamic marine – structure – seabed* is due to the fact that there is still uncertainty in modeling and characterizing each part separately. Therefore, within this first part of the work, an improvement is proposed in modeling the interaction of the sea oscillatory regime with the seabed. Specifically, a hydrodynamic and sediment numerical model has been developed that determines the transport of cohesive and non-cohesive sediment under the combined action of waves and tidal currents. In the hydrodynamic module, Reynolds-averaged momentum equations are formulated and the Menter turbulence model is incorporated, which solves the problem from the sea bottom up to the free-surface, including all regions of the boundary layer. This turbulence model facilitates the description of the flow structure within the boundary layer and, with it, the velocity profile and sediment transport throughout the water column. The sediment concentration and transport for a mixture of cohesive and non-cohesive sediments is determined in the sediment transport module. To validate the model, the predictions were compared with laboratory measurements and field data from other studies on rippled beds in two estuaries with different tidal conditions. Likewise, the model was applied to Punta Umbría (Huelva, Spain) study area, with different wave conditions, tidal currents and sediment mixtures. The results obtained in this study area

showed that, in order to quantify the transport of cohesive and non-cohesive sediment, it is necessary to adequately model the turbulent structure of the boundary layer.

In the second part of the thesis, the analysis of the transformation of the incident wave energy with the mound breakwater is addressed. To do this, the physical processes that dominate the incident wave energy transformation, when it interacts with a mound breakwater, and its correlation with the breaker type are investigated. This part of the work is based on (i) dimensional analysis of the main variables that influence the hydraulic performance for each type of breakwater slope, (ii) numerical experimentation of an impermeable slope using the model IH-2VOF and (iii) physical experimentation in a 2D wave flume of a homogeneous permeable slope and a permeable slope with cubes armor layer. The application of the dimensional analysis and the experimental results show that, for the impermeable slope, the product of the relative water depth and steepness of the incident wave train at the breakwater, $(h/L)(H/L)$, delimits the experimental scattering better than the Iribarren number and locates the maximum deviation of the reflected, transmitted energy coefficients and the dissipation rate, (K_R^2, K_T^2, D^*), with regard to a fitted sigmoid function. In addition, $(h/L)(H/L)$ identifies the regions of incident energy transformation and the evolution of breaker type: (i) dissipated-dominated region, with weak plunging breakers, (ii) reflection-dominated region, with surging breakers, and (iii) transition between the previous two, with at least three breaker types, weak bore, strong bore and strong plunging, and where the scattering of experimental data increases. For the permeable slopes, the regions are located in smaller intervals of $(h/L)(H/L)$ and the experimental scattering of the energy coefficients as a function of $(h/L)(H/L)$ follows different trajectories according to the values of relative core diameter, $D_{50,p}/L$, and relative width, B^*/L. When a value of $(h/L)(H/L)$ is selected in the transition region, K_R^2 increases since both values of B^*/L and $D_{50,p}/L$ decrease, and the breaker type varies: strong bore, weak bore and surging. This variability in the energy transformation mode and breaker type can occur when the Iribarren number remains constant.

An advantage of the application of dimensional analysis is that it allows developing an experimental space of the incident wave train of the type: $[\ln(h/L), \ln(H/L)]$. This implemented experimental method allowed designing laboratory tests with wave conditions that (i) optimized the number of tests, (ii) fulfilled the design criteria between model-prototype and the wave generation requirements, and (iii) allowed identifying the regions of wave energy transformation and breaker types for intervals of $(h/L)(H_I/L)$.

A further step has been achieved with the study of dissipation sources in the main armor layer of mound breakwater. For this, the Π-Buckingham theorem is applied to properly group the dimensionless variables that remain constant in an experiment. In addition, the work is based on two sets of data obtained at the University of Aalborg and the University of Granada. Specifically, main armor layers were tested with different unit type, rocks or cubes, and different sizes of cubes. It is concluded that the dissipation of the incident energy in the main armor with different sizes of cube sizes is relevant at specific intervals of $(h/L)(H/L)$, related to the transition region and breaker type, from weak bore to strong plunging. Finally, it is shown that the stability number of the unit (rock or cube) and the dissipation in the main armor are functionally related and its relationship depends on h/L, H/L, the characteristics of the core and the slope of the breakwater. This result is relevant because it joins the design of the breakwater, clarifies and complements the role of the Iribarren number, and helps to reduce the variability and uncertainty of the common calculation formulas.

"*Drift all you like, from ocean to ocean, search the whole world"*

Tom Yorke – Radiohead

Contents

List of Symbols

Part I. On the breakwater seabed

Roman letters

a	Empirical constant for settling velocity - hindered effects
b	Parameter for the stretched variable
c_a	Bottom reference volumetric sediment concentration
c_{nd}	Dimensionless concentration of cohesive sediment
c_i	Volumetric sediment concentration
$c_{\max}$	Maximum volume concentration
C_s	Dimensionless steady current gradient
C_0	Dimensionless oscillatory pressure gradient
d_i	Representative sediment diameter
D	Partial derivate of fluid velocity in the y-direction
D_T	Diffusion coefficient
E_i	Erosion rate
F_1	Blending function of Menter's model
g	Gravity acceleration
G	Elastic shear module
G^*	Complex shear module
h	Water depth
H	Wave height
k	Turbulent kinetic energy per unit mass
k_m	Empirical constant for settling velocity flocculation
k_s	Bottom roughness
k_s^+	Roughness parameter
K_h	$= \mu_s$ in Bingham model
L	Wavelength
M_e	Coefficient of erosion rate
n_s	Sediment porosity
N	Number of grid points
p	Total pressure

P_k	Product term of k
P_ω	Product term of ω
P_u	Wave-induced pore pressure
$\overline{q}_{B,i}$	Time-averaged transport rate of bed load
$\overline{q}_{S,i}$	Time-averaged transport rate of suspended load
R_p	Sediment Reynolds number
R_δ	Reynolds number = $U_0\delta/\nu$
s	Ratio between the sediment and water densities
S_c	Schmidt number
S_R	Function for the bottom roughness
SC	Depth-averaged suspended sediment concentration
t	Time
T	Wave period
u	Horizontal fluid velocity in the x direction
u_s	Horizontal displacement of the soil in the x-direction
u_τ	Wave bottom shear velocity
U	Horizontal Reynolds-averaged fluid velocity
U_c	Steady current velocity
U_0	Wave amplitud velocity close to the bottom
U	Vertical Reynolds-averaged velocity
v	Vertical fluid velocity in the y direction
v_s	Vertical displacement of the soil in the y-direction
$w_{s,i}$	Sediment settling velocity
w_{s0}	Fall velocity for a single particle
x	Horizontal axes
y	Vertical axis
y_a	Bottom reference level of sediment concentration
y_{fin}	Numerical reference level of free-surface
y_{int}	Numerical reference level close to the bottom

Greek letters

α_i	Percentage of sediment fraction
δ	Thickness of the bottom boundary layer
δ_p	Specific energy loss
Δ_t	Time step
η_r	Ripple height

ε_e	Elastic normal strain
ε_p	Plastic normal strain
γ	Shear strain
$\dot{\gamma}$	Strain rate
γ_{ws}	Empirical constant for settling velocity function
μ	Water viscosity
μ_s	Soil viscosity
ν	Kinematic water viscosity
ν_T	Kinematic eddy viscosity
ω	Pseudo-vorticity
ψ	Generic constant for the Menter's model
ψ_1	Generic constant for the $k-\omega$ model
ψ_2	Generic constant for the $k-\varepsilon$ model
Ψ	Sediment mobility number
ρ	Water density
ρ_s	Soil density
σ	Angular frequency
$\sigma_s^{'}$	Effective normal stress
σ_s	Total normal stress
τ	Shear stress of the soil
$\tau_{cr,d}$	Critical shear stress for deposition
$\tau_{cr,e}$	Critical shear stress for erosion
$\tau_{cr,susp}$	Critical shear stress for the suspended load
τ_B	$= \tau_y$ in Bingham model
τ_y	Initial creep stress
τ_w	Wave bottom shear stress
θ	Shields parameter
θ_c	Shields parameter related only to the steady current
θ_{cr}	Critical Shields parameter for the bed load
$\theta_{cr,susp}$	Critical Shields parameter for the suspended load
ε	Turbulent dissipation
ς	Stretched variable for the numerical approach

Subscripts

$i = nc, c$	Non-cohesive and cohesive fraction, respectively
c	Only the steady current

$w-c$	Combined action of waves and the steady current

Superscript

$\hat{}$	Depth-averaged value
$'$	Turbulent Reynolds fluctuations
$*$	Variables with dimensions

Part II. On the breakwater performance

Roman letters

a	Limit of $(h/L)(H/L)$ for the reflection-dominated region
a_z	Inflection point of the sigmoid function
A_{eq}	Porous area per unit section under the mean water level
b	Limit of $(h/L)(H/L)$ for the dissipation-dominated region
B	Width of the caisson
B_b	Width of the top of the mound breakwater
B^*	Characteristic width of the breakwater $= B_b + (0.5F_{MT}\cot(\alpha))$
c	Wave phase speed
c_1	Lower limit of $(h/L)(H/L)$ for the transition region
c_2	Upper limit of $(h/L)(H/L)$ for the transition region
c_A	Added mass coefficient
$C_{g,i}$	Linear theory wave group speed
d_j^*	Source process of wave energy dissipation ($j=1, 2, 3$)
D_a	Diameter of the main armor layer
D_{eq}	Equivalent diameter of the main armor layer
$D_{50,f}$	Filter diameter
$D_{50,p}$	Granular core diameter
$D^{'*}$	Mean bulk dissipation
D^*	Mean dissipation rate
e	Thickness of the armor layer
E_i	Wave energy per unit surface
f	Frequency component of the wave spectrum
f_p	Peak frequency
f_L, f_T, f_I	Laminar, turbulent and inertial frictional resistance forces
F_c	Freeboard
F_{Gi}	Resistive or friction forces by the soils skeleton
F_i	Mean energy flow

F_{MT}	Porous medium height
g	Gravity acceleration
h	Water depth
h_b	Caisson foundation depth
H_i	Wave height
H_{m0}	Spectral incident wave height
$H_{mean,i}$	Averaged wave height
$H_{phase-averaged,i}$	Phase-averaged wave height
$H_{rms,i}$	Root-mean square wave height
$H_{s,i}$	Significant wave height
I_r	Number of Iribarren
I_r^*	Number of Modified Iribarren
k	Wave number
k_F	Subset of independent quantities constant in a test
k_π	Subset of independent quantities
KC_a	Armor Keulegan-Carpenter number
KC_p	Grain Keulegan-Carpenter number
K_R^2	Reflected energy coefficient
K_T^2	Transmitted energy coefficient
l	Size of the piece of cube for the armor layer
L	Wavelength related to T_z
L_p	Peak wavelength
m_0	Zero-order momentum
n	Number of independent quantities
n_F	Number of independent quantities constant in a test
n_l	Real number
n_p	Core porosity
N_S	Stability number
p	Pressure
P	Notional permeability
Q_c	Overflow rate
R^2	Determination coefficient
R_d	Run-down
R_u	Run-up
R_{e,D_a}	Armor Reynolds number
$R_{e,p}$	Granular Reynolds number

$R_{e,w}$	Reynolds number
S_p	Wave steepness related to T_p
t	Time
T	Wave period
T_{m0}	Spectral mean wave period
T_p	Peak wave period
T_z	Mean wave period
u	Horizontal Reynolds average velocity
$u^{'}$	Horizontal turbulent Reynolds fluctuations
U_c	Characteristic instantaneous wave velocity
U_p	Characteristic seepage velocity in the porous medium
$v^{'}$	Vertical turbulent Reynolds fluctuations
x	Horizontal axes - origin of coordinates at the breakwater toe
x_m	$= h/\tan(\alpha)$ intersection of the S.W.L. with the seaward slope
$X_{0,R}$	Distance from the toe of seaward slope to the reflector point
$X_{0,T}$	Distance from the toe of landward slope to the transmitter point
$X(Z)$	Physical entity of the sigmoid function
X_0, X_1	Chosen limit values of $X(Z)$
z	Vertical axis - origin of coordinates at S.W.L.
Z	Independent variable of the sigmoid function

Greek letters

α	Seaward slope angle
β	Landward slope angle
η_i	Free surface elevation
η_t	Free surface time series
γ	Partial coefficients to quantify the permeability effect
γ_p	Enhancement factor of Jonswap spectrum
γ_z	Blending coefficient of the sigmoid function
μ	Water viscosity
ν	Kinematic water viscosity
ϕ_R	Reflection phase
ϕ_T	Transmitted phase
Ψ	Similarity function
ρ	Water density
ρ_s	Soil density

$\rho_{s,a}$	Armor piece density
$\rho_{s,p}$	Core density
σ	Angular frequency
θ	Incident angle

Subscripts

$i = I, R, T$	incident, reflected and transmitted, respectively
$target$	Theoretical wave parameters generated
wb	wave-breaking

List of Figures

List of Tables

Introduction

General overview

Breakwaters are the main maritime infrastructures according to its functionality, cost, design complexity and social, economical and environmental impacts. These maritime structures protect ports and coasts against the marine dynamics and its function will be even more important in the upcoming years due to sea level rise and coastal regression as a result of global warming. In fact, the impacts of the sea level rise represent an important threat for the future (Hinkel et al., 2014; Hogarth, 2014; Vousdoukas et al., 2017; Mentaschi et al., 2017; Sayol and Marcos, 2018; Del-Rosal-Salido et al., 2019; PROTOCOL, 2020). Regarding maritime structures and nearby environments, effects will include (Moragues et al., 2018; Moragues et al., 2019b): increasing levels of erosion, higher impacts of the wave energy on breakwaters, loss of stability and overtopping events, etc. On the other hand, the need to expand ports due to the increases of maritime traffic, as well as to achieve a balance between coastal human intervention, costs and environmental impacts, makes indispensable to study the interaction *dynamic marine–structure–seabed*.

It is common knowledge that depending on their typology, breakwaters reflect, dissipate, transmit and radiate the incoming wave energy in different proportions. Mound breakwaters are the most constructed typology worldwide, since they dissipate a large amount of wave energy, using different types and sizes of armor pieces, and have a relatively low environmental impact. Although the overall design appears relatively simple, they are composed by different layers and their construction demands large amounts of material, with a high risk of structural damage due to wave action not only after being completed, but also during construction. For example, in Spain more than 50% of failures in recent years were produced in rubble mound breakwaters (Díaz-Carrasco et al., 2014). In addition, the correct design of mound breakwaters should include physical modeling in laboratory, which is an essential tool for its evaluation and analysis, since it allows simulating complex physical processes involved in the wave-structure interaction, including both the wave energy transformation and the stability of the structure.

The breakwater design must satisfy the project requirements and mainly control wind-wave actions (ROM 0.0-01, 2001; ROM 1.0-09, 2009). The project of a breakwater must address the requirement that the joint probability of all principal failure modes under ultimate and serviceability limit states, must be bounded both during the service life and during different project stages. In case of mound breakwater, the calculation begins applying empirical formulas based on the Iribarren's number (Hudson, 1959; Ahrens and McCartney, 1975; Losada and Giménez-Curto, 1979; Van der Meer, 1992), that provide the armor units weight of the main layer, and according to this value, the remaining structural parts (second layers and core) are designed. However, these design formulas, which are generally applied to calculate the transformation of the incident wave energy, run-up and run-down on the slope, and when applicable, the overtopping volume and the stability of the breakwater units, are based on experimental data, whose variability is maximum in the interval of Iribarren number corresponding to the critical design conditions. In addition to this design methodology, the physical experimentation is still based on the working hypothesis that the Iribarren number is a dynamic similarity parameter between model and prototype. All of this could have the following consequences, not only in project design but also in laboratory experimentation: (1)

an oversizing of the breakwater geometry, increasing the costs; and (2) an uncertainty in the design with unexpected damages and the collapse of the structure (Figure 1).

FIGURE 1: Scheme of the collapse of the main armor layer of a rubble mound breakwater.

For several years the *Environmental Fluid Dynamics Group* of the University of Granada has been working to quantify the hydraulic performance of various breakwater typologies supported by analytical, numerical and experimental works. Specifically, Benedicto (2004) studied for a rubble mound breakwater the influence of wave-breaking type and the geometry of the main armor in the reflection process. These results were applied by Clavero (2007) to concluded that the dissipation by wave-breaking strongly conditions the overtopping phenomenon in rubble mound breakwaters. During the last ten years, the mentioned research group has focused on developing an unified methodology to verify breakwater design based on the hydraulic performance, namely the reflected, transmitted and dissipated energy. The national projects, VIVALDI (2019) and ROM 1.1-18 (2018), and research papers, such as Pérez-Romero et al. (2009), Vílchez et al. (2016a), Vílchez et al. (2016b), and Vílchez et al. (2016c), performed numerical and physical experimentation with important results on this topic. These results are an starting point of this PhD thesis, but it is still necessary to deepen into the knowledge of wave energy transformation on breakwaters with a theoretical approach that explains the physical and numerical results obtained so far.

The uncertainty in the design of the maritime structure worsens when its environment is also considered, in particular, the seabed as a foundation of the breakwater. In recent years, significant progress has been made in the analysis of the interaction between the sea oscillatory regime, the maritime structure and the seabed, usually assuming a foundation with high bearing capacity. However, seabeds do not always have idyllic characteristics to build on them, this being the case of those that are formed by soft soils, totally or partially cohesive. Soft seabeds are vulnerable to wave-induced liquefaction and fluidization due to excess of pore pressure (McAnally et al., 2007). As a consequence, these geotechnical failure modes can provoke important structural failures on breakwaters, such as for example: the sinking of the submerged breakwater on the “Santa María del Mar” beach (Cádiz, Spain) in 1998 (Muñoz-Pérez et al., 2015; Mozahedy, 2016); the sinking of the caisson of the vertical breakwater in the Port of Barcelona (Spain) in 2001 (Alexander et al., 2010).

As a results of these structural damages due to geotechnical failures on the seabed, research studies have analyzed the problem of wave–soft seabed interaction, and its effects on maritime

structures. In this regard, we highlight analytical studies, such as Kumagai and Foda (2002) and Liao et al. (2018), and its verification with numerical models, for example Ye et al. (2013) and Elsafti and Oumeraci (2017). The results provided by the previous researches are a mainstay to advance and to solve the geotechnical problems in the wave-breakwater-seabed interaction. However, these analytical studies have complex solutions to be implemented in numerical models, as well as to extrapolate its results in practical design recommendations. Moreover, the correct experimentation of wave-breakwater-seabed interaction in laboratory is far from being achieved. In this topic, international projects, such as LIMAS (2004) and AREDIS (2015), have carried out laboratory tests and provided some practical guidelines for design and maintenance with regard to geotechnical failures modes of seabed.

Objectives

The main objective of this PhD thesis is to improve the theoretical analysis and characterization of the hydraulic performance of mound breakwaters and its interaction with wind-waves and the seabed. To accomplish this overall objective, the wave-breakwater-seabed interaction is studied in two parts with the following specific objectives:

1. To review and describe the behavior and geotechnical problems of soft soils against wind-waves action and to propose practical recommendations for the design and experimentation of breakwaters on soft seabeds.
2. To deepen in the behavior of dynamic marine-seabed interaction from improving the modeling of sediment transport, cohesive and non-cohesive, under the action of sea oscillations.
3. To apply dimensional analysis for studying the physical processes that dominate the wave energy transformation on mound breakwater, impermeable and permeable.
4. To collate the dependence of the experimental results of wave energy transformation and wave-breaking with Iribarren number.
5. To analyze the experimental variability and study the influence of the physical variables that characterize the hydraulic performance of mound breakwaters.
6. To propose a design methodology for its application in laboratory that identifies the wave generation requirements and the number of wave conditions to quantify the energy transformation on the breakwater.
7. To describe the sources of wave energy dissipation on the main armor layer of mound breakwaters.

Thesis outline

This thesis is structured in two main parts that contains a total of six chapters, in which the specific objectives are addressed.

- *Part I. On the breakwater seabed*, mainly describes the interaction between the sea oscillations and the seabed, with an improvement in its numerical modeling. It also includes the consequences on breakwater and recommendations for the design.
- *Part II. On the breakwater performance*, presents the analysis of wave energy transformation on mound breakwater, which gathers the methodology, results, applications and conclusions.

In Part I, Chapter 1 introduces a revision of properties and behavior models of soft seabeds under wave action. The main structural failures modes associated with geotechnical failures and practical guidelines recommendation are also presented in this chapter. Chapter 2 presents a coupled hydrodynamic and sediment model that quantifies the sediment concentration and transport of a mixed seabed, cohesive and non-cohesive, in the whole water column, from the free-surface down to the seabed.

In Part II, Chapter 3 develops the dimensional analysis and the physical and numerical experimentation to determine the wave energy transformation on mound breakwaters, impermeable and permeable. Chapter 4 presents the experimental results derived from the previous chapter, which includes (1) the dependence of the experimental data with Iribarren number, (2) the analysis of the experimental variability and the similarity parameters that characterize the hydraulic performance on mound breakwaters, and (3) the proposed experimental design methodology for laboratory tests based on the dimensional analysis. Chapter 5 applies the design methodology to a conventional homogeneous mound breakwater and studies the influence of the geometrical variables in the wave energy transformation modes. Finally, Chapter 6 analyzes the role of the main armor layer in the bulk energy dissipation.

The main conclusions of the thesis and some future lines of work are presented in the last chapter. As support of the thesis, Appendix A presents some additional sediment formulas; Appendix B includes wave-breaking description and pictures; and finally, Appendix C gathers the wave generation and method used in this study.

Publications derived from this thesis

The work done throughout this thesis has resulted in the following publications:

Journal Papers

- Díaz-Carrasco, P., Vittori, G., Blondeaux, P. and M. Ortega-Sánchez, M. (2019a). "Non-cohesive and cohesive sediment transport due to tidal currents and sea waves: A case study". In: Continental Shelf Research 183, 87–102. DOI: https://doi.org/10.1016/j.csr.2019.06.008.

- Díaz-Carrasco, P., Moragues, M.V., Clavero, M. and Losada M.A. (2019b). "2D water-wave interaction with permeable and impermeable slopes: dimensional analysis and experimental overview". In: Coastal engineering (under review CENG_ 2019_299_R1).

- Díaz-Carrasco, P., Moragues, M.V., Clavero, M., Ortega-Sánchez, M. and Losada M.A. (Under preparation). "Hydraulic performance of a conventional mound breakwater: experimental design". In: Coastal engineering.

- Clavero, M., Díaz-Carrasco, P., and Losada M.A. (Under preparation). "Bulk wave energy dissipation in the main layer of slope rock and cube armored breakwaters". In: Ocean engineering.

International Conferences

- Vílchez, M., Díaz-Carrasco, P., Clavero, M. and Losada, M.A. (2016). "Verification of the crown wall stability taking into account the hydraulic performance curves". In: Proceedings of 35th International Conference on Coastal Engineering. Estambul, Turquia.

- Díaz-Carrasco, P., Moragues, M.V., Clavero, M., M. Ortega-Sánchez,M. and Losada M.A. (2017). "Wave overtopping on mixed breakwaters and design curves". In: Proceedings of the 8th International Short Course/Conference on Applied Coastal Research. Santander, Spain.

- Díaz-Carrasco, P., Moragues, M.V., Clavero, M., Ortega-Sánchez, M. and Losada M.A. (2018). "Similarity on rubble mound breakwaters tests: analysis and discussion". In: Proceedings of the 7th International Conference of the Application of Physical Modelling in Coastal and Port Engineering and Science. Santander, Spain.

- Clavero, M., Folgueras, P., Díaz-Carrasco, P., Ortega-Sánchez, M. and Losada M.A. (2018). "A similarity parameter for breakwaters: the modified Iribarren number". In: Proceedings of 36th International Conference on Coastal Engineering. Baltimore, Maryland, USA.

- Moragues, M.V., Díaz-Carrasco, P., Clavero, M., Ortega-Sánchez, M. and Losada M.A. (2019). "Climate change impact on the hydraulic performance of breakwaters". In: Proceedings of the 38th International Association for Hydro-Environment Engineering and Research World Congress. Panama City, Panama.

- Moragues, M.V., Díaz-Carrasco, P., Clavero, M., Ortega-Sánchez,M. and Losada M.A. (2020). "Generalized Buckingham's analysis on breakwaters". In: Proceedings of the 8th International Conference of the Application of Physical Modelling in Coastal and Port Engineering and Science. Zhoushan, China.

- Clavero, M., Díaz-Carrasco, P., Losada M.A. (2020). "Bulk wave energy dissipation in cube armored breakwater". In: Proceedings of 37th International Conference on Coastal Engineering. Sydney, Australia.

National Conferences

- Díaz-Carrasco, P., Ortega-Sánchez, M. and Losada M.A. (2016). "Comportamiento de los diques de abrigo frente a la dinámica marina en presencia de suelos blandos". I Jornadas de Investigadores en Formación Fomentado la Interdisciplinariedad. Granada, Spain.

- Díaz-Carrasco, P., Moragues, M.V., Clavero, M., Ortega-Sánchez, M. and Losada M.A. (2018). "Efecto de la subida del nivel del mar en la estabilidad de los diques de abrigo". III Jornadas de Investigadores en Formación Fomentado la Interdisciplinariedad. Granada, Spain.

- Moragues, M.V., P. Díaz-Carrasco, P., Clavero, M., Ortega-Sánchez, M. and Losada M.A. (2018). "Análisis del rebase sobre diques de abrigo". In: III Congreso transfronterizo sobre el Cambio Climático y Litoral - UHINAK. Bilbao, Spain.

- Díaz-Carrasco, P., Moragues, M.V., Clavero, M. and Losada M.A. (2019). "Semejanza dinámica de los diques en talud: 2D re-análisis". In: Proceedings of the 15th National Conference of Jornadas Españolas de Puertos y Costas. Málaga, Spain.

- Losada, M.A., Díaz-Carrasco, P., Moragues, M.V., Clavero M. (2019). "Variabilidad intrínseca en el comportamiento de los diques rompeolas". In: Proceedings of the 15th National Conference of Jornadas Españolas de Puertos y Costas. Málaga, Spain.

- Moragues, M.V., P. Díaz-Carrasco, P., Clavero, M. and Losada M.A. (2019). "Sobre el máximo remonte y rebase potencial en los diques rompeolas". In: Proceedings of the 15th National Conference of Jornadas Españolas de Puertos y Costas. Málaga, Spain.

Others publications reached during the PhD were:

- Magaña, P., Bergillos, R.J., Del-Rosal-Salido, J., Reyes-Merlo, M.A., Díaz-Carrasco, P. and Ortega-Sánchez M. (2018). "Integrating complex numerical approaches into a user-friendly application for the management of coastal environments". In: Science of the Total Environment 624, 979-990. doi:10.1016/j.scitotenv.2017.12.154
- Chiapponi, L., Addona, F., Díaz-Carrasco, P., Losada, M.A. and Longo, S. (2019). "Statistical analysis of the interaction between wind-waves and currents during early wave generation". In: Coastal Engineering (under-review CENG_ 2019_230_R1).

Others conferences reached during the PhD were:

- Díaz-Carrasco, P., Ortega-Sánchez, M. and Losada M.A. (2017). "Generación de oleaje en aguas someras: enfoque teórico aplicado al saco interno de la Bahía de Cádiz". In: Proceedings of the 14th National Conference of Jornadas Españolas de Puertos y Costas. Alicante, Spain.
- Chiapponi, L., Díaz-Carrasco, P., Addona, F., Losada, M.A. and Longo, S. (2018). "Interaction between wind-generated waves and currents". In: Proceedings of the 36th Convegno Nazionale di Idraulica e Costruzioni Idrauliche. Ancona, Italy.

Part I

On the breakwater seabed

Chapter 1

Insights for the behavior of breakwater-seabed interaction

Comment

The results of this section are integrated in the following works:

P. Díaz-Carrasco, M. Ortega-Sánchez, and M.A. Losada (2015). "Recomendaciones para caracterizar y describir la interacción de la dinámica marina con diques de gravedad en suelos blandos". PhD thesis. Master Program in Environmental Hydraulics, University of Granada (Spain): Master Program in Environmental Hydraulics

IBK 10-658. "Diseño de adecuaciones para robustecer la estabilidad de diques en suelos fangosos – AREDIS". Centro para el Desarrollo Tecnológico Industrial. Programa Iberoamericano de Ciencia y Tecnología para el Desarrollo. University of Granada (Spain).

In recent years, significant progress has been made in the characterization and modeling of the interaction of marine dynamics with breakwaters, usually assuming a seabed with high bearing capacity. However, seabeds do not always have suitable characteristics to build on them, such as the cases of soft soils. This chapter reviews and describes the main characteristics and problems that may arise in the wave-structure-seabed interaction. For that purpose, Section 1.2 gathers the properties of different types of seabed and the rheological models that characterize the wave-seabed interaction. Section 1.3 defines the main structural failure modes associated with soil geotechnical failures, based on some real cases founded in the literature. In Section 1.4, recommendations for decision-making during the design and construction of breakwaters are proposed. Finally, Section 1.5 summarizes the main conclusions and future challenges.

1.1 Introduction

The project agents that condition the behavior of maritime structures in general, and breakwaters in particular, are usually the maritime (waves, wave groups and long waves) and the seabed. However, in recent decades, research work has been focused on characterizing and modeling the interaction of sea oscillatory regimes with breakwaters, assuming that the seabed is non-cohesive with high bearing capacity, that is, mainly composed by rocks or coarse gravel. However, the seabed composition does not always present idyllic characteristics to build on them, this being the case of those that are composed by the so-called "soft soils". Soft soils

are composed of different fractions of totally or partially cohesive soils, with low quality and low bearing capacity (Lambe and Whitman, 1991; Mehta, 2013).

On the other hand, ports expansion to achieve higher water depths, as well as problems regarding the management of coastal areas, make necessary to study the behavior of soft soils against marine dynamics, as well as their application for breakwaters foundation. Marine structures are vulnerable to wave-induced liquefaction and fluidization due to wave-induced excessive pore pressure (McAnally et al., 2007). Liquefaction is a physical process of loss of bearing capacity due to the cyclical wave action (seabed settlement). The fluidization process is a particular case of liquefaction, in which soil is an aggregate of particles that flows by accumulation of the pore pressure (seabed slide). Some failure examples of breakwater have been reported in previous literature (Harlow, 1980; Silvester and Hsu, 1989; Sorenson, 1992; Oumeraci, 1994; Franco, 1994; Zhang and Ge, 1996; Guillén, 2008; Alexander et al., 2010; Mozahedy, 2016).

The main reason for the failure of breakwater built on soft seabed in offshore areas could be attributed to the lack of good understanding of the wave–structure-seabed interaction by coastal engineers involved in the design and maintenance of marine structures. In general, the soft seabed has always been dredged and filled with other material with high bearing capacity, generally rocks, gravels or consolidated sands. These actions imply a high economic impact and environmental problems derived from the destruction of marine ecosystems.

Over the last fifty years, research studies have analyzed the problem of wave–soft seabed interaction, and more importantly, its effects on breakwater and other maritime structures. Within these works, we highlight the study of seabed behavior with mechanical models (Maa and Mehta, 1987; Foda et al., 1993), and the wave influence on these models (Maa, 1986; Dalrymple and Liu, 1987), until the advance of wave–structure–soft soil interaction with analytical solutions (Biot, 1901; McDougal et al., 1990; Kumagai and Foda, 2002; Liao et al., 2018) and its verification with numerical models (Ye et al., 2014; Jeng et al., 2012; Ye et al., 2013; Zhao and Jeng, 2015; Elsafti and Oumeraci, 2017). On the other hand, experimental laboratory tests were performed to simulate the seabed behavior under the wave action, when it is composed by sandy soils (Lindenberg et al., 1989) and cohesive soils (Tzang, 1998; Tzang and Ou, 2006; Tzang et al., 2009; Hsu et al., 2013). Moreover, some experimental tests were done to monitor prefabricated structures in beaches (Muñoz-Pérez et al., 2015) and to study the breakwater behavior on soft soils (Chávez et al., 2017).

However, analytical studies have complex and difficult solutions to be implemented in numerical models. The latter not only delays the proper characterization of wave-structure-seabed interaction, but also makes difficult to verify laboratory tests and to extrapolate it in the breakwater design. In addiction, laboratory tests with breakwater on soft soils are still highly complex to be managed due to of the properties of these soils. Consequently, the main purpose of this chapter is to review and describe the behavior of soft soils against marine dynamics, with some recommendations to apply in the design and experimentation of breakwater on soft seabeds. For that purpose, Chapter 1 includes: (1) a comprehensive review and classification of the properties and behavior models of soft soils under wave action, (2) an analysis of the wave-structure-seabed response with the definition of geotechnical and structural failures modes, and (3) some recommendations for the breakwater design depending on the type of soft soil.

1.2 Properties and rheological models

According to the particle size, the importance of the interactive forces and its behavior under the wave action, the soft seabed composition can be classified as,

- Non-cohesive soils: dense, medium and loose sand fall into this group. The attraction and repulsion properties between the particles are irrelevant. The medium to very loose sands are progressively affected by water seepage and can induce liquefaction and fluidization phenomena (Tzang et al., 2009; Muñoz-Pérez et al., 2015).

- Cohesive soils: this group constitutes a complex medium due to the high spatial and temporal variability of their properties. For this reason, it is practically impossible to establish a closed classification of all its variables. Within this group are clays and silts, including transitions between them (silty clays, clayey silts). The physical-chemical relations are determinants of the strong attraction between them. Because of its low permeability, the water filtration through silt or clay progresses so slowly that the liquefaction phenomenon induced by an increase in pore pressure does not usually happen. However, despite its low permeability, under long period of time, these sediments can lose its bearing capacity, and so, undergo fluidization (McAnally et al., 2007).

- Partially cohesive soils (mixed): Between cohesive and non-cohesive soils, there are partially cohesive soft soils as a transition from these two large groups; mainly, we are talking about seabed composed by sand mixed with silt and clay (Lindenberg et al., 1989).

A closed classification and characterization of the soft soils properties entails a high degree of uncertainty associated with the data and also a statistical uncertainty. In ROM 0.5 (2005), ROM 1.1-18 (2018), and Benedicto (2004), there is a detailed classification of the physical-chemical and mechanical parameters that characterize the soils behavior, as well as laboratory and in-situ tests necessary to obtain the values of these parameters.

Soft marine soils can be associated with different behavior models depending on the hydrodynamic conditions and the physical-chemical and mechanical parameters (Maa, 1986). The response of the wave-seabed interaction can be evaluated by rheological models, which relate the stress and the strain of the soil under the wave cyclic action. In this work, we classified the rheological models in two groups: (1) for non-cohesive soils, and (2) for cohesive soils. Figure 1.1 summarizes the main characteristics and conditions of these models, which are described down below.

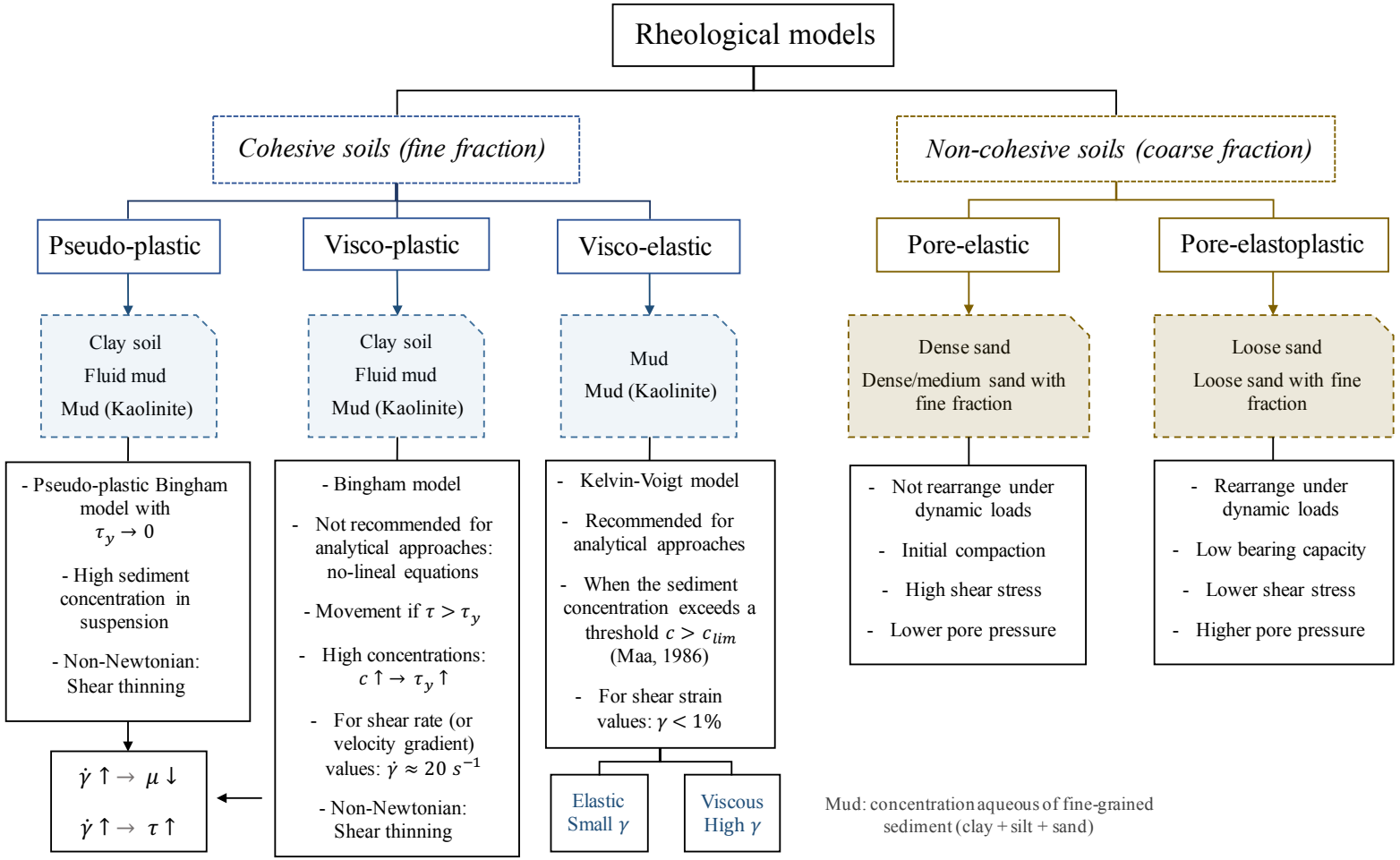

FIGURE 1.1: Classification of the soft soils rheological models.

Non-cohesive rheological models

The non-cohesive soils that fall within this characterization (see Figure 1.1) are dense-loose sands, as well as sands mixed with fine fraction. These soils behave primarily as elastic materials that, in contact with water, have a pore-elastic or pore-elastoplastic behavior (Ye et al., 2014). However, two cases found in the literature are highlighted: silty soil of Foda and Tzang (1994) and Tzang (1998) and soft clay soil (Kaolinite) of Wit and Kranenburg (1997), which behave like pore-elastic materials despite being cohesive soils. These are specific commercial materials for laboratory tests, and so, they are not totally cohesive and can be modeled elastically.

Pore-elastic model

In this model, the material has a non-rigid skeleton, but it is elastic and its pores are occupied by water. In this type of materials, a clear separation can be established between the liquid and solid fraction (Cortés et al., 2004). Thus, soft soils that behave according to a pore-elastic model are those characterized by dense-medium sand or dense-medium sand with fine fraction (Mei and Foda, 1981; Mostafa et al., 1999), which have undergone a prior compaction process due to the rearrangement of its particles.

The pore-elastic model constitutive equation relates the shear stress and the shear strain by the following expression (Mehta, 2013):

$$\tau = G^* \cdot \gamma \tag{1.1}$$

being τ, the shear stress of the soil; γ, the shear strain; and G^*, the complex shear module defined by $G^* = G(1 + i\delta_p)$; where G is the elastic shear module and δ_p the specific energy loss. Yamamoto and Takahashi (1985) proposed empirical expressions of G and δ_p. The Biot (1901)'s analytical model incorporates the pore-elastic behavior of the soil and solves the two- and three-dimensional equations of the wave-structure-seabed interaction.

Pore-elastoplastic model

Unlike the pore-elastic materials, the pore-elastoplastic materials are rearranged under the wave dynamic load, looking for a stable configuration. For this reason, the soils that behave according to a pore-elastoplastic model are those formed by loose sands or sands with fine fraction (Ye et al., 2013; Ye et al., 2014). In fact, these soils can be modeled as pore-elastic materials once they are sufficiently compacted.

In this research line, some experimental tests and numerical models have incorporated the pore-elastoplastic behavior, such as the FSSI-CAS 2D model, but there is no an exact expression of its constitutive equation. Nevertheless, Boroomand and Zienkiewicz (1998) pointed out that the final deformation of the soil will be the sum of the elastic deformation (returnable) and the plastic deformation; that is:

$$\varepsilon = \varepsilon_e + \varepsilon_p \tag{1.2}$$

being ε_e and ε_p the elastic and plastic normal strain, respectively. Ye et al. (2014) investigated the nonlinear interaction mechanism between ocean wave, a composite breakwater and its loose elastoplastic sand bed foundation by utilizing the semi-coupled numerical model FSSI-CAS 2D. Figure 1.2 shows the time history curve of wave-induced pore pressure (P_u) and effective normal stresses ($\sigma_s^{'}$) in the sand seabed. It is observed that, there is a significant increase in the pore pressure (Figure 1.2a) inside the soil, as well as a decrease in the effective stresses (Figure 1.2b), optimal conditions to occur the seabed liquefaction.

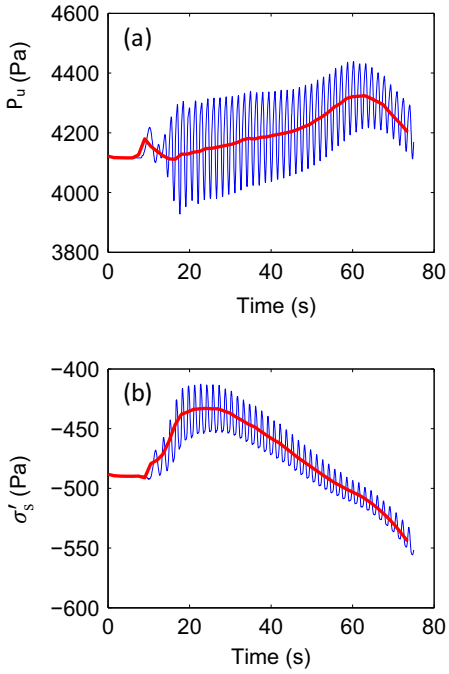

FIGURE 1.2: Time history curve of wave-induced (a) pore pressure (P_u) and (b) effective normal stresses (σ_s') in the sand seabed that behave as pore-elastoplastic model. Figure adapted from Ye et al. (2014).

Cohesive rheological models

The cohesive soft soils behave as no Newtonian (that is, not constant viscosity, μ_s) with deformation and creep properties that are no longer proportional to the strain rate ($\dot{\gamma}$). In these cases, the boundary between the fluid and the solid is not well defined, and the following rheological models appear: visco-elastic, visco-plastic and pseudo-plastic (Maa, 1986; Mehta, 2013).

Visco-elastic model

The response of visco-elastic materials to oscillatory waves is expressed in terms of (i) an elastic energy storage, and (ii) a viscous energy loss. The visco-elastic models are the most used to develop numerical models, and its predicted velocities and movements are coherent with the experimental measurements. The soft soils that behave as a visco-elastic materials are the soils composed by a mixture of clay, silt and water (mud) and soils with Kaolinite (mineral of soft clay) (Maa and Mehta, 1987; Foda et al., 1993; Kessel and Kranenburg, 1998; Kessel, 1998). The conventional visco-elastic model is the "Kelvin-Voigt", which clearly identifies the solid part of the soil and the solid-liquid behavior is independent of the frequency of the wave load. The constitutive equation is:

$$\tau = G \cdot \gamma + \mu_s \cdot \dot{\gamma} \tag{1.3}$$

where G is the elastic shear module; μ_s is the soil viscosity; γ is the shear strain and $\dot{\gamma}$ is the shear rate (Kessel, 1998; Hsu et al., 2013): $\dot{\gamma} = \partial\gamma/\partial t = \partial u_s/\partial y = \partial v_s/\partial x$, being (u_s, v_s), the soil displacements in the horizontal (x) and vertical (y) directions, respectively. For small shear strain, the material can behave like an elastic material (before fluidization phenomenon), while for very large strain it behaves like a viscous material (after fluidization phenomenon) (Foda et al., 1993).

Visco-plastic model

The visco-plastic models are characterized by the existence of an initial creep stress, τ_y, property of the material, and its value is greater as the soil concentration increases (McAnally et al., 2007). Cohesive soils that behave according to a visco-plastic model are clay soils and mud presented in different forms: soft-fluid mud and mud with Kaolinite (Hsu et al., 2013). The extended visco-plastic model is the "Bingham" model, which is a particular case of "Herschel-Bulkley" model (Maa, 1986; Mehta, 2013): $\tau = \tau_y + K_h \cdot \dot{\gamma}^n$. In "Bingham" model, the relation between the shear stress and the shear strain in linear ($n = 1$) and $K_h = \mu_s$. Hence, the constitutive equation remains as

$$\tau = \tau_B + \mu_s \cdot \dot{\gamma} \tag{1.4}$$

where $\tau_y = \tau_B$ is the initial creep stress of "Bingham". The "Bingham" model can be solved, but it does not take into account the momentum transferred through the soil surface. In addition, it does not allow to accurately predict the movements of the material, since it records soil movement if $\tau > \tau_B$. Due to this great uncertainty, it is not recommended for analytical approaches with nonlinear equations (Maa, 1986), or for situations with small shear rates (Kessel, 1998).

Figure 1.3 shows the measured rheological shear stress, τ, and mud viscosity, μ_s, against the shear rate, $\dot{\gamma}$, for four different volumetric concentrations of a soil composed by Kaolinite. It is observed how, as the rate of deformation of the soil increases due to the wave action, the shear stresses increase and the viscosity of the soil decreases. In addition, the initial creep stresses, τ_y, are higher for high soil concentrations.

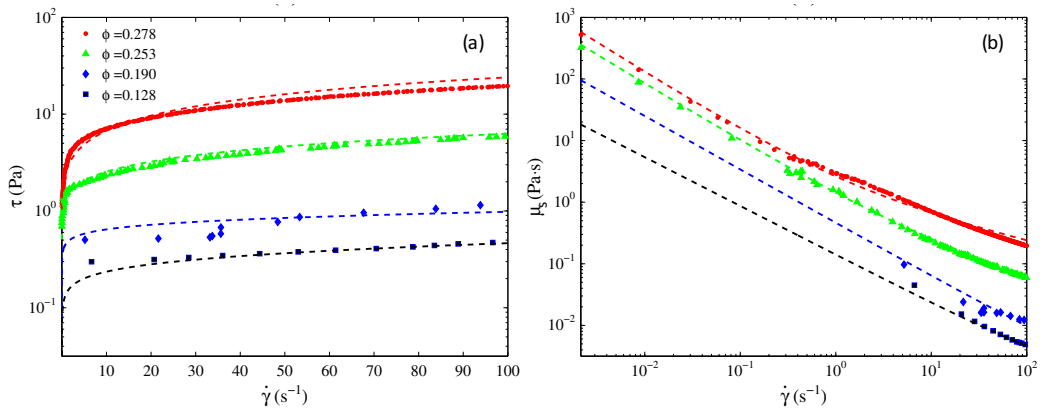

FIGURE 1.3: (a) Shear stress and (b) mud viscosity against the shear rate for four volumetric concentration of a soil composed by Kaolinite. Figure adapted from Hsu et al. (2013).

Pseudo-plastic model

The main characteristic of the pseudo-plastic models is that the initial creep stress tends to zero: $\tau_y \to 0$. The soft soils modeled as pseudo-plastic are the same as the visco-plastic, with the following requirements: (1) soils in suspension, and (2) soils with low shear strains (Maa, 1986). In certain cases, if sediment concentrations are low and the material is in suspension, the soil could be characterized as a Newtonian fluid (elastic).

NOTE

There are analytical solutions that incorporates the rheological models and evaluate the response of the soil under the wave action, as well as the wave-structure-seabed interaction. The reader can find a description in Benedicto (2004) and Chávez (2013).

1.3 Geotechnical and structural failures modes

The lack of knowledge and analysis of soft seabeds entails structural failures modes in maritime structures associated with geotechnical seabed problems. The construction of a breakwater modifies the actions on the seabed with the following consequences:

- The structure transmits a high pressure to the seabed due to its own weight.
- The presence of the breakwater modifies the characteristics of progressive waves, which becomes stationary or partially stationary and, therefore, pressures transmitted directly by the waves to the seabed are modified.
- The interaction between waves and breakwater is also transmitted to the seabed in the form of pressures.

Therefore, there is a wave-induced and structure-induced excessive pore pressure on the seabed foundation, which is the main cause of geotechnical failures modes: liquefaction and fluidization.

Geotechnical failures modes

Liquefaction

Liquefaction is a physical process of loss of bearing capacity of the soil, because the aggregate of particles loses its resistance due to the cyclic action of the oscillatory regime. This type of failure generates seabed differential settlement and occurs in non-cohesive or partially cohesive soft soils, with high permeability (McAnally et al., 2007). There are two types of liquefaction (Ye et al., 2014): (1) instant liquefaction, which occurs in a reduced time frame without drainage, and it does not lead to structural failures; and (2) residual liquefaction, which occurs in a broader time frame with drainage, and it is one of the main risks to loss of stability of breakwater.

The liquefaction phenomenon happens when the soil effective stresses are canceled due to an increase of the pore pressure (general verification equation):

$$\sigma_s^{'} = \sigma_s - P_u \leq 0 \tag{1.5}$$

being σ_s, the total normal stress; $\sigma_s^{'}$, the effective normal shear stress; and P_u, the pore pressure. Chávez et al. (2017) reproduced the failure of a submerged structure on a clayey bed in the presence of waves with laboratory tests. They observed the liquefaction of the clayey bed and defined a set thresholds for bed composition, below which soil liquefaction is likely to occur.

Fluidization

The fluidization failure mode is a particular case of liquefaction and it is more common in cohesive soft soils (low permeability), although it can also occur in non-cohesive soils (McAnally et al., 2007). When waves propagates into the bed, the aggregate of particles is suspended in a fluid matrix that is destroyed by accumulation of pore pressure. The soil

behaves as a fluid and causes seabed slide. The verification equation of fluidization failure mode is the same as of liquefaction.

Tzang and Ou (2006) studied the fluidization of two seabeds with laboratory experiments. Figure 1.4 shows the pore pressure responses of a sandy bed and a silty bed under different wave conditions. In both seabeds, fluidization failure mode was observed, due to significant increase in pore pressure and the permanence of its maximum value for a long interval of time.

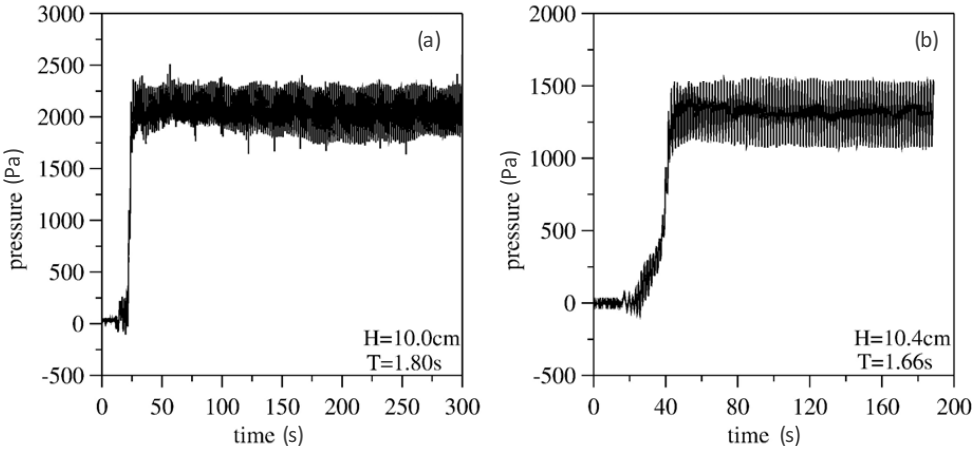

FIGURE 1.4: Typical wave-induced fluidized pore pressure responses in: (a) sandy bed and (b) silty bed. Figure adapted from Tzang and Ou (2006).

Surface erosion

Surface erosion is a failure mode for all types of soils, not just soft soils. It is a major geotechnical failure mode to verify in the design of any maritime structure, since it can causes several structural failures. The surface erosion of the seabed occurs when the wave velocity near to the bottom (friction velocity) generates a shear stress greater than the critical shear stress for erosion (general verification equation):

$$\tau_{cr,e} - \tau_w \leq 0 \tag{1.6}$$

where τ_w is the wave bottom shear stress and $\tau_{cr,e}$ is the soil critical shear stress for erosion. Figure 1.5 adapted from Ye et al. (2014)'s paper represents the velocity field of fluid motion in front of a breakwater on a porous seabed at a fixed time, obtained with the numerical model FSSI-CAS 2D. Velocity field lines are denser in the vicinity of the breakwater, that is, higher velocity values in water column and, thus, greater friction stresses, τ_w, in front of the structure. In addition, there is a partially stationary oscillation with nodes and anti-nodes in front of the breakwater, which contributes to surface erosion of the seabed.

Surface erosion is one of the most frequent problems in coastal areas and in the vicinity of breakwaters. In Chapter 2 the sediment transport under the sea oscillatory regime is studied in order to properly understand the wave-seabed interaction and, with it, to gain deeper insight into this geotechnical failure mode.

Structural failures modes

Soft seabed failure modes can lead to failures in the entire maritime structure or in parts of it. In Oumeraci (1994), there is a review of vertical breakwater failures, being some of them consequence of the seabed by: (1) scour and erosion, (2) differential settlement and (3) sliding.

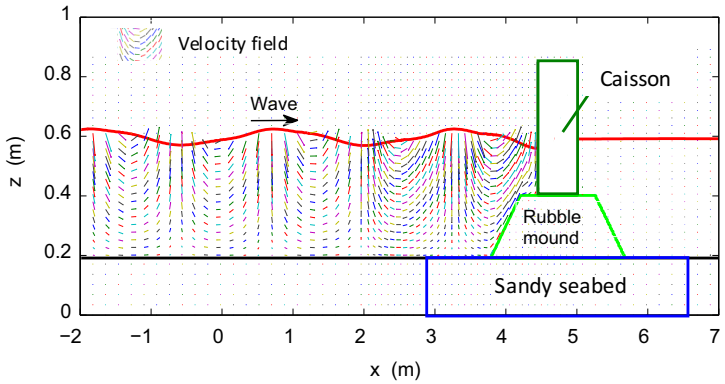

FIGURE 1.5: Velocity field of fluid motion in front of a breakwater on a porous seabed at a fixed time, obtained with the numerical model FSSI-CAS 2D. Figure adapted from Ye et al. (2014)

Scour and erosion of the breakwater toe

The seabed surface erosion may causes erosion of the material of the slope toe or the berm, depending on the breakwater typology. This failure mode progressively generates others structural problems, such as (Figure 1.6): (1) extraction or sliding of pieces of the main armor layer, (2) progressive scour of the breakwater base, and (3) seaward tilt of the caisson.

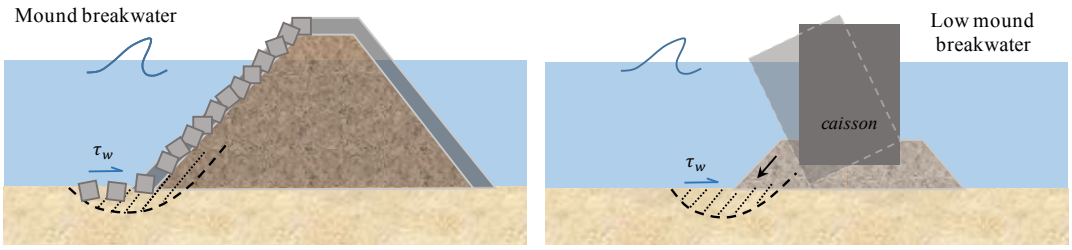

FIGURE 1.6: Scheme of structural failures modes associated to the seabed surface erosion.

Sinking and sliding of the breakwater

As a result of the bearing capacity loss of the seabed by liquefaction or fluidization, the total or partial collapse of the structure occurs. Other failure modes that derive from the breakwater sinking and sliding are (Figure 1.7): (1) seaward tilt of the caisson, (2) internal cracks in the caisson or in the berm/slope, and (3) extraction or sliding of pieces of the main armor layer.

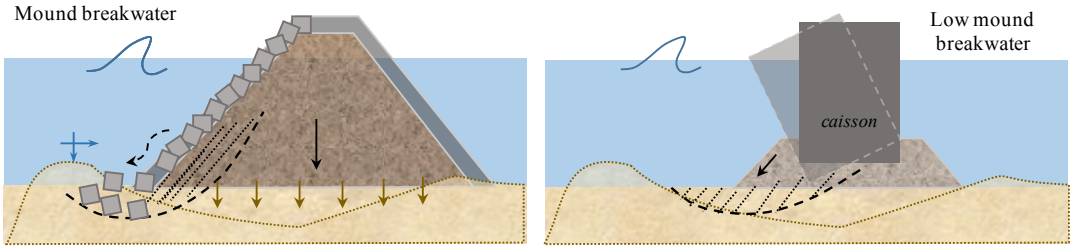

FIGURE 1.7: Scheme of structural failures modes associated to the seabed liquefaction or fluidization.

Even though many structural failures modes are consequence of the mismatch between the breakwater load and the seabed bearing capacity, most of them are due to the wave

action on the breakwater. Hence, Part II of this Thesis presents the analysis of wave energy transformation on mound breakwaters in order to characterize the wave-breakwater interaction and, with it, to prevent the structural failures modes and properly design breakwater.

1.4 Design recommendations

This section proposes project recommendations for the design of breakwaters on soft seabeds under wave action. The recommendations are subdivided in two groups: (i) seabed composed by soils that must be replaced by other material; and (ii) seabed that with treatment can be used as foundation for breakwaters. To know in which group the seabed is found, experimental tests must be done to quantify the response and characteristics of its composition. These experimental tests may consist of: (1) measurements in field campaigns (in situ); (2) laboratory tests, and (3) physical-chemical and mechanical tests, such as oedometer test, triaxial test, etc.

(I) Dredged and fill materials

Clay o partially clay soils

Seabed with more than 40% of clay content should be dredged and filled by other materials, whose consistency and bearing capacity are more adequate, such as a refill of gravels or consolidated sands. Hence, this type of soil marks the threshold value to considered inadmissible the seabed as a foundation of breakwaters. The reasons are:

- Clay deformation is plastic and non-returnable.
- In wave-clayey seabed interaction, mud viscosity significantly decreases under the cyclic wave action and the soil behaves as a fluid.
- The potential to liquefy increases with soils of 40% or more clay content (Chávez et al., 2017).
- These soils can continue to reduce its thickness to an additional 10% compared to the primary soil settlement.
- Clays expand and can lead to seabed expansion problems and, thereby, structural failures in breakwaters.

Homogeneous cohesive soils

The following recommendations are proposed for these soils:

- If experimental tests prove that the soil is too soft: replace and fill the first layers in contact with the structure.
- Room for improvement with: (1) complete drainage with drains and filters; (2) columns of gravel or sand to achieve more dense and heterogeneous soil with higher consistency and bearing capacity.

Despite these treatments, geotechnical failures modes usually occur in cohesive soft soils. Therefore, it is advisable and necessary also to follow the project recommendations for non-cohesive or partially cohesive soils (described below).

(II) Soil treatments

Non-cohesive or partially cohesive soils (mixed with fine fraction) can be used as a foundations of breakwater as long as they are previously treated. In this section, project recommendations are proposed according to the three geotechnical failure modes described in Section 1.3.

Recommendations against surface erosion

To mitigate and avoid the surface erosion failure mode, the following project recommendations are proposed:

- To carry out maintenance activities: (i) periodic revisions of the berm/slope; (ii) to replace damaged units pieces of the berm/slope.
- To change the type of pieces for others with a more resistant configuration.
- To add one or more layers in order to increase the resistance of the breakwater berm/slope.
- To inject under the toe of the berm/slope a granular material refill with greater diameters than those of the soft seabed. This treatment increases the soil resistance and reduces the critical shear stress under the toe of the berm/slope.
- To increase the height of the berm in order to achieve greater wave energy dissipation and lower friction stresses transmitted to the seabed.
- To place drains that collect water from the toe and base of the breakwater.

Recommendations against liquefaction and fluidization

To prevent the liquefaction and fluidization failures modes, we propose:

- To perform maintenance activities.
- To construct equi-spaced drainage joints inside the breakwater caisson. This treatment allows draining the water inside the breakwater and reduces the pore pressure transmitted to the seabed.
- To position filters in the berm, slope and granular core of the breakwater that collect the water infiltrated and reduce the pore pressure.
- If pore pressure is very high, its value should be reduced with:
  - Soil drainage: number of drains and filters according to the soil cohesion.
  - Drainage joints in the breakwater base, caisson base and in other structural parts where the pore pressure can become large.
- If soil is too soft, total normal stress (σ_s) must be increased to not be canceled with the pore pressure. The latter is achieved by increasing soil density (ρ_s) with the following techniques:
  - Vibroflotation compaction technique: recommended for non-cohesive soils with 10-15 % fine content. This technique is valid up to the first 20 m deep.
  - Dynamic compaction technique: more complicated to carry out in seabeds due to its methodology.

  - Gravel columns: very useful for mixed soils in which its cohesion prevents compaction of particles by vibration.

- If bearing capacity and consistency of the soil are very low, it is recommended:

  - Structural joints along the breakwater, which divide the structure in independent parts. With this method, lower shears and effective stresses are achieved.
  - Solution by special foundations and piles that transmit the stresses of the structure to resistant layers of the seabed.

1.5 Conclusions

This chapter presents a review of the properties, rheological models and failures modes that arise in the wave-structure-seabed interaction. Furthermore, some projects recommendations for the design and construction of breakwaters on soft seabeds are proposed according to the composition of the seabed and the geotechnical failures mode to prevent. The main conclusions derived from this study are:

1. Non-cohesive or partially cohesive soft soils behave according to a pore-elastic or pore elastoplastic model, depending on the soil compaction degree. For soft cohesive soils, the best model that suits the behavior of the soil under wave action is the visco-elastic model. Noticed that, these models have a high degree of uncertainty, since they are a limited and restricted version of the reality.

2. There are analytical solutions that incorporates rheological models and evaluates the response of the soil under wave action, as well as the wave-structure-seabed interaction. The reader can find a description of analytical models in Benedicto (2004) and Chávez (2013).

3. Soft seabeds are mainly affected by liquefaction or fluidization phenomenons. The excess pore pressure due to the wave action and the presence of the breakwater cancels the effective stresses of the soil and it loses its bearing capacity.

4. The surface erosion is also an important failure mode that usually occurs in any composition of the seabed.

5. Seabed with 40% or more clay content is the threshold to considered inadmissible the seabed as a foundation of breakwaters and should be dredged and filled by other materials.

6. Homogeneous cohesive soils should be very treated to improve its resistance. If they are too soft it is recommended to replace them with other materials.

7. In general, it is advisable and necessary to always treat seabeds composed by soft soils. Specifically, a treatment can be made to a greater or lesser extent according to the maximum probability of failure by surface erosion and/or liquefaction and fluidization.

This work is a starting point to get more fully acquainted with the behavior of the seabed with direct application in the management and design of breakwaters. Nevertheless, after the extensive review in the literature of this topic, we observed that part of the complexity in modeling and characterizing the wave-breakwater-seabed interaction, is due to the fact that both wave-breakwater interaction and wave-seabed interaction are not still completely dominated. Consequently, this thesis has focused on analyzing and improving the characterization of each interaction separately in order to address the complete interaction as a future challenge.

Chapter 2

Sediment transport due to tidal currents and sea waves

Comment

The present chapter presents a theoretical model to determine the sediment transport rate published on:

P. Díaz-Carrasco, G. Vittori, P. Blondeaux, and M. Ortega-Sánchez (2019a). "Non-cohesive and cohesive sediment transport due to tidal currents and sea waves: A case study". In: *Continental Shelf Research* 183, pp. 87–102. DOI: https://doi.org/10.1016/j.csr.2019.06.008

Coastal regions are the most exploited areas settled by humans, with managements problems due to the sediment transport, such as both scouring and sedimentation near marine structures. To properly manage the coastal environments in these shallow water areas, it is essential to accurately model the wave-current interaction and its effects on sediment transport. Therefore, the main purpose of this chapter is to improve the modeling of sediment transport rate under the action of sea oscillations, in particular, under the combined action of sea waves and tidal currents. For that, the chapter is structured as follows: the hydrodynamic and morphodynamic modules are outlined in Section 2.2. The numerical approach used to determine the flow field and the sediment transport is presented in Section 2.3 which also describes the validation of the model. Section 2.4 presents the results focusing on (i) the effects of the combined action of waves and steady currents on the sediment concentration and the bed/suspended load transport and (ii) the influence of cohesive material on sediment concentration. Finally, the conclusions are summarized in Section 2.5.

2.1 Introduction

Estuaries, lagoons and coastal regions are the most important and intensely exploited areas settled by humans (Masselink and Hughes, 2003). Some management problems of these areas, such as scour and pollution near marine structures, silting of navigation channels, self-burial of pipelines and sedimentation at tidal inlets (Zhang et al., 2016; Reyes-Merlo et al., 2017; Tang et al., 2017; Yao and Liu, 2018), strongly depend on the time development of the seabed morphology, which in turn is related to sediment transport processes. Despite relevant achievements over the last decades (Van Rijn, 1993; Blondeaux and Vittori, 1999; Blondeaux, 2012; Park and Latrubesse, 2014; Belde and Back, 2017; Forsberg et al., 2018; Dale et al., 2018), to the author's knowledge, the understanding of the sediment behavior

in these shallow water areas still requires further studies and, in particular, the investigation of the region closest to the bottom (buffer layer and viscous sublayer for a smooth bottom), which is usually not considered in detail.

The suspended sediment concentration and sediment transport in estuarine and coastal regions are mainly dominated by the combined action of waves and currents (Wang, 1989; Lee and Dade, 2004; Franz et al., 2017). Indeed, the hydrodynamic conditions control and affect sediment resuspension, mixing, and transport processes. In particular, the oscillating bottom shear stress induced by the interaction of currents and propagating surface waves determines the pick-up rate of the sediments from the bottom (Vittori, 2003). Then, the sediments are diffused by turbulence and transported mainly by the currents. Consequently, to properly manage the coastal environment and design sustainable strategies to control sediment problems, it is essential to accurately model the wave-current interaction and to evaluate the flow close to the bottom where the pick-up of the sediment from the seabed takes place (Amoudry and Liu, 2010; Zhang et al., 2011).

In the recent decades, significant improvements have been achieved in the analytical and numerical modeling of the concentration of suspended sediments and their transport (Van Ledder et al., 2006; Sanford, 2008; Waeles et al., 2008; Lu et al., 2015). The study of wave-current interaction and sediment transport has been conducted using both experimental and numerical approaches. The first attempts to model the turbulent boundary layer induced by propagating waves close to the bottom were based on a time-invariant eddy viscosity (see for example Grant and Madsen, 1979). Yu et al. (2010) studied the sediment transport induced by asymmetrical wave groups and Myrhaug et al. (2015) investigated the turbidity distribution forced by the combined action of waves and tidal currents. More recently, Lu et al. (2017) modeled the wave-current-sediment interaction over rippled bed. Others, such as Xu and You (2017) and Santoro et al. (2017), applied different transport models to the coastal region. However, to save computational resources, the numerical codes commonly used, in particular for practical applications (e.g. DELFT3D, ROMS, GOTM/GEMT), do not consider the flow in (a) the buffer layer, where the viscous and the Reynolds stresses are both not negligible, and (b) the viscous sublayer (when the sea bottom behaves as a smooth wall), where the Reynolds stresses are still small here because of the dominance of viscous effects.

Indeed the turbulence models, which are usually implemented, enforce the boundary conditions at "some distance" from the seabed (larger than $30\nu^*/u_\tau^*$, being ν^*/u_τ^* the viscous length, ν^* the kinematic viscosity of the water and u_τ^* the shear velocity), assuming the presence of an "equilibrium layer", where the velocity is assumed to follow a logarithmic profile and the turbulent kinetic energy to satisfy a Neumann condition. This logarithmic profile reasonably describes the velocity as function of the distance from the bottom in the equilibrium layer when the flow is steady (current case), but laboratory measurements (e.g. Jensen et al., 1989; Akhavan et al., 1991) show that there are phases of the wave cycle during which a logarithmic profile does not exist (oscillatory flow case). A better evaluation of the flow close to the seabed, that is, in the buffer region and in the viscous sublayer is of particular relevance to investigate the behavior of mixed (non-cohesive and cohesive) sediments because the turbulent eddies, which are generated in the near-bed region, pick-up a lot of sediments from the bottom and put them into suspension, thus determining the sediment transport rate.

Consequently, in order to extend our knowledge of sediment behavior under wave-current conditions, the present chapter quantifies the sediment concentration and the sediment transport by means of a model able to consider the whole water column, from the free surface downward till the seabed. Moreover, since in particular coastal areas (e.g. lagoons, estuaries) the sediment is a mixture of sand and mud, the seabed is assumed to be composed by both cohesive and non-cohesive sediments. The method is based on a sediment transport module, which

calculates the suspended sediment concentration and transport in a mixed seabed, associated to a hydrodynamic module that reproduces the oscillatory motion induced by (a) an isolated steady current and (b) the combined action of waves and steady currents. The proposed model is conceived as an extension and advance in the simulation of sediment concentration and transport by wave-current interaction since (i) it includes the Menter's turbulence model (Menter, 1994), which reproduces well the turbulence structure both within the bottom boundary layer and above it up to the free surface, and (ii) it provides an accurate description of the vertical distribution of both the non-cohesive and cohesive sediment concentration.

Unfortunately, even though an appropriate modeling of turbulence dynamics allows to obtain a reliable description of the sediment transport, one of the main weaknesses of modeling the sediments is the behavior of the cohesive fraction, which is associated with the amount of empirical formulations (fall velocity, erosion and deposition rates) and empirical parameters (critical shear stress for erosion and deposition) that should be introduced to describe the dynamics of the cohesive fraction. Moreover, due to the limitations of the devices for the measurement of the suspended sediment concentration very close to the bed (Rose and Thorne, 2001), it is also difficult to have a comprehensive assessment of the concentration profile and to validate the numerical/analytical formulations developed for cohesive sediments.

2.2 Formulation of the problem

The suspended sediment concentration and sediment transport due to the simultaneous presence of steady currents and wind waves propagating in shallow waters is studied by an integrated numerical model, which is made up of two modules: the hydrodynamic module and the sediment transport module. In the first subsection (§2.2.1), the flow field, generated by the interaction of a propagating surface wave and a steady current in shallow waters, is determined using the Reynolds Average Navier-Stokes approach (RANS approach) and introducing an appropriate turbulence model. In particular, the two-equation turbulence model of Menter et al. (2003) is chosen to describe the turbulence structure both in the bottom boundary layer and in the "core" region, i.e. the region extending from the boundary layer up to the free surface. In the second subsection (§2.2.2), the sediment transport module, which determines the vertical distribution of sediment concentration and the sediment transport when the seabed is composed of a mixture of non-cohesive and cohesive sediments, is described.

2.2.1 The hydrodynamic module

In shallow areas, the tidal currents are often significant and their interaction with the waves largely affects the hydrodynamic and morphodynamic processes. Therefore, the oscillatory flow due to the interaction of sea waves and currents in shallow waters (Figure 2.1) is investigated by assuming that the ratio between the water depth h^* and the length of the sea waves L^* is small enough to make it possible the use of the shallow water approximation. Hence, the pressure distribution turns out to be hydrostatic and the forcing term driving the fluid motion is simply the surface slope, which is assumed to be the sum of a constant value plus an oscillatory value. Moreover, because of the assumption $\frac{h^*}{L^*} \ll 1$, the diffusive terms in the horizontal directions can be neglected with respect to the diffusive terms in the vertical direction. A detailed description of the derivation of the three-dimensional shallow water equations can be found in Vreugdenhil (2013). In particular, Vreugdenhil (2013) states that the x^*- and z^*-derivatives of the viscous and turbulent stresses can be neglected with respect to the y^*-derivatives even though they are usually retained to simplify the derivation of the depth-averaged version of the equations. Finally, the wave amplitude is assumed to be small

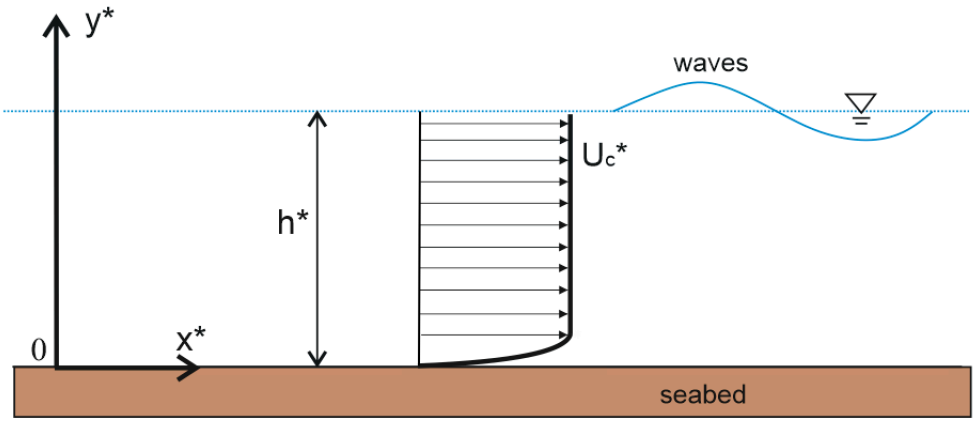

FIGURE 2.1: Sketch of the problem.

enough to use a linear approach to describe wave propagation, thus neglecting non-linear terms (Dalrymple and Dean, 1991).

The hydrodynamic module makes use of dimensionless variables. Since the aim of the analysis is the evaluation of both the bed load and the suspended load during the wave cycle, an accurate description of the flow close to the sea bottom is necessary. Hence, the vertical coordinate y^* is scaled with the Stokes thickness $\delta^* = \sqrt{2\nu^*/\sigma^*}$ of the bottom boundary layer, even though the possible presence of cohesive sediments, which can be more easily transported far from the bottom, makes it necessary to determine the flow field over the whole water column. Moreover, the angular frequency σ^* of the surface wave is used to scale the time t^* and ν^* indicates the kinematic viscosity of the water. Finally, the amplitude of the velocity oscillations close to the bottom induced by the waves, U_0^*, is the velocity scale. Assuming the direction of the waves propagation, x^*-axis, to be coincident with the current direction and the vertical y^*-axis pointing upward, the following dimensionless variables are introduced

$$(x,y) = \frac{(x^*,y^*)}{\delta^*}; \quad t = t^*\sigma^* \tag{2.1}$$

$$(u,v,\hat{U}_c) = \frac{(u^*,v^*,\hat{U}_c^*)}{U_0^*}; \quad p = \frac{p^*}{\rho^*(U_0^*)^2}$$

where u^*, v^* are the fluid velocity components along the x^*- and y^*-directions, respectively; $\hat{U}_c^*$ is the depth-averaged value of the velocity due to the steady current; p^* indicates the total pressure; and ρ^* is the density of the water.

Because of the presence of a steady current (U_c^*), the flow induced by the interaction of the waves and the current is assumed to be turbulent and Reynolds-averaged quantities are introduced. Following the shallow water approximation, the momentum equation along the x^*-axis reads

$$\frac{\partial U}{\partial t} = C_0(t) + C_s + \frac{1}{2}\frac{\partial}{\partial y}\left[R_\delta\langle -u'v'\rangle + \frac{\partial U}{\partial y}\right] \tag{2.2}$$

where $C_0(t) = \frac{\partial U_0}{\partial t} = \cos(t)$ indicates the dimensionless oscillatory pressure gradient which drives the flow associated with the propagating waves and C_s is the dimensionless steady pressure gradient that drives the current; u', v' are the turbulent velocity fluctuations defined by $u' = u - U$ and $v' = v - V$ along the x^*- and y^*-axes, respectively; U and V are the

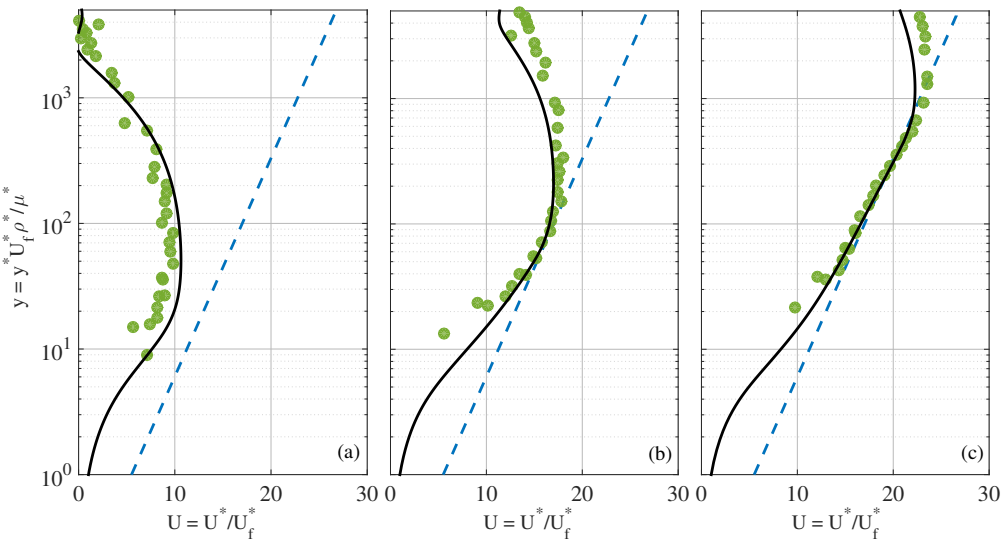

FIGURE 2.2: Experimental data of test 10 Jensen et al. (1989) (green points) together with the log-law (blue broken line) and results obtained by means of Menter's model (black solid line). The three panels indicate different phases: (a) t=0^o, (b) t=15^o, (c) 45^o. The y and x-axis are dimensionless according to Jensen et al. (1989)'s figures: U_f^* is the bed friction velocity.

Reynolds-averaged velocity components in the streamwise direction and upward direction, respectively; and $\langle X \rangle$ indicates the Reynolds-averaged value of the quantity X. In Equation 2.2, the Reynolds number,

$$R_\delta = \frac{U_0^* \delta^*}{\nu^*} \tag{2.3}$$

appears. To quantify the turbulence stress $\langle -u'v' \rangle$ and to close the hydrodynamic problem, a turbulence model should be introduced. For practical application, the Boussinesq's eddy-viscosity concept is commonly introduced and the turbulent stress is written in the form

$$\langle -u'v' \rangle = \frac{\nu_T}{R_\delta} \frac{\partial U}{\partial y} \tag{2.4}$$

where $\nu_T = \nu_T^*/\nu^*$ is the dimensionless kinematic eddy viscosity, which in our problem depends on both y and t.

The kinematic eddy viscosity is modeled by means of a two–equation RANS model. The most appropriate model for the problem under investigation should provide an accurate description of the flow both close to the bottom, in order to allow a reliable evaluation of the amount of sediment picked up by the flow, and far from the bottom, where the suspended sediments are present. Many turbulence models assume that close to the wall the velocity profile follows the log-law. However, experimental measurements (see for example the data by Jensen et al., 1989) show that there are phases of the oscillation cycle during which the velocity profile deviates from the log-law. Considering the well-documented weaknesses of the $k-\varepsilon$ model in describing boundary layers with strong pressure gradients and of the $k-\omega$ model in predicting turbulent quantities in the wake region of the boundary layer, (see Pope (2000) and Menter (1994) for an extended discussion of the characteristics and shortcomings of the two turbulence models), we choose to use Menter's model, because it overcomes both shortcomings (Menter, 1994). Figure 2.2 shows the performance of Menter's model in predicting the velocity profile of test 10 by Jensen et al. (1989) at the phases during which the velocity profiles does not follow the log-law. In this respect, Menter's model can be regarded as superior to both $k-\varepsilon$ and $k-\omega$ models for the problem under investigation.

The basic idea of Menter's model is to keep the formulation of the $k-\omega$ model (Wilcox, 1988) in the near-bottom region and to take advantage of the more accurate description of the eddy viscosity, provided by the $k-\varepsilon$ model (Jones and Launder, 1972), far from the bottom. The blending between the two models is obtained by using a blending function $F_1(y)$, which changes gradually from 1 to 0 moving from the bottom to the free surface (see Appendix A.2). The interested reader is referred to Menter (1994) for more details of the model and for a discussion of the improvements of this model with respect to the original $k-\varepsilon$ and $k-\omega$ models.

The turbulent kinetic energy per unit mass k^* and the pseudo-vorticity ω^* are determined by solving the advection-diffusion equations which, with the assumptions already introduced, read as

$$\frac{\partial k}{\partial t} = \frac{1}{2}\frac{\partial}{\partial y}\left[(1+\nu_T\sigma_k)\frac{\partial k}{\partial y}\right] + P_k - \frac{R_\delta}{2}\beta_k\omega k \tag{2.5}$$

$$\frac{\partial \omega}{\partial t} = \frac{1}{2}\frac{\partial}{\partial y}\left[(1+\nu_T\sigma_\omega)\frac{\partial \omega}{\partial y}\right] + R_\delta\left[\gamma P_\omega - \frac{\beta_\omega}{2}\omega^2 + (1-F_1)\sigma_{\omega 2}\frac{1}{\omega}\frac{\partial k}{\partial y}\frac{\partial \omega}{\partial y}\right] \tag{2.6}$$

where k^* is made dimensionless using $U*_0^2$ as scale quantity and ω^* by using U_0^*/δ^*. The kinematic eddy viscosity, introduced by Boussinesq assumption, turns out to be

$$\nu_T = \frac{\nu_T^*}{\nu^*} = \min\left(R_\delta\frac{k}{\omega}, R_\delta\frac{a_1 k}{DF_2}\right). \tag{2.7}$$

and D has the following expression

$$D = \left|\frac{\partial U}{\partial y}\right| \tag{2.8}$$

The production terms P_k and P_ω along with the blending function F_1 and the values of the constants, which appear into the model equations, are given in Appendix A.2.

At the lower boundary of the fluid domain, where the bottom is located, the no-slip condition is enforced. Moreover, the turbulent kinetic energy should vanish and the pseudo-vorticity is given a value which depends on the roughness parameter k_s^+:

$$U = 0,\ \ k = 0,\ \ \omega = 2\tau_w S_R(k_s^+)\ \text{ at }\ y = 0 \tag{2.9}$$

where τ_w is the dimensionless bottom shear stress

$$\tau_w = \frac{\tau_w^*}{\rho^* U_0^* \sigma^* \delta^*} = \frac{1}{2}\left[\frac{\partial U}{\partial y}\right]_{y=0} \tag{2.10}$$

k_s^+ is equal to $\frac{k_s^* u_\tau^*}{\nu^*} = k_s\sqrt{2R_\delta\tau_w}$, being k_s^* the bottom roughness, $u_\tau^* = \sqrt{\tau_w^*/\rho^*}$ the shear velocity and $k_s = k_s^*/\delta^*$ is the dimensionless roughness size. The function S_R was provided by Wilcox (1988). Herein, taking into account that (i) k_s^+ varies during the wave cycle and (ii) for values of k_s^+ smaller than 2 the bottom behaves like a smooth bottom, we assume:

$$S_R = 625 \text{ for } k_s^+ < 2;\ \ S_R = \left(\frac{50}{k_s^+}\right)^2 \text{ for } 2 \le k_s^+ < 25;$$

$$S_R = \frac{100}{k_s^+} \text{ for } k_s^+ \ge 25 \tag{2.11}$$

On the free surface, a symmetric free slip condition is enforced. Taking into account the assumption of wave amplitudes much smaller than the local water depth, the boundary conditions can be enforced at $y = h^*/\delta^*$

$$\frac{\partial U}{\partial y} = \frac{\partial k}{\partial y} = \frac{\partial \omega}{\partial y} = 0 \text{ at } y = h^*/\delta^* \tag{2.12}$$

A relationship to compute τ_w, alternative to Equation 2.10 but less prone to numerical errors, can be obtained by using momentum equation and the vanishing of the shear stress at the free surface

$$\tau_w(y) = -\int_y^{h^*/\delta^*} \left(\frac{\partial U}{\partial t} - C_0(t) - C_{sl} \right) dy \tag{2.13}$$

2.2.2 The sediment transport module

Often in estuaries, lagoons and coastal regions, the presence of cohesive material on the bottom makes it necessary to consider both non-cohesive and cohesive sediments. There is no general agreement on the modeling of the behavior of mixtures of non-cohesive and cohesive sediments. Moreover, many models require the evaluation of empirical parameters which are difficult to measure. In this study, the non-cohesive and cohesive fractions are dealt with separately.

To investigate the suspension distribution in a turbulent flow, most studies computed the suspended load as the flux of the sediment concentration, which is obtained by the solution of the advection-diffusion equation (Ni and Wang, 1991; Schumer et al., 2001) which, because of the assumptions already introduced reads:

$$\frac{\partial c_i}{\partial t} = \frac{1}{2} \left[\frac{R_\delta}{\sqrt{\Psi}} \frac{\partial (w_{s,i} c_i)}{\partial y} + \frac{\partial}{\partial y} \left(D_T \frac{\partial c_i}{\partial y} \right) \right] \tag{2.14}$$

where the sub-index i ($i =$ nc, c) indicates the non-cohesive fraction and cohesive fraction, respectively. In Equation 2.14, c_i is the volumetric sediment concentration (the mass concentration can be simply obtain by means its definition $c_i^* = \rho_s c_i$); $\Psi = \frac{U_0^{*2}}{(s-1) g^* d_{nc}^*}$ is the sediment mobility number, being d_{nc}^* the representative diameter of non-cohesive sediment, and $s = \rho_s^*/\rho^*$ ($s = 2.65$) is the ratio between the sediment and water densities; $w_{s,i}$ is the dimensionless settling velocity of the sediment (see the expression in Appendix A.1), which is scaled for both non-cohesive and cohesive fractions with the velocity $\sqrt{(s-1) g^* d_{nc}^*}$; and D_T is the dimensionless diffusion coefficient ($D_T = D_T^*/\nu^*$).

There is a large debate on the value of D_T^* and on its relation with the eddy viscosity. In a turbulent flow the centrifugal forces acting on the sediment particles (being of higher density) are greater than those on the fluid particles, thereby causing the sediment particles to be thrown to the outside of the turbulent eddies, with a consequent increase in the effective mixing length (Fredsoe and Deigaard, 1992). Hence, in this study the diffusion coefficient

$$D_T = \frac{\nu_T}{S_c} \tag{2.15}$$

is expressed in terms of the Schmidt number S_c, which herein is set equal to 0.7 if not otherwise specified.

The sediment concentration is controlled by the boundary condition at the bottom. As already mentioned, the non-cohesive and cohesive fractions are handled separately by taking into account that the bottom is made up by known percentages of non-cohesive and cohesive sediments. For the non-cohesive fraction, a pick-up function is used to fix the erosion rate and to quantify the time-dependent vertical gradient of the sediment concentration at the reference level $y = y_a$:

$$\left[\frac{\partial c_{nc}}{\partial y}\right]_{y_a} = \begin{cases} 0 & \text{if } \tau_w^* \leq \tau_{cr,susp}^* \\ -\frac{R_\delta}{D_T\sqrt{\Psi}}(\alpha_{nc}E_{nc}) & \text{if } \tau_w^* > \tau_{cr,susp}^* \end{cases} \tag{2.16}$$

where α_{nc} indicates the percentage of the non-cohesive sediment fraction of the bed material. In Equation 2.16, $\tau_{cr,susp}^*$ is the critical shear stress for the inception of the suspended load (Van Rijn, 1984b). Moreover, the erosion rate E_{nc} is computed as $c_a w_{s,nc}$, being c_a a reference volumetric sediment concentration that is evaluated by means of different empirical relationships depending on the seabed morphology (flat/rippled bed). The relationships of c_a and y_a are given in Appendix A.1.

For the cohesive sediment fraction, the pick-up rate vanishes if the bottom shear stress is smaller than the critical shear stress for erosion ($\tau_{cr,e}^*$), which is assumed equal to the critical shear stress for deposition ($\tau_{cr,d}^*$). Otherwise, the cohesive fraction is eroded and the flocs (cohesive mass formed by aggregation of individual particles) are broken by the bottom shear stress and there is no settling ($w_{s,c} = 0$). The values of $\tau_{cr,e}^*$ and $\tau_{cr,d}^*$ depend of the characteristics of the bed material (e.g. mineral composition, salinity, amount of organic material), bed structure and other variables (Van Rijn, 1993; Chen et al., 2018). Field studies or laboratory measurements must be made to obtain the critical shear stress for erosion and deposition at a given site. Herein, we fix $\tau_{cr,e}^* = \tau_{cr,d}^* = 0.35$ N/m^2. The boundary condition for cohesive sediment at the reference level $y = y_a$ is:

$$\left[\frac{\partial c_c}{\partial y}\right]_{y_a} = \begin{cases} 0 & \text{if } \tau_w^* \leq \tau_{cr,e}^* \\ -\frac{R_\delta}{D_T\sqrt{\Psi}}(\alpha_c E_c) & \text{if } \tau_w^* > \tau_{cr,e}^* \end{cases} \tag{2.17}$$

where α_c denotes the percentage of cohesive sediment fraction; y_a is equal to $2d_c^*/\delta^*$ (d_c^* being the representative diameter of the cohesive sediment); and E_c is the erosion rate for the cohesive sediment, which is computed by using the formula of Partheniades (1965) and made dimensionless as

$$E_c = \frac{M_e^*}{\rho_s^*\sqrt{(s-1)g^* d_{nc}^*}}\left(\frac{\tau_w^*}{\tau_{cr,e}^*} - 1\right) \tag{2.18}$$

where M_e^* is a coefficient of erosion rate. The values of M_e^* suggested in the literature differ by orders of magnitude. Often, field studies or laboratory measurements must be made to obtain the erosion constant rate M_e^* at the considered site. In this study, following the numerical investigation of fine sediment re-suspension of Cheng et al. (2015), we take $M_e^* = 8.0825 \cdot 10^{-4}$ kg/(m^{2}s).

At the free surface boundary, zero flux conditions for both the non-cohesive and cohesive sediments are imposed:

$$w_{s,i}c_i + \frac{\sqrt{\Psi}D_T}{R_\delta}\frac{\partial c_i}{\partial y} = 0 \text{ at } y = h^*/\delta^* \tag{2.19}$$

The time-averaged transport rate of sediment in suspension both for the cohesive and the non-cohesive sediments ($\overline{q}_{S,i}$) is computed by evaluating the average over a wave cycle ($t = T^*\sigma^* = 2\pi$, being T^* the period of the sea waves) of the flux of sediment concentration:

$$\overline{q}_{S,i} = \frac{\overline{q}_{S,i}^*}{U_0^*\delta^*} = \frac{1}{2\pi}\int_{2\pi}\left(\int_{y_a}^{\eta} U c_i \, dy\right) dt \tag{2.20}$$

Finally, the time-averaged bed load over a cycle is computed by using Van Rijn (1991) formula, which accounts for the effects of the oscillatory motion induced by the waves:

$$\overline{q}_B = \frac{\overline{q}_B^*}{\sqrt{(s-1)g^* d_{nc}^{*3}}} = \frac{0.25}{R_p^{0.2}} \left(\frac{\theta - \theta_c}{\theta_c} \right)^{1.5} \sqrt{\theta_c} \tag{2.21}$$

where θ_c is the Shields parameter related only to the steady current. Depending on the considered case, θ is calculated either by considering only the steady current or the combined action of waves and steady current.

2.3 The sediment transport solution

This section presents the numerical solution obtained by programming in "Fortran 95" the hydrodynamic module combined with the sediment transport module, and implementing the boundary conditions described in Section 2.2.

2.3.1 Numerical approach

The hydrodynamic and sediment transport equations are solved numerically by means of the finite difference approach. A standard centered second-order finite difference approximation of the spatial derivatives along the y-direction is employed and the temporal derivatives are approximated by means of the second order Runge-Kutta method. In order to increase the accuracy of the numerical results, the grid points are denser close to the bottom, where the velocity and the concentration gradients are larger. The non-uniform distribution of the grid points is obtained by introducing the following stretched variable, with an appropriate value of b:

$$\varsigma = \log \left(\frac{y^*/h^* + b}{b} \right) \tag{2.22}$$

In the numerical simulations, the flow and sediment concentrations are computed up to the free surface $y_{\text{fin}} = h^*/\delta^*$ and, to adequately reproduce the flow in the wave boundary layer, N grid points are distributed in such a way that $N/2$ points fall between the bottom ($y^* = 0$) and a value $y_{int} = y_{\text{int}}^*/\delta^*$ close to the bottom. Table 2.1 shows an example of the numerical parameters used to validate the model (section 2.3.2). Indeed, the value of b is obtained by means of $b = \frac{y_{\text{int}}^2}{y_{\text{fin}} - 2y_{\text{int}}}$ and the grid points are uniformly distributed along the ς-axis. The time step Δt is chosen of order 10^{-6}, to keep the calculations stable. Finally, the initial conditions of velocity and concentration are set to zero, and very small initial values are given to k and ω. The simulations are carried out till a periodic flow and concentration distribution are attained and the wave-averaged quantities turn out to be constant.

2.3.2 Model validation

To ascertain the capability of the model to describe the flow generated by wave-current interaction, the model results are compared with the laboratory data by Dohmen-Janssen (1999), who measured the velocity and concentration profiles in a water tunnel where both a steady current and a current plus an oscillatory flow were generated. Figure 2.3, where the data of Dohmen-Janssen (1999) are plotted along with the model results, shows that the model correctly reproduces the effects of the wave-current interaction and it provides reliable prediction of the velocity profiles. Indeed, when the oscillatory flow is superimposed to the steady current, both the laboratory measurements and the numerical results show that the time averaged velocity near the bottom of the water tunnel is reduced while it is increased near the tunnel axis. Moreover, the model reproduces the phenomenon not only qualitatively but also quantitatively, since the numerical predictions are able to correctly describe the effects that the

Simulations	N	y_{int}	y_{fin}	t_{fin}
Vessel 1	6000	1000	5285	60
Vessel 5	5000	1000	4568	60
Record 3	1500	300	1042	60
Record 6	1600	300	1569	60
G0, G5, G6	600	528	30	60
T1	750	708	50	60
T2	450	409	20	60
Ebb tidal	800	50	723	180
Flood tidal	2200	100	2170	180

TABLE 2.1: Values of the numerical parameters of the simulations carried out to (a) validate the model: field data from Van Rijn et al. (1990) (vessel 1 and 5), Rose and Thorne (2001) (records number 3 and 6) and laboratory data from Dohmen-Janssen (1999) (G0, G5, G6, T1 and T2); and (b) to obtain the results: typical ebb and flood conditions in a coastal region South-West of Spain (Punta Umbría, Huelva).

characteristics (period and amplitude) of the oscillatory flow have on the profile of the time averaged velocity.

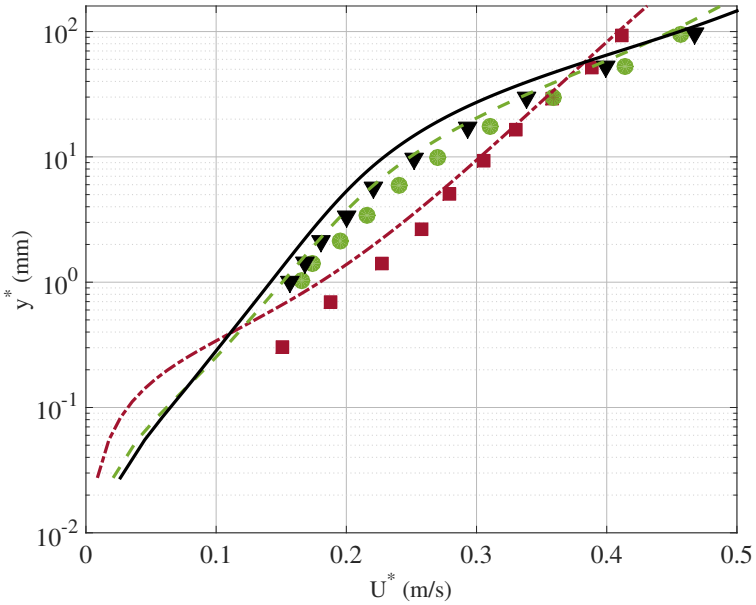

FIGURE 2.3: Comparison of the velocity profiles of the model results (lines) with the data (G0, G5 and G6) by Dohmen-Janssen (1999) (symbols). G0: red dash-dot line (model) and square (data); G5: green dash line (model) and circle (data); G6: black solid line (model) and triangle (data).

The model provides also reliable predictions of the sediment concentration generated by the simultaneous presence of a steady current and an oscillatory flow over a cohesionless sandy bottom. Figure 2.4 shows a comparison between the time-averaged concentration profiles measured by Dohmen-Janssen (1999) and those predicted by the model when oscillatory flows of different periods are superimposed to a steady current. The reader can find more details on the parameters of the phenomenon taking into account that the experiments reproduced by means of the numerical model in Figure 2.3 are named G0, G5 and G6 in Dohmen-Janssen (1999) while those in Figure 2.4 are named T1 and T2.

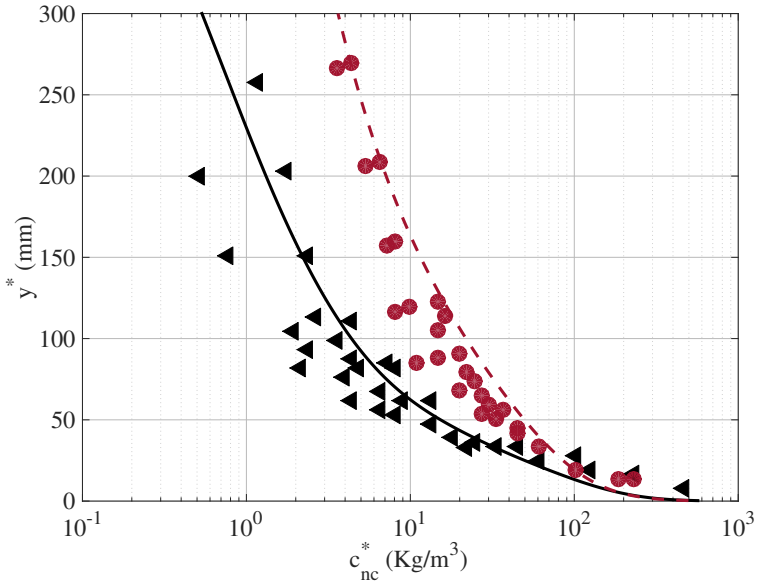

FIGURE 2.4: Comparison of the concentration profiles of the model results (lines) with the data (T1 and T2) by Dohmen-Janssen (1999) (symbols). T1: black solid line (model) and triangle (data); T2: red dash line (model) and circle (data).

The results of the model are compared also with the concentration of non-cohesive sediment measured in two tidal estuaries. The suspended sediment data are obtained from field surveys collected over sandy rippled beds in: (a) the Scheldt estuary in the Netherlands by using a pump sampler (Van Rijn et al., 1990), and (b) the river Taw estuary in North Devon UK by using a multi-frequency acoustic backscatter system and a pump sampler (Rose and Thorne, 2001). In the model, the small scale bed forms (ripples) are assimilated to a large roughness that depends on the geometrical characteristics of the ripples (Soulsby, 1997). The height and length of the ripples are evaluated by using the empirical predictors by Soulsby and Whitehouse (2005). The data selected to validate the model for the former case are concentration and flow velocity of vessel 1 and 5. For the Taw estuary, the concentrations records number 3 and 6 are considered.

The numerical parameters used in the model to simulate these data sets (laboratory and field data), as well as the main input parameters for the calculation of the velocity profile and the calculation of the suspended sediment concentration are summarized in Table 2.1 and Table 2.2.

Measures	$\hat{U}_c^*$ (m/s)	h^* (m)	d_{nc}^* (mm)	k_s^* (m)	y_a^* (m)	S_c
Vessel 1	0.97	9.43	0.250	0.2	k_s^*	0.7
Vessel 5	1.42	8.15	0.250	0.3	k_s^*	0.7
G0, G5, G6	0.5025	0.8	0.21	0.00029	$2\,d_{nc}^*$	-
T1	0.2658	0.8	0.13	d_{nc}^*	$2\,d_{nc}^*$	0.7
T2	0.2658	0.8	0.13	d_{nc}^*	$2\,d_{nc}^*$	0.7
Record 3	1.02	1.86	0.126	$2.5\,d_{nc}^*$	0.019	0.7
Record 6	0.69	2.80	0.131	$2.5\,d_{nc}^*$	0.028	0.5

TABLE 2.2: Summary of the relevant quantities characterizing the data of Van Rijn et al. (1990) (vessel 1 and 5), Rose and Thorne (2001) (records number 3 and 6) and Dohmen-Janssen (1999) (G0, G5, G6, T1 and T2). Note: $\hat{U}_c{}^*$ is the steady current averaged over the water depth.

The Schmidt number is set equal to 0.7 for vessel 1, vessel 5 (Van Rijn et al., 1990), record 3 (Rose and Thorne, 2001) and T1, T2 (Dohmen-Janssen, 1999). For record 6, according to the author's results (Rose and Thorne, 2001), the ratio between sediment diffusivity and eddy viscosity is set close to 2, that is $S_c = 0.5$. To estimate the roughness size, the theoretical approach of Jensen et al. (1989) was adopted for record 3 and 6, while for vessel 1 and 5 of Van Rijn et al. (1990) data, the roughness size are obtained from the Figure 3 of Van Rijn et al. (1990)'s paper. For Dohmen-Janssen (1999)'s data, the roughness sizes were also obtained from the Thesis document. Finally, for the field data, since both estuaries have bed forms (ripples) the reference level y_a^* in (Equation A.5 Appendix A.1) for record 3 and 6 was equal to the measured bed form height and to k_s^* for vessel 1 and 5, since the bed form height is not available. For the laboratory data, the reference level was chosen following the equation of Zyserman and Fredsoe (1994b) (Equation A.3 Appendix A.1).

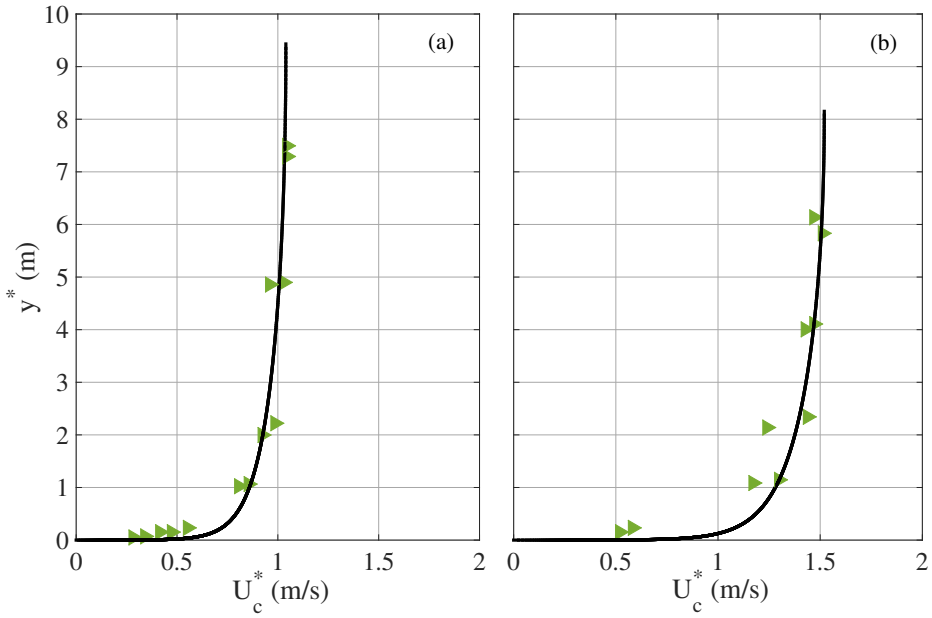

FIGURE 2.5: Comparison of the model results (solid line) with the measured values (triangles) of the streamwise velocity (a): vessel 1 and (b) vessel 5 (Van Rijn et al., 1990).

Figures 2.5-a and 2.5-b show the velocity profiles predicted by the model along with the measurements of Van Rijn et al. (1990) for two different depth-averaged velocities, namely 0.97 m/s and 1.42 m/s respectively, measured when the ebb tidal current attained its maximum value (vessel 1 and vessel 5). In the two cases, the water depth had similar values (9.43 m and 8.15 m, respectively). The agreement between the predicted and measured values is good and supports the hydrodynamic module of the model. As expected, the depth-averaged values of the steady current are equal to the mean velocity measured in vessel 1 and 5.

The evaluation of the sediment concentration in the coastal region is a major challenge to engineers and oceanographers concerned with morphodynamic problems and in the following paragraphs it will be shown that the model appears to provide fair results. Figures 2.6-a and 2.6-b show the comparison between the predicted and measured sediment concentration at the same locations, for the hydrodynamic conditions characterizing in Figures 2.5-a and 2.5-b, respectively. Incidentally, let us point out that in the Figures the mass concentration $c_{nc}^* = \rho_s^* c_{nc}$ is plotted instead of the volumetric concentration. The agreement between the predicted and measured values is good, even though for the weaker velocity (Figure 2.6-a), sediment concentration is slightly over-predicted close to the bed and under-predicted near the free surface.

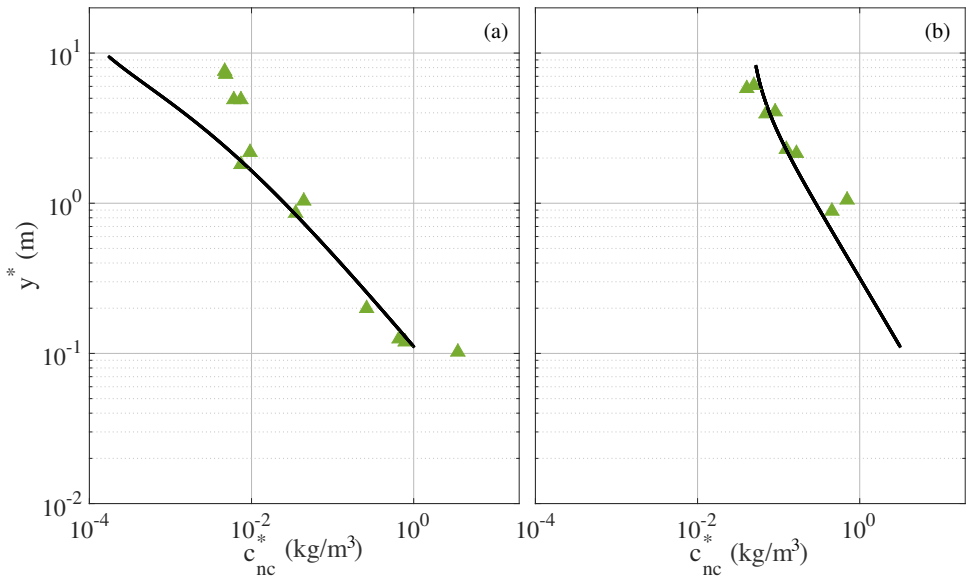

FIGURE 2.6: Comparison of the model results (solid line) with the measured values (triangles) of the sediment concentration: (a) vessel 1 and (b) vessel 5 (Van Rijn et al., 1990).

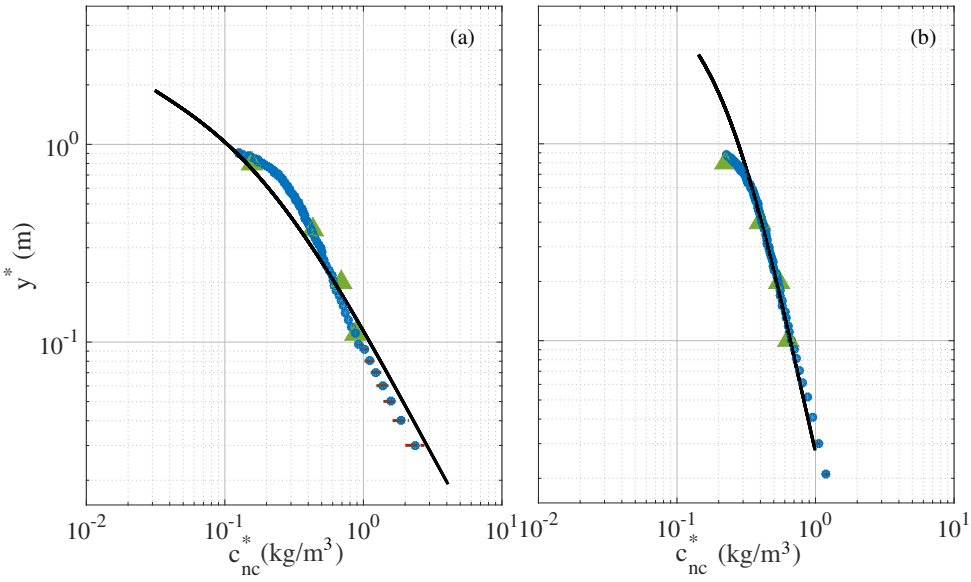

FIGURE 2.7: Comparison of the model results (solid line) with the measured values (triangles – pumped-sample; circles – acoustic backscatter system) of the sediment concentration: (a) record number 3 and (b) record number 6 (Rose and Thorne, 2001). The red lines are the instrument errors associated to the measurements close to the bottom.

Figures 2.7-a and 2.7-b show the comparison between the numerical predictions and the values of sediment concentration measured by Rose and Thorne (2001) during the flood tide. Also in this case the agreement is satisfactory. Indeed the vertical distribution of sediment concentration is well reproduced by the model even close to the bottom where the acoustic backscatter system used by Rose and Thorne (2001) was able to collect reliable data points.

The present comparisons support both the hydrodynamic and sediment transport modules, and show that the turbulence model is appropriate to describe the turbulence structure both in the bottom boundary layer and in the core region.

2.4 Results: application on a coastal region

The analysis of the results is carried out focusing on a case study. The region of interest is in the coastal region south-west of Spain (Punta Umbría, Huelva) and is characterized by several management problems related to sediment transport (see more details in Reyes-Merlo et al., 2017). The typical values of the parameters are considered to investigate (i) the effects of the current on sediment concentration and on the bed/suspended load transport, (ii) the effects of the waves on the flow field induced by the steady current, on the sediment concentration and on the bed/suspended load transport and (iii) the influence of the cohesive material on the sediment transport. Two typical tidal conditions are considered that correspond to the flood and ebb tidal conditions calculated from the software platform presented by Magaña et al. (2018). This software was validated with data measured by a tidal gauge between May and October 2014 (Reyes-Merlo et al., 2015).

Steady current				
Tidal conditions	$\hat{U_c}^*$ (m/s)	h^* (m)	H^* (m)	T^* (s)
Ebb	0.9	1	0	0
Flood	0.6	3	0	0
Wave + steady current				
Tidal conditions	$\hat{U_c}^*$ (m/s)	h^* (m)	H^* (m)	T^* (s)
Ebb	0.9	1	1	6
Flood	0.6	3	1	6

TABLE 2.3: Summary of the idealized flow conditions at Punta Umbría (Huelva) used in the numerical simulations.

The hydrodynamic conditions are summarized in Table 2.3. The maximum and minimum values of the tidal currents are modeled as steady currents since, as already pointed out, the unsteadiness of the flow plays a minor role due to the large value of the Keulegan-Carpenter number of the tidal flow. The sea state selected for the wave conditions ($H^* = 1$ m, $T^* = 6$ s) is one of the most frequent occurring in the south-west coast of Spain: the probabilities of occurrence of $H^* = 1$ m and $T^* = 6$ s are 27 % and 16 %, respectively. The characteristics of the seabed are summarized in Table 2.4 and, for all the cases, the seabed is assumed to be flat as observed at Punta Umbría.

2.4.1 Sediment transport by currents

As already pointed out, the tidal current is modeled as a steady current but the characteristics of both the flood and ebb phases are considered (Table 2.3). The sediment concentration and

Seabed composition	% of cohesive	d_{nc}^* (mm)	d_c^* (mm)	k_s^* (m)
Non-cohesive	0	0.250	0	2.5 d_{nc}^*
Mixed 1	20	0.250	0.04	2.5 d_{nc}^*
Mixed 2	40	0.250	0.04	2.5 d_{nc}^*

TABLE 2.4: Summary of the characteristics of the seabed composition used in the numerical simulations.

transport induced by a steady current for the 100 % non-cohesive seabed can be seen in Figure 2.8 and Table 2.5, while the results for the Mixed 1 and Mixed 2 seabeds are shown in Figures 2.9- 2.10 and Table 2.6.

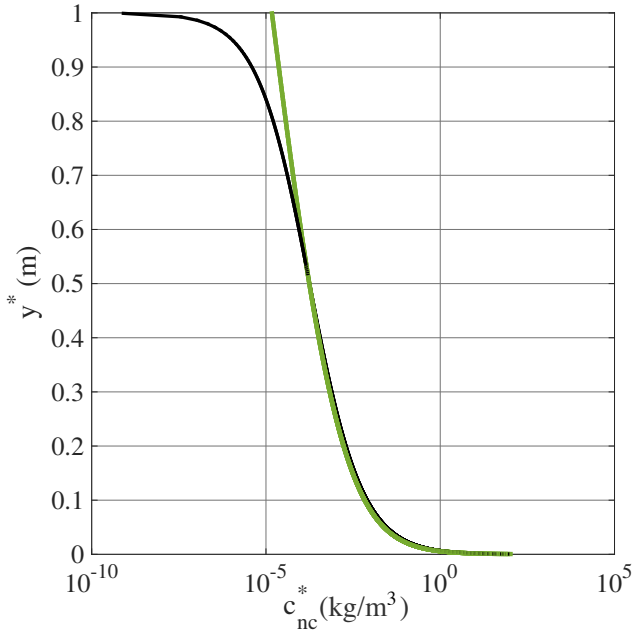

FIGURE 2.8: Suspended sediment concentration (c_{nc}^*) induced by a steady current for the ebb tidal conditions (green solid line) and the Rouse concentration profile (black solid line). The concentration induced by the flood tidal current is negligible over the whole water column and it is not plotted in the figure.

Non-cohesive			
Tidal conditions	τ_w^* (N/m^2)	$\overline{q}_B^*$ (m^2/s)	$\overline{q}_{S,nc}^*$ (m^2/s)
Ebb	1.3712	2.45 e$-$4	4.68 e$-$5
Flood	0.4825	1.92 e$-$6	0

TABLE 2.5: Summary of the values of the bottom shear stress, the wave-averaged bed load transport rate and suspended load transport rate for the steady current case and 100 % non-cohesive sediment.

For the 100 % non-cohesive seabed (Figure 2.8), the suspended sediment concentration induced by the ebb tidal current is significant only near the bottom: $c_{nc}^* = c_a^* > 100$ kg/m^3. The results for the flood current are not shown since the concentration is negligible both far and close to the bottom. Indeed, the bottom shear stress induced by the flood tidal current (see

Table 2.5) does not exceed the threshold value for which the sediment is picked-up from the bed ($\tau^*_{cr,susp} = 0.5146$ N/m^2).

Furthermore, in Figure 2.8 the predicted non-cohesive sediment concentration is compared with the Rouse concentration profile (Rouse, 1937) (see among others Soulsby, 1997). The agreement is excellent, which supports the sediment transport module under steady current conditions. The different behavior of c^*_{nc} near the free surface is due to the vanishing value of the eddy viscosity at the free surface which was used by Rouse (1937) while in the present model the eddy viscosity decreases moving towards the free surface but it does not vanish.

Mixed 1				
Tidal conditions	τ^*_w (N/m^2)	$\overline{q}^*_B$ (m^2/s)	$\overline{q}^*_{S,nc}$ (m^2/s)	$\overline{q}^*_{S,c}$ (m^2/s)
Ebb	1.3712	1.96 e−5	6.6 e−6	4.98 e−4
Flood	0.4825	1.57 e−6	0	3.14 e−4
Mixed 2				
Tidal conditions	τ^*_w (N/m^2)	$\overline{q}^*_B$ (m^2/s)	$\overline{q}^*_{S,nc}$ (m^2/s)	$\overline{q}^*_{S,c}$ (m^2/s)
Ebb	1.3712	1.47 e−5	5 e−6	5.13 e−4
Flood	0.4825	1.17 e−6	0	3.16 e−4

TABLE 2.6: Summary of the values of the wave averaged bottom shear stress, bed load transport rate and suspended load transport rate for the non-cohesive ($\overline{q}^*_{S,nc}$) and cohesive ($\overline{q}^*_{S,c}$) mixtures. The model was run with only a steady current as a forcing term.

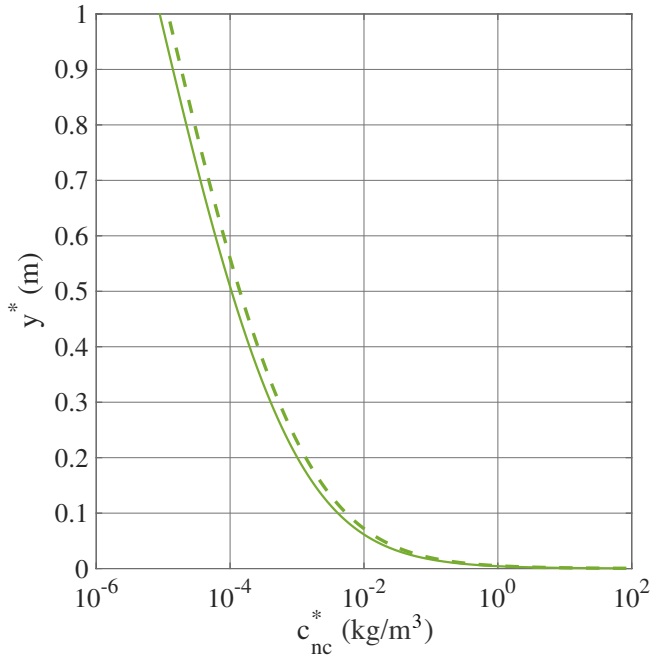

FIGURE 2.9: Suspended sediment concentration (c^*_{nc}) of the non-cohesive sediment for Mixed 1 (80% non-cohesive broken line) and Mixed 2 seabeds (60% non-cohesive solid line) and for a steady current and ebb tidal conditions. As in Figure 2.8, the concentration induced by the flood tidal current is negligible over the whole water depth.

Figure 2.9 depicts the vertical profile of sediment concentration of the non-cohesive fraction for Mixed 1 and Mixed 2 seabeds (see Table 2.4). The vertical concentration of the non-cohesive fraction has hardly any difference between the Mixed 1 (80 % non-cohesive) and

Mixed 2 (60 % non-cohesive) mixtures. As in the 100% non-cohesive seabed, the sediment concentration is negligible in the flood tidal case. The profile of the non-cohesive sediment concentration and suspended load transport induced by the ebb tidal current is slightly higher for the 100 % non-cohesive seabed (Figure 2.8 and Table 2.5) than for Mixed 1 and 2 seabeds (Figure 2.9 and Table 2.6).

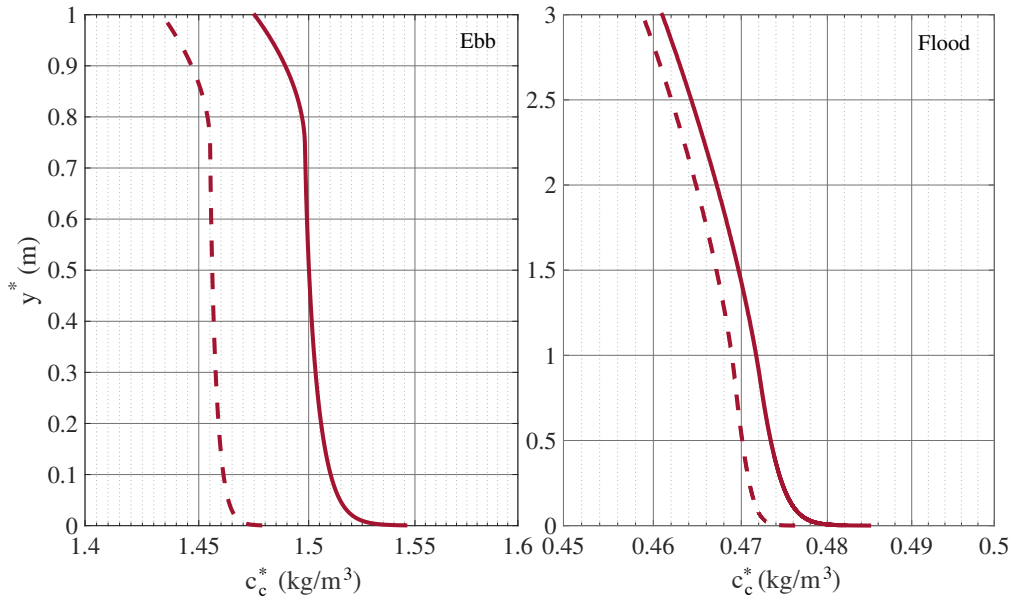

FIGURE 2.10: Vertical profiles of the cohesive fraction of the suspended sediment concentration (c_c^*) induced by a steady current for Mixed 1 (broken line) and Mixed 2 (solid line) seabeds: (left-panel) ebb tidal current, (right-panel) flood tidal current.

The cohesive sediment is well mixed over the water depth both for ebb and flood tidal currents, and its concentration is almost constant (see Figure 2.10). Indeed, for the flood tidal current, the wave-averaged suspended load transport ($\overline{q}_{S,c}^*$) is practically the same for both seabeds (Mixed 1 and Mixed 2). On the other hand, the cohesive sediment concentration and the suspended load transport induced by the ebb tidal current is higher for the Mixed 2 – more percentage of cohesive sediment – than for the Mixed 1 seabed.

Finally, as shown in Tables 2.5 and 2.6, for the non-cohesive sediment, the main mechanism of transport is the bed load transport ($\overline{q}_B^*$), which is higher than the non-cohesive suspended load transport ($\overline{q}_{S,nc}^*$) for all the seabeds simulated. On the other hand, for the cohesive fraction (as expected), the suspended load transport is the main mechanism of transport and it is even higher than the bed load transport for all the mud seabeds simulated.

2.4.2 Wave effects on sediment transport

A further aim of this study was to investigate the effects of the waves on (1) the flow field, (2) the sediment concentration and (3) the sediment transport induced by the steady currents. Figures 2.11 and 2.12 show the effects of the waves on the steady current. The pressure gradient driving the steady current is the same as that used for the steady current only case. It is observed that the flow discharge per unit width decreases if the waves are superposed to the current. Indeed, the velocity profile (U^*) induced by the combined action of waves and a steady free surface slope decreases with respect to the value (U_c^*) found when waves are absent both for the ebb and flood tidal conditions. For the flood tide case, the decrease of the velocity profile is smaller because the strength of the current is also smaller. Moreover, a simple analysis of the order of magnitude of the terms of continuity equation shows that the

horizontal velocity component induced by a surface wave propagating in shallow waters is of order $\frac{H^*}{T^*}\frac{L^*}{h^*}$. Since $L^* = \sqrt{g^* h^*} T^*$, it follows that $\frac{H^*}{T^*}\frac{L^*}{h^*} = \frac{H^*\sqrt{g^*}}{\sqrt{h^*}}$ thus showing that the effects of a wave of given height and period increase as the water depth decreases. Figure 2.12 shows that the bottom shear stress induced by the simultaneous presence of waves and currents is periodic and, as expected, lower for the flood tidal conditions. The bottom shear stress is not symmetric between the maximum and the minimum: the asymmetry of the bottom shear stress corresponds to the influence of the τ_w^* induced by only the steady current (see Tables 2.5 and 2.6), when the flow induced by the waves close to the bottom reverses direction.

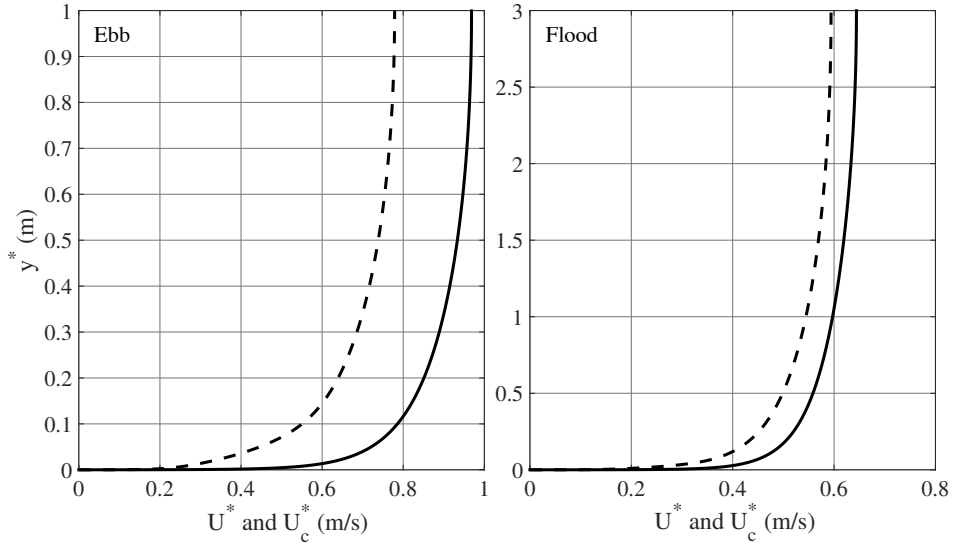

FIGURE 2.11: Time averaged velocity profile for the steady current (U_c^*) only (solid line) and the combined action of waves and currents (U^*) (broken line).

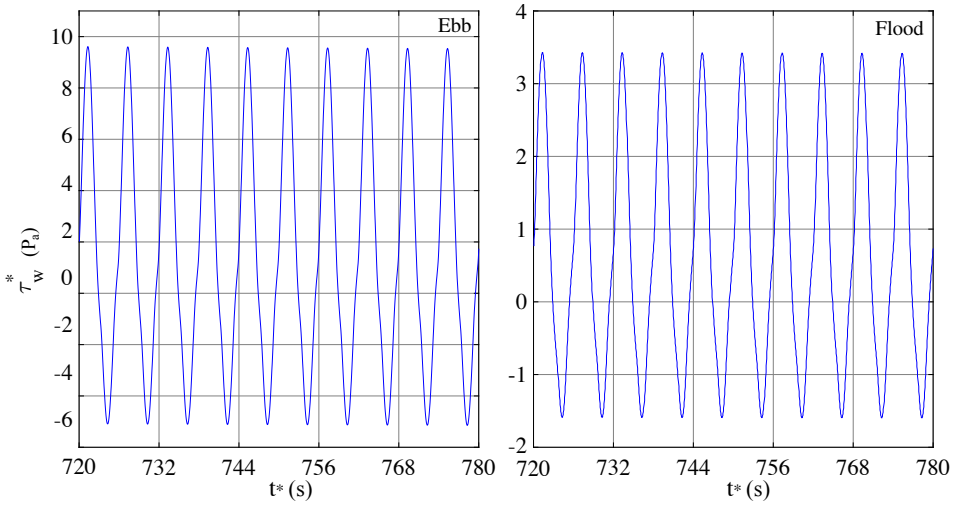

FIGURE 2.12: Plot of the bottom shear stress (τ_w^*) versus time (t^*) for the combined action of waves and steady currents: ebb tide case (left plot), flood tide case (right panel).

Figures 2.13 and 2.14 represent the vertical distribution of sediment concentration of the non-cohesive and cohesive fractions, respectively. The results show that the sediment concentration induced by the wave-current interaction is higher than that without wave effects, for all the three seabeds which were simulated. Although, as discussed previously, the velocity attains lower values, the maximum of the bottom shear stress increase because of the wave

effects. Hence, larger volumes of sediments are put into suspension. The effects of the waves are higher in the ebb tidal conditions than in the flood tidal conditions, since the intensity of the flood current is lower.

The non-cohesive sediment concentration (Figure 2.13) for the ebb and flood tidal conditions does not vary much between the three seabeds considered, however, the values of q_B^* and $q_{S,nc}^*$ are larger when the non-cohesive fraction is larger (see Table 2.7). On the other hand, Figure 2.14 shows that the cohesive sediment concentration is well-mixed over the water depth due to the combined action of waves and steady currents.

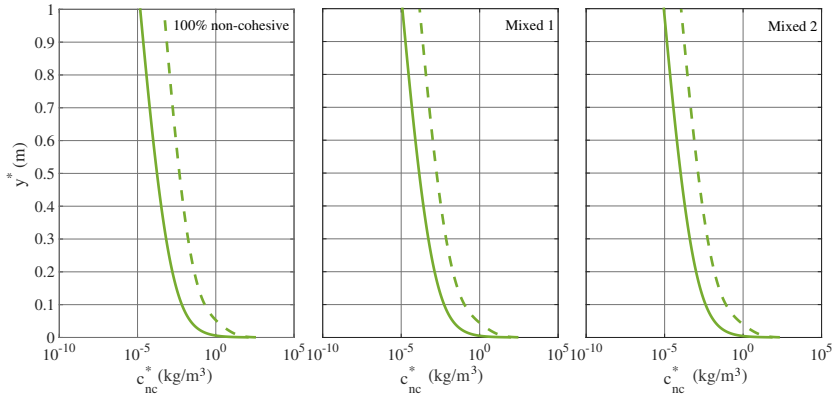

(a) At the ebb tidal current.

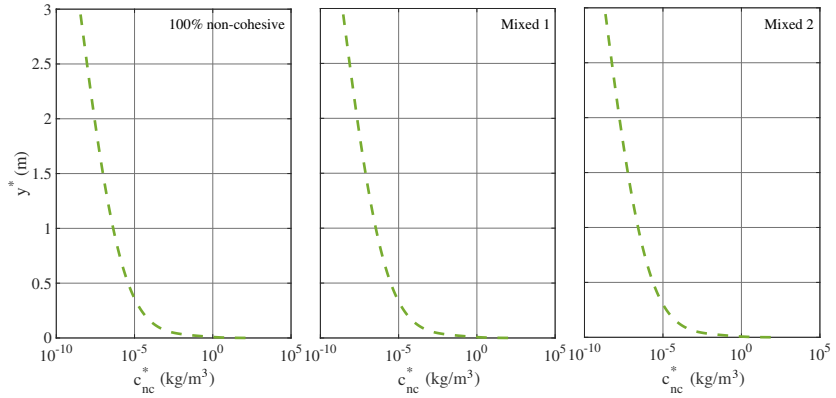

(b) At the flood tidal current.

FIGURE 2.13: Time averaged vertical profile of the concentration of the non-cohesive fraction of the suspended sediment for the three seabeds which were simulated. Flow conditions: (solid line) only steady current, (broken line) combined action of waves and currents.

To quantify the contribution of the waves on sediment concentration, the ratio between the average suspended sediment concentration over the water depth with (SC_{c-w}) and without (SC_c) the effects of waves is assessed (see Table 2.8). The contribution of the waves to the suspended sediment concentration for the non-cohesive fraction is higher than for the cohesive fraction. Indeed, the non-cohesive sediment is carried into suspension more easily than the cohesive sediment (higher interparticle force), even though the concentration and suspended load transport is larger for the cohesive sediment. Moreover, for the cohesive sediment the ratio of $SC_{c-w,c}$ to $SC_{c,c}$ decreases with the decrease of the current (or increase of the water depth).

Because the time scale of the morphological changes of the seabed is much larger than the period of the sea waves, up to now both the sediment concentration and sediment transport are discussed looking at their values averaged over the wave period. However, even though the

significant effects that sea waves have on sediment transport can be gathered looking at the results plotted in Figures 2.13 and 2.14 and shown in Tables 2.7 and 2.8, it might be interesting to look at sediment dynamics during the wave cycle. Figure 2.15 shows the concentration of both the non-cohesive and cohesive fractions of the sediment mixture "Mixed 2" (see Table 2.4) for the ebb tidal conditions and for different phases during the wave cycle.

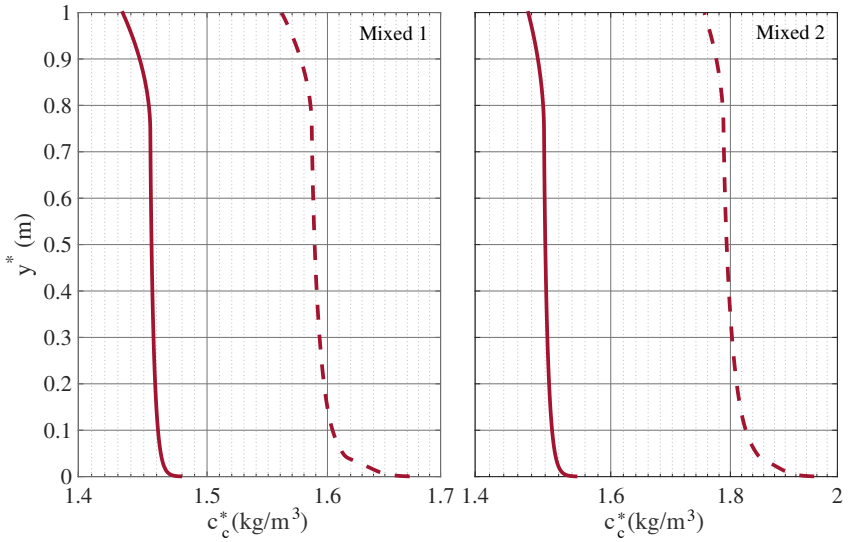

(a) At the ebb tidal current.

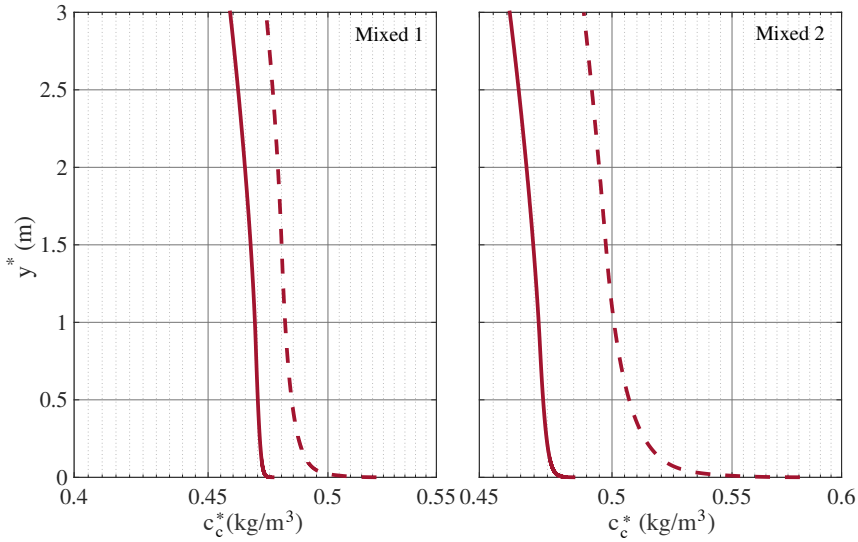

(b) At the flood tidal current.

FIGURE 2.14: Time averaged vertical profile of the concentration of the cohesive fraction of the suspended sediment for the two sediment mixtures. Flow conditions: (solid line) only steady current, (broken line) combined action of waves and currents.

As expected, the concentration of non-cohesive sediment is significant only close to the bottom and it oscillates in a wide range. Moreover, because of the presence of a steady current, the concentration at time $t^* + T^*/2$ differs from that at time t^*. On the other hand, the concentration of the cohesive fraction does not vary significantly during the wave cycle but is assumes significantly values over the whole water column. Similar results are found for the flood tidal conditions even though the decreased strength of the tidal current causes a significant reduction of the suspended load (see Figure 2.16). For the mixture "Mixed 1" (see

Non-cohesive			
Tidal conditions	$\overline{q}^*_B$ (m^2/s)	$\overline{q}^*_{S,nc}$ (m^2/s)	$\overline{q}^*_{S,c}$ (m^2/s)
Ebb	6.45 e−4	1.81 e−4	–
Flood	7.22 e−5	1.53 e−5	–
Mixed 1			
Tidal conditions	$\overline{q}^*_B$ (m^2/s)	$\overline{q}^*_{S,nc}$ (m^2/s)	$\overline{q}^*_{S,c}$ (m^2/s)
Ebb	5.16 e−4	1.23 e−4	3.85 e−4
Flood	5.8 e−5	1.22 e−5	2.9 e−4
Mixed 2			
Tidal conditions	$\overline{q}^*_B$ (m^2/s)	$\overline{q}^*_{S,nc}$ (m^2/s)	$\overline{q}^*_{S,c}$ (m^2/s)
Ebb	3.87 e−4	9.26 e−5	4.35 e−4
Flood	4.35 e−5	9.2 e−6	3.05 e−4

TABLE 2.7: Summary of time-averaged bed load ($\overline{q}^*_B$), the time-averaged suspended load for the non-cohesive ($\overline{q}^*_{S,nc}$) and cohesive ($\overline{q}^*_{S,c}$) materials for the three seabeds presently simulated. The model was run for the combined action of waves and currents.

Seabed	$SC_{c-w,nc}/SC_{c,nc}$		$SC_{c-w,c}/SC_{c,c}$	
	Ebb tidal	Flood tidal	Ebb tidal	Flood tidal
100% non-cohesive	14.70 %	0 %	–	–
Mixed 1	13.89 %	0 %	1.1 %	1.03 %
Mixed 2	13.89 %	0 %	1.2 %	1.06 %

TABLE 2.8: Ratio between the suspended sediment concentration with and without wave effect. $SC_{c,i}$ is the average sediment concentration over the water depth induced by only the steady current, and $SC_{c-w,i}$ is the average sediment concentration over the water depth induced by the combined action of waves and the steady current ($i = nc$, c is the non-cohesive or cohesive fractions, respectively).

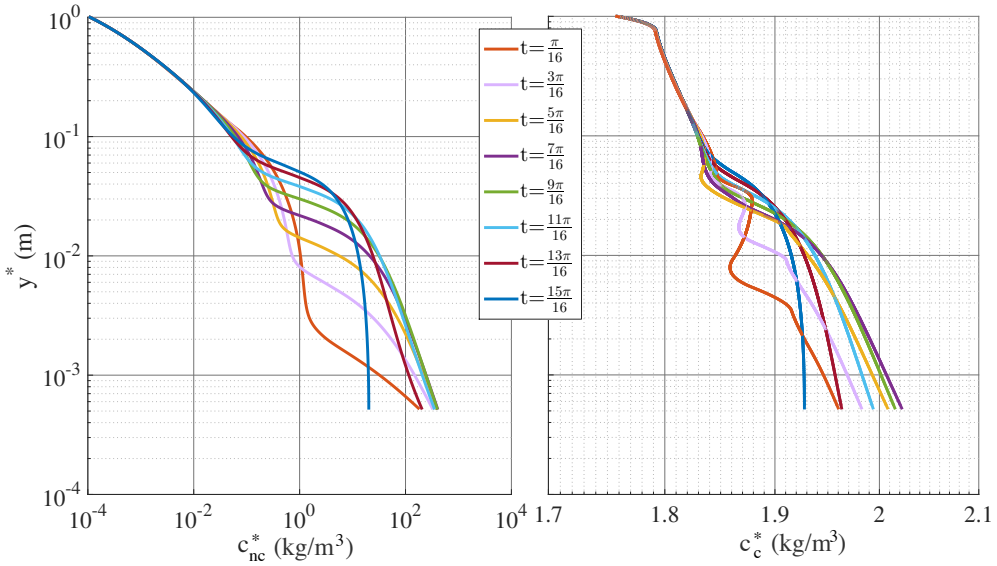

FIGURE 2.15: Concentration profiles of the non-cohesive (left panel) and cohesive (right panel) fractions of the mixture "Mixed 2" at different phases during the cycle for the ebb tidal current.

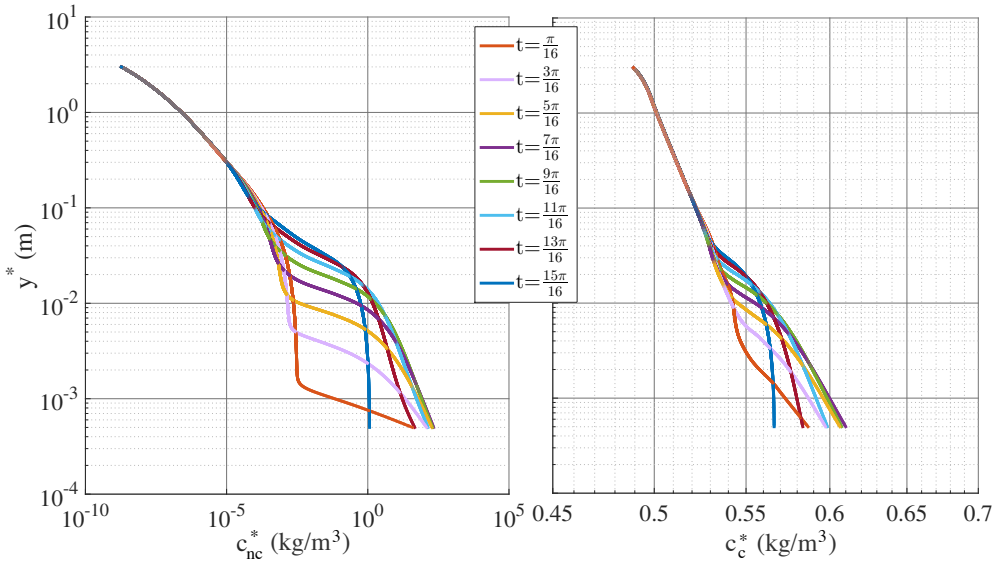

FIGURE 2.16: Concentration profiles of the non-cohesive (left panel) and cohesive (right panel) fractions of the mixture "Mixed 2" at different phases during the cycle for the flood tidal current.

Table 2.4) the concentration of the cohesive fraction decreases while that the non-cohesive fraction increases almost proportionally to the values of the concentration within the bed.

2.5 Conclusions

This chapter assesses the effects of sea waves and of the presence of cohesive material on the sediment transport in a coastal region by considering idealized conditions derived from measurements at Punta Umbría (Huelva, Spain). Tidal currents, are modeled as a sequence of steady currents while an intra-wave model is adopted to describe the effects of sea waves. The sediment behavior under wave-current interaction is described by means of an integrated numerical model that includes both a hydrodynamic module and a sediment transport module. The model solves the hydrodynamic problem from the sea bottom up to the free surface including the buffer layer and the viscous sublayer, when the bottom behaves like a smooth wall. Hence, there is no need to assume the existence of a logarithmic velocity profile, the presence of which becomes questionable at some phases of oscillatory flows.

First, the model is validated against field data from two tidal estuaries. Then, a case study is carried out that is loosely based on two typical tidal conditions at Punta Umbría (South-western Spain). Three compositions of the seabed are considered: 100% non-cohesive, Mixed 1 – 20% cohesive and Mixed 2 – 40% cohesive. Both steady currents and currents interacting with sea waves are considered. After the analysis of the results, the following conclusions can be drawn:

1. The good agreement between the field data and the results of the numerical model supports the approximations introduced in the hydrodynamic module. In particular, it appears that modeling the tidal current as a sequence of steady currents is reasonable. Moreover, the turbulence model of Menter et al. (2003) appears to properly describe the turbulence flow–structure within the boundary layer generated by propagating sea waves both close to the bed and far from it. Hence, the sediment module predicts accurately the sediment transport in suspension over the entire water column.

2. The cohesive sediment fraction turns out to be well mixed over the water depth, both for the ebb and flood tidal currents. On the other hand, the non-cohesive sediment concentration is only significant near the bottom and practically negligible far from it.

3. For the three seabeds simulated, the sediment concentration and transport induced by the wave-current interaction are higher than those determined without wave effects, although the velocity resulting from the interaction decreases. This result is due to the increase of the maximum of the bottom shear stress by the wave effects, which puts more sediments into suspension.

4. The contribution of the waves to the suspended sediment concentration is higher for the non-cohesive fraction than for the cohesive fraction, since the higher interparticle forces in the cohesive sediment makes it difficult to bring this fraction into suspension. In addition, the contribution of the waves to the cohesive sediment concentration decreases when reducing the current intensity or increasing the water depth.

5. The main contribution to the sediment transport comes from the cohesive fraction because of the large amount of cohesive sediment which is picked-up from the seabed and carried into suspension.

Part II

On the breakwater performance

Chapter 3

Wave energy transformation on mound breakwaters (I): context and methods

Comment

This chapter presents the problem formulation and the experimental methodology published on :

P. Díaz-Carrasco, M.V. Moragues, M. Clavero, and M.A. Losada (2019c). "2D water-wave interaction with permeable and impermeable slopes: dimensional analysis and experimental overview". In: *Coastal engineering* (Under review)

The design of breakwaters is still based on the working hypothesis that Iribarren number is one of the main variables for assessing the wave energy transformation on breakwaters (K_R^2, K_T^2, D^*) and the breaker types. The verification of the stability of the structure requires physical and numerical experimentation that also consider Iribarren as a dynamic similarity parameter between model and prototype. However, the experimental results of other studies show that the values of K_R^2, K_T^2 and D^* tend to scatter as Iribarren increases. The latter generates a high degree of uncertainty in the design of these maritime structures. Consequently, this chapter presents the methodology developed in this Thesis to obtain the main physical processes that dominate the energy transformation of a regular wave train when it interacts with a mound breakwater, impermeable or permeable. For that, Section 3.2 presents the definition of the problem and the dimensional analysis applied by identifying a complete set of parameters and independent variables that govern wave transformation processes at the breakwater. Section 3.3 outlines the numerical and physical experimental setup as well as the experimental design. The results and specific conclusions are presented in the following Chapter 4. This work is also supported and completed with the Appendix B and C.

3.1 Introduction

The main function of breakwaters is to protect harbors and other coastal infrastructures from wave action. Hence, they are an important type of coastal structure because of their functionality as well as their cost, design complexity, and environmental and socioeconomic impacts. The conception, design, and verification of a mound breakwater mainly depends on the slope of the sea bottom, water depth at the breakwater toe, h, and the characteristic values of incident waves H, T, θ (height, period, and incidence angle). They also depend on the available materials, construction methods and repair techniques, and the possible consequences

if objectives are not attained. The performance of the breakwater against wind waves is mainly determined by the slope on both sides of the breakwater, shape and weight of the unit pieces, number of armor layers, thickness and emplacement of the main layer/secondary layers and the width, crest elevation, and size of the core materials (ROM 0.0-01, 2001; ROM 1.1-18, 2018).

Battjes (1974) proposed that the Iribarren number (Iribarren and Nogales, 1949), $I_r = \tan(\alpha)/\sqrt{H/L}$ can be used as the dynamic similarity parameter to analyze the behavior of a wave train over an infinite impermeable flat slope, where α is the slope angle and L is the characteristic wavelength. He also conjectured that the value of I_r identified breaker type as spilling, plunging, collapsing, or surging (Iversen, 1952; Cyril and Galvin, 1968). Furthermore, he advanced its capacity to determine the phase difference and wave-breaking index, wave run-up and run-down, mean level, and the reflection and dissipation (absorption) of the waves on the breakwater slope.

In the field of harbor and maritime structures (and also beach morphodynamics), the seminal work of Battjes (1974) led to research whose objective was to determine the transformation of incident energy when waves interacted with the breakwater by means of the reflected energy coefficient, K_R^2, transmitted energy coefficient, K_T^2, and the bulk dissipation rate, D^*. Still another objective was to develop formulas for wave run-up, run-down, overtopping and stability of the main armor layer in the domain of interest, $I_r > 1.5$, as reflected in the following references, among others: Bruun and Günbak (1976), Losada and Giménez-Curto (1981), Seeling and Ahrens (1981), Allsop and Channell (1989), Martin et al. (1999), Zanuttigh and Van der Meer (2008), Burcharth and Andersen (2010), Van der Meer (2011), Gómez-Martín and Medina (2014), and Vílchez et al. (2016a).

These studies show that in the domain, $I_r > 1.5$, the Iribarren number reveals the general tendency of coefficients [K_R^2, K_T^2], but the values tend to scatter as the value of I_r increases, depending on the slope angle, with maximum scattering in the interval of I_r corresponding to the critical design conditions. In addiction, despite of talking about three energy transformation modes, there are relatively few articles on the calculation of wave dissipation and is still an open question. Such studies include the following: Seeling and Ahrens (1981), Kobayashi and Wurjanto (1992), Pérez-Romero et al. (2009), Van Gent (2013), and Vílchez et al. (2016b), among others. Energy transmission at a non-overtopped breakwater is usually small, $K_T^2 < 0.15$, but this information is necessary in order to evaluate the bulk dissipation at the structure.

Forty years after Battjes (1974), physical experiments on breakwaters are still based on the working hypothesis that the Iribarren number is a dynamic similarity parameter between model and prototype. Despite the scattering in the region $I_r > 1.5$, the Iribarren number is the main variable in formulas that determine the wave energy transformation coefficients [K_R^2, K_T^2, D^*] for a breakwater and related hydrodynamic performance. In this regard, over the last thirty years, research studies have questioned the dependence of $K_R^2 = f(I_r)$. Hughes and Fowler (1995) and Sutherland and O'Donoghue (1998) applied the parameter x_m/L (where $x_m = h/\tan(\alpha)$, and h the water depth) to also quantify the phase of the reflected wave train. Davidson et al. (1996) defined a reflection number that includes I_r and the characteristic diameter of the armor layer. Van der Meer (1988) and Van der Meer (1992) incorporated a permeability parameter P and fit the exponents of I_r by means of a multiple regression analysis. Benedicto (2004) analyzed wave reflection, depending on h/L and grain size. Finally, Vílchez et al. (2016a) incorporated the grain diameter, and the width and depth of the breakwater core in a single parameter to quantify the hydraulic performance [K_R^2, K_T^2, D^*].

3.1.1 Theoretical background

The dissipation of a wave train on a mound breakwater is mainly caused by the generation, transport, and dissipation of turbulence during the following processes: (i) wave evolution and eventually wave-breaking on the free surface of the slope; (ii) interaction (circulation and friction) with the main armor layer; and (iii) wave propagation through the secondary layers and porous core. The reflection of the incident flow is activated by changes in the characteristics of the medium during wave propagation on the slope, main armor layer, secondary layers, and core, and finally when it is transmitted landward of the section (Losada et al., 2019).

Reflection-dissipation-transmission in a porous medium

Theoretical formulation for the propagation of a regular or irregular wave train through a porous medium has been widely studied (Sollitt and Cross, 1972; Dalrymple et al., 1991). Numerical and physical experiments have also been performed to address this topic. For the purposes of this study, the behavior of the reflection-dissipation-transmission system in a porous medium has five important aspects:

- The Forchheimer equation is able to provide a reasonably accurate representation of the bulk resistance over the porous medium with coefficients that depend on the Reynolds and Keulegan-Carpenter numbers (R_e, KC_p) (Van Gent, 1995; Pérez-Romero et al., 2009; Jensen et al., 2014a; Jensen et al., 2014b).

- The equivalent hypothesis of Lorentz can be used to calculate wave reflection as well as global and local dissipation in the breakwater core (Vílchez et al., 2016a), depending on a 2D scattering parameter $A_{eq}/L^2 \approx (h/L)(B^*/L)$ to linearize the Forchheimer equation; where B^* is a characteristic width of the porous medium (Kortenhaus and Oumeraci, 1998). In addiction, the scale effect is analyzed by a single friction coefficient that monotonically decreases as the relative diameter $D_{50,p}/L$, increases (Pérez-Romero et al., 2009; Vílchez et al., 2016b).

- The dissipation rate increases and the reflected energy decreases as the friction coefficient reaches a maximum value (saturation), depending on the relative width B^*/L (Requejo et al., 2002) and relative diameter $D_{50,p}/L$ (Pérez-Romero et al., 2009). Moreover for specific values of the relative width, the reflected energy attains relative minimums and maximums (Losada et al., 1993). Even though this behavior is fairly common in the laboratory, it is much less so in the prototype since generally $B^*/L < 0.15$.

- The mean water level inside the porous medium and the generation of an undertow responds to the usual pattern of dissipating-reflecting systems, (Méndez et al., 1998; Wellens and Van Gent, 2012).

Spatial-temporal evolution of wave-breaking on a slope

In the last 20 years, there have been various studies on numerical predictions of wave-breaking on a smooth impermeable slope by means of different techniques (Christensen and Deigaard, 2001; Lara et al., 2006; Zhang and Liu, 2006; Madsen and Fuhrman, 2008; Gíslason et al., 2009; Lakehal and Liovic, 2011). In the interval, $1.5 < I_r < 3.5$, they identified four breaker types: weak plunging and strong plunging (Lakehal and Liovic, 2011) and weak bore and strong bore (Zhang and Liu, 2008). These four breakers types are relevant to the results and discussion of our work.

However, reflection and dissipation during shoaling and the eventual breaking of the wave on a slope with a permeable core do not have a theoretical model equivalent to the Forchheimer equation, and most studies are based on numerical and physical experiments (Kobayashi and Wurjanto, 1992; Lara et al., 2008; Zanuttigh and Van der Meer, 2008; Ruju et al., 2014; Jensen et al., 2014a; Jensen et al., 2014b; Vanneste and Troch, 2015). When the slope is rough and permeable, the turbulent dissipation sources increase but also its scales (Losada et al., 2019).

When a wave train interacts with a permeable breakwater, its behavior depends on the transformation process that dominates the spatial-temporal evolution of the wave train that propagates into the slope and porous core. In the case of spilling breakers, the process is gradually dissipative and depends on the characteristics of the wave train at undefined depths, $(H/L)_0$ and its shoaling at the slope. The shoaling depends on x_m/L, where $x_m = h/\tan(\alpha)$ should be very small. In other words, reflection should be negligible on the slope as well as in the porous core. Spilling breakers and weak plunging breakers satisfy these conditions. If the wave train surges on the slope and propagates through the porous core, the transformation process is essentially reflective, and is described by the slope angle α, relative depth h/L, width B^*/L, and the relative diameters of the core, $D_{50,p}/L$. Dissipation, which is small, occurs on the main armor layer (or the rough granular bed) as well as inside the breakwater core. The phase depends on x_m/L and $D_{50,p}/L$, B^*/L, and determines the location of the nodes and anti-nodes of the wave.

3.1.2 Objectives and organization

To address this topic, the main objectives of Chapters 3 and 4 are the following: (1) to collate the dependence of wave energy transformation processes (reflection, transmission, and bulk dissipation rate) with Iribarren number; (2) to apply dimensional analysis to the design of experiments for both a permeable and impermeable slope; and (3) to analyze the variability of the results and identify those characterized by the hydrodynamic performance of the breakwater.

This study involves numerical experiments using an undefined, impermeable, rigid slope and the application of the IH-2VOF model (Lara et al., 2008). These are combined with laboratory experiments in the 2D flume of a non-overtoppable mound breakwater with a cube layer and porous core of finite width. Linear wave theory was applied to separate the incident, reflected, and transmitted time series of the data records of the vertical displacement of the free surface at different points in the experimental setup. The wave energy conservation equation was applied to obtain the bulk dissipation rate on the breakwater.

3.2 Problem definition and dimensional analysis

3.2.1 Wave-mound breakwater interaction: energy transformation modes

This section formulates the main physical processes occurring when a wave train, with known heights (H), periods (T) and normal incidence, interacts with a 2D mound breakwater section (ROM 1.0-09, 2009). The presence of a non-overtoppable maritime structure transforms the incident wave energy in: (1) energy reflected and returned to the sea; (2) energy transmitted through the breakwater (if it is permeable), spreading to landward side; and (3) energy that is global dissipated and thus extinguished.

The analysis of the wave energy transformation modes can be achieved by defining in a finite control volume (CV) with a unit width and constant depth that includes the breakwater, the positive inflow, negative outflow and dissipation flow (see Figure 3.1). The wave energy

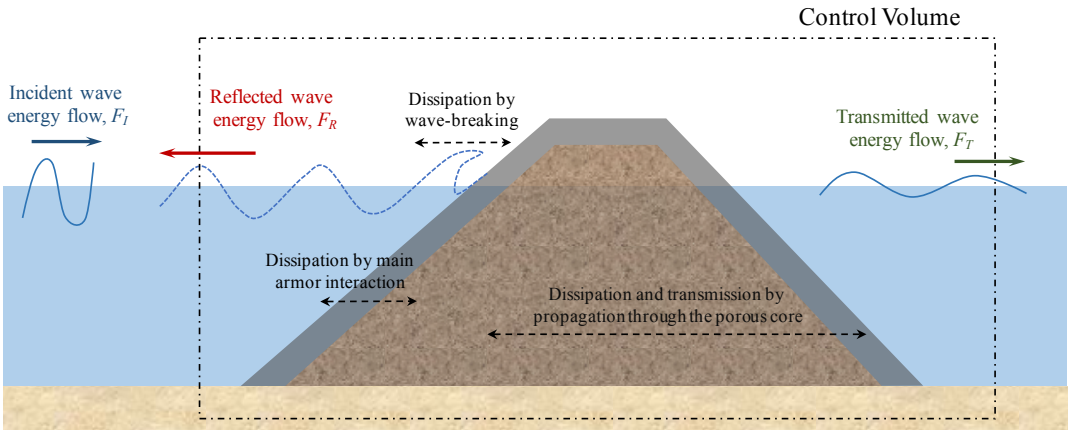

FIGURE 3.1: Scheme of the wave energy distribution for a non-overtoppable mound breakwater.

conservation equation in the control volume is given by Equation 3.1, when the linear theory is applied and the energy to higher harmonics are considered negligible (Losada et al., 1997),

$$F_I - F_R - F_T - D'^* = 0 \tag{3.1}$$

where $F_i = C_{g,i}E_i$; $i = I, R, T$ represents the mean energy flow of the incident, reflected and transmitted wave trains, respectively; $E_i = (1/8)\rho g H_i^2$ represents the wave energy; H_i is the wave height; ρ is the water density and g is the gravity acceleration; and $C_{g,i} = f(h,L)$ is the linear theory group celerity of the energy propagation, which depends on the water depth, h, and the wavelength, L:

$$C_g = \frac{1}{2}c\left(1 + \frac{2kh}{\sinh(2kh)}\right) \tag{3.2}$$

where $c = L/T$ and $k = 2\pi/L$ are the wave phase celerity and the wave number, respectively; and T is the wave period that, in this work, we consider the mean wave period as representative of the wave train $T = T_z$. The wave number is related with the angular frequency, $\sigma = 2\pi/T_z$, by means of the linear dispersion equation:

$$\sigma^2 = gk\tanh(kh) \tag{3.3}$$

In the Equation 3.1, D'^* is the mean bulk dissipation, due to (i) wave-breaking on the slope and, depending of the breakwater type, (ii) propagation through the porous medium, (iii) wave interaction with the main armor layer. Equation 3.1 is also fulfilled for the total flow; that is, multiplying the energy of each train by its wavelength. In this case, the mean bulk dissipation would be the total dissipation rate in the wave train, D^*.

NOTE

In this work we highlight that the global dissipation depends on the local dissipation due to (i) wave-breaking on the slope, (ii) wave-interaction with the main armor and (iii) wave propagation through the porous medium. However, we want to point out that local dissipation is described qualitatively and not quantitatively, being the value calculated in experimental test the total dissipation rate D^*.

3.2.2 Wave-mound breakwater interaction: dimensional analysis

In this section, the dimensional analysis is applied in oder to determine the functional relations between the dimensionless independent quantities and dependent quantities of the first and second kind. Linear theory provides the freedom (not arbitrary) necessary to apply the dimensional analysis, which involves the following four stages:

1. Identification of a complete set of n independent quantities that determine the value of the dependent quantities. In this work, the first kind dependent variables are the total reflected wave energy per unit horizontal surface, E_R, and (if the breakwater is permeable) the total transmitted wave energy per unit horizontal surface, E_T. The second kind is the total dissipation rate, D^*, which is obtained from the first kind quantities by the energy conservation equation (Equation 3.1).

2. List the dimensions of all quantities; choose a complete subset of k_π dimensionally independent quantities; express the dimensions of the remaining $(n-k_\pi)$ quantities of the complete set; and express the two first kind dependent quantities as a power products of the subset quantities.

3. Definition of $(n-k_\pi)$ independent quantities, based on the power products of the k_π quantities selected.

4. Application of the Π-Buckingham theorem to express dependent quantities as a function of the $(n-k_\pi)$ independent quantities.

Following the methodology of Vílchez (2016), the independent variables that influence the wave energy transformation are refereed to the wave train parameters and geometric parameters of the mound breakwater. In this work, depending on the geometric configuration and composition of the mound breakwater, we distinguish the dimensional analysis of three slope types: (1) impermeable slope, (2) permeable and homogeneous slope, and (3) permeable with main armor slope.

A smooth, rigid, flat slope impermeable and non-overtoppable

The complete set of independent variables that participate in the transformation of the wave train on a non-overtoppable, impermeable, smooth, rigid, flat slope consists of the following: (i) seaward slope angle, α; (ii) water depth, h; (iii) incident wave height, H_I; (iv) wave period, T_z (or wave length, L); (v) gravity acceleration, g; (vi) dynamic viscosity, μ; and water density, ρ. The effect of the surface tension and water compressibility is negligible. Excluding α $(n=6)$,

$$X = f(h, \rho, \mu, g, H_I, L)$$

where X represents the dependent variable of the first kind. Accordingly, $\{\rho, g, L\}$ are selected as the complete subset of the dimensionally independent quantities ($k_\pi = 3$). The remaining variables of the set and the dependent quantities (i.e. characteristics of the reflected wave train) can be expressed as power products of this dimensional base, $(n-k_\pi)=3$. Applying the Π-Buckingham theorem, the following functional relation (hereinafter called "similarity equation") is obtained,

$$X^* = [H_R/L,\, X_{0,R}/L] = f(h/L,\, H_I/L,\, R_{e,w})$$

where H_R is the wave height of the reflected wave train; and $X_{0,R}$ is the distance measured from the toe of the slope to the point reflector location of the reflected wave train. When the

kinematic viscosity is represented by $\nu = \mu/\rho$, the third dimensionless variable, $R_{e,w} \approx U_c h/\nu$, is a Reynolds number, whose value should be sufficiently high for the regime to be regarded as fully developed turbulence. U_c is a characteristic instantaneous velocity of the oscillatory movement in the water column.

The slope angle, α, is not included since it is a dimensionless quantity, and thus can not be expressed in terms of the base. Since dimensional analysis cannot provide information about the way that wave transformation depends on the slope angle, $(n - k_\pi) = 3$. For the same reason, it is not possible to include the reflection phase ϕ_R, and the distance $X_{0,R}$ is considered a first kind quantity like H_R. Sutherland and O'Donoghue (1998) experimentally verified that the reflection phase ϕ_R depends on h/L and the slope angle. They proposed that it should be determined by the dimensionless variable x_m/L; where x_m is the horizontal distance of the slope from the toe to the cut with the surface of the sea at rest. Thus, alternatively, x_m/L can be included in the complete set of independent variables, then $(n = 7)$ and $(n - k_\pi) = 4$,

$$X = f(h, x_m, \rho, \mu, g, H_I, L)$$
$$X^* = [H_R/L,\ X_{0,R}/L] = f(h/L,\ x_m/L,\ H_I/L,\ R_{e,w})$$

However, in this work, for clarity of exposition, the slope angle has been chosen to use as an "identificative parameter" of the results, instead of incorporating x_m/L in the function. Recall that, by definition $x_m/L = (1/\tan(\alpha))(h/L)$.

Therefore, taking the independent base $\{\rho, g, L\}$, the total energy of the incident and reflected wave trains are derived quantities, $E_I/(\rho g L) = (1/8)H_I^2$, $E_R/(\rho g L) = (1/8)H_R^2$, expressed as follows:

$$K_R^2 = E_R/E_I = H_R^2/H_I^2$$
$$\phi_R \propto X_{0,R}/L$$

Finally, the dependent quantities (reflected energy coefficient and phase of the reflected wave train) are:

$$\left[K_R^2, \frac{X_{0,R}}{L}\right] = \Psi_R\left(\frac{h}{L}, \frac{H_I}{L}, R_{e,w}\right) \tag{3.4}$$

Although the function Ψ_R is undetermined, its form is similar for all possible slope angles. Finally, the dissipation rate for the mean incident energy flow, which is a dimensionless variable of the second kind, is calculated as follows (Equation 3.1),

$$D^* = \frac{D'^*}{E_I C_g} = 1 - \Psi_R\left(\frac{h}{L}, \frac{H_I}{L}, R_{e,w}\right) \tag{3.5}$$

Non-overtoppable, permeable and homogeneous flat slope with a finite width

The presence of a porous core is relevant to the hydrodynamic performance of the breakwater because of (i) the dissipation and transmission inside the breakwater core and (ii) its importance in the determination of the incident and reflected (phase and modulus) wave trains and its impact on breaker type. Hence, the complete set of independent variables participating in the transformation of the wave train is considerably larger than in the case of an impermeable slope. Again, excluding α and β, the seaward and landward slope angles, respectively,

$$(X_1, X_2) = f(h, \rho, \mu, g, H_I, L, D_{50,p}, B^*)$$

The permeable porous medium is represented by the characteristic width of the core, B^*, and the diameter of the uniform granular core, $D_{50,p}$, which has associated a porosity, n_p. (X_1, X_2) are the two dependent variables, which in this case are the statistical or spectral descriptors of the wave height and reflected wave train, [H_R or $(m_{0,R})^{1/2}$, $X_{0,R}$], and of the transmitted wave train, [H_T or $(m_{0,T})^{1/2}$, $X_{0,T}$], respectively. Generally, $X_{0,T}$, is the distance measured from the toe of landward slope to the point transmitter location of the transmitted wave train. Alternatively, as the impermeable slope, it had be possible to include $x_{m,s}$ and $x_{m,l}$, seawards and landwards horizontal length of the slope, respectively.

In the same way as for the impermeable slope, $\{\rho, g, L\}$ are selected as the complete subset of dimensionally independent quantities ($k_\pi = 3$). The remaining variables of the set and the dependent variable, can be expressed as the power product of this dimensional base, $(n - k_\pi) = 5$, (similarity equation),

$$X_1^* = [H_R/L,\, X_{0,R}/L] = f(h/L,\, H_I/L,\, D_{50,p}/L,\, B^*/L,\, R_{e,p})$$
$$X_2^* = [H_T/L,\, X_{0,T}/L] = f(h/L,\, H_I/L,\, D_{50,p}/L,\, B^*/L,\, R_{e,p})$$

The similarity equations incorporate three new dimensionless quantities. The dimensionless quantity $D_{50,p}/L$ governs the dissipation of the flow and quantifies the scale effects in the wave energy transformation processes (Pérez-Romero et al., 2009). Likewise, Vílchez et al. (2016a) defined the scattering parameter $A_{eq}/L^2 \approx (h/L)(B^*/L)$, which controls the reflection and phase inside the porous core. Following Gu and Wang (1991) and Van Gent (1995), the Forchheimer hydrodynamic regimes inside the core are determined by $R_{e,p}$ and $R_{e,p}/KC_p$; where $R_{e,p} = U_p D_{50,p}/(n_p \nu)$ is the grain Reynolds number (Burcharth and Andersen, 1995) and KC_p is the grain Keulegan-Carpenter number. $U_p \approx n_p H/T$ is the characteristic seepage velocity in the porous medium.

Again, the total energy of the incident, reflected, and transmitted wave trains are derived dimensionless quantities of the first kind, and the dependent quantities (reflected and transmitted energy coefficient and phase of the reflected and transmitted wave train) are expressed as follow:

$$\left[K_R^2, \frac{X_{0,R}}{L}\right] = \Psi_R\left(\frac{h}{L}, \frac{H_I}{L}, \frac{D_{50,p}}{L}, \frac{B^*}{L}, R_{e,p}\right) \tag{3.6}$$

$$\left[K_T^2, \frac{X_{0,T}}{L}\right] = \Psi_T\left(\frac{h}{L}, \frac{H_I}{L}, \frac{D_{50,p}}{L}, \frac{B^*}{L}, R_{e,p}\right) \tag{3.7}$$

where, despite the fact that functions (Ψ_R, Ψ_T) are undetermined, their form is similar for the value pairs of the seaward and landward slope angles considered. Moreover, in order to apply the results to the scale of the prototype (for experimental tests), the values of the Reynolds number, $R_{e,w}$, and the grain Reynolds number, $R_{e,p}$, should be sufficiently high so that the hydrodynamic regime is totally turbulent in the water column and inside the core.

Bulk dissipation includes the shoaling-associated dissipation and the evolution of the wave profile, which would include eventual wave-breaking, and the dissipation during the propagation and transmission of the wave train through the porous core. This bulk dissipation (D'^*), a dimensionless quantity of the second kind, is determined on the basis of experimental results, solving the conservation energy equation:

$$D^* = \frac{D'^*}{E_I C_g} = 1 - \Psi_R - \Psi_T \tag{3.8}$$

Non-overtoppable, permeable, flat slope with a finite width and a main armor layer

The dimensions of the main armor layer significantly influence the values of the reflected wave energy as well as the dissipation rate. When the slope is composed by a main armor layer with a type and shape of unit piece positioned with a specific placement criterion, the complete set of independent variables includes: the equivalent diameter of the armor, D_a, and the thickness, e. Excluding α and β,

$$(X_1, X_2) = f(h, \rho, \mu, g, H_I, L, D_{50,p}, B^*, D_a, e)$$

The thickness can be expressed in terms of the equivalent diameter of the unit piece, $e = n_l D_a$, being n_l a real number. Therefore, adding the equivalent diameter as independent variable and with the base $\{\rho, g, L\}$, the similarity equation remains as

$$X_1^* = [H_R/L,\ X_{0,R}/L] = f(h/L,\ H_I/L,\ D_{50,p}/L,\ B^*/L,\ R_{e,p},\ D_a/L,\ R_{e,D_a})$$
$$X_2^* = [H_T/L,\ X_{0,T}/L] = f(h/L,\ H_I/L,\ D_{50,p}/L,\ B^*/L,\ R_{e,p},\ D_a/L,\ R_{e,D_a})$$

where D_a/L, and R_{e,D_a} are the relative armor diameter and an armor Reynolds number, respectively, which govern the turbulence regime on the slope due to the breaking and interaction of the wave train with the main armor layer, mainly dissipation (see more details in Chapter 6). Like the forces inside the core, the force regimes in the armor layer are determined as a function of R_{e,D_a} and $R_{e,D_a}/KC_a$, where $KC_a \approx H_I/D_a$ is the armor Keulegan-Carpenter number. $R_{e,D_a} \approx \sqrt{gH_I}D_a/\nu$ is a reformulation of $R_{e,w}$. Again, the values $R_{e,w}$, R_{e,D_a} and $R_{e,p}$ should be sufficiently high so that the hydrodynamic regime is totally turbulent in the water column, inside the main layer and inside the core.

Finally, the dependent quantities of first kind (K_R^2, K_T^2, ϕ_R, ϕ_T) and second kind (D^*) are expressed as,

$$\left[K_R^2, \frac{X_{0,R}}{L}\right] = \Psi_R\left(\frac{h}{L}, \frac{H_I}{L}, \frac{D_{50,p}}{L}, \frac{B^*}{L}, R_{e,p}, \frac{D_a}{L}, R_{e,D_a}\right) \tag{3.9}$$

$$\left[K_T^2, \frac{X_{0,T}}{L}\right] = \Psi_T\left(\frac{h}{L}, \frac{H_I}{L}, \frac{D_{50,p}}{L}, \frac{B^*}{L}, R_{e,p}, \frac{D_a}{L}, R_{e,D_a}\right) \tag{3.10}$$

$$D^* = \frac{D'^*}{E_I C_g} = 1 - \Psi_R - \Psi_T \tag{3.11}$$

NOTE

It should be highlighted that even though the $R_{e,w}$, R_{e,D_a} and $R_{e,p}$ values exceed the threshold (fully turbulent regime) and can be omitted, this does not signify a reduction in the number of independent variables in the initial set. The similarity equation cannot be simplified, and since the dependence of the Reynolds numbers is implicit in the experimental results, and it cannot be ignored.

3.3 Materials and methods

In order to test the different breakwater slopes defined in Section 3.2, two method were implemented: (a) numerical experiments, using the IH-2VOF model (Lara et al., 2008), on a mound breakwater with an undefined, impermeable, rigid slope; and (b) physical experiments, using a wave flume on a mound breakwater with a non-overtoppable constant slope, a cube

armor layer, and a porous core of constant finite width and grain size, $D_{50,p}$. The experimental tests for a permeable and homogeneous slope are summarized in Chapter 5, as an example application of the methodology and results obtained in Chapters 3 and 4.

Experimental tests in this study involved the following:

1. Generation of linear wave trains with a minimum of 100 waves, for which the absorption of the reflected wave train was monitored and pairs of target values were specified, namely, the height, H_{target}, and period, T_{target}, defining a target Iribarren number, $I_{r,target}$.

2. Application of linear wave theory to relate the different variables in the analysis of the following experimental measurements: (i) wavelength, L_{target} calculated to resolve the dispersion equation (Equation 3.3), depending on h and $T_{z,target}$; (ii) wave celerities, $c_{target} = L_{target}/T_{target}$, and $C_{g,target} = f(C_{target}, h/L_{target})$; (iii) and the total target energy of the incident wave train, $E_{target} = (1/8)\rho g H^2_{target}$.

3. Application of linear wave theory following Baquerizo (1995) in order to separate the time series of the incident and reflected wave train, based on the time records of the vertical displacement of the free surface in a sufficient number of sensors (≥ 3).

4. Statistical analysis of the time series to obtain the following: (a) spectral density function, a characteristic wave height related to this function $(m_0)^{1/2}$ and the phase lag between them ϕ; (b) the marginal and joint probability density functions of the height and period of the individual waves in the wave train and their corresponding statistical descriptors. The wave height and period are also identified by the zero up-crossing criterion.

5. Repetition of the runs and evaluation of the experimental scattering of all the variables participating in the transformation process. The application of linear theory facilities this step.

3.3.1 Physical experimental tests

The experimental tests were performed in the wave flume (23 x 0.65 x 1 m) of the Andalusian Interuniversity Institute for Earth System Research (IISTA) at the University of Granada (Spain). Figure 3.2 shows a diagram of the physical model that was tested, namely, a permeable mound breakwater with a main armor layer consisting of two layers of cubes with a porous core. The flume bottom is horizontal and the water depth in the wave generation zone and in the flume up to the toe of the slope is constant, $h = 0.4$ m.

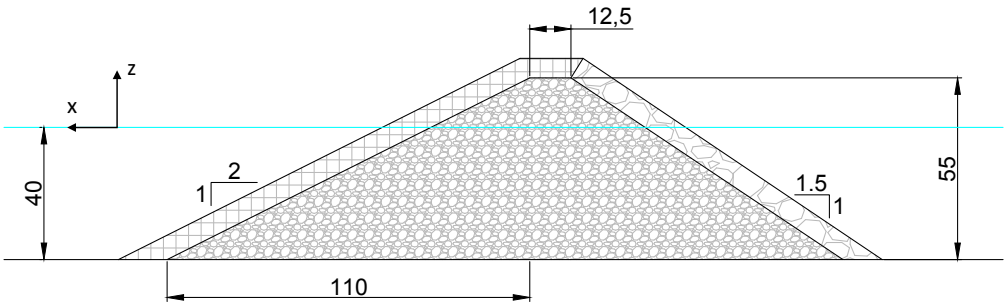

FIGURE 3.2: Physical model of the breakwater tested: mound breakwater composed of a main armor layer of cubes and a porous core (measured in centimeters).

Table 3.1 gathers more details regarding the geometrical configuration of the breakwater model, where: B_b is the width of the top of the breakwater; F_{MT} is the porous medium height;

D_{eq} is the equivalent diameter of the main armor layer, considering the cube volume equated to the volume of a sphere; A_{eq} is the area of the porous core per section unit below mean sea level (Vílchez et al., 2016a); $\cot(\alpha)$ and $\cot(\beta)$ are the seaward and landward slopes of the breakwater, respectively; ρ_s is the density of the unit pieces; and n_p is the porosity of the core, according to CIRIA et al. (2007).

Breakwater geometry				
Armor unit: cubes (m)	B_b (m)	ρ_s (t/m^3)	$\cot(\alpha)$	$\cot(\beta)$
$1 = 0.033$ $D_{eq} = D_a = 0.0409$	$3D_a = 0.125$	2.18	2	1.5
Porous medium				
F_{MT} (m)	$D_{50,p}$ (mm)	A_{eq} (m^2)	ρ_s (t/m^3)	n_p
0.55	12	0.2125	2.83	0.39

TABLE 3.1: Geometric parameters of the physical model: permeable mound breakwater with a main armor layer.

Wave conditions

Tests were performed in the wave flume with a VTI controller. The AwaSys software package was used to generate waves with the simultaneously active absorption of reflected waves. Regular waves were simulated and defined by a wave height, H_{target}, and wave period T_{target}. They impinged perpendicularly onto the breakwater. Wave-breaking was only caused by wave-breakwater interaction, and the experiments were under non-overtopping and non-damage conditions. Table 3.2 shows the target wave parameters run in each configuration.

Four Iribarren numbers, $I_{rtarget}$ were tested (see Table 3.2) in the domain where experimental results of other studies tend to scatter as I_r increases ($I_r > 1.5$). For that, two ways of wave generation sequence were programmed: (1) $I_{rtarget,H}$, the wave height ($T_{target,H}$), remained constant, whereas the wave period varied; (2) $I_{rtarget,T}$, the wave period (T_{target}) remained constant, whereas the wave height ($H_{target,T}$) varied. Each test was repeated three times, and 100 waves were simulated in each test.

$I_{rtarget}$		2.30	3.00	3.70	5.00
$I_{rtarget,H}$	$H_{target}(m)$	[0.07 - 0.12]	[0.05 - 0.12]	[0.04 - 0.10]	[0.02 - 0.08]
	$T_{target}(s)$	[1.00 - 1.47]	[1.14 - 2.30]	[1.31 - 2.86]	[1.23 - 4.10]
$I_{rtarget,T}$	$T_{target}(s)$	[1.05 - 1.50]	[1.25 - 2.50]	[1.25 - 3.00]	[1.25 - 3.00]
	$H_{target}(m)$	[0.075 - 0.124]	[0.057 - 0.133]	[0.038 - 0.105]	[0.021 - 0.058]

TABLE 3.2: Wave conditions tested in the laboratory: target vales for the two ways of wave generation sequence.

3.3.2 Numerical experimental tests

The IH-2VOF numerical model (Lara et al., 2008) was used to study a breakwater with a non-overtoppable, impermeable, smooth slope. This numerical model was chosen because, although its main characteristic is to solve the flow in the porous medium, it also allows to model any impermeable geometry, as well as to simulate wave conditions and calculate the wave-structure interaction response.

Description of the model

The IH-2VOF numerical model solves the flow both inside and outside the porous medium. It is based on the Volume - Averaged Reynolds - Averaged Navier - Stokes equations (VARANS) in a two-dimensional domain. These equations are obtained when RANS equations are integrated in a control volume, both inside and outside the porous medium. The final form of these equations are (more details in Hsu et al., 2002):

$$\frac{\partial \langle u_i \rangle}{\partial x_i} = 0 \tag{3.12}$$

$$\frac{1+c_A}{n_p}\frac{\partial \langle u_i \rangle}{\partial t} + \frac{\langle u_j \rangle}{n_p^2}\frac{\partial \langle u_i \rangle}{\partial x_j} = -\frac{1}{\rho}\frac{\partial \langle p \rangle}{\partial x_i} + \frac{\nu}{n_p}\frac{\partial^2 \langle u_i \rangle}{\partial x_i \partial x_j} - \frac{1}{n_p}\frac{\partial \langle u_i' u_j' \rangle}{\partial x_j} - F_{Gi} \tag{3.13}$$

where t denotes time; u is the Reynolds-averaged velocity; p is the pressure; n_p is the core porosity; ν is the kinematic viscosity; and i, j =1, 2 where 1 and 2 denote the horizontal and vertical directions, respectively. The $\langle\,\rangle$ represents the volume-averaged and the single primes ($'$) are the Reynolds-averaged fluctuations. F_{Gi} quantifies the resistive or friction forces created by the solid skeleton of the porous medium. The mass added term appears on the left side of the equation, which affects the acceleration term, where $c_A = \gamma_p(1-n_p)/n_p$ is the added mass coefficient. The value of $\gamma_p = 0.34$ (Van Gent, 1995) is generally considered to be constant.

Since the breakwater tested with the numerical model was impermeable, parameters related with the porous medium and the friction term were not taken into account. However, the reader can find in Vílchez (2016)'thesis an example of calibration of the coefficients involved in the flow inside and outside the porous medium for five breakwater typologies.

Volume of fluid (VOF) method is followed to compute the free surface. IH-2VOF uses a finite difference scheme to discretize the time and spacial derivations of the equations. Wave conditions are introduced in the model by imposing a velocity field and a time evolution of the free surface on one side of the numerical mesh domain. Furthermore, the active wave absorption can be also considered.

Numerical experiments description

The IH-2VOF numerical model (Lara et al., 2008) was used to study a breakwater with a non-overtoppable, impermeable, smooth slope with three seaward slope angles: $\cot(\alpha)$ = 2, 3 and 10. Since the breakwater was impermeable and non-overtoppable, the maritime structure was modeled with a vertical wall at the landward side (β = 90º). For more details of the configuration of the numerical model see Table 3.3.

Breakwater geometry				
Slope type	B_b (m)	$\cot(\alpha)$	$\cot(\beta)$	F_{MT} (m)
Impermeable	0.50	2	vertical	0.75
	0.50	3	vertical	0.65
	0.50	10	vertical	0.65

TABLE 3.3: Geometric parameters of the numerical models: impermeable mound breakwater.

The wave flume of IISTA - University of Granada (see Figure 3.3) was reproduced in the numerical model with a 2D domain. The numerical set-up was the same used and calibrated in Vílchez et al. (2016b), formed by a uniform grid on the y-axis with a grid cell size of 0.5

cm, and horizontally (on the x-axis) grid with three regions: (i) a center region, 5 m long, containing the breakwater section with the finest resolution and a cell size of 1 cm; two regions (ii) at the beginning and (iii) at the rear of the numerical wave flow with a cell size of 2 cm. A mesh sensitivity analysis was performed to assess the computational costs and the accuracy of the results. The total number of cells in the numerical domain was 1304 x 162. Active wave absorption was used at the generation boundary, and the dissipative ramp at the end of the flume was reproduced with a porous medium. The characteristics of this porous medium were previously calibrated by comparison between the reflection coefficient measured in laboratory and calculated numerically in absence of the maritime structure for different wave conditions following Higuera et al. (2014).

h (m)	T_{target} (s)	$I_{rtarget}$
0.4	[1 - 2.2]	[2.3, 3.0, 3.5, 4, 5]
0.35	[1 - 2.2]	[1.5, 1.8, 2.3, 3.0, 3.5, 4.0, 5.0]
0.35	[1 - 2.2]	[0.5, 1.5, 1.8, 2.3, 3.0, 3.5, 4.0]

TABLE 3.4: Wave conditions tested in the numerical model: target values setting T_{target} and varying H_{target} to cover the Iribarren domain $(I_r > 1.5)$.

Regular waves were simulated by setting T_{target} and varying H_{target} to cover the Iribarren domain $(I_r > 1.5)$, with two water depths (Table 3.4): (1) $h = 0.35$ m, the same as in Moraes (1998); and (2) $h = 0.4$ m, the same as in the physical experimentation. To complete the study of breakwater performance, some cases were simulated for $I_r < 1.5$ with the slope 1:10. The minimum number of Iribarren tested for each slope in Table 3.4 is limited by the maximum wave height in non-overtopping conditions. Each test was simulated three time with 100 waves.

3.3.3 Data acquisition and time series analysis

Figure 3.3 shows the five resistance wave gauges (G1 to G5) located along the wave flume of IISTA and used to measure the free surface elevations with a sampling frequency of 20 Hz. In both numerical and physical experimental tests, the positions of gauges G1, G2, G3 and G5 were the same for all the models tested. Gauge G4 was fixed and positioned at the toe of the core for the physical tests and moved to the toe of the slope for each impermeable breakwater tested in the numerical model. G5 was positioned in numerical model to check if there was or not overtopping.

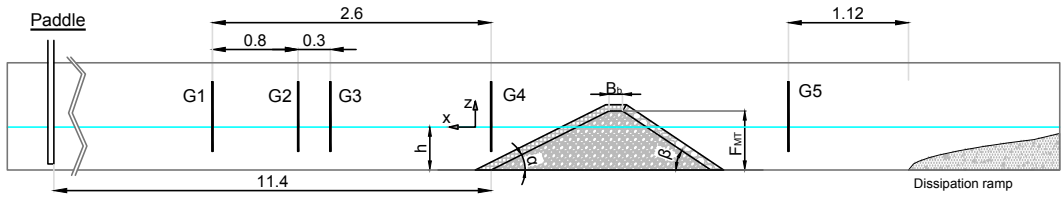

FIGURE 3.3: Scheme of the wave flume of IISTA - University of Granada. Location of wave gauges.

The data acquisition obtained from the wave gauges were the following:

1. Instantaneous values of the free surface elevation:

   - The incident, $\eta_I(t)$, and reflected, $\eta_R(t)$, wave trains were separated by applying Baquerizo (1995), (based on Mansard and Funke (1987) three-gauge method),

providing the magnitude and phase of the reflected wave train. The values were calculated with the data measured by gauges G1, G2 and G3 (see Figure 3.3). This method is based on linear theory.

- The total free surface time series, $\eta_t(t,x_i)$, in each position of the wave gauges (x_i).

2. Statistical parameters obtained from the time series analysis of the free surface elevation. Both temporal and spectral statistical analysis were implemented (see more details in Appendix C).

   - Incident and reflected parameters: the incident wave height and period H_I, $T_{z,I}$ and the reflected wave height and phase, H_R, ϕ_R were calculated. In all cases, for regular waves: $H_i \approxeq H_{mean,i} \approxeq H_{phase-averaged,i} \approxeq H_{s,i}$ with $i = I$ (incident), $= R$ (reflected). The same was true for the wave period. The reflected wave energy, E_R, and its respective reflection (K_R^2 and phase ϕ_R) coefficient were obtained by applying power spectral analysis.
   - Transmitted parameters: for the physical tests, the transmitted wave height H_T, and the energy transmitted (E_T and K_T^2) were obtained by applying the temporal and spectral analysis, respectively. These variables were computed with the data measured with gauge G5. For the numerical tests, there was no transmission.
   - Dissipation parameter: The wave energy dissipation rate, D^*, was calculated by applying Equation 3.1 for the total flow.
   - The total wave height: Gauge G4, located at the toe of the structure, provided the total wave height at the toe of the breakwater (due to the interaction of the incident and reflected wave trains).

Wave gauges along the slope of the breakwater were also positioned in the numerical and experimental setups. The purpose of these gauges was to measure the free surface elevation on the slope (run-up and run-down) and its relation with wave-breaking. However, these measures are not studied in this work and will be the subject of the future research.

3.3.4 Analysis of wave generation and hydrodynamic flow regimes

As discussed throughout this section, the generation and analysis of the data has been done by applying linear theory. This implies that the experimental data (numerical and physical) must be in the Stokes I generation zone. Moreover, the hydrodynamic flow regimes in the water, inside the main layer and inside the core should be totally turbulent. Figures 3.4 and 3.5 show the characteristics of the wave generation and hydraulic regime for the data.

As can be observed in Figure 3.4 , the waves generated in the laboratory as well as in the numerical study are mainly in the Stokes I regime and do not break before interacting with the slope. Furthermore, given the wave flume dimensions and the range of values H_I, T, the Reynolds number ($R_{e,w}$) is greater than a minimum value in exceed of which the turbulence regime is fully developed. Except when the breakwater model is very small (scale $< 1:80$), $R_{e,w} \approx Hh/(T\nu) > 10^4$, and it can be assumed that the flow in the water column on the permeable or impermeable slope is turbulent (Dai and Kamer, 1969), at least, before and during the propagation-dissipation-reflection process of the wave train. The highest values of $R_{e,w}$, R_{e,D_a} occur at the medium level.

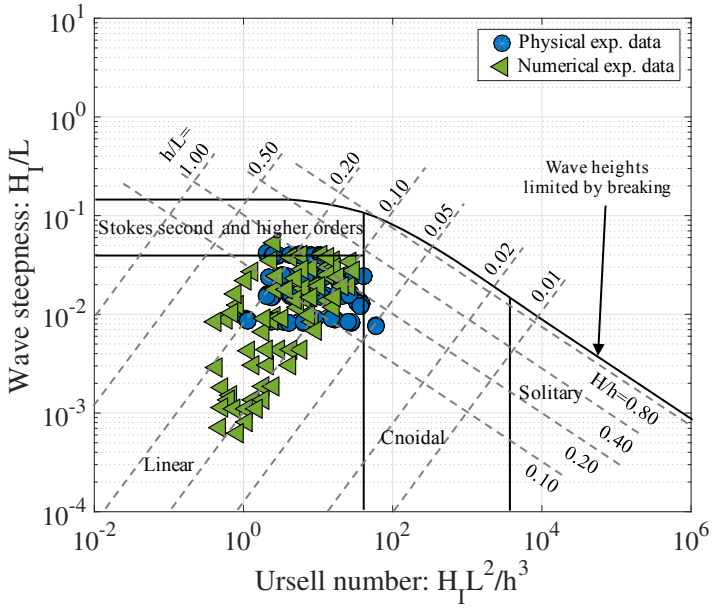

FIGURE 3.4: Wave generation characteristics: wave steepness (H_I/L) against the Ursell number ($H_I L^2/h^3$, which relates the three magnitudes to characterize the incident wave). Adapted from Dalrymple and Dean (1991).

Figure 3.5 represents the flow in the porous core for the physical tests, using the diagram proposed by Gu and Wang (1991) in terms of the following dimensionless quantities: grain Reynolds number, $R_{e,p}$, and the Keulegan-Carpenter number, KC_p. All of the tests conducted with the porous core and main armor layer took place in the region where the three forces (laminar f_L, inertial f_I and turbulent f_T) are equally important with values exceeding the threshold where the flow regime is fully turbulent ($R_{e,p} > 300$, following the criteria of Jensen et al., 2014b). The values of the dimensionless quantities were obtained, following Van Gent (1995), Pérez-Romero et al. (2009), and Vílchez et al. (2016b).

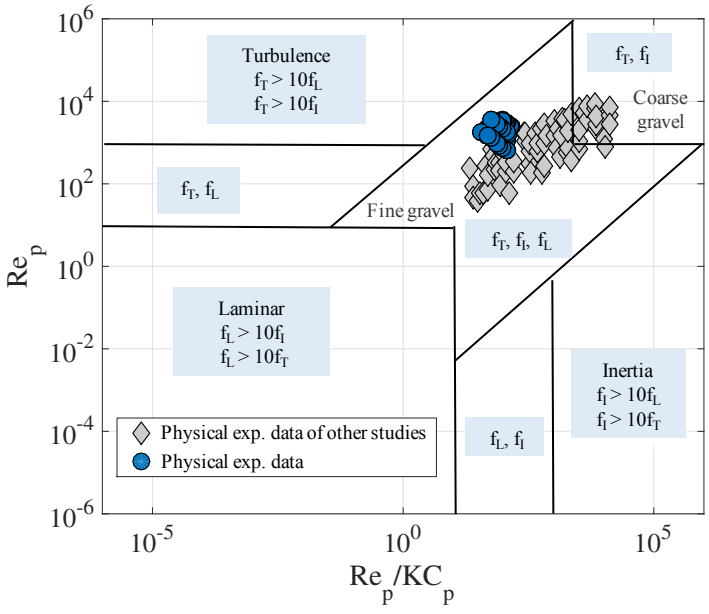

FIGURE 3.5: Importance of drag forces in the porous medium (adapted from Gu and Wang, 1991): (circle) Physical experimental data of the IISTA-UGR, (diamond) physical experimental data of other studies (Van Gent, 1995; Pérez-Romero et al., 2009; Vílchez et al., 2016b).

However, because of the dissipative nature of the flow in the porous medium and, if the width of the core is sufficient, the value of $R_{e,p}$ decreases towards the inner zone of the breakwater. The regime gradually varies from fully turbulent to transitional, and then from transitional to Forchheimer, and eventually, from Forchheimer to Darcy. In other words, there is also a spatial variation in the regime inside the breakwater core. This type of gradation, which has evident consequences for the rate of energy dissipated, reflected, and transmitted, mainly depends on B^*/L and $D_{50,p}/L$.

Chapter 4

Wave energy transformation on mound breakwaters (II): results and discussion

Comment

This chapter presents the main results derived from Chapter 3 an published on:

P. Díaz-Carrasco, M.V. Moragues, M. Clavero, and M.A. Losada (2019c). "2D water-wave interaction with permeable and impermeable slopes: dimensional analysis and experimental overview". In: *Coastal engineering* (Under review)

This chapter addresses the analysis of the physical processes that dominate the incident wave energy transformation on each mound breakwater tested in Chapter 3. For that, Section 4.1 previously studies the dependence of the physical and numerical experimental data with Iribarren number. Section 4.2 proposes a similarity parameter for mound breakwaters that (i) controls the wave energy distribution and breaker type, (ii) and allows to fit similar sigmoid curves with different trajectories because of the porous medium and the main armor layer. A design methodology for the laboratory tests is also proposed in Section 4.3, according to the results obtained in the previous section. Finally, the main conclusions of this work (Chapter 3 and 4) are summarized in Section 4.4.

4.1 Analysis of Iribarren number as a similarity parameter

The experimental and numerical results [K_R^2, K_T^2 and D^*] of other studies tend to scatter as the value of I_r increases ($I_r > 1.5$). Some examples of this variability can be found in: Battjes (1974), Seeling and Ahrens (1981), Davidson et al. (1996), and Zanuttigh and Van der Meer (2008), among others. Most of these researches represent $K_R = f(I_r)$ and we can observe that, the reflection increases with I_r but, likewise, its adjustment deteriorates significantly depending on the slope angle. Under such relation, it is also assumed that Iribarren number is a similarity parameter between model and prototype for experimental tests.

Therefore, the dependence of the wave energy transformation modes is questioned in this section. To do this, the experimental (numerical and physical) results for the impermeable slope and the permeable with main armor layer slope are compared with Iribarren number. Moreover, the variability of the independent quantities that govern similarity equations (Section 3.2.2) with I_r is analyzed.

4.1.1 Experimental variability of different slope types

A smooth, rigid, flat slope impermeable and non-overtoppable

Figure 4.1 represents the values of K_R^2 and D^* against the Iribarren number, which were obtained with the numerical model that identifies the $I_{rtarget}$, $[0.5 \leq I_{rtarget} \leq 5.0]$ (Figures 4.1-a1, 4.1-b1), and the three slopes, $[1/10 \leq \tan(\alpha) \leq 1/2]$ (Figures 4.1a2, 4.1-b2). The behavior of the data is similar to the results obtained by (Battjes, 1974) (his Figure 2) with data from (Moraes, 1998). The left panels of Figure 4.1 provide the values of $I_{rtarget}$ for each experiment, which were generated by fixing T and varying H. The x-axis shows the experimental Iribarren number, $I_{r,I}$, calculated with incident wave height H_I. With the calculation method (energy conservation equation) used, the behavior of the bulk dissipation, D^*, against I_r mimics that of the reflected energy coefficient, K_R^2. Moreover, the blue bands indicate the confidence interval (5%-95%) of the values thus calculated for each chosen $I_{rtarget}$.

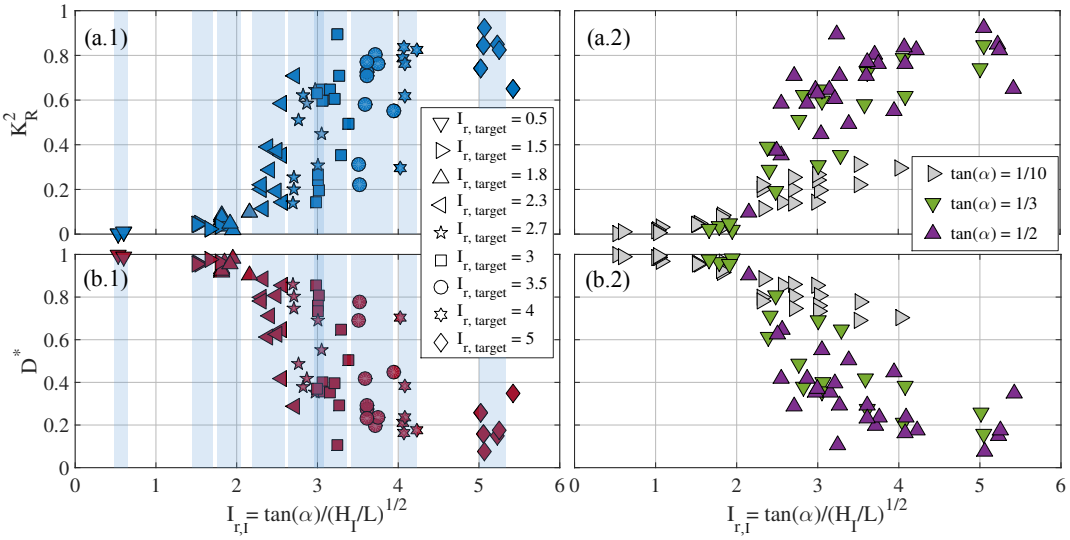

FIGURE 4.1: Experimental numerical results (IH-2VOF) of the transformation of incident waves against the experimental Iribarren number ($I_{r,I}$): (a) modulus of the reflected energy coefficient (K_R^2) and (b) simulated bulk wave dissipation (D^*), numerically simulated according to (a1, b1) $I_{rtarget}$; and (a2, b2) the slope angle. The blue bands represent the confidence intervals of 5%-95% for each $I_{r,I}$ respect to the target value.

For the three slopes, K_R^2 values are ordered depending on the slope angle. Scattering decreases as the slope decreases, and increases when $I_{r,I}$ is in the interval $[I_{r,I} \geq 2.2]$. As can be observed, the variability of each slope angle in each interval (blue band) is significant with slight changes in the value of $I_{r,I}$. This variation partially stems from small variations in the incident wave height H_I. Nevertheless, local scattering for $I_{r,I}$ intervals did not decrease when the set of wave trains corresponding to a value of $I_{rtarget}$ was repeated. Since the slope is impermeable, this local scattering suggests that, the behavior of the K_R^2 values depends on the form of wave-breaking train (breaker type), and it seems that Iribarren number does not capture this process.

Non-overtoppable, permeable, flat slope with a finite width and a main armor layer

Figure 4.2 presents the experimental results of K_R^2, K_T^2 and D^*, based on $I_{r,I}$ (inside the domain $I_r \geq 1.5$), obtained from the physical experiments for the breakwater with a permeable slope with a slope of 1:2. $I_{rtarget}$ values were set either by maintaining H constant and varying

T, or by maintaining T constant and varying H. These experiments also determined the transmitted energy, K_T^2, (Figure 4.2c), whose values are one order of magnitude lower than the reflected energy. The energy conservation equation was applied to obtain the bulk dissipation D^* (Figure 4.2-b).

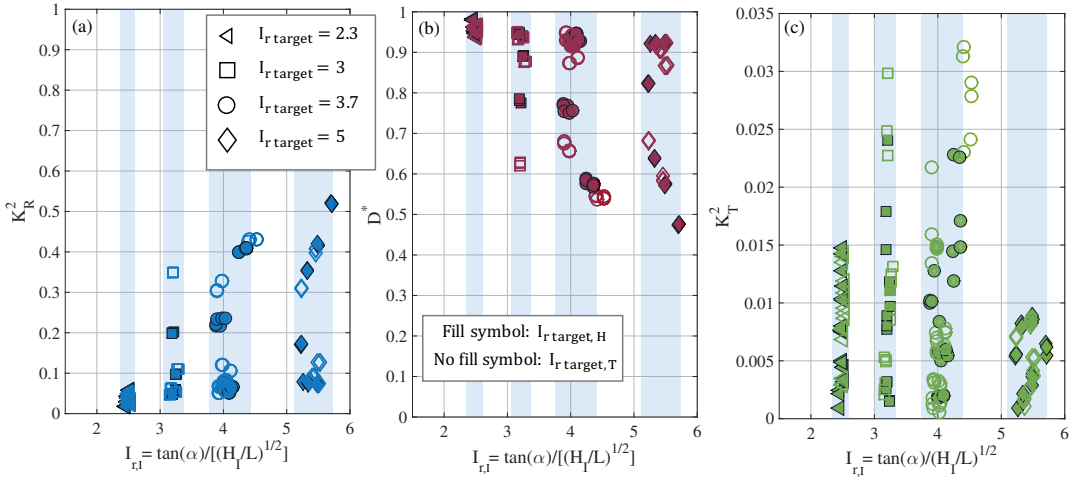

FIGURE 4.2: Experimental physical results (IISTA-UGR) of the transformation of incident waves against the experimental Iribarren number ($I_{r,I}$): (a) modulus of the reflected energy coefficient (K_R^2), (b) bulk wave dissipation (D^*) and (c) modulus of the transmitted energy coefficient (K_T^2) according to the $I_{rtarget}$. The blue band represents the confidence level (5%-95%) for each $I_{r,I}$ respect to the target value.

Similar to behavior of the impermeable slope, experimental scattering increases with $I_{r,I}$ in the interval $[I_{r,I} \geq 2.2]$. The experimental scatter of each interval (blue band) is significant with slight changes in the value of $I_{r,I}$. This variation is partially due to small variations in the incident wave height, H_I, and interaction with the reflected wave train, (modulus and phase). The same value of the Iribarren number have different energy transformation modes and, consequently, the potential breaker types. The local scattering for intervals of $I_{r,I}$ did not decrease when the experiment for a given value of $I_{rtarget}$ was repeated. Since the slope is permeable, this local scattering can be attributed to: (i) wave-breaking on the slope, (ii) wave interaction with the main armor layer, and (iii) wave propagation through the porous core.

Variability of the independent variables

The variability of the experimental results grows when the reflection is relevant in the wave transformation process on the slope. Small variations in the wave height causes significant variation in the breaker type (see Appendix B), related with the phase lag between the incident and reflected wave trains. As mentioned in Section 3.2.2, Sutherland and O'Donoghue (1998) verified that the reflected phase depends on the dimensionless magnitude x_m/L. Hence, Figure 4.3-a represents the values pairs ($I_{r,I}$, x_m/L). In this figure it can be observed that a value of $I_{r,I}$ corresponds to a wide range of x_m/L and, therefore, there is not a relationship between Iribarren number and the phase of the reflected train.

If the breakwater is permeable, the relation between I_r, the energy transformation modes and breaker type deteriorates significantly compared to the impermeable slope, since other processes come into play, namely the reflection and dissipation associated with the dimensionless magnitudes: $D_{50,p}/L$, B^*/L, D_a/L, $n_l D_a/L$ (see Section 3.2.2). Figure 4.3-b shows that to a value of $I_{r,I}$ a wide range of B^*/L corresponds to it. Given that $D_{50,p}$ and B^* are constant for the physical model and become dimensionless with the wavelength, the experimental scatter for $D_{50,p}/L$ is equivalent as for B^*/L.

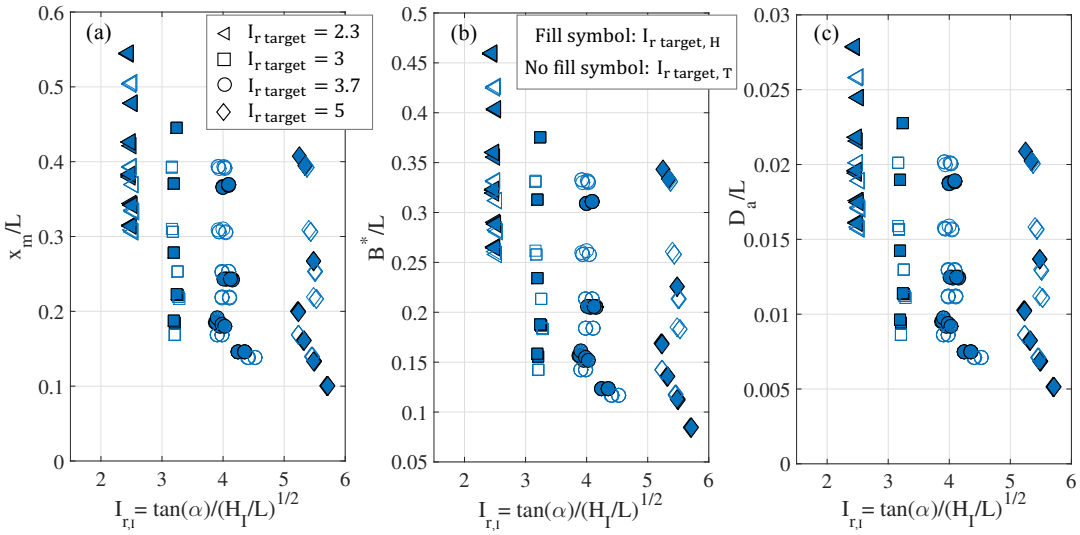

FIGURE 4.3: Experimental physical values (IISTA-UGR) of (a) x_m/L, (b) B^*/L and (c) D_a/L, against the experimental Iribarren number ($I_{r,I}$), clustered according to the $I_{rtarget}$ tested in the laboratory.

Finally, Figure 4.3c represents the value pairs ($I_{r,I}$, D_a/L). As with the other parameters, there is a variability of the relative diameter of the main armor and the number of layers with I_r (Benedicto, 2004; Clavero et al., 2018). Each D_a/L value dissipates a different amount of incident wave energy. The variability due to the main armor layer is better analyzed in Chapter 6.

4.1.2 Preliminary advanced results: the modified Iribarren number

The results show the lack of agreement of the functional relationship between I_r and the quantities that quantify the transformation of the wave train into an impermeable slope (K_R^2, D^*) and permeable slope (K_R^2, K_T^2, D^*). In this regard, during the last five years the "Environmental Fluid Dynamics Group" of the University of Granada has been working to properly quantify the wave transformation and propagation inside the porous medium (Pérez-Romero et al., 2009; Vílchez et al., 2016a; Vílchez et al., 2016b).

Vílchez et al. (2016a) analyzed the hydraulic performance for all breakwater typologies with a unified expression that depends on the scattering parameter, A_{eq}/L^2 (being A_{eq} the area of the porous core under the still water level). This study improved the characterization of the porous medium with the relative grain diameter, $D_{50,p}/L$, (scale effects) and the scattering parameter, A_{eq}/L^2, which controls the averaged transformation of the wave inside the porous medium. Then, based on Dalrymple et al. (1991) and for seeking the possibility of full similarity, Clavero et al. (2018) modified the Iribarren number by introducing into I_r the scattering parameter to evaluate the wave dissipation, reflection and transmission inside the core of mound breakwaters:

$$I_r^* = \frac{A_{eq}/L^2}{\sqrt{H_{trms}/L}} \tag{4.1}$$

being H_{trms}, the total wave train at the toe of the breakwater following a Rayleigh distribution (Vílchez et al., 2017). The modified Iribarren number was also defined as an approach of full similarity between model and prototype in experimental tests, if and only if the flow inside the porous medium is adequately scaled, basically by choosing properly $D_{50,p}/L$, $R_{e,p}$ and KC_p values (Vílchez et al., 2016b). Several properties ot the wave-breakwater interaction

were related with I_r^*, as: the wave overtopping phenomenon in Díaz-Carrasco et al. (2017) and Moragues et al. (2019a); or the stability of armor units (berm and slope) in Díaz-Carrasco et al. (2018) and Díaz-Carrasco et al. (2019b).

The application of the modified Iribarren number, I_r^*, significantly corrects the behavior of the Iribarren number. The regions can thus be identified since the deviation decreases in the transition region and the reflection-dominated region, whereas it increases in the dissipation-dominated region. In other words, I_r^* improves prediction when the transformation processes in the core, particularly in the case of reflection, dominate those on the slope. Nevertheless, this representation does not permit the identification of the possible breaker types in each region. Consequently, it is not possible to assume I_r^* as a parameter that controls (i) the wave energy transformation modes on mound breakwater and (ii) full the similarity in laboratory tests.

4.2 Principal similarity parameters for mound breakwater

The previous results for the permeable and impermeable slopes show that the transformation of incident energy on an undefined slope roughly depends on I_r, with a great dispersion of the experimental data. Nevertheless, they also raise questions regarding the application of the Iribarren number as a relevant parameter, to quantify the energy transformation modes and, consequently, the potential breaker types. This section presents the physical and numerical data derived from the reformulation of the dimensional analysis presented in Section 3.2.2.

4.2.1 Similar curve for mound breakwaters

The sigmoid function is defined by Churchill and Usagi (1972) and has the following expression:

$$X(Z) = (X_1 - X_0)\left[1 + \left(\frac{Z}{a_z}\right)^{\gamma_z}\right]^{-1} \; ; \; Z > 0 \tag{4.2}$$

where $X(Z)$ is the physical entity that describes a transport phenomenon, and X_0 and X_1 are the chosen limit values of $X(Z)$ for fitting the similar curves for small and large values of the independent variable Z. It describes a uniform transitions between the asymptotes with a blending coefficient, γ_z, and a parameter of the process inherent to the sigmoid shape, a_z. In this research, the physical entities are the wave energy transformation modes: $[K_R^2, K_T^2, D^*]$.

The independent variable is chosen according to the dimensional analysis. For all the mound breakwater slope types, there is a "dimensionless parameters base" that governs the similarity equations (Equations 3.4-3.5, 3.6-3.7-3.8, 3.9-3.10-3.11) and represents the incident wave train: $Z = (h/L)(H_I/L)$.

A smooth, rigid, flat slope impermeable and non-overtoppable

According to Equation 3.4, $K_R^2 = \Psi_R(h/L, H_I/L)$, so the shape of the sigmoid function should be similar for the three slopes tested in the numerical model. Figure 4.4 represents K_R^2 and D^* against the product of relative wave steepness and relative depth. In the same way as Figure 4.1, the slope is also identified. The x-axis is represented on a semi-logarithmic scale to facilitate the visualization of the data. The values are separated, depending on the slope, and the experimental scattering for a constant value of $(h/L)(H_I/L)$ becomes greater as the slope angle increases. This experimental deviation is intrinsic and it is analyzed in detail in Section 4.2.3.

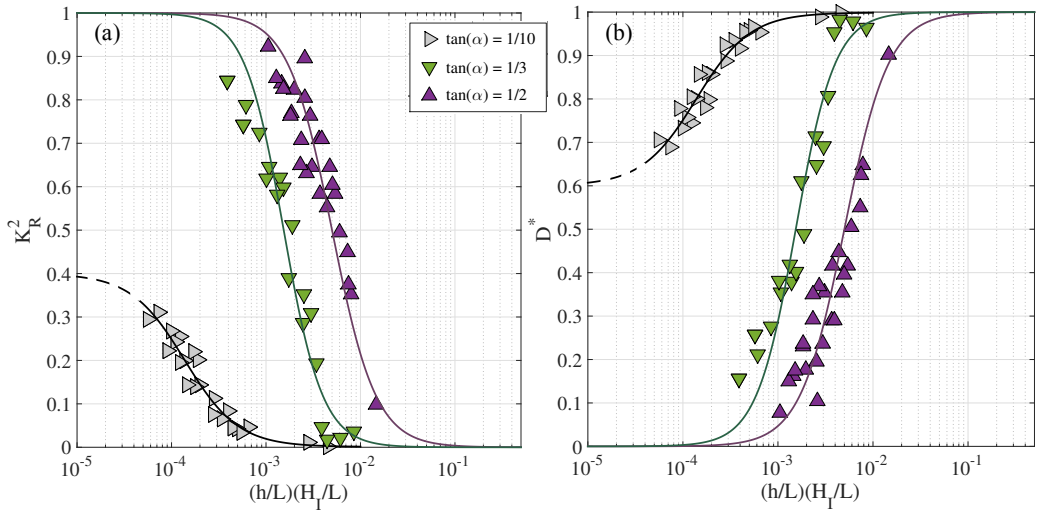

FIGURE 4.4: Experimental numerical results (IH-2VOF) of the incident wave energy transformation against $(h/L)(H_I/L)$: (a) modulus of the reflected energy coefficient (K_R^2 - Equation 3.4); (b) bulk wave dissipation (D^* - Equation 3.5) depending on the slope angle. The solid line represent the sigmoid curves fit to each slope, whose parameters are shown in Table 4.1 and the dash line represents the chosen limit values for fitting the curves.

The fit parameters for each slope are shown in Table 4.1 and the sigmoid curve of the wave bulk dissipation is calculated based on Equation 3.5, that is: $D^*_{sigmoid} = 1 - K^2_{R,sigmoid}$. The error between the experimental data of K_R^2 and the theoretical data of sigmoid curve is calculated by mean of the determination coefficient, R^2.

Slope type	**Sigmoid function**	**Fit parameters**				
		K^2_{R0}	K^2_{R1}	a_z	γ_z	R^2
Impermeable	$\tan(\alpha) = 1/2$	0	1	0.005	1.8	0.87
	$\tan(\alpha) = 1/3$	0	1	0.002	2.1	0.94
	$\tan(\alpha) = 1/10$	0.001	0.4	0.00012	1.5	0.94
Permeable	$\tan(\alpha) = 1/2$	0.03	0.65	0.0008	2.1	0.7

TABLE 4.1: Parameters for the sigmoid curves fitted to the physical and numerical experimental data of: $K_R^2 = (K_{R1}^2 - K_{R0}^2)\left[1 + \left(\frac{(h/L)(H_I/L)}{a_z}\right)^{\gamma_z}\right]^{-1} + K_{R0}^2$.

Non-overtoppable, permeable, flat slope with a finite width and a main armor layer

The reflected and transmitted energy in a mound breakwater of finite width and with a main armor layer and porous core should fulfill the following function, (Equations 3.9, 3.10):

$$\left[K_R^2, K_T^2\right] = \Psi_R\left(\frac{h}{L}, \frac{H_I}{L}, R_{e,w}, \frac{D_{50,p}}{L}, \frac{B^*}{L}, R_{e,p}, \frac{D_a}{L}, R_{e,D_a}\right)$$

In these tests, D_a, n_l, $D_{50,p}$, B^* and the slope angle remained constant. The difference in performance in this breakwater and the one with the impermeable slope stems from the additional dissipative regimes, in other words: (1) in the main armor layer, which depends on the relative size of the unit piece, D_a/L, and the relative thickness, $n_l D_a/L$; (2) during wave propagation in the porous medium, which depends on the relative diameter, $D_{50,p}/L$, and the characteristic relative width of the core, B^*/L.

Figures 4.5-a, 4.5-b, and 4.5c represents the values of K_R^2, D^* and K_T^2, respectively, based on the product of the relative wave steepness and the relative width on the x-axis at a semi-logarithmic scale. They show the sigmoid curves (Equation 4.2) that best fit the experimental data of K_R^2 (Table 4.1), and so, $D^* = 1 - K_{R,sigmoid}^2 - K_{T,sigmoid}^2$ (Equation 3.5). Since K_T^2 values are an order of magnitude lower than K_R^2 values, the sigmoid curve does not appear in Figure 4.5c.

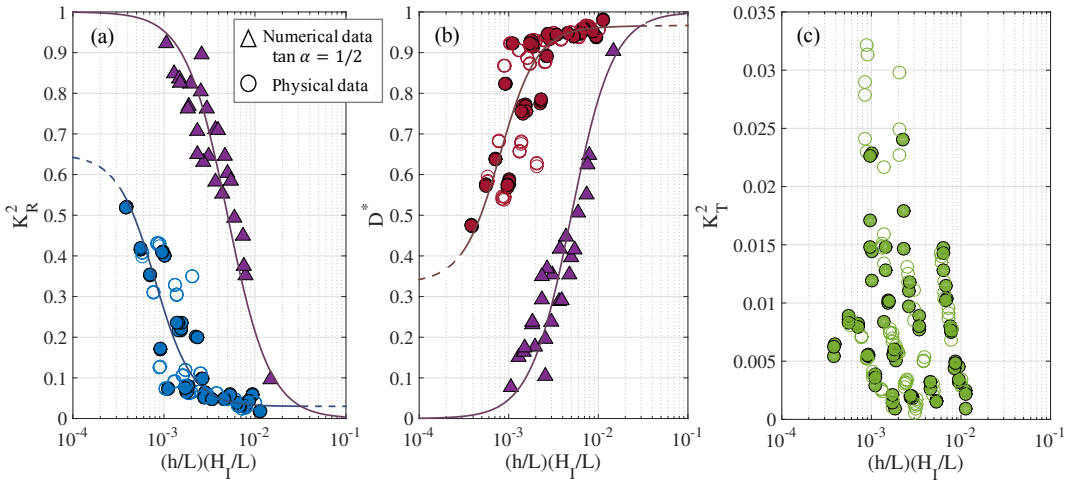

FIGURE 4.5: Physical results (circles - IISTA-UGR) and numerical results of the slope 1:2 (triangles - IH-2VOF) for the incident wave energy transformation against $(h/L)(H_I/L)$: (a) modulus of the reflected energy coefficient (K_R^2 - Equation 3.9), (b) bulk wave dissipation (D^* - Equation 3.11), and (c) modulus of the transmitted energy coefficient (K_T^2 - Equation 3.10). The solid line represents the sigmoid curves with the best fit to the experimental data K_R^2 and D^*, whose parameters are shown in Table 4.1 and the dash line represents the chosen limit values for fitting the curves.

For purposes of comparison, the figures also represent the experimental data numerically obtained for the same 1:2 slope. The permeable and impermeable fit curves are similar (i.e. a sigmoid function). However, for the permeable slope, the vertical dispersion of K_R^2 is greater in the interval $5 \cdot 10^{-4} < (h/L)(H_I/L) < 3 \cdot 10^{-3}$, which differs from the interval of greatest dispersion for the impermeable slope. The horizontal dispersion (same value of the energy coefficient) is possibly due to the different mode of energy transformation and the potential associated breaker types. This experimental deviation is well analyzed in Section 4.2.3.

In all cases, the energy transmitted is very small, and thus the increase in K_R^2 is mostly compensated by the decrease in dissipated energy D^* (Figure 4.6). The vertical scale of the figure highlights the fact that the data of K_T^2 cluster, based on the relative width (or relative diameter) of the breakwater. Its value increases when there is a decrease in B^*/L, (or $D_{50,p}/L$) as well as its growth rate. This behavior is also observed in K_R^2 (and consequently in D^*), especially when the reflected energy reaches a minimum value (saturation) and energy dissipation is the dominant process (Figures 4.6-a and Figure 4.6-b). Given that $D_{50,p}$ and B^* are constant and become dimensionless with the wavelength, the experimental scatter for $D_{50,p}/L$ is equivalent as for B^*/L in Figure 4.6.

4.2.2 Regions of wave energy transformation modes

For practical engineering purposes, it is advisable to identify at least three regions of incident wave behavior according to $(h/L)(H_I/L)$ values. The chosen threshold values are indeed arbitrary, but indicative of the predominant mode of energy transformation. Comparing the two slope types with the same slope angle, the following regions are distinguished:

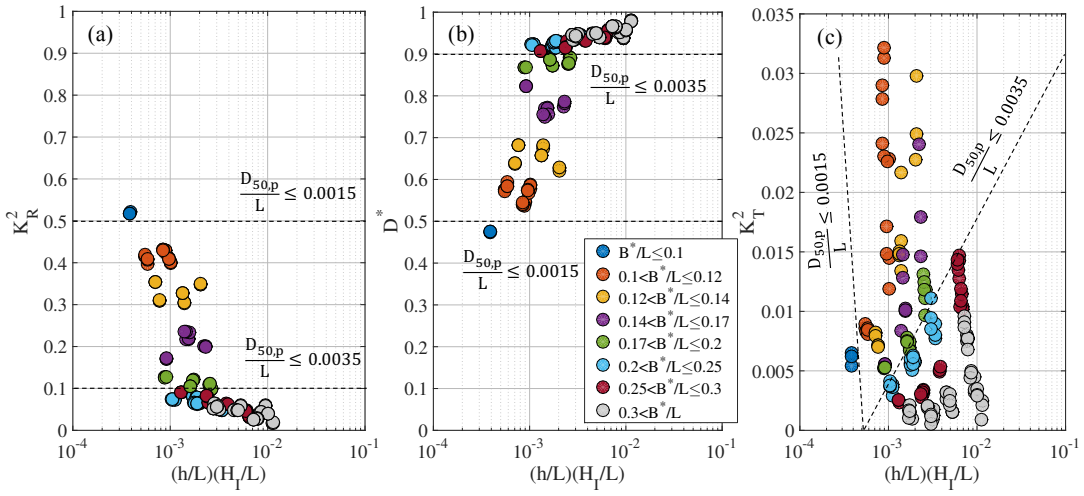

FIGURE 4.6: Experimental physical results (IISTA-UGR) of the incident wave energy transformation against $(h/L)(H_I/L)$: (a) modulus of the reflected energy coefficient (K_R^2 - Equation 3.9), (b) bulk wave dissipation (D^* - Equation 3.11), and (c) modulus of the transmitted energy coefficient (K_T^2 - Equation 3.10), according to intervals of B^*/L values. The dotted lines mark the limit of $D_{50,p}/L$ where $K_R^2 > 0.5$ and $D^* > 0.9$.

For an impermeable breakwater with slope $\tan(\alpha) = 1/2$,

- Reflection-dominated region, $\{K_R^2 \geq 0.9\}$: $(h/L)(H_I/L) < 1.1 \cdot 10^{-3}$,
- Dissipation-dominated region, $\{D^* \geq 0.6\}$: $(h/L)(H_I/L) > 8 \cdot 10^{-3}$,
- Transition region, $\{0.4 < K_R^2 < 0.9\}$: $1.1 \cdot 10^{-3} < (h/L)(H_I/L) \leq 8 \cdot 10^{-3}$,

For a permeable breakwater with a constant slope, $\tan(\alpha) = 1/2$, and a core with a relative width and relative grain diameter (B^*/L, $D_{50,p}/L$), the threshold and intervals of the regions change respect to the impermeable slope, due to the influence of the porous medium and its impact on breaker type in the wave energy transformation. For our present experimental tests,

- Reflection-dominated region, $\{K_R^2 \geq 0.5\}$: $(h/L)(H_I/L) \leq 4 \cdot 10^{-4}$, with
  - $D_{50,p}/L \leq 0.0015$,
  - $B^*/L \leq 0.10$,
- Dissipation-dominated region, $\{D^* \geq 0.9\}$: $(h/L)(H_I/L) \geq 3 \cdot 10^{-3}$, with
  - $D_{50,p}/L > 0.0035$,
  - $B^*/L \geq 0.25$,
- Transition region, $\{0.1 < K_R^2 < 0.5\}$: $5 \cdot 10^{-4} < (h/L)(H_I/L) < 3 \cdot 10^{-3}$, with
  - $0.0015 < D_{50,p}/L < 0.0035$,
  - $0.10 < B^*/L < 0.25$,

The reflected energy and the dissipation rate are almost equal (or are in equilibrium) when $[K_R^2 \approx 0.5;\ D^* \approx 0.5]$. This state can exist whenever $(h/L)(HI/L) \approx 4 \cdot 10^{-4}$, $D_{50,p}/L \approx 0.0015$, $B^*/L \approx 0.10$. The boundaries of these regions can change with the type of unit piece, the number of layers and configuration of the main armor layer, and definitively with the slope

angle. Recall that, the variability of the relative armor diameter and the number of layers in the main armor is analyzed in Chapter 6.

Notice that, present intervals of the regions of energy transformation defined for the permeable breakwater may be different if the tests are carried on in a flume with different wave generator and the breakwater (materials and layouts).

4.2.3 Experimental deviation: discussion

The experimental deviation of the results presented in Sections 4.1 and 4.2 may come from two sources: (1) experimental scattering from the generation, analysis and separation methods used in this work, and (2) experimental scattering from the physical processes. The wave generation and separation method is analyzed in Appendix C. From the discussion and results shown in the appendix, we can assert that the experimental technique and method of analysis in themselves are not sufficient to explain the variability of the experimental values, which is reflected in certain intervals of the value of I_r, as well as of $(h/L)(H_I/L)$.

Experimental deviation for an impermeable slope

Figure 4.7 represents the fit of a sigmoid curve to the experimental values of K_R^2 of the impermeable slope 1:2 against $I_{r,I}$ and $(h/L)(H_I/L)$ (Figures 4.7-a.1 and 4.7-a.2), as well as the residual values that fit a t-Student (Figures 4.7-b.1 and 4.7-b.2). The x-axis is on a semi-logarithmic scale to facilitate the visualization of data. Figure 4.7-a.1 shows that the scattering of the experimental results are higher against I_r (as already highlighted in Section 4.1), with a determination coefficient $R^2 = 0.56$.

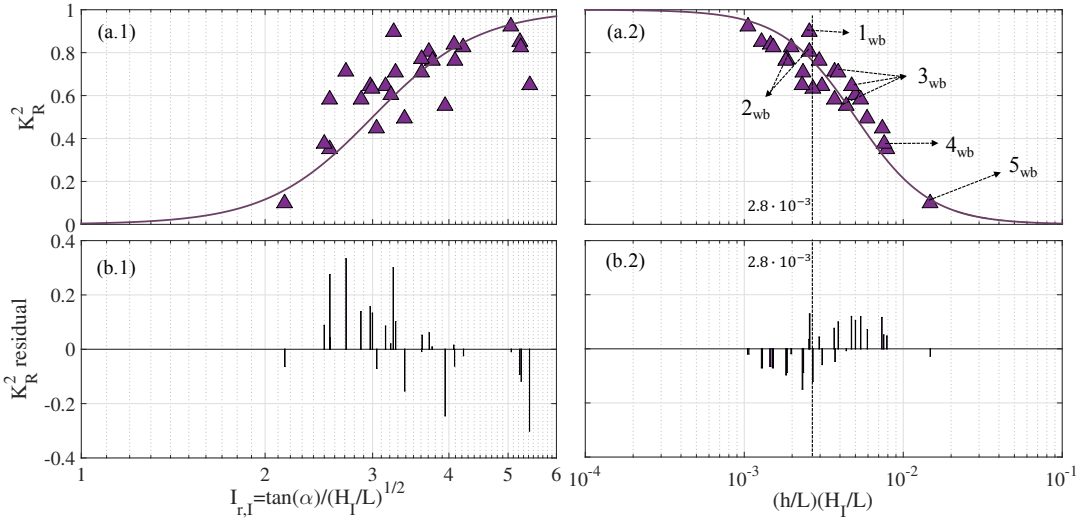

FIGURE 4.7: (a) Fit of the sigmoid curve to the experimental values of K_R^2 for the impermeable 1:2 slope against the experimental Iribarren number ($I_{r,I}$) and the product of relative depth and steepness $(h/L)(H_I/L)$. (b) Values of the residual deviation: experimental value minus the theoretical value calculated by the sigmoid curve. The number j_{wb} ($j = 1:5$) identifies the wave breaker types on the slope: 1_{wb} – surging, 2_{wb} – weak bore, 3_{wb} – strong bore, 4_{wb} – strong plunging, 5_{wb} – weak plunging.

When the relative depth is incorporated on the x-axis (Figure 4.7-a.2), the experimental data alignment satisfactorily identifies the transition region, dissipation-dominated region, and reflection-dominated region: $[1.1 \cdot 10^{-3} < (h/L)(H_I/L) \leq 8 \cdot 10^{-3}]$, $[(h/L)(H_I/L) > 10^{-2}]$, $[(h/L)(H_I/L) \leq 10^{-3}]$, respectively. Furthermore, the distribution of the residual

values evidence that the deviation of the K_R^2 values, in absolute terms, is small in dissipation-dominated region. However, the scatter increases in the transition region and decreases in the reflection-dominated region. The latter is also applicable to the dissipation rate D^* values.

As has been described throughout the document, the deviation of the energy transport modes could be due to the wave-breaking type on the slope. To this effect, in this study we expand the traditional list and adopt the four breaker types: weak plunging and strong plunging (Lakehal and Liovic, 2011) and weak bore and strong bore (Zhang and Liu, 2008). Hence, the breaker type sequence is (see number j_{wb} in Figure 4.7): surging, weak bore, strong bore, strong plunging, weak plunging and spilling. For more details on the breaker types and its shape on the slope see Appendix B, which also collects and describes pictures taken during the experimental tests.

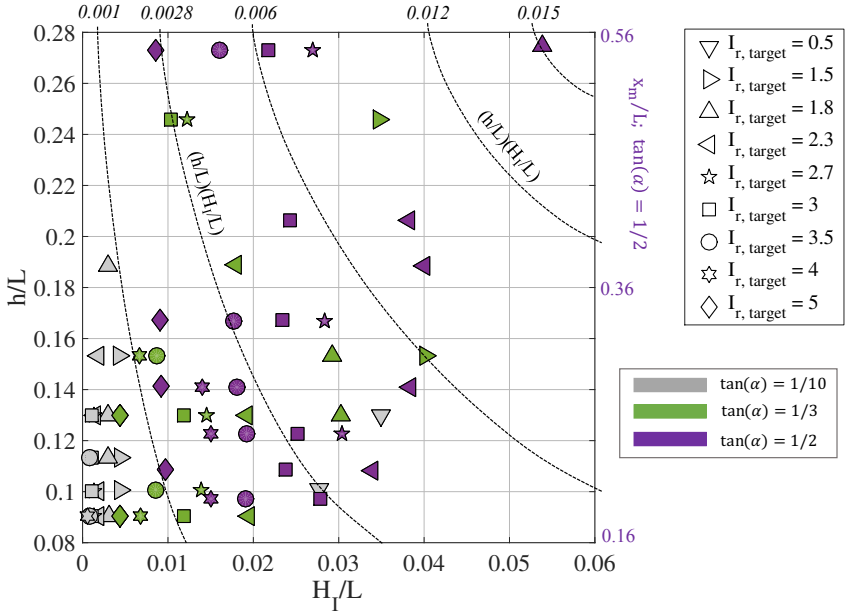

FIGURE 4.8: Experimental values for relative depth, h/L, against relative steepness, H_I/L, for the impermeable slope, according to the $I_{rtarget}$ (symbols) and slope angle (colors), which were numerically simulated. The dotted lines represent the isolines of the constant product $(h/L)(H_I/L)$.

Figure 4.8 represents the isolines of a constant $(h/L)(H_I/L)$. After the selection of a given wave steepness, $H_I/L = 0.020$, the reflected energy coefficient is found in interval $0.42 < K_R^2 < 0.90$ (see Figure 4.7-a.2). If a relative depth is also selected in the interval, for example, $h/L = 0.14$, $(x_m/L = 0.28)$, then $(h/L)(H_I/L) \approx 2.8 \cdot 10^{-3}$. In other words, the experimental values are in the transition zone. In this transition zone, the values of the reflected energy coefficient are in interval $0.58 < K_R^2 < 0.92$ for the slope angle 1:2 (Figure 4.7-a.2).

This behavior anticipates the experimental result, if the experiment maintains the wave steepness $(H_I/L = 0.020)$. In this case, the options are either to simultaneously increase or decrease the height and length (period) of the wave train. If both values increase, then $h/L < 0.14$ and $x_m/L < 0.28$ decrease, and $(h/L)(H_I/L) < 2.8 \cdot 10^{-3}$ too. Figure 4.7-a.2 shows that in this case, the reflection increases and the dissipation rate decreases, and that the breaker type evolves from a strong bore to strong plunging breaker. In contrast, if the wave steepness is kept constant by simultaneously decreasing H_I and L, then $h/L > 0.14$ and $x_m/L > 0.28$, $(h/L)(H_I/L) > 2.8 \cdot 10^{-3}$. According to Figure 4.7-a.2, wave reflection decreases, dissipation increases, and the breaker type evolves from a strong plunging breaker

to a strong bore and perhaps a weak bore. Consequently, small simultaneous variations of H_I and L, with no modification of wave steepness (i.e. Iribarren number) causes changes in the transformation mode of the incident energy related to different breaker types. Wave run-up and run-down as well as the velocity and acceleration of water particles on the slope also respond to these changes.

In addition, it is possible to analyze expected changes in the transformation mode and breaker type by simultaneously modifying h and L, while maintaining the relative depth h/L (Figure 4.8). In this case, if $h/L = 0.12$, and h and L (or T) are simultaneously increased or decreased (while the relative depth remains constant), H_I/L decreases (or increases) and x_m/L decreases. If a certain steepness value $H_I/L = 0.020$ is chosen, then $(h/L)(H_I/L) < 0.0024$ when h and L are increased, and $(h/L)(H_I/L) > 0.0024$ when h and L are decreased. The curve $(h/L)(H_I/L) > 2.8 \cdot 10^{-3}$ (Figure 4.8) shows that in the first case, there is an increase in h and L, wave steepness decreases, and the type of wave-breaking evolves from a weak bore to surging. If h and L decrease, the type of wave-breaking moves in the opposite direction, from a weak bore to a strong bore and strong plunging (see Figure 4.7-a.2).

To sum-up, in the regions in which either reflection or dissipation is completely dominant, the variability of the energy transformation mode and of the breaker type is delimited: (i) dissipative mode typical of spilling breakers and weak plunging breakers; (ii) reflective mode for surging "breakers". Then, the values of K_R^2 and D^* do not change significantly with $(h/L)(H_I/L)$, contrary to what happens in the transition zone. In the more reflection-dominated region inside the transition zone, the type of wave-breaking remains practically constant: weak and strong bore. However, in the more dissipation-dominated region inside the transition zone, if the slope and relative depth remain constant, the type of wave breaking also depends on wave steepness. In contrast, if h and L simultaneously increase, the breaker type evolves from a weak plunging to a strong plunging. if h and L simultaneously decrease, the breaker type evolves from a strong plunging to a weak plunging.

Experimental deviation for a permeable slope

A comparison of physical results to those of the impermeable breakwater with the same slope angle highlighted significant changes in the performance of the permeable breakwater (Figure 4.5). The reflected energy decreased throughout the experimental interval, in other words, in all the modes of incident energy transformation and wave-breaking. The domains shifted towards lower values of $(h/L)(H_I/L)$, and the variation curves of K_R^2, K_T^2 and D^* depended on both $(h/L)(H_I/L)$ and B^*/L (and $D_{50,p}/L$, D_a/L). Figure 4.9 shows the fit of a sigmoid curve to the experimental values of K_R^2 for the permeable slope angle 1:2 against $I_{r,I}$ and $(h/L)(H_I/L)$ (Figure 4.9-a), as well as the residual values that fit a Student-t model (Figure 4.9-b). The physical results scatter more with $I_{r,I}$ than $(h/L)(H_I/L)$, and the sigmoid function fit has a determination coefficient of $R^2 = 0.27$.

When the relative depth is incorporated on the x-axis (Figure 4.9-a.2), the alignment of the experimental data provides a reasonably good identification of the transition region $[5 \cdot 10^{-4} < (h/L)(HI/L) < 3 \cdot 10^{-3}]$, dissipation-dominated region $[(h/L)(HI/L) \geq 3 \cdot 10^{-3}]$, and the reflection-dominated region $[(h/L)(HI/L) \leq 4 \cdot 10^{-4}]$. Furthermore, it is visually evident, and confirmed by the residual distribution, that the deviation of the K_R^2 and D^* values is more pronounced in the transition region. The evolution of the modes of energy transformation and breaker type depends on the values of B^*/L (and $D_{50,p}/L$, D_a/L) with specific trajectories.

As in the case of the impermeable slope, it is possible to analyze the change in hydrodynamic performance by conducting an experiment in which wave steepness (or relative depth) remains constant while the incident wave height and wavelength are simultaneously increased

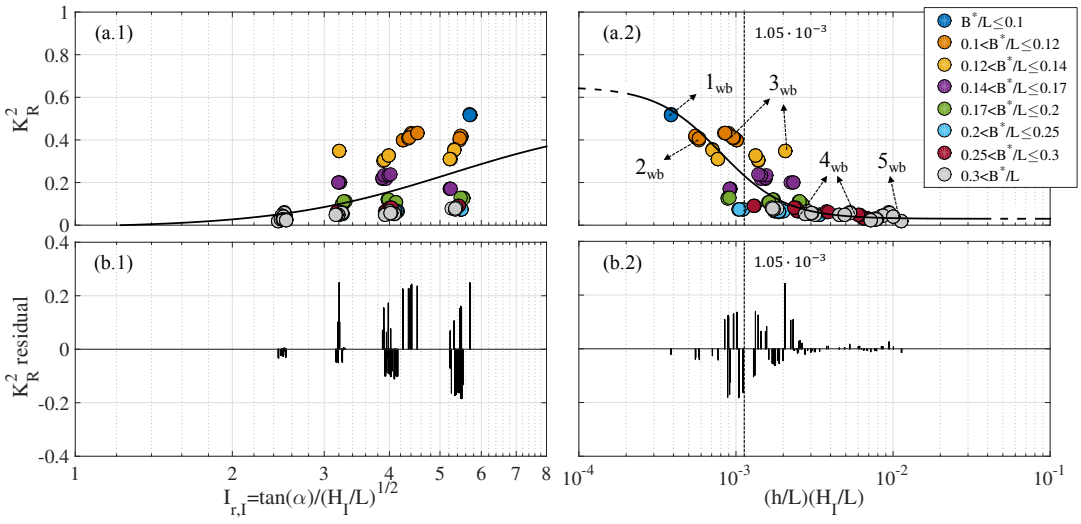

FIGURE 4.9: (a) Fit of the sigmoid curve to the experimental values of K_R^2 for the permeable 1:2 slope against the experimental Iribarren number ($I_{r,I}$) and the product of relative depth and steepness $(h/L)(H_I/L)$ according to intervals of B^*/L values. (b) Values of the residual deviation: experimental value minus the theoretical value calculated by the sigmoid curve. The number j_{wb} ($j = 1:5$) identifies the wave breaker types on the slope: 1_{wb} – surging, 2_{wb} – weak bore, 3_{wb} – strong bore, 4_{wb} – strong plunging, 5_{wb} – weak plunging.

or decreased. For example, by selecting a value of $(h/L)(H_I/L) \approx 1.05 \cdot 10^{-3}$, the energy transformation modes and breaker type vary, depending on B^*/L (and $D_{50,p}/L$, D_a/L). As shown in Figure 4.6, different trajectories of constant values are crosschecked, in this case, the value of B^*/L (or in the experiments of $D_{50,p}/L$). The reflection coefficient varies in interval $0.08 < K_R^2 < 0.42$ and the breaker type evolves from strong plunging to weak bore (Figure 4.9-a.2). This result reflects the correlation between values of K_R^2, K_T^2 and D^* and the characteristics of the breakwater core. It depends on the hydrodynamic regimes of the wave train effectively tested in the flume.

4.3 Experimental design in laboratory for mound breakwaters

4.3.1 Introduction

According to the Recommendations of Maritime Works (ROM 0.0-01, 2001; ROM 1.0-09, 2009; ROM 1.1-18, 2018), the design project of a breakwater must require that the failures modes, which can affect its security, functionality and operationality in its useful life, are bounded. To fulfill this requirement, the following steps must be addressed: (1) to pre-design a prototype based on a detail study of the site conditions, costs (MEIPOR-16, 2016) and maintenance; (2) to verify the design equations of the failures modes; and (3) to test the breakwater pre-design prototype in laboratory. Laboratory tests are one of the most important phases in the breakwater design and, therefore, require a proper modeling and programming.

Currently, for the relevance given to the Iribarren number, it is assumed I_r as a similarity parameter between model and prototype in experimental laboratory tests. For example, some research studies, such as, Burcharth and Andersen (2010), Gómez-Martín and Medina (2014), and Van Gent and Van der Werf (2014) tested wave conditions with constant values for the wave steepness (so same I_r). The main point of these laboratory tests was to keep the same breaker type in both model and prototype. However, the physical and numerical results presented in this research show that there is not a biunivocal relationship between I_r and the type of breaker.

On the other hand, the correct scale of the breakwater model is essential to properly quantify the behavior of the structure and to verify it. In addition to fulfilling the Froude scale, the hydrodynamic regime in the water column, inside the main layer and inside the core (scale effects) should be similar in both model and prototype. In this regard, there are many studies that have advanced in the model scale, with the importance of the drag forces and the calibration of a friction coefficient for each breakwater typology (Van Gent, 1995; Benedicto, 2004; Pérez-Romero et al., 2009; Vílchez et al., 2016b).

Since the Froude scale until now, significant progresses have been made in the this topic but there are still three questions to solve: (1) are the wave conditions forcing I_r a criterion enough to ensure similitude between model and prototype?, (2) is it possible to combine the wave conditions to be tested with the behavior of the wave-breakwater interaction?, and with it, (3) can a minimum and sufficient number of tests be programmed to quantify the hydraulic performance of the structure?. In this section, following the dimensional analysis and the results obtained in this study, we propose a experimental design in laboratory for mound breakwater in order to answer the questions posed.

4.3.2 Design criteria for laboratory tests

Within the framework of laboratory tests, limitations of the wave generation system and threshold design conditions should be established. For example, in the case of the physical experiments tested in this work, the design criteria were:

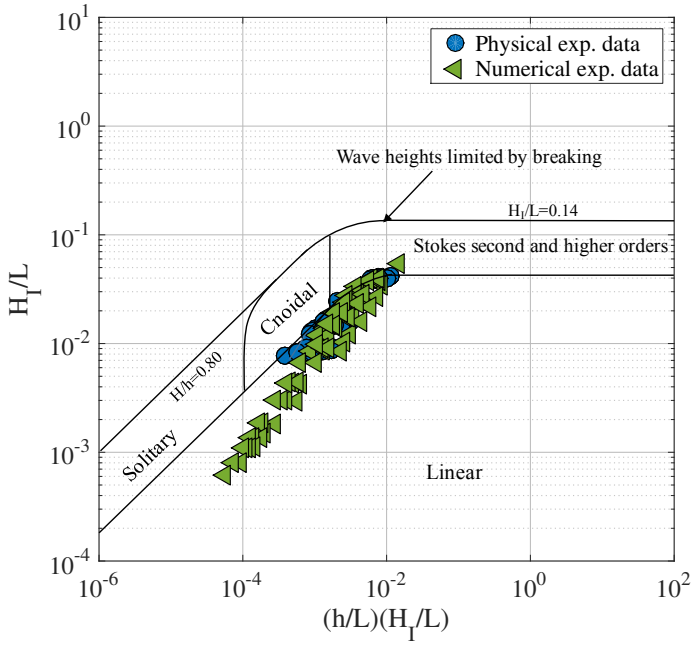

FIGURE 4.10: Wave generation characteristics: wave steepness (H_I/L) against $(h/L)(H_I/L)$.

- Non-overtopping and non-damage conditions: $F_{MT,total} = 0.55 + 2D_a$, $D_a = 40.9$ mm $\rightarrow H_{target} < 0.14$ m,
- Water wave: short periods $T_{target} \leq 4$ s,
- Minimum conditions of paddle generation: $H_{target} > 0.02$ m and $T_{target} > 1$ s,
- Linear theory: $[H_{target}, T_{target}]$ in Stokes I regime (see Figure 3.4),

- Wave-breaking is caused by wave-breakwater interaction: $\frac{H_{target}}{L_{target}} \leq 0.14\tanh(kh)$
- Hydrodynamic flow regimes should be totally turbulent:
  - In the water column and inside the main armor layer: $R_{e,w}$, $R_{e,D_a} > 10^4$,
  - Inside the porous media, $D_{50,p} = 12$ mm: $R_{e,p} > 300$ (see Figure 3.5)

Following the dimensional analysis, we got that the incident wave train is characterized by the water depth, h/L, and the wave steepness, H_I/L. Based on that, we modified the x-axis of Figure 3.4 that covers the wave generation theories adapted from Dalrymple et al. (1991). Figure 4.10 represents the physical and numerical data of the wave steepness against the product $(h/L)(H_I/L)$. As can be observed, the waves generated in the experimental tests are mainly in the Stokes I regime and do not break by bottom friction (two design criteria).

4.3.3 The log-transformation of the experimental space

The response of the dependent dimensionless quantities, $[K_R^2, \frac{X_{0,R}}{L}, K_T^2, \frac{X_{0,T}}{L}]$ are functions of the set of independent dimensionless quantities (dimensional analysis). In the case of the impermeable slope, $\Psi : \mathbb{R}^2 \rightarrow \mathbb{R}^3$ whereas for the sloping breakwater with a porous core and a main armor layer, $\Psi : \mathbb{R}^2 \rightarrow \mathbb{R}^5$ (where $\mathbb{R}^n$ is the real space of n dimensionless quantities). In all cases, wave generation were chosen based on two dimensionless quantities that characterize the incident wave train at the toe of the slope breakwater: the wave steepness, (H_I/L), and relative depth, (h/L).

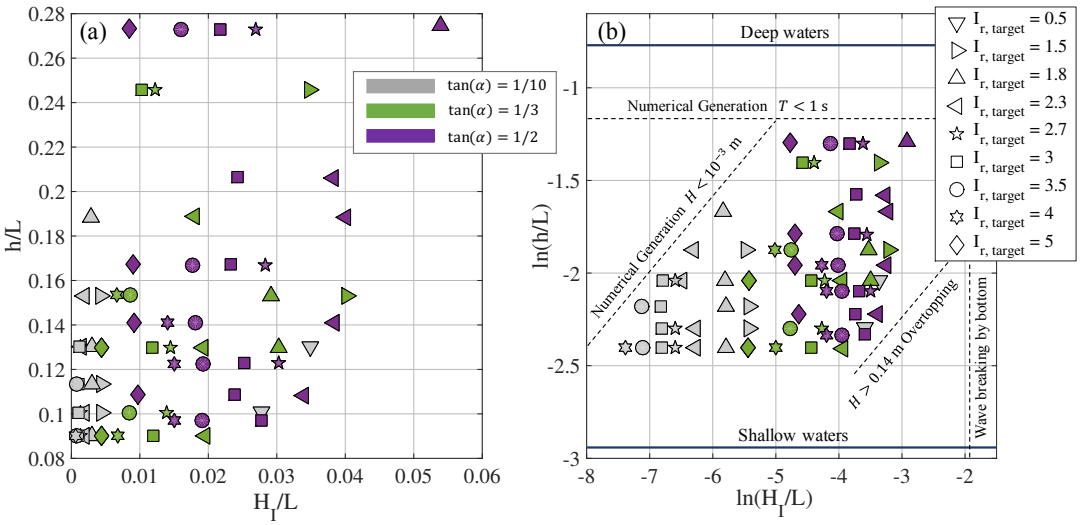

FIGURE 4.11: Experimental value of the impermeable slope for each $I_{rtarget}$ (symbols) and three slope angles (colors) numerically simulated in: (a) space $[h/L, H_I/L]$; (b) log-transformation space $[\ln(h/L), \ln(H_I/L)]$. Figure 4.11-b shows the experimental limits for wave generation in the numerical model, wave-breaking due to the water depth, and the condition of non-overtoppable breakwater.

Figure 4.11 represents the pairs of experimental values of the impermeable breakwater in space $[h/L, H_I/L]$ (Figure 4.11-a), and in the space $[\ln(h/L), \ln(H_I/L)]$ (Figure 4.11-b), after log-transformation. The corresponding values of the permeable porous breakwater are shown in Figure 4.12-a. Figure 4.12-b identifies the two dimensionless quantities for the porous medium, $[\ln(B^*/L), \ln(D_{50,p}/L)]$, and the "four-dimension" quantity is the double layer of cube armor diameter. The x-axis logarithmic transformation facilities the cluster and

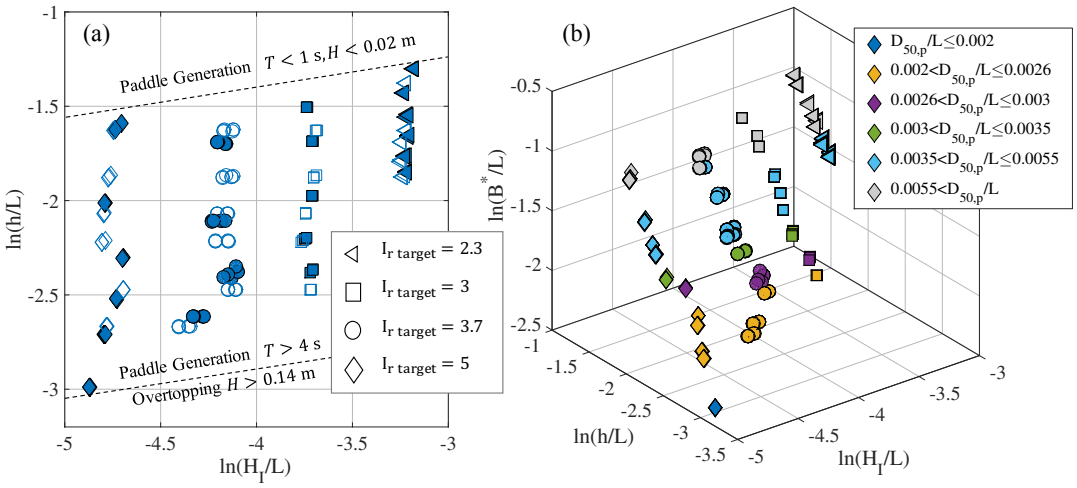

FIGURE 4.12: Experimental values of the permeable slope with a main layer and porous core: (a) space $[h/L, H_I/L]$ for each $I_{rtarget}$ tested; (b) log-transformation space $[\ln(h/L), \ln(H_I/L), \ln(B^*/L)]$, which uses different colors to show the value ranges of the monomial $D_{50,p}/L$. Figure 4.12-a represents the experimental limits for wave generation in laboratory and the condition of non-overtoppable breakwater.

visualization of the data, especially with several slope angles (compare Figure 4.11-a and 4.11-b).

After the log-transformation, the dimensionless quantities $[h/L, H_I/L]$ may become more independent (fewer interactions) and facilitate: (1) the selection of highly representative experimental results, (2) the optimization of the number of experiments and (3) the minimum number of repetitions in order to satisfactorily combine multivariate dimensional analysis with statistical analysis (Albrecht et al., 2013). In other words, from the log-transformation experimental space $[\ln(h/L), \ln(H_I/L)]$, the necessary and sufficient wave conditions $[H_{target}, T_{target}]$ could be determined to quantify the wave energy transformation on mound breakwaters.

Figure 4.13-a represents the space $[\ln(h/L), \ln(H_I/L), \ln(B^*/L)$ (or $D_{50,p}/L)]$ of the experimental values obtained in the laboratory. Figure 4.13-b represents the space $[\ln(h/L), \ln(H_I/L)]$ of the experimental values with slope angle 1:2 obtained in the numerical model. The tendency (solid blue arrows) and the wave-breaking bands are identifies, as well the isolines of the constant product $(h/L)(H_I/L)$. It is observed that there is not a biunivocal relationship between I_r and the type of breaker. In both figures the following regions are also perfectly identified: (1) reflection-dominated region; (2) dissipation-dominated region; and (3) transition region, located between regions (1) and (2). Figure 4.13 facilitates the creation of a suitable experimental design in the laboratory, since it includes the information needed to fulfill the prototype-model equivalent hypothesis of Lorentz $(B^*/L, D_{50,p}/L)$. Additionally, Figure 4.13 programs runs of H and T that delimit the three intervals of the energy transformation modes for any mound breakwater typology and the breaker types. Chapter 5 includes the application of the experimental design proposed in this section.

In a real breakwater located in intermediate/shallow waters (e.g., h = 10 m, T = 10 s, H = 5 m, 5 m < B^* < 10 m and 0.10 m < $D_{50,p}$ < 0.25 m, $R_{e,p} > 10^5$, fully turbulent regime), it is improbable that all of the regime changes observed in the laboratory will occur. For the values of $[K_R^2, K_T^2, D^*]$ obtained in a model to be representative of the prototype values, besides complying with the Froude scale, the dissipation-reflection-transmission processes of the wave train in the core should be similar to those of the prototype. One way to verify this condition is to select the two dimensionless quantities, B^*/L, $D_{50,p}/L$ in order to satisfy

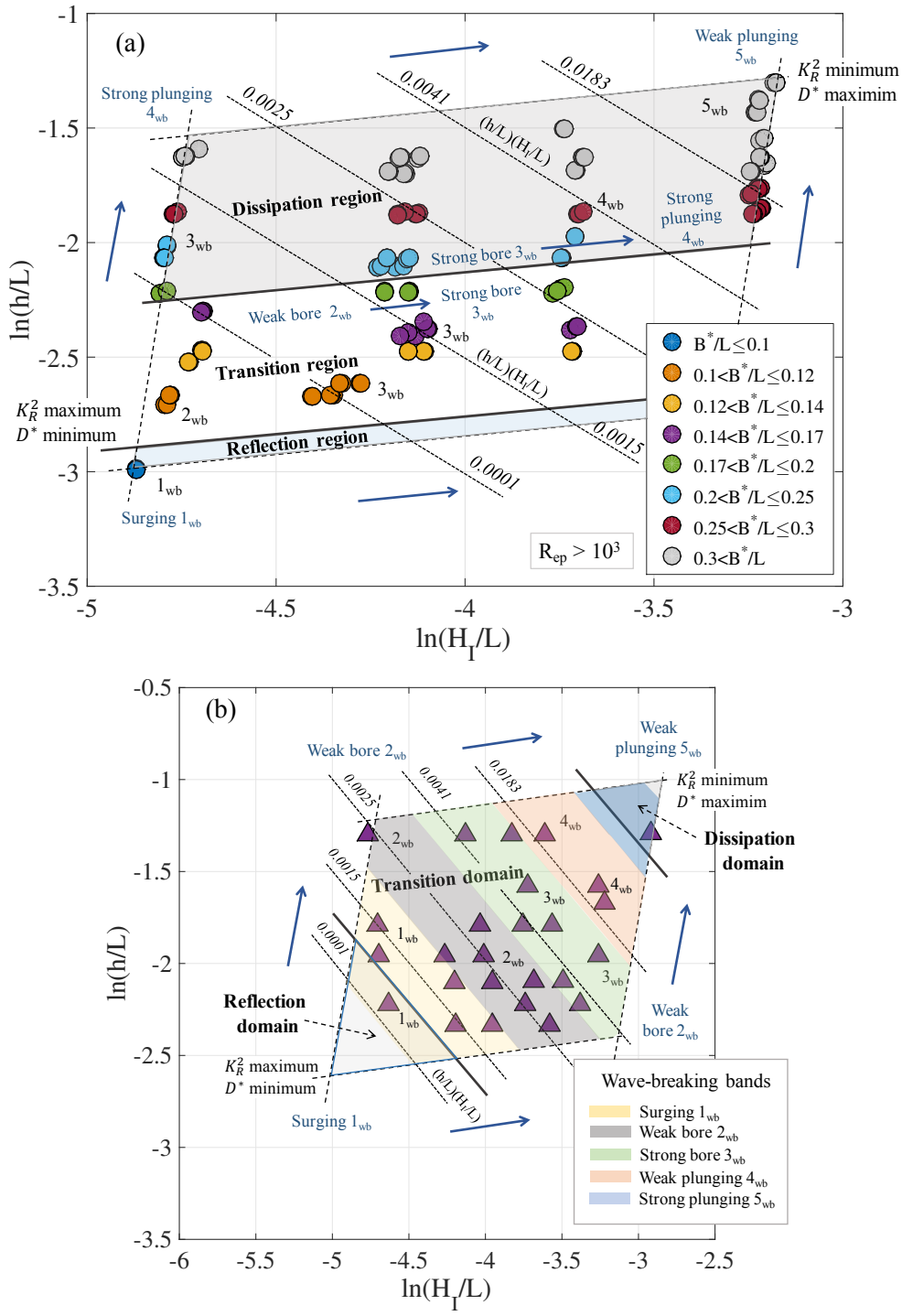

FIGURE 4.13: Experimental space $[\ln(h/L), \ln(H_I/L)]$ of: (a) the laboratory tests with a slope angle 1:2, according to ranges of values of the monomial B^*/L (colors); (b) the numerical tests with a slope angle 1:2 and wave-breaking bands represented by colors. In both figures the tendency of the wave-breaking is marked with solid blue arrows and the following regions were also identified: (1) reflection-dominated region; (2) dissipation-dominated region; and (3) transition region, located between regions (1) and (2).

the model-prototype equivalent hypothesis Lorentz (Pérez-Romero et al., 2009; Vílchez et al., 2016b) in each run of H and T. From an engineering point of view, it is advisable to run the test considering both experimental deviation: the experimental scattering from the methods and the hydrodynamic intrinsic scattering, and work accordingly. In another case, before applying the experimental results, or the formulas derived from them, it is advisable to quantify the expected experimental deviations.

4.4 Conclusions

The objectives of Chapters 3 and 4 were (1) to collate the dependence of wave energy transformation processes (reflection, transmission, and bulk dissipation rate) with Iribarren number; (2) to apply dimensional analysis to the design of experiments for both a permeable and impermeable slope; and (3) to analyze the variability of the results and identify those characterized by the hydrodynamic performance of the breakwater. An undefined, impermeable, rigid slope was the object of numerical tests with the IH-2VOF model. The physical tests was performed in a 2D wave flume of a non-overtoppable mound breakwater with a cube armor layer and a porous core of finite width. The depth of the wave generation zone up to the toe of the slope was constant, and the bottom was horizontal. Only monochromatic linear wave trains were considered, and the energy transformation processes occurred as the wave propagated onto the breakwater. The following conclusions can be derived from this study:

1. In the case of an impermeable slope, the application of dimensional analysis results in the independent variables, h/L and H_I/L, and dependent variables namely, wave height and phase of the reflected wave train. The reflected energy coefficient, K_R^2, is obtained as a derived quantity of the first kind, and the bulk dissipation as a derived quantity of second kind, thus resolving the energy conservation equation and using the same dimensional base. The slope angle is a parameter of the problem since it cannot be expressed in terms of the dimensional base.

2. The reflected energy coefficient, K_R^2, can be expressed by a sigmoid function whose variable shows values of $(h/L)(H_I/L)$ that identify three regions: (i) a reflection-dominated region; (ii) a dissipation-dominated region; (iii) a transition region between the two, in which reflection and dissipation processes compete with each other.

3. When the independent variable of the sigmoid curve is the Iribarren number, the dissipation-dominated region is clearly evident and can be delimited, unlike the other two regions. The representation of the residual values (Figures 4.7-b and 4.9-b) shows how the deviation with I_r in all regions is significantly greater than in the case of $(h/L)(H_I/L)$.

4. To analyze the possible breaker types in each region, the traditional list was expanded to subdivide the breakers into weak and strong types of plunging breaker and bore (or collapsing). Then the breaker sequence is the following: surging, weak bore, strong bore, strong plunging, weak plunging, and spilling (see also Appendix B).

5. When a value of $(h/L)(H_I/L)$ is selected in the first region, reflection-dominated region, the breaker type can move in both directions between weak bore and surging. If the value is in the second region, dissipation-dominated region, the move is between weak plunging and spilling. If the value is in the transition region, the move is between strong plunging, strong bore and weak bore. This variability in the energy transformation mode and breaker type can occur with a constant wave steepness value, in other words, when the Iribarren number remains constant. There is not a biunivocal relationship

between I_r and the type of breaker, except in the dissipation-dominated region (weak plunging and spilling breakers).

6. In the case of a permeable slope with a main armor layer and a porous core, in addition to $(h/L)(H_I/L)$, the experimental design includes $D_{50,p}/L$, B^*/L, D_a/L, $n_l D_a/L$ for each slope angle. When these results are compared with those for an impermeable slope with the same angle, significant changes are identified. The regions are located in smaller intervals of $(h/L)(H_I/L)$ values, and in each region, the value of the reflected energy coefficient, K_R^2, is lower.

7. The sigmoid functions, above all in the transition region, have different trajectories, depending on the relative width B^*/L and stone diameter $D_{50,p}/L$. When a value of $(h/L)(H_I/L)$ is selected in the transition region, K_R^2 increases since the value of B^*/L decreases (when $D_{50,p}$ is constant, there was a simultaneous decreases in $D_{50,p}/L$) and there is a variation in the corresponding breaker type: weak bore, strong bore and strong plunging.

8. When the independent variable of the sigmoid is the Iribarren number, the dissipation-dominated region is recognizable and can be delimited. However, this is not true for the other two when the experimental scattering significantly increased. The application of the modified Iribarren number (Clavero et al., 2018) significantly corrects this behavior though it is still not possible to differentiate the breaker types.

9. In a laboratory experiment, there is frequently a spatial variation of hydrodynamic performance inside the core. This spatial performance has important consequences for the rate of energy dissipation, energy reflection, and transmitted energy. It mainly depends on B^*/L (and $D_{50,p}/L$) with specific trajectories and evolution of the breaker type, depending on the value of $(h/L)(H_I/L)$.

10. It is unusual for this spatial variability to occur in a real breakwater. For the values of $[K_R^2, K_T^2, D^*]$ obtained in a model to be representative of the prototype values, in addition to fulfilling the Froude scale, the dissipation-reflection-transmission process of the wave train in the core should be similar to those of the prototype. Accordingly, Figure 4.13 helps to elaborate a suitable experimental design and applicable to other tests. Indeed, its application makes the outcome of the experiments predictable.

11. The experimental design significantly also improves when the experimental space was defined by taking logarithms of h/L and H_I/L. In this transformed design space, it is possible to identify the wave generation requirements and the relevant points where there was a change of behavior in the wave train. The number of tests is optimized such that the repetition facilitates the statistical analysis of the results.

Chapter 5

Experimental design and performance of a conventional mound breakwater

Comment

This chapter presents the main results integrated in the following work:

Díaz-Carrasco, P., Moragues, M.V., Clavero, M., Ortega-Sánchez, M. and Losada M.A. (Under preparation). "Hydraulic performance of a conventional mound breakwater: experimental design". In: *Coastal engineering*.

This chapter studies the wave energy transformation on a conventional rubble mound breakwater, which is permeable and is composed by a homogeneous core. For that, Section 5.2 outlines the application of the proposed log-transformation experimental space to the laboratory tests of the homogeneous mound breakwater. Section 5.3 presents the results of energy transformation modes obtained from the log-experimental space, as well as the influence of the geometrical variables in the hydraulic performance. Finally, Section 5.4 gathers the discussion and design recommendation for practical engineering purposes.

5.1 Introduction

In the field of harbor and maritime structures, the rubble mound breakwater is the most frequent typology in the world due to its ability to dissipate the wave energy, its relatively simple design method and the possibility to be constructed using different types and sizes of armor pieces; also, the have a relatively low environmental impact. The most conventional mound breakwater section is the homogeneous and permeable, whose performance against the incident wave train is mainly determined by the slope, α, and the dimension and size of the core materials, B^* and $D_{50,p}$ (Section 3.2.2). The presence of a porous core is relevant to the hydrodynamic performance of the breakwater because of its influence on the phase lag between the incident and reflected wave trains and its impact on breaker type.

Nowadays, design formulas for rubble mound breakwaters, which are generally applied to calculate the transformation of incident energy, run-up and run-down on the slope, and when applicable, the overtopping volume and the stability of the breakwater units, are based on experimental data, whose scattering is maximum in the interval of I_r corresponding to the critical design conditions. To address this point, in Chapters 3 and 4, we developed a dimensional analysis of the physical processes that determine the wave energy transformation and breaker types according to the mound breakwater slope types. In particular, numerical

and physical results were presented for the impermeable and the permeable slopes with main armor layer, respectively. The main conclusions from these previous chapters were: (1) to properly quantify the wave energy transformation by similar curves, whose variable shows values of $(h/L)(H_I/L)$ that identify three regions: (i) a reflection-dominated region, (ii) a dissipation-dominated region, and (iii) a transition region; and (2) to elaborate an experimental design methodology based on the log-transformation space of h/L and H_I/L, which optimizes the number of test in laboratory to determine the transformation modes and breaker types. This previous work involves an advance in the theoretical analysis of the hydraulic performance of mound breakwaters and also proposes improvements to perform laboratory tests.

Furthermore, the experimental results for the permeable slope with main armor showed a spatial deviation of the hydraulic performance, which depends on B^*/L and $D_{50,p}/L$, with specific trajectories and evolution of the breaker type, depending on the value of $(h/L)(H_I/L)$. The source of this scatter was identified, but it was only tested with a physical model with a constant characteristic width, B^*, and constant granular core diameter, $D_{50,p}$. Moreover, part of this experimental deviation can be due to the interaction (circulation and friction) between the incident wain train and the main armor layer (Losada et al., 2019).

Consequently, the main objective of this chapter is to study the hydraulic performance of a conventional homogeneous and permeable mound breakwater by (1) applying the proposed experimental test design methodology, and (2) studying the influence of the physical processes involved in the dimensional analysis. Hence, we carried out experimental tests for a non-overtoppable, homogeneous and permeable mound breakwater in the 2D wave flume of IISTA. Two characteristic widths and two slopes were tested with regular and irregular waves. The experimental results were also compared with other laboratory tests with different breakwater geometry and water depth. Linear wave theory was applied to separate the incident, reflected, and transmitted time series of the data records at different points in the experimental setup. The wave energy conservation equation was applied to obtain the bulk dissipation rate on the breakwater.

5.2 Application of the experimental design: methodology

Section 5.2 gathers the application of the experimental design in laboratory for mound breakwaters proposed in Section 4.3. For that, a conventional rubble mound breakwater was tested with different configurations following the physical processes involved in the dimensional analysis of Section 3.2.2.

5.2.1 Physical mound breakwater models

The experimental tests were performed in the wave-current flume of the Andalusian Inter-University Institute for Earth System Research (IISTA) at the University of Granada. Figure 5.1 shows a diagram of the physical model tested, namely, a homogeneous permeable mound breakwater with a granular diameter, $D_{50,p} = 26$ mm. Two different widths of the top ($B_b = 0.1$, 0.24 m) and two seaward slope angles ($\tan(\alpha) = 1/1.5$, 1/2) were tested. The water depth in the wave generation zone and in the flume was kept constant and equal to $h = 0.4$ m.

Table 5.1 shows the geometrical configuration for each physical model tested, whose geometrical parameters are defined in Chapter 3. Three homogeneous permeable mound breakwaters were studied, identified hereinafter as: HP-MB 1, for $B_b = 0.24$ m and $\tan(\alpha) = 1/2$; HP-MB 2, for $B_b = 0.24$ m and $\tan(\alpha) = 1/1.5$; and HP-MB 3, for $B_b = 0.10$ m and $\tan(\alpha) = 1/2$.

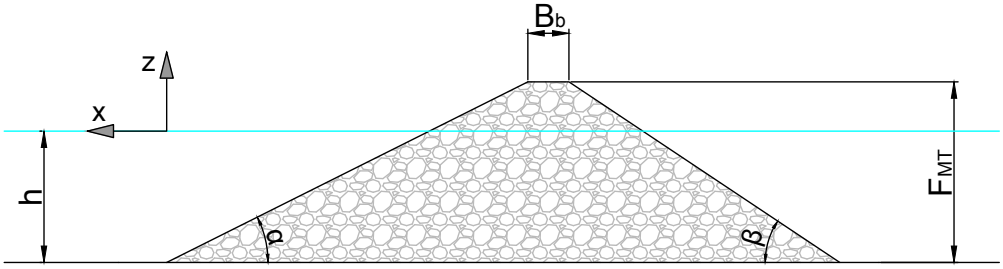

FIGURE 5.1: Physical model of the homogeneous permeable mound breakwater (HP-MB).

Configuration	B_b (m)	cot(α)	cot(β)	F_{MT} (m)	B^* (m)	$D_{50,p}$ (mm)	A_{eq} (m^2)	ρ_s (t/m^3)	n_p
HP-MB 1	0.24	2	1.5	0.55	0.79	26	0.586	2.84	0.462
HP-MB 2	0.24	1.5	1.5	0.55	0.65	26	0.516	2.84	0.462
HP-MB 3	0.10	2	1.5	0.55	0.65	26	0.530	2.84	0.462

TABLE 5.1: Geometric parameters of the physical model: homogeneous permeable mound breakwater (HP-MB).

5.2.2 Experimental spaces: wave conditions

Wave conditions for the homogeneous permeable mound breakwater tests were chosen according to: (1) the design criteria for laboratory tests (Section 4.3.2), and (2) the log-transformation of the experimental space (Section 4.3.3). The design methodology is explained by separating the wave conditions for each slope angle tested.

In common, tests for all physical models were performed in the wave flume with a VTI and the AwaSys software package was used to generate waves with the simultaneously active absorption of reflected waves. Regular waves were simulated for all the physical models and irregular waves were only simulated for the HP-MB 1 model. Each test of regular waves was repeated three times with 100 number of waves. For irregular waves, each test was repeated two times and 1000 waves were programed. Wave-breaking was only caused by wave-breakwater interaction and the experiments were also under non-overtopping and non-damage conditions.

Wave conditions for the physical models with slope angle 1:2

Regular waves were simulated and defined by a wave height, H_{target}, and wave period T_{target}. Figure 5.2 shows the experimental space for the physical models with slope angle 1:2. It was designed based on Figure 4.13-a, which represents the log-experimental space of the permeable mound breakwater with main armor layer. Hence, on Figure 4.13-a, the experimental space was drawn and it includes the following:

- To ensure the design criteria of wave generation in Stokes I regime, the space [ln(h/L), ln(H/L)] was reduced (black solid lines) with respect to the space of the permeable mound breakwater with main armor layer (blue dash lines):
  - Side A-B represents the limit between cnoidal and Stokes I regimes.
  - Side B-C represents the limit between Stokes II and Stokes I regimes.
- Wave conditions of point A and C to provide the values of $K_R^2 < 0.1$ and $K_R^2 > 0.5$ of the experimental space; namely the dissipation-dominated region and reflection-dominated region, respectively.

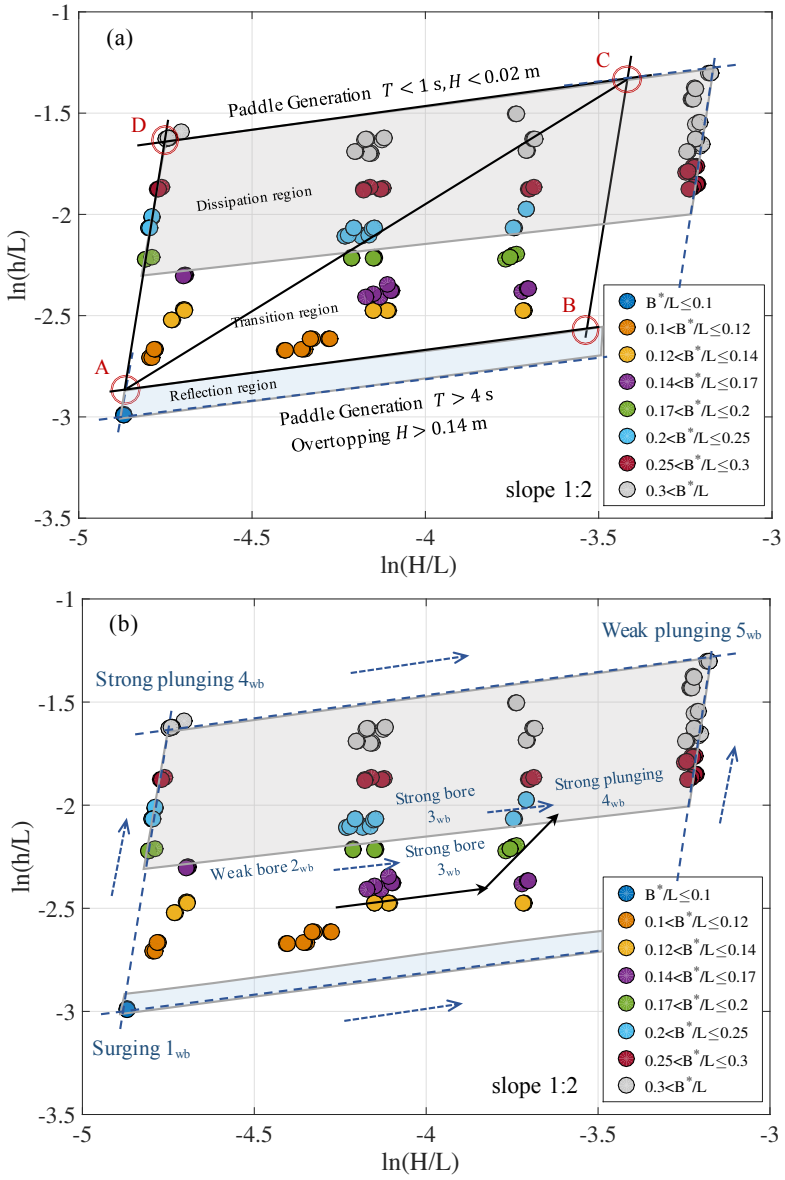

FIGURE 5.2: Experimental space $[\ln(h/L), \ln(H/L)]$ for the homogeneous permeable mound breakwaters with $B_b = [0.1, 0.24]$ m and $\tan(\alpha) = 1/2$ (HP-MB 1 and 3). (a) Black solid lines, regular wave conditions chosen to cover: reflection, dissipation and transition regions; (b) black solid arrows, regular wave conditions chosen for the transition region with breaker types: strong plunging, strong bore and weak bore. Note that, colors of B^*/L range values and the breaker types are from the experimental results of the permeable mound breakwater with main armor.

- Wave conditions of point B to limit the wave height for non-overtopping conditions ($H_{target} < 0.14$ m) and Stokes I regime. This maximum wave height also ensures the non-damage conditions.
- Wave conditions of point D to mark the technical limitations of paddle generation: $H_{target} > 0.02$ m.
- Wave conditions of side A-C to quantify the behavior outside the limits of the design criteria (Section 4.3.2).

- Wave conditions in the transition region to cover the breaker types, strong plunging, strong bore and weak bore, where the experimental deviation is higher (see results of Chapter 4).

- For the HP-MB 1 model, additional wave conditions were tested to the left of side A-D to properly quantify the wave energy transformation: $T_{target} = [1.65 - 3.6]$ s and $H_{target} = [0.02 - 0.0425]$ m.

Table 5.2 gathers the regular wave conditions programed for the physical models with slope angle 1:2. The pattern to increase or decrease T_{target} and H_{target} and the tendency of the breaker types are indicated to follow each side of the experimental space (black lines). The number of tests was (3 x 38) for HP-MB 1 model and (3 x 19) for HP-MB 3 model.

Side	Wave conditions	$[(h/L)(H/L)]_{target}$	Pattern	Breaker types
A→B	T_{target} = 3.0 s - H_{target} = 0.0458 m T_{target} = 2.5 s - H_{target} = 0.121 m	[0.0003 - 0.0022]	T decreases H increases	Surging → Strong bore
B→C	T_{target} = 2.5 s - H_{target} = 0.121 m T_{target} = 1.02 s - H_{target} = 0.0313 m	[0.0022 - 0.0055]	T decreases H decreases	Strong bore → Weak plunging
C→D	T_{target} = 1.02 s - H_{target} = 0.0313 m T_{target} = 1.25 s - H_{target} = 0.0205 m	[0.0019 - 0.0055]	T increases H decreases	Weak plunging → Strong plunging
D→A	T_{target} = 1.25 s - H_{target} = 0.0205 m T_{target} = 3.0 s - H_{target} = 0.0458 m	[0.0003 - 0.0019]	T increases H increases	Strong plunging → Surging
A→C diagonal	T_{target} = 3.0 s - H_{target} = 0.0450 m T_{target} = 1.02 s - H_{target} = 0.0313 m	[0.0003 - 0.0055]	T decreases H decreases	Surging → Weak plunging
Transition region	T_{target} = 1.75 s - H_{target} = 0.10 m T_{target} = 2.5 s - H_{target} = 0.08 m	[0.0014 - 0.004]	T increases H decreases	Weak bore → Strong plunging

TABLE 5.2: Regular wave conditions tested for the homogeneous permeable mound breakwater with $B_b = [0.1, 0.24]$ m and $\tan(\alpha) = 1/2$ (HP-MB 1 and 3). The target values were obtained from the experimental space $[\ln(h/L), \ln(H/L)]$ of Figure 5.2. Additional wave conditions for the HP-MB 1 model were tested to the left of side A-D: $T_{target} = [1.65 - 3.6]$ s, $H_{target} = [0.02 - 0.0425]$ m.

Irregular waves were also programed for HP-MB 1 model with the wave absorption system AwaSys software activated. They impinged perpendicularly onto the breakwater and were generated imposing a Jonswap type spectrum with a peak enhancement factor $\gamma_p = 3.3$. Each tests was repeated two times with 1000 waves. The target parameters used for irregular waves are defined by the peak period, $T_p = T_{target}$, and the spectral incident wave height, $H_{m0} = H_{target}$, where T_{target} and H_{target} are the regular wave conditions gathered in Table 5.2.

Once the wave conditions were selected, the next step was to verify that these conditions, together with the model geometry, fulfilled the totally turbulent flow regimes inside the porous medium and in the water column; and indeed: $R_{e,p\,target} > 300$ and $R_{e,w\,target} > 10^4$ for all runs $[T_{target}, H_{target}]$ selected. Note that, the relative characteristic width takes values between $B^*/L = [0.11 - 0.54]$ for $B_b = 0.24$ m, and $B^*/L = [0.10 - 0.45]$ for $B_b = 0.10$ m.

Wave conditions for the physical model with slope angle 1:1.5

As we mentioned in the dimensional analysis of Section 3.2.2, in this work the slope angle has been used as an "identificative parameter" of the results. The latter means that the experimental results (see Chapter 4) are ordered depending on the slope angle but the shape of the sigmoid function is similar for all the slope angles tested. Following this assumption, the experimental space $[\ln(h/L), \ln(H/L)]$ should be representative of the slope 1:1.5 and different to the space of 1:2. The process that was followed to select the wave conditions of this physical model are shown in Figure 5.3.

Therefore, regular wave conditions for the slope 1:1.5 were programed keeping constant the wave period of the slope 1:2 and varying H_{target} to remain constant the Iribarren number; that is,

$$\left[\frac{h}{L_{target}}\right]_{1:1.5} = \left[\frac{h}{L_{target}}\right]_{1:2}$$

$$\frac{H_{target,1:1.5}}{L_{target}} = \frac{H_{target,1:2}}{L_{target}}\left(\frac{1/1.5}{1/2}\right)^2$$

Figure 5.4 shows the experimental space for the HP-MB 2 model and Table 5.3 gathers the runs $[T_{target}, H_{target}]$ selected from this experimental space. To fulfill non-overtopping and non-damage conditions, as well as Stoke I regime, some tests were replaced and completed by runs with the same experimental space $[\ln(h/L), \ln(H/L)]$ of the slope 1:2 (black dash lines). Wave conditions for the transition region was also different to cover the breaker types: strong plunging, strong bore and weak bore.

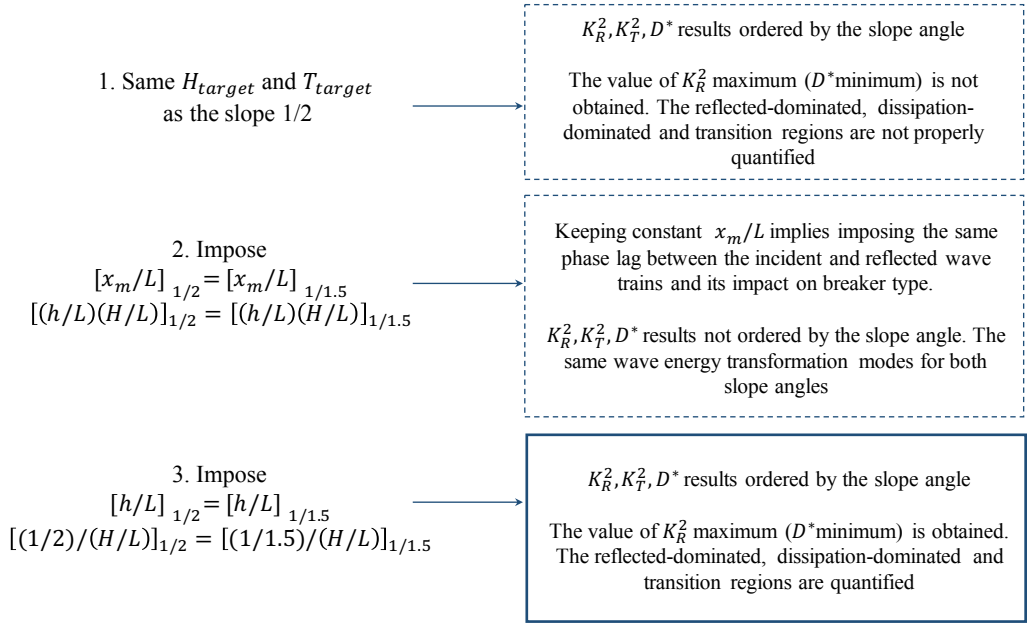

FIGURE 5.3: Decision scheme to select the wave condition for the physical model with slope angle 1:1.5.

Side	Wave conditions	$[(h/L)(H/L)]_{target}$	Pattern	Breaker types
A→B**	T_{target} = 3 s - H_{target} = 0.081 m T_{target} = 2.5 s - H_{target} = 0.121 m	[0.00066 - 0.0022]	T decreases H increases	Weak bore → Strong bore
B**→C	T_{target} = 2.5 s - H_{target} = 0.121 m T_{target} = 1.02 s - H_{target} = 0.0556 m	[0.0022 - 0.0097]	T decreases H decreases	Strong bore → Weak plunging
C→D	T_{target} = 1.02 s - H_{target} = 0.0556 m T_{target} = 1.25 s - H_{target} = 0.0364 m	[0.0034 - 0.0097]	T increases H decreases	Weak plunging → Strong plunging
D→A	T_{target} = 1.25 s - H_{target} = 0.0364 m T_{target} = 3 s - H_{target} = 0.081 m	[0.00066 - 0.0034]	T increases H increases	Strong plunging → Strong bore
Transition region	T_{target} = 2.14 s - H_{target} = 0.12 m T_{target} = 2.5 s - H_{target} = 0.08 m	[0.0014 - 0.003]	T increases H decreases	Strong bore → Strong plunging

TABLE 5.3: Regular wave conditions tested for the homogeneous permeable mound breakwater with $B_b = 0.24$ m and $\tan(\alpha) = 1/1.5$ (HP-MB 2). (**) wave conditions imposing the same experimental space $[\ln(h/L), \ln(H/L)]$ of the slope angle 1:2.

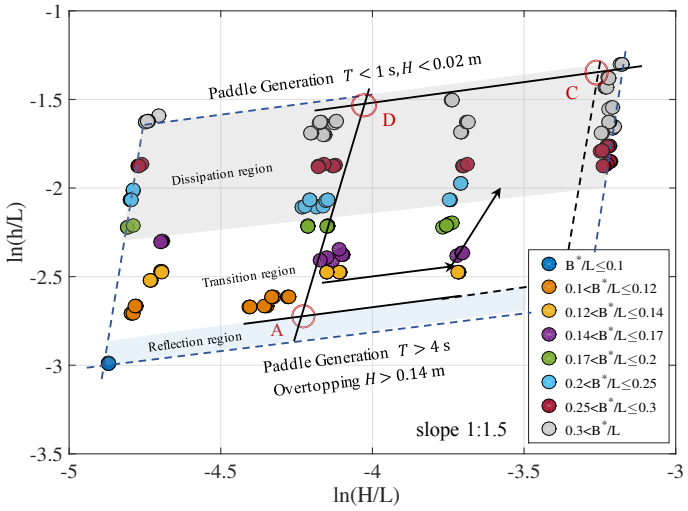

FIGURE 5.4: Experimental space $[\ln(h/L), \ln(H/L)]$ for the homogeneous permeable mound breakwaters with $B_b = 0.24$ m and $\tan(\alpha) = 1/1.5$ (HP-MB 2). Black solid lines. wave conditions chosen to cover: reflection, dissipation and transition regions. Black solid arrows: wave conditions chosen for the transition region with breaker types: strong plunging, strong bore and weak bore. Black dash lines: wave conditions with the same $[\ln(h/L), \ln(H/L)]$ of the slope angle 1:2.

5.2.3 Analysis of the experimental data

Five resistance wave gauges (G1 to G5) were located along the wave flume in the same position as the physical ones for the breakwater with main armor layer (Figure 3.3 Chapter 3). The data acquisition and analysis of the free surface elevations measured by wave gauges was the same as we explained in Section 3.3.3. Hence, the incident and reflected wave train were separated by Baquerizo (1995)'s method, and the reflection and transmission coefficients (K_R^2, ϕ_R, K_T^2) were obtained by applying the power spectral analysis. The wave energy dissipation rate (D^*) was calculated by Equation 3.1 (Chapter 3).

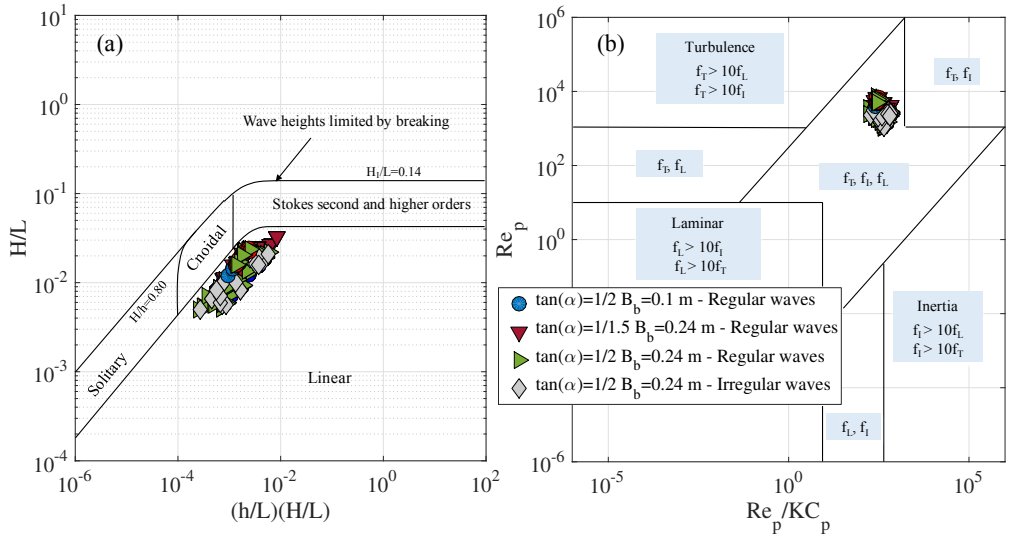

FIGURE 5.5: (a) Wave generation: wave steepness (H/L) against the variable that characterize the wave incident train,$(h/L)(H/L)$. (b) Importance of drag forces in the porous medium (adapted from Gu and Wang, 1991). Note that, the wave parameter, H and L are: H_I and L for the regular waves, and H_{m0} and L_p for irregular waves.

The statistical parameters were obtained from the temporal and spectral analysis of the time series. For regular waves, as the physical tests of the permeable breakwater with main armor, the incident wave train was characterized by the incident wave height, H_I, and the mean wave period T_z (or wave length, L), which comply: $H_I \cong H_{mean,I} \cong H_{phase-averaged,I} \cong H_{s,I} \cong H_{rms,I}$, and the same for the wave period (see Appendix C). For irregular waves, the spectral parameters used to characterize the incident wave train were: spectral incident wave height, H_{m0}, and peak wave period, T_p (or peak wave length, L_p) since it is the parameter associated with the maximum energy of the Jonswap spectrum. Appendix C shows the comparison between the spectral and temporal statistical analysis.

Figure 5.5 shows the characteristic of the wave generation and hydraulic regime for the data. As can be observed, the experimental data obtained in laboratory are well generated, since they fulfill: (i) wave generation in Stokes I regime, and (ii) totally turbulent flow regimes inside the porous medium.

5.3 Results

This section presents the results of the wave energy transformation processes and the log-experimental spaces for the three configurations of the homogeneous permeable mound breakwater. First, we present the wave energy transformation results of the HP-MB 1 physical model obtained following the proposed experimental design in laboratory. Then, Section 5.3.2 analyzes the influence of the geometrical parameters, B^*, $D_{50,p}$ and α, in the hydraulic performance. The influence of the core granular diameter, $D_{50,p}$, is analyzed by comparing our experimental data with other laboratory tests.

5.3.1 Experimental design and hydraulic performance

Following the proposed experimental test design for mound breakwater, the results of the physical model with $B_b = 0.24$ m and $\tan(\alpha) = 1/2$, which has more runs of regular and irregular wave conditions, is presented in this section. Figure 5.6-a shows the results of the experimental space $[\ln(h/L), \ln(H_I/L)]$, which gathers the tendency of the breaker types and the regions of energy transformation modes. Figure 5.6-b represents the values of K_R^2, K_T^2 and D^* based on the product $(h/L)(H_I/L)$ on the x-axis at a semi-logarithmic scale. The breaker types of some tests are also identified. By comparing Figure 5.6-a and 5.6-b, it is observed that the application of the proposed experimental design provides the information needed to: (1) optimize the number of experiments in laboratory, (2) fulfill the design criteria between model-prototype in laboratory tests, and (3) delimit the regions of wave energy transformation and the breaker types.

The reflected and transmitted energy in a homogeneous permeable mound breakwater should fulfill Equations 3.6 and 3.7 of the dimensional analysis:

$$[K_R^2, K_T^2] = \Psi(h/L, H_I/L, D_{50,p}/L, B^*/L, R_{e,w}, R_{e,p}).$$

In these tests, $D_{50,p}$ remained constant. Figure 5.6-b shows that it is possible to identify the regions of the incident wave behavior and the breaker types according to $(h/L)(H_I/L)$, namely: (i) reflected-dominated region $K_R^2 \geq 0.5$, with surging "breakers"; (ii) dissipation-dominated region $K_R^2 < 0.1$, with weak plunging breakers; and (iii) transition region $0.1 < K_R^2 < 0.5$, in which the results seem to follow two "branches". The vertical dispersion of K_R^2 (and D^*) is greater in the transition region, $5 \cdot 10^{-4} < (h/L)(H_I/L) < 3 \cdot 10^{-3}$, which takes the same values of $(h/L)(H_I/L)$ as the interval of greatest dispersion for the permeable with main armor layer slope. As we highlighted in Chapter 4, the horizontal dispersion is possibly due to the different mode of energy transformation and the potential associated breaker types.

From the videos recorded in laboratory, it has been observed that for $(h/L)(H_I/L) < 1.1 \cdot 10^{-3}$ and $H_I/L < 0.009$ in the transition region, the incident wave train does not break on the slope with a perfect surging breaker, and the flow inside the porous medium increases. Consequently, the values of K_T^2 are greater in this branch dominated by the porous medium. On the contrary, for values of $(h/L)(H_I/L) > 10^{-3}$ and $H_I/L > 0.009$ in the transition region, the incident wave train interacts with the slope and the breaker type evolves from a weak bore to a strong plunging.

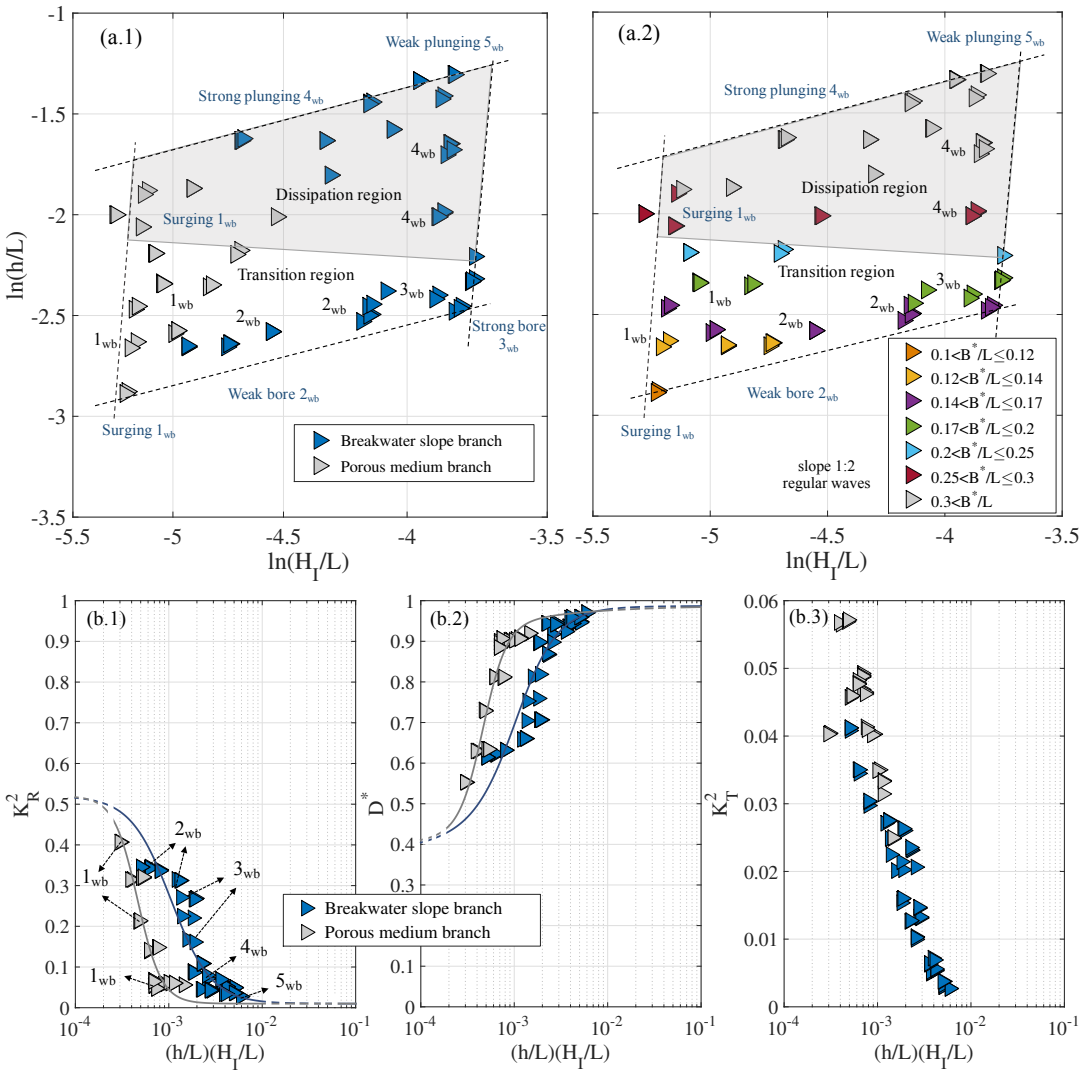

FIGURE 5.6: (a) Results of the regular experimental space $[\ln(h/L), \ln(H_I/L)]$ for the HP-MB 1 physical model according to: (a.1) whether the porous medium or the wave-breakwater slope interaction control the wave energy transformation; (a.2) ranges of values of B^*/L. The tendency of the breaker types and the regions of wave energy transformation are identified. (b) Experimental results $[K_R^2, K_T^2, D^*]$ against $(h/L)(H_I/L)$. The solid and dash lines represent the sigmoid curve and the chosen limit values for fitting the curve, respectively. The number j_{wb} $(j = 1:5)$ marks the breaker types of some tests.

The sigmoid curves are represented for the two branches obtained in the transition region with the best fit to the experimental data K_R^2 and D^* whose fit parameters are shown in Table 5.4. The tendency of the experimental data indicates that the sigmoid curves of the two branches meet at limits of K_{R0}^2 and K_{R1}^2 (the same for D^*), as a "hysteresis loop". Nevertheless,

this behavior requires further study with experimental tests. The results of K_T^2 are an order of magnitude lower than K_R^2 values.

Figures 5.7-a and 5.7-b represent the log-experimental space and the wave energy transformation modes based on $(h/L_p)(H_{m0}/L_p)$, respectively, for the irregular wave conditions. The experimental space $[\ln(h/L_p), \ln(H_{m0}/L_p]$ allows identifying the regions of wave energy transformations and the breaker types. The horizontal and vertical scatter occurs in the same transition region, $5 \cdot 10^{-4} < (h/L_p)(H_{m0}/L_p) < 3 \cdot 10^{-3}$, which also follows two branches in the same intervals of $(h/L)(H_I/L)$ as the results of regular waves.

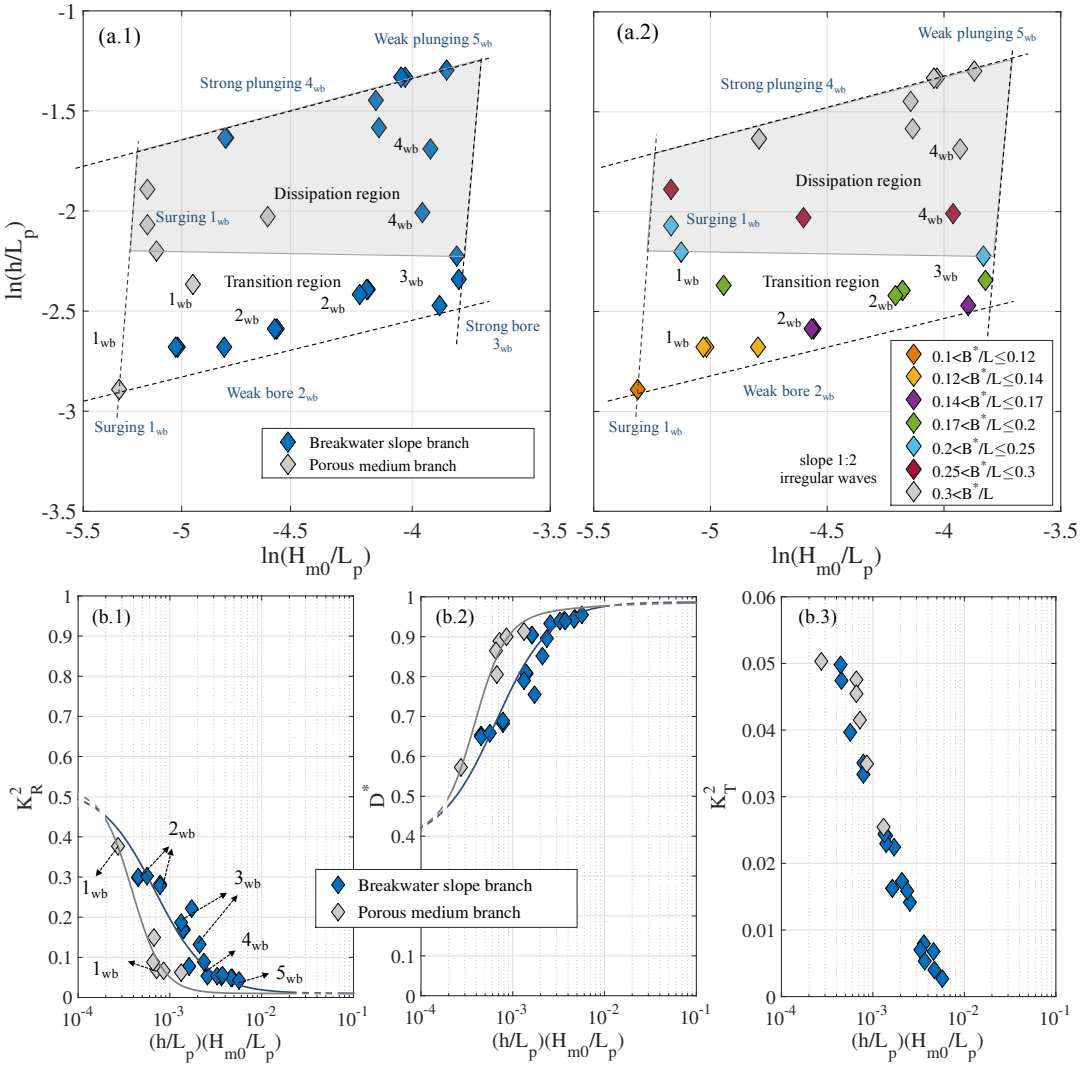

FIGURE 5.7: (a) Results of the irregular experimental space $[\ln(h/L_p), \ln(H_{m0}/L_p)]$ for the HP-MB 1 physical model according to: (a.1) whether the porous medium or the wave-breakwater slope interaction control the wave energy transformation; (a.2) ranges of values of B^*/L_p. The regions of wave energy transformation are identified. (b) Experimental results $[K_R^2, K_T^2, D^*]$ against $(h/L_p)(H_{m0}/L_p)$. The solid and dash lines represent the sigmoid curve and the chosen limit values for fitting the curve, respectively. The number j_{wb} $(j = 1:5)$ marks the breaker types of some tests.

The breaker types for the results of irregular waves were specified according to the most probable wave-breaking associated to the value of $(h/L_p)(H_{m0}/L_p)$. Nevertheless, by the nature of irregular waves, each individual wave characterized by H/L and h/L generated is different from the previous one and, consequently the breaker type varies greatly during the

test. To properly identify the wave-breaking on the slope, the frequency of each breaker type within a test should be recorded and adjusted a probability function according to H_{m0}/L_p and h/L_p simulated (future research line).

Configuration	Sigmoid function	Fit parameters				
		K_{R0}^2	K_{R1}^2	a_z	γ_z	R^2
HP-MB $\tan(\alpha) = 1/2$ Regular waves	Porous medium branch	0.01	0.55	0.0005	3.4	0.84
	Breakwater slope branch	0.01	0.55	0.0011	2.0	0.83
HP-MB $\tan(\alpha) = 1/2$ Irregular waves	Porous medium branch	0.01	0.55	0.0004	2.6	0.95
	Breakwater slope branch	0.01	0.55	0.0007	1.5	0.88
HP-MB $\tan(\alpha) = 1/1.5$ Regular waves	Breakwater slope branch	0.01	0.65	0.0015	1.93	0.80
Benedicto (2004)'s data	$D_{50,p} = 6.97$ mm and $B^* = 0.75$ m	0.08	1	0.00066	0.85	0.97

TABLE 5.4: Parameters of the sigmoid curves fitted to the two slope angles tested of the homogeneous permeable mound breakwater. The parameters of the sigmoid curve fitted to Benedicto (2004)'s data are also shown.

5.3.2 Influence of geometrical variables in the hydraulic performance

Figure 5.8 represents the values of K_R^2, D^* and K_T^2 against $(h/L)(H_I/L)$ for the two models with different breakwater width, B_b (and so B^*). The dimensionless variable B^*/L (relative width) keeps the hydraulic performance of the breakwater, namely the range of values of B^*/L are grouped in the same intervals of $(h/L)(H_I/L)$ for both widths. The values of [K_R^2, K_T^2] increases (D^* decreases) as B^*/L decreases. When $B^*/L \geq 0.25$, the saturation of the breakwater in laboratory is reached: the dissipation rate is maximum and the reflected energy is minimum. The regions of wave energy transformation and the breaker types are in the same intervals $(h/L)(H_I/L)$ for both models.

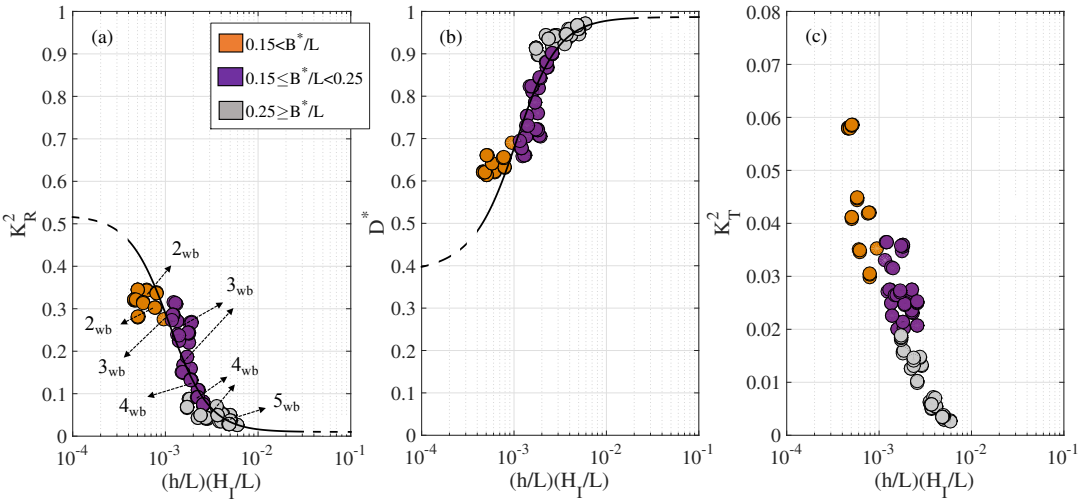

FIGURE 5.8: Experimental results [K_R^2, K_T^2, D^*] against $(h/L)(H_I/L)$ according to range of values of B^*/L (colors) for the HP-MB 1 ($B_b = 0.24$ m) and HP-MB 3 models ($B_b = 0.10$ m). The solid and dash lines represent the sigmoid curve and the chosen limit values for fitting the curve, respectively. The number j_{wb} ($j = 2:5$) marks the breaker types of some tests: 2_{wb} – weak bore, 3_{wb} – strong bore, 4_{wb} – strong plunging, 5_{wb} – weak plunging. The number of ranges of B^*/L is reduced with respect to Figure 5.6 and 5.7 to facilitate the data visualization.

In absolute terms (with dimensions), the influence of B^* in the hydraulic performance is reflected in the reflection and transmission processes, which slightly increases and decreases, respectively, as the width (or area of the porous medium) increases. This vertical displacement between both models is more pronounced in the transition region: $5 \cdot 10^{-4} < (h/L)(H_I/L) < 2 \cdot 10^{-3}$.

Figure 5.9 represents the influence of the seaward slope angle in the hydraulic performance. The values of $[K_R^2, K_T^2, D^*]$ are ordered by the slope angle and the experimental scattering for a constant value of $(h/L)(H_I/L)$ is slightly greater for the slope 1:1.5. The values of K_R^2 and D^* increases and decreases, respectively, as the slope angle increases. This behavior is more pronounced in the interval, $8 \cdot 10^{-4} < (h/L)(H_I/L) < 2 \cdot 10^{-3}$, corresponding to the transition region for the slope 1:1.5. The transmitted energy is too small to distinguish the difference between slope angles. For the slope angle 1:1.5, there is a displacement on the x-axis in the transition region and the breaker types observed in laboratory were: weak bore, strong bore and strong plunging. In fact, for a same value of $(h/L)(H_I/L)$, the wave-breaking on the slope 1:1.5 tended to more reflected breaker types than for the slope 1:2. In the dissipation-dominated region, $(h/L)(H_I/L) > 2 \cdot 10^{-3}$, the saturation of the breakwater in laboratory is reached ($B^*/L \geq 0.25$) and both models dissipate and reflect practically the same.

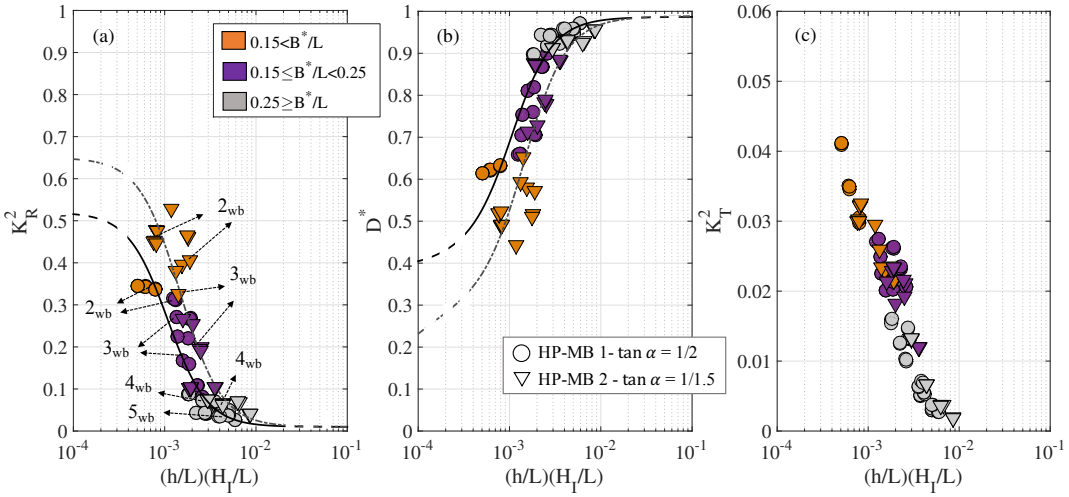

FIGURE 5.9: Experimental results $[K_R^2, K_T^2, D^*]$ against $(h/L)(H_I/L)$ according to range of values of B^*/L (colors) for the HP-MB 1 ($\tan(\alpha) = 1/2$) and HP-MB 3 models ($\tan(\alpha) = 1/1.5$). The solid and dash lines represent the sigmoid curve and the chosen limit values for fitting the curve, respectively. The number j_{wb} ($j = 2:5$) marks the breaker types of some tests: 2_{wb} – weak bore, 3_{wb} – strong bore, 4_{wb} – strong plunging, 5_{wb} – weak plunging. The number of ranges of B^*/L is reduced with respect to Figures 5.6 and 5.7 to facilitate the data visualization.

The experimental result $[K_R^2, D^*]$ of Benedicto (2004) for a homogeneous permeable mound breakwater was used to compare physical models with different granular diameter, characteristic width and water depth. Benedicto (2004) studied the reflection process for a rubble mound breakwater with and without main armor layer. Her physical model with only the porous core had the following geometric configuration: $D_{50,p} = 6.95$ mm, $B^* = 0.75$ m, $\tan(\alpha) = 1/1.5$, $\tan(\beta) = 1/1.25$ and $n_p = 0.42$. Regular wave conditions were also tested and water depth was constant an equal to $h = 0.5$ m. The stability of the granular material was assured by means of a fine wire mesh (non-damage conditions) and the tests were done under non-overtopping conditions. The HP-MB 2 model was selected to compare with Benedicto (2004)'s data since has the same slope 1:1.5.

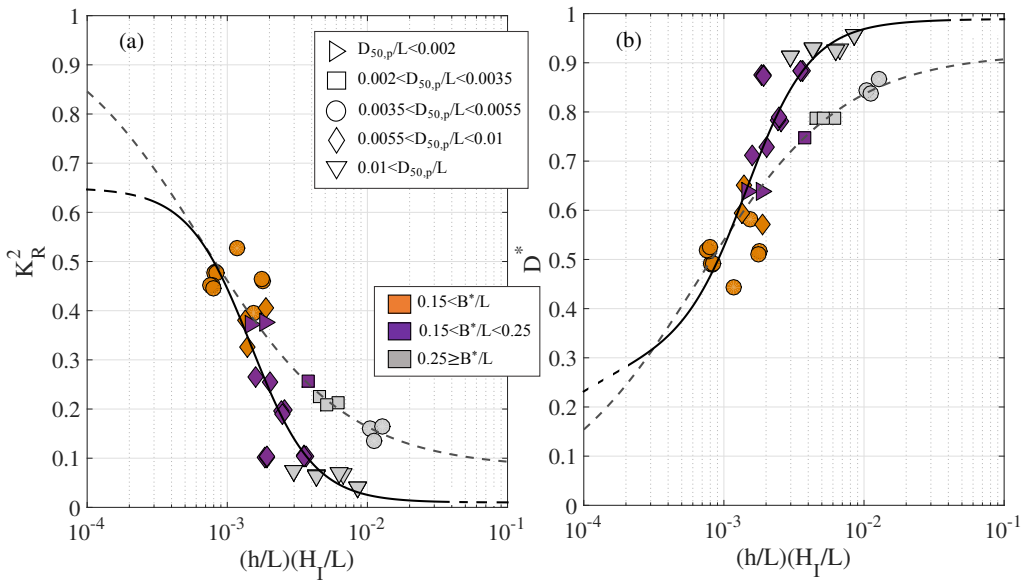

FIGURE 5.10: Experimental results $[K_R^2, D^*]$ against $(h/L)(H_I/L)$ for the HP-MB 2 ($D_{50,p} = 26$ mm, $B^* = 0.65$ m, $h = 0.4$ m) and Benedicto (2004)'s results ($D_{50,p} = 6.95$ mm, $B^* = 0.75$ m, $h = 0.5$ m), according to: (colors) range of values of B^*/L, (symbols) range of values of $D_{50,p}/L$. The lines represent the sigmoid curves.

Figure 5.10 shows the experimental results of $[K_R^2, D^*]$ based on the product $(h/L)(H_I/L)$ for both models according to ranges of values of relative width, B^*/L (colors), and relative granular core diameter, $D_{50,p}/L$ (symbols). The ranges of B^*/L for both models are ordered in the same values of $(h/L)(H_I/L)$. On the contrary, the ranges of $D_{50,p}/L$ for Benedicto (2004)'s data significantly move on the x-axis, with lower values than our physical models. In fact, there is a horizontal displacement on the x-axis and the experimental data of Benedicto (2004) are all in the transition region, $0.5 \cdot 10^{-3} < (h/L)(H_I/L) < 1.5 \cdot 10^{-2}$, and the energy transmitted is negligible. In the transition region, there is also a significant vertical displacement on the y-axis and the physical model of Benedicto (2004) reflects more and dissipates less than the HP-MB 2 model.

As we pointed out in Chapter 3, the reflected and transmitted energy as well as the dissipation inside the core depend on the hydrodynamic regime in the porous medium. According to Burcharth and Andersen (1995), the flow regime inside the core is totally turbulent, since $R_{ep} = [800 - 1000]$ for Benedicto (2004)'s model, and $R_{ep} > 2500$ for HP-MB 2 model. However, because of the dissipative nature of the flow in the porous medium and if the width of the core is sufficient, the value of R_{ep} decreases towards the inner zone of the breakwater, and the regime gradually varies from fully turbulent to transitional, and then from transitional to Forchheimer, and eventually, from Forchheimer to Darcy. In other words, the difference in the x-axis and y-axis on Figure 5.10 may be explained by the spatial variation in the regime inside the breakwater core with $D_{50,p} = 6.95$ mm and $B^* = 0.75$ m, and also because of the differences in wave-breaking. Moreover, in absolute terms, for a constant value of $(h/L)(H_I/L)$, the reflection increase and the dissipation decreases with a lower $D_{50,p}$ and a higher B^*.

In all cases, for each region delimited by $(h/L)(H_I/L)$, the evolution of the modes of energy transformation and breaker types depend on the values of B^*/L, $D_{50,p}/L$ and α. When a value of $(h/L)(H_I/L)$ is selected in the transition region, K_R^2 increased since the value of B^*/L decreases and $D_{50,p}/L$ (constant for our physical models) decreases too. In the transition region, there is a variation in the corresponding breaker type: weak bore, strong bore, and

strong plunging. For the HP-MB 2 model with slope angle 1:1.5, the breaker types observed in the transition region were only weak bore and strong bore.

Table 5.4 gathers the fit parameters of the sigmoid curves with the best fit for the homogeneous permeable physical models tested. The sigmoid curve is the same for breakwaters with different width; while, as we observed with the numerical results of impermeable slopes, the shape of the function is similar for models with different seaward slope angle. The limits of the sigmoid function, K_{R1}^2 and K_{R0}^2 are arbitrary, since Benedicto (2004) tested few data for long periods and wave conditions in Stokes I regime.

5.4 Discussion and recommendations

This section discusses the aspects of the experimental results obtained and proposes recommendations according to the geometrical configuration of the breakwater and its impact on the wave energy transformation.

The results show that the vertical deviation of the wave energy transformation modes is higher in the transition region in which two "branches" are identified: (1) the flow inside the porous medium increases and perfect surging breakers were observed in this branch; (2) the incident wave train interacts with the slope and the breaker type evolves from a weak bore to a strong plunging. It seems that the possibility to identify these behaviors is because the number of dimensionless quantities involved in the dimensional analysis is reduced with respect to the permeable mound breakwater with main armor layer. The interaction (circulation and friction) of the incident wave train with the main armor layer generates a local dissipation, which is difficult to quantify and requires more study (see Chapter 6 and Losada et al., 2019).

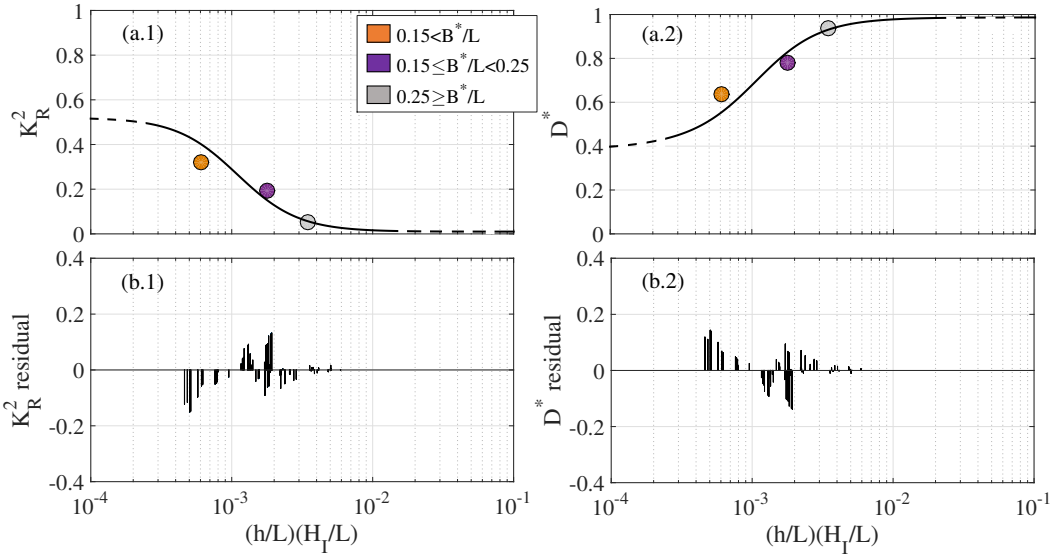

FIGURE 5.11: (a) Average experimental results of $[K_R^2, D^*]$ against $(h/L)(H_I/L)$ for the HP-MB 1 ($B_b = 0.24$ m) and HP-MB 3 models ($B_b = 0.10$ m). (b) Values of the deviation obtained from the residual values: experimental value less the theoretical value calculated by the sigmoid curve. The solid and dash lines represent the sigmoid curve and the chosen limit values for fitting the curve, respectively.

As we explained in Section 4.2.3, it is evident that the experimental technique and method of analysis in themselves (see Appendix C) are not sufficient to explain the variability of the experimental values, which is reflected in certain intervals of $(h/L)(H_I/L)$ values. Figure 5.11-a represents the sigmoid curve fitted to the average experimental values of K_R^2 and D_*

with the same relative width B^*/L, for the models with the same slope 1:2 (HP-MB 1 and HP-MB 3). Figure 5.11-b shows the residual values of all the experimental results that fit a t-Student. The residual error, which is small in dissipation-dominated region and increases in the transition region, gathers (i) the experimental scattering from the laboratory techniques, methods and time series analysis, and (ii) the experimental scattering that is intrinsic and is a consequence of physical processes.

A rubble mound breakwater with main armor and porous core dissipates more wave energy (reflects less) than a breakwater composed only by the same porous core (Benedicto, 2004), since there is a turbulence dissipation during the interaction (circulation and friction) of the incident wave train with the main armor layer. However, by comparing the two permeable breakwater mound typologies tested in this research, with the same slope angle 1:2 (the homogeneous and the permeable with main armor), we observe that, homogeneous physical models reflect less, transmit more and dissipate more than the physical model with main armor. As we highlighted in Section 5.3.2, the latter is due to spatial variation in the flow regimes inside the porous media and the evolution of the breaker types.

The regions of incident wave behavior according to $(h/L)(H_I/L)$ values are identified based on the experimental results. The chosen threshold values are indeed arbitrary, but indicative of the predominant mode of energy transformation on a homogeneous permeable mound breakwater. Notice that, the intervals of the regions of energy transformation for the homogeneous permeable breakwater may be different if the tests are carried on in a flume with different wave generator and the breakwater (materials and layouts). Table 5.5 gathers the limits of the regions according to the slope angles tested.

Hence, for a homogeneous permeable mound breakwater with slope 1:2 and 1:1.5, the regions are:

- Reflection-dominated region, $\{K_R^2 \geq 0.5\}$: $(h/L)(H_I/L) \leq a$. Our experimental data are not within in the reflected-dominate region and the limit in $(h/L)(H_I/L)$ was selected by the trend of the sigmoid function.
- Dissipation-dominated region, $\{D^* \geq 0.9\}$: $(h/L)(H_I/L) \geq b$, with
  - $D_{50,p}/L > 0.01$,
  - $B^*/L \geq 0.25$
- Transition region, $\{0.1 < K_R^2 < 0.5\}$: $c_1 < (h/L)(H_I/L) < c_2$, with
  - $0.0035 < D_{50,p}/L < 0.01$,
  - $0.10 < B^*/L < 0.25$

Slope angle	Reflection-dominated region	Dissipation-dominated region	Transition region
1:2	$a = 2 \cdot 10^{-4}$	$b = 2 \cdot 10^{-3}$	$c_1 = 5 \cdot 10^{-4}$ $c_2 = 3 \cdot 10^{-3}$
1:1.5	$a = 7 \cdot 10^{-4}$	$b = 2 \cdot 10^{-3}$	$c_1 = 8 \cdot 10^{-4}$ $c_2 = 3 \cdot 10^{-3}$

TABLE 5.5: Values of the limits that define the regions of wave energy transformation for homogeneous permeable mound breakwater with slope angles 1:2 and 1:1.5.

For practical engineering purposes, Figure 5.12 presents a scheme of how the incident wave train behaves according to the geometrical parameters involved in the dimensional analysis and its impact in the hydraulic performance.

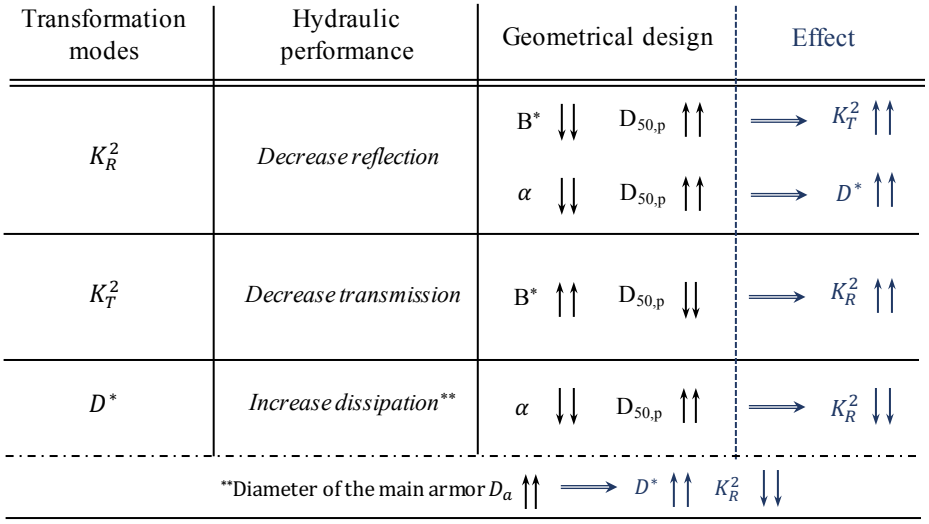

FIGURE 5.12: Recommendation for geometrical parameters involved in the dimensional analysis of permeable mound breakwater according to its impacts on the hydraulic performance.

5.5 Conclusions

The purposes of this research were (1) to apply the proposed experimental design in laboratory to a conventional rubble mound breakwater, and (2) to properly quantify the influence in the hydraulic performance of the physical processes involved in the dimensional analysis. For that, physical experimentation was performed in a 2D wave flume for a conventional homogeneous and permeable mound breakwater with two characteristic width, B^*, two seaward slope angles, α, and a constant granular core diameter, $D_{50,p}$. The experimental results of wave energy transformation modes were also compared with other laboratory tests with different breakwater geometry and water depth. The following conclusions can derived from this study:

1. The application of the log-experimental space $[\ln(h/L), \ln(H/L)]$ to analyze the hydraulic performance of the homogeneous permeable mound breakwater optimizes the number of experiments in laboratory and provides the information needed to (i) fulfill the design criteria between model-prototype and wave generation requirements, and (ii) identify the regions of wave energy transformation and breaker types for intervals of $(h/L)(H_I/L)$.

2. The scattering of the experimental results of $[K_R^2, D^*]$ is higher in the transition region and seems to follow two branches with $(h/L)(H_I/L)$ according to the transformation processes are controlled by (1) the porous medium or (2) the interaction of the incident wave train with the slope of the breakwater. The energy transmitted es very small.

3. In the transition region, for lower values of H_I/L, the flow inside the porous medium increases and the breaker type observed is a perfect surging for all $(h/L)(H_I/L)$ values. On the contrary, for higher values of H_I/L in the transition region, the incident wave train interacts with the breakwater slope and the move of wave-breaking is between weak bore and strong plunging, in the transition region.

4. The experimental results for irregular waves conditions of $[\ln(h/L_p), \ln(H_{m0}/L_p)]$ identifies the same regions of wave transformation and breaker types as the results of regular waves conditions $[\ln(h/L), \ln(H_I/L)]$. Therefore, the hydraulic performance for irregular waves defined by $[h/L_p, H_{m0}/L_p]$ could be extrapolated to regular waves with $[h/L, H_I/L]$ conditions.

5. The relative characteristic width keeps the hydraulic performance of the breakwater (regions and breaker types) and the range of B^*/L values are grouped in the same intervals of $(h/L)(H_I/L)$ for breakwater models with different width.

6. The slope angle is an identificative parameter which separates the hydraulic performance of breakwater models with different slopes. The values of K_R^2 and D^* increases and decreases, respectively, as the slope angles increases. This vertical displacement on y-axis is more pronounced in the transition region, which also has a displacement on the x-axis and the breaker type moves between weak bore and strong bore for the higher slope. In the dissipation-dominated region, the saturation of the breakwater in laboratory is reached and both models dissipate and reflect practically the same.

7. When the characteristic width and, above all, the granular core diameter are very different between models, the hydraulic performance of the breakwater changes on the x- and y-axis. The ranges of B^*/L values are grouped in the same intervals of $(h/L)(H_I/L)$, but the ranges of $D_{50,p}/L$ move on the x-axis. The reflected energy and the dissipation rate increases and decreases, respectively, as B^*/L and $D_{50,p}/L$ decreases, and more for the breakwater with lower core diameter and higher width. This spatial variation on the x- and y-axis could be explained by the variability of the flow regime inside the porous medium and the evolution of wave-breaking.

Chapter 6

Bulk wave dissipation in the main layer of mound breakwaters

Comment

This chapter compiles some of the results and the future challenges presented on:

M.A. Losada, P. Díaz-Carrasco, M.V. Moragues, and M. Clavero (2019). "Variabilidad intrínseca en el comportamiento de los diques rompeolas". In: *Proceedings of the 15th National Conference of Jornadas Españolas de Puertos y Costas*. Málaga, Spain

Clavero, M., Díaz-Carrasco, P., and Losada M.A. (Under preparation). "Bulk wave energy dissipation in the main layer of mound breakwaters: a 2D analysis". In: *Ocean engineering*.

Reflection, transmission and bulk dissipation (determined globally in a control volume) are the three main processes that controls the behavior of a breakwater against the incident waves. Considering that the wave train is reflected and dissipated (locally) during its propagation through the slope, main armor and secondary layers, core and when leaving the section of the structure, their values may not be in equilibrium. In this Chapter a further step is achieved in this topic with the study of the dissipation process due to the interaction of the incident wave train with the main armor layer. For that, Section 6.2 presents the definition of the problem and the dimensional analysis applied by identifying the independent variables of the main armor layer that impact the wave transformation processes at the breakwater. Furthermore, this section outlines the physical experimental setups from two laboratories: (1) IISTA - University of Granada, (2) Aalborg University. The results of the log-transformation spaces from the two sets of experimental data and the bulk energy dissipation in the main armor are presented in Section 6.3. Finally, Sections 6.4 and 6.5 gather the discussion and the specific conclusions of this work, respectively.

6.1 Introduction

The dissipation of a wave train on a breakwater slope is mainly caused by the generation, transport, and dissipation of turbulence during the following processes: (i) wave evolution and eventually wave-breaking on the free surface of the slope; (ii) interaction (circulation and friction) with the main armor layer; and (iii) wave propagation through the secondary layers and porous core. Simultaneously, part of the incident energy is reflected by the changes in

the characteristics of the breakwater during its propagation through the slope, main armor layer, secondary layer and porous core, and also part of the wave energy is transmitted to the landward of the structure (Losada et al., 2019). If the reflected and transmitted energy flows are known, the global dissipation $D^{'*}$ due to the interaction with the breakwater is determined by solving the conservation equation of the incident energy (Equation 3.1). Consequently, $D^{'*}$ is a bulk energy dissipation rate per unit length of breakwater section per flux of the wave incident energy impinging normally to the breakwater section.

The research works dedicated to the calculation of the wave dissipation on a mound breakwater are a small proportion of those that are dedicated to calculate the flow of reflected or transmitted wave energy. In the last two decades, numerical predictions of the wave-breaking on a smooth and impermeable slope have been published using different numerical techniques (Christensen and Deigaard, 2001; Lara et al., 2006; Zhang and Liu, 2006; Madsen and Fuhrman, 2008; Gíslason et al., 2009; Lakehal and Liovic, 2011). These results provide detailed information on the transport of turbulent kinetic energy due to the interaction process of the wave train with the slope. On the other hand, the propagation of a wave train (regular or irregular) through a porous medium is widely analyzed, both theoretically and experimentally (physical and/or numerical). As we mentioned in Chapter 3, the Forchheimer equation represents reasonably well the amount of movement consumption in the porous medium (bulk resistance over the porous medium) (Sollitt and Cross, 1972; Dalrymple et al., 1991; Van Gent, 1995), and its extension to energy dissipation; the equivalent hypothesis of Lorentz provides satisfactory results for practical maritime engineering (Pérez-Romero et al., 2009; Vílchez et al., 2016b).

Unfortunately, reflection and dissipation during shoaling and the eventual breaking of the wave on a slope with a permeable core do not have a theoretical model equivalent to the Forchheimer equation, and most studies are based on numerical (Kobayashi and Wurjanto, 1992; Lara et al., 2008; Van Gent, 2013; Ruju et al., 2014; Jensen et al., 2014a; Jensen et al., 2014b; Vanneste and Troch, 2015) and physical experimentation (Losada et al., 1991; Scarcella et al., 2007; Zanuttigh and Van der Meer, 2008; Pérez-Romero et al., 2009; Vílchez et al., 2016a; Vílchez et al., 2016b). In all of these studies, it is confirmed that the dimensions of the main armor layer and the type of piece significantly affect the values of the reflected energy coefficient, K_R^2, and the dissipation rate, D^*, as well as the run-up, R_u, run-down, R_d, and, where appropriate, the overflow rate due to the overtopping Q_c.

In practical maritime engineering, it is usual to quantify design values by means of formulas obtained from tests in different laboratories and with different techniques and analysis tools. As we have highlight during this Thesis, most of these formulas include the number of Iribarren as a parameter of dynamic similarity of the hydrodynamic behavior of a wave train in a flat, impermeable and indefinite slope with angle α (Battjes, 1974). In addition, biunivocal correspondence between the value of I_r and the type of wave-breaking on the slope is accepted.

Over the years, the experimental dispersion of the data and the uncertainty of the formulas with I_r promoted both the identification of the sources of uncertainty and the revision of such formulas. Among others, the following were proposed: the notional permeability, P (Van der Meer, 1988), and the partial coefficients γ, that mainly "quantify" the effect of the permeability with a value chosen according to the geometric configuration and the type of piece of the main armor layer and the core (Van der Meer et al., 2018; Eldrup et al., 2019). The value of partial coefficients is associated with some relevant characteristics of the breakwater geometry (EurOtop, 2018). Both P and the coefficients γ, affected or not by a fit exponent, multiply a "base formula" which, in all cases, still includes the Iribarren number as an independent variable.

The experimental results showed in Chapter 4, question the validity of I_r, specially when $I_r > 1.5$, (1) as a necessary and sufficient parameter for dynamic similarity and, (2) the biunivocal relationship between the type of wave-breaking and I_r. Moreover, the results presented in the previous chapters showed that the fit of the experimental data with a sigmoid function, whose independent variable is the product $(h/L)(H_I/L)$, significantly improves the prediction of the coefficients K_R^2, K_T^2 and the bulk dissipation. With this previous work, an improvement in the characterization of the hydraulic performance of mound breakwaters has been achieved, and we have also marked that the sources of energy dissipation on the breakwater have influence on its final hydraulic performance.

In Chapter 6, we take a further step on this topic and we study the dissipation process due to the interaction of the incident wave train with the main armor layer. For that, this work is supported by (i) the review of the dimensional analysis of the physical processes of the main armor that influence in the wave energy transformation, and (ii) two series of data obtained experimentally in the wave flume of Aalborg University and also in the wave flume of IISTA - University of Granada. These experimental data allow calculating the bulk wave dissipation of different sizes and type of pieces for the main armor layer. The experimental technique of Aalborg University is analogous to that followed in the IISTA and the analysis of the records adapts to the methods implemented by that laboratory (Aalborg University, 2007b).

6.2 Problem formulation and methods

The bulk dissipation per unit of incident energy on a permeable mound breakwater with a main armor layer depends on the following dimensionless variables (Equation 3.11),

$$D^* = 1 - \Psi_{R,T}\left(\frac{h}{L}, \frac{H_I}{L}, \frac{D_{50,p}}{L}, \frac{B^*}{L}, \text{main armor}\right) \tag{6.1}$$

The main armor is represented, generically, by the type and shape of the unit piece with a characteristic diameter D_a, and the specific placement criterion. From these three descriptors it is possible to define and calculate the thickness of the main armor, $e = n_l D_a$, its porosity/permeability and the equivalent roughness, among others (ROM 1.1-18, 2018).

When a mound breakwater with a seaward slope angle (α), porous core (B^*, $D_{50,p}$), and a given main armor layer is selected, its bulk dissipation depends on the characteristics of the incident wave train: the relative water depth, h/L, and the steepness at the toe of the structure, H/L. This dissipation can be subdivided in its three main components:

$$D^* = d_1^* + d_2^* + d_3^* \tag{6.2}$$

where d_j^* (j= 1, 2, 3) represents the contribution to bulk dissipation due to: ($j = 1$) wave evolution and eventually wave-breaking on the free surface of the slope, ($j = 2$) interaction (circulation and friction) with the main armor layer, and ($j = 3$) wave propagation through the porous core. If the main armor is constructed with the same type of unit pieces but of a different size (for example, rocks, cubes, cubipods), different thickness or placement criterion, the differences between the bulk dissipation D^* are mainly due to the variation in d_2^*, that is,

$$(D^*)_{ma1} - (D^*)_{ma2} \approx (d_2^*)_{ma1} - (d_2^*)_{ma2} + \text{error} \tag{6.3}$$

where the subscripts $ma1$ and $ma2$ identify two breakwaters with the same geometry but different type of unit pieces, size or material of the main armor layer.

6.2.1 Dimensional analysis

As we explained in Section 3.2.2, the complete set of independent variables that determine the transformation of the wave train on a non-overtoppable permeable mound breakwater composed by a porous core and a main armor layer, is

$$(X_1, X_2) = f(h, \rho, \mu, g, H_I, L, D_{50,p}, B^*, D_a, e, \rho_s)$$

where ρ_s is the density of the armor pieces, which is included in the dimensional analysis of this chapter to study the influence of the type of unit piece on the bulk dissipation. Remember that (X_1, X_2) represent the dependent variables of the first kind, i.e., the reflected and transmitted energy. From this complete set of independent variables, the variables whose value remains fixed during a part or all the experimentation can be separated. In this case, we select $(\rho, g, h, L, D_{50,p}, B^*, e)$, $n_F = 7$ as the complete set of independent variable constant in a test. From this subset of variables, the dimensionally base is (ρ, g, L), then $k_F = 3$, and the set of $(n_F - k_F) = 3$ dimensionless variables is formed by $(h/L, D_{50,p}/L, B^*/L, e/L)$ which, for a fixed period, are fixed quantities. As a consequence,

$$(X_1, X_2) = f\left[(H_I, D_a, \rho_s, \mu); (\rho, g, L)\right]$$

Hence, (X_1, X_2) is completely determined with $n - n_F + k_F = 7$ dimensionless variables. Therefore, if a new dimensionally base is formed from the previous complete set of n independent variables, that is: (μ, ρ_s, H_I), $k_\pi = 3$, then the following similarity relation is defined

$$\left[K_R^2, \frac{X_{0,R}}{L}\right] = \Psi_R\left(\frac{H_I}{L}, \frac{D_a}{H_I}, R_{e,D_a}, \frac{\rho}{\rho_s}\right) \tag{6.4}$$

$$\left[K_T^2, \frac{X_{0,T}}{L}\right] = \Psi_R\left(\frac{H_I}{L}, \frac{D_a}{H_I}, R_{e,D_a}, \frac{\rho}{\rho_s}\right) \tag{6.5}$$

being $R_{e,D_a} = \frac{D_a\sqrt{gH_I}}{\mu/\rho}$ the armor Reynolds number, and ρ/ρ_s the specific density of the unit pieces of the main armor. Finally, applying the Equation 3.1 to the experimental results, the bulk dissipation due to the interaction of the wave train with the breakwater slope is determined by

$$D^*_{i,j} = 1 - [K_R^2 + K_T^2]_{i,j} \tag{6.6}$$

where the subscript j specifies the experiment with a fixed wave period, T (or L), and i identifies the experimental run with a wave height, H_I, of the incident wave train. Grouping the partial results (and inverting some dimensional variables), the following relation is finally obtained,

$$D^* = \Psi\left(\frac{h}{L}, \frac{H_I}{L}, \frac{D_{50,p}}{L}, \frac{B^*}{L}, \frac{e}{L}, R_{e,D_a}, N_s\right) \tag{6.7}$$

being $N_s = \frac{H_I}{D_a\Delta}$ the Stability Number, and $\Delta = \frac{\rho_s}{\rho} - 1$, the submerged relative density. To sum up, the bulk dissipation due to the interaction of the incident wave train with the breakwater depends, mainly, on:

1. Wave evolution and eventually wave-breaking on the free surface of the slope, $d_1^* = \Psi_1(h/L, H_I/L)$
2. Interaction (circulation and friction) of the incident wave train with the main armor, layer, $d_2^* = \Psi_2(N_s, e/L)$; $e \approx n_l D_a$.

3. Wave propagation through porous core, $d_3^* = \Psi_3(B^*/L, D_{50,p}/L)$

NOTE

Notice that the values of $R_{e,w}$, R_{e,D_a} and $R_{e,p}$ should be sufficiently high to assure that the hydrodynamic regime is totally turbulent in the water column, inside the main layer and inside the core.

6.2.2 Experimental setups

Physical tests from IISTA-University of Granada

Laboratory tests were performed in the wave-current flume of IISTA - University of Granada, in order to quantify the influence of the geometric characteristics of the main armor layer in the bulk energy dissipation. Figure 6.1 shows a sketch of the physical model tested: a rubble-mound breakwater with crown wall composed of a main armor of two layer of cubes and a permeable core of fine gravel with $D_{50,p} = 12$ mm. The water depth was kept constant and equal to $h = 0.4$ m.

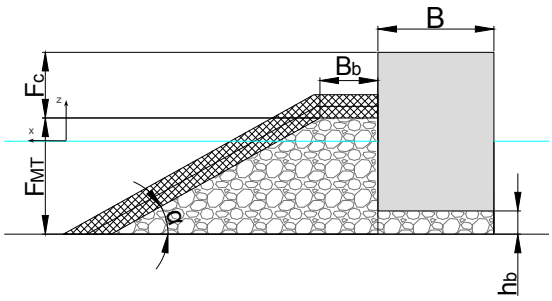

FIGURE 6.1: Physical model of the breakwater tested: rubble-mound breakwater with crown wall composed of a main armor layer of cubes and a porous core.

The main armor layer was tested with five different sizes of cubes, l. Table 6.1 gathers more details regarding the geometrical configurations, where B_b is the width of the top of the breakwater; F_{MT} is the porous media height; D_{eq} is the equivalent diameter of the main armor layer, where the cube volume is equated to the volume of a sphere; α is the seaward slope of the breakwater, respectively; are the densities of the armor pieces and core, respectively; F_c is the free-board; B is the width of the caisson; h_b is the caisson foundation depth; and n_p is the porosity of the core, according to CIRIA et al. (2007).

Armor unit cubes size (mm)	$D_a = D_{eq}$ (mm)	B_b (m)	$\rho_{s,a}$ (t/m^3)	F_c (m)	h_b (m)	$\cot(\alpha)$	B (m)	F_{MT} (m)	$D_{50,p}$ (mm)	$\rho_{s,p}$ (t/m^3)	n_p
l = 25 mm	31. 0		2.07								
l = 33 mm	40.9		2.18								
l = 38 mm	47.1	0.25	2.2	0.25	0.10	1.5	0.5	0.55	12	2.83	0.391
l = 44 mm	54.6		2.21								
l = 65 mm	80.6		2.27								

TABLE 6.1: Geometric parameters of the rubble mound breakwater with crown wall tested in the laboratory of IISTA-University of Granada.

Tests were performed in the wave flume with a VTI controller. The AwaSys software package was used to generate waves with the simultaneously active absorption of reflected

waves. Irregular waves were generated with a Jonswap spectrum defined by a spectral wave height. $H_{m0,target}$, the peak wave period, $T_{p,target}$, and the peak enhancement factor of 3.3. Test were run with 1000 waves, keeping constant the wave period and increasingly the incident wave height in steps of 0.02. The maximum wave height tested in each period was limited until the initial damage happened (non-damage conditions). Table 6.2 shows the target wave parameters run in each configuration. Wave-breaking was only caused by wave-breakwater interaction and the experiments were also under non-overtopping conditions.

Armor unit cubes size (mm)	$T_{p,target}$ (s)	$H_{m0,target}$ (m)
l = 25 mm	[1.05–3]	[0.04–0.08]
l = 33 mm	[1.05–3]	[0.04–0.10]
l = 38 mm	[1.05–3]	[0.04–0.10]
l = 44 mm	[1.05–3]	[0.04–0.10]
l = 65 mm	[1.05–3]	[0.04–0.12]

TABLE 6.2: Wave conditions tested in the laboratory of IISTA-University of Granada: target parameters for irregular waves generated with a Jonswap spectrum.

Physical tests from Aalborg University

The analysis of the experimental data obtained from other laboratory tests is also included in this chapter in order to complete our experimental results and to verify the role of the main armor in the bulk energy dissipation. These laboratory tests were done in the Wave Flume of Aalborg University, where a conventional rubble mound breakwater were performed with two types of pieces for the main armor layer and a core composed by a fine gravel (see Figure 3.2 of Chapter 3). Table 6.3 summarizes the geometric configuration of the two armor units tested placed in two layers. The water depth was kept constant and also equal to $h = 0.4$ m.

Armor unit	$D_a = D_{eq}$ (mm)	B_b (m)	$\rho_{s,a}$ (t/m^3)	Filter $D_{50,f}$ (mm)	$\cot(\alpha)$	$\cot(\beta)$	F_{MT} (m)	$D_{50,p}$ (mm)	$\rho_{s,p}$ (t/m^3)	n_p
Cubes l = 40 mm	49.6	$3D_a$	2.30	15	1.5	1.5	0.55	5.8	2.80	0.37
Rocks	44 0	$3D_a$	2.62	15	1.5	1.5	0.55	5.8	2.80	0.37

TABLE 6.3: Geometric parameters of the conventional rubble mound breakwater tested in the laboratory of Aalborg University. The values of core porosity, n_p, and densities, $\rho_{s,a}$, $\rho_{s,p}$, were provided by Aalborg University.

Irregular waves were generated by a hydraulically powered piston wavemaker with steering signals generated by the AwaSys4 software using the white noise filtering method (Aalborg University, 2007). The tests were done with 1000 waves, keeping the steepness constant in each test. For that, the tests were carried out increasing the wave height by steps of 0.02 m in each test and varying the peak period to maintain the steepness. The irregular wave conditions tested are shown in Table 6.4. Wave-breaking is only caused by wave-breakwater interaction and the experiments were also for non-overtopping and non-damage conditions.

6.2.3 Time series analysis and the log-experimental space

Figure 6.2 shows the scheme of both wave flumes of IISTA and Aalbog University. Six resistance wave gauges (G1 to G6) were located along the wave flume of IISTA and used to measure the free surface elevations with a sampling frequency of 20 Hz. For the tests of

S_p	$H_{m0,target}$ (m)	$T_{p,target}$ (s)
0.01	0.04	1.60
	0.06	1.96
	0.08	2.26
	0.10	2.53
	0.12	2.77
0.02	0.04	1.13
	0.06	1.39
	0.08	1.60
	0.10	1.79
	0.12	1.96
0.035	0.04	0.86
	0.06	1.05
	0.08	1.46
	0.10	1.35
0.045	0.04	0.75
	0.06	0.92
	0.08	1.17

TABLE 6.4: Wave conditions tested in the laboratory of Aalborg University: target parameters for irregular waves. $S_p = H_{m0}/L_p$ is the wave steepness, being L_p the wavelength corresponding to the peak wave period, T_p.

Aalborg University, six resistance type wave gauges were placed near the structure to separate incident and reflected waves and one wave gauge at the toe of the breakwater.

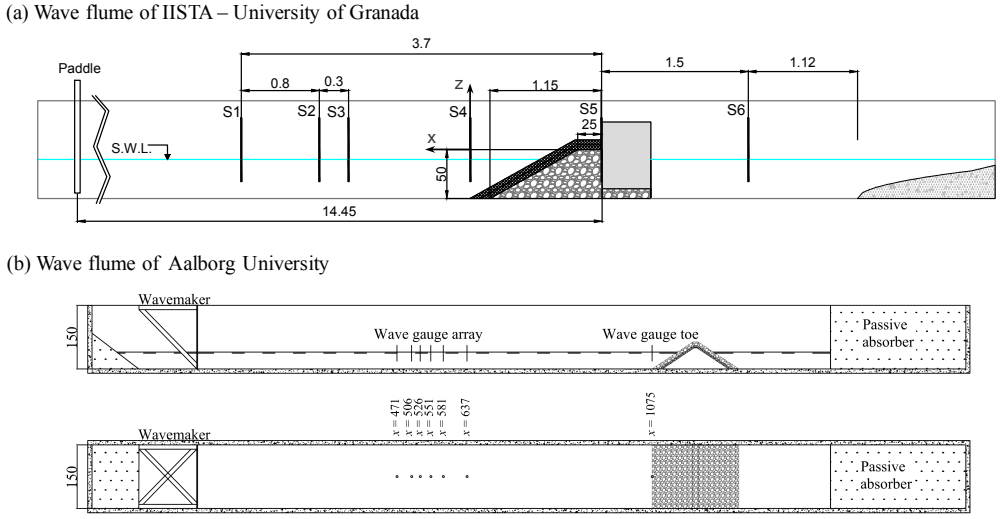

FIGURE 6.2: Scheme of the wave flumes of: (a) IISTA - University of Granada - 23 x 0.65 x 1 m (dimensions in meters), and (b) Aalborg University - 21.5 x 1.2 x 1.5 m (dimensions in centimeters). The location of wave gauges positioned in each laboratory is included.

For the tests of IISTA, the data acquisition and analysis of the free surface elevations measured by wave gauges was the same as we explained in Chapters 3 and 5. Hence, the incident and reflected wave train were separated by Baquerizo (1995)'s method, and the reflection and transmission coefficients (K_R^2, ϕ_R, K_T^2) were obtained by applying the power spectral analysis. K_R^2 and ϕ_R were calculated with the data measured by gauges G1, G2 and G3.

The transmission coefficient (K_T^2) was computed as the radio of the incident root-mean-square wave height, H_{Irms}, and the transmitted root-mean-square wave height, H_{Trms} measured with gauge G6. Gauge G4, located at the toe of the structure (x = 0), provided the total wave height at the toe of the breakwater. Waves gauge G5 measured the wave height at the crown wall of the breakwater. The wave energy dissipation rate (D^*) was calculated by Equation 3.1 for the total flow.

For the tests performed in Aalborg University, the method of Eldrup and Andersen (2019), which is an extension of Andersen et al. (2017)'s method, was applied to calculate the incident and reflected wave spectrum. The SIRW method of Frigaard and Brirsen (1995) was used to calculate the time domain incident and reflected wave trains. All this analyses of wave signal were performed with the Wave-Lab3 software package (Aalborg University, 2015). Wave signals were filtered using an analog low-pass filter with a cut-off frequency of 8 Hz and a digital filter with cut-off frequencies of 1/3 and 3 times the peak frequency, f_p.

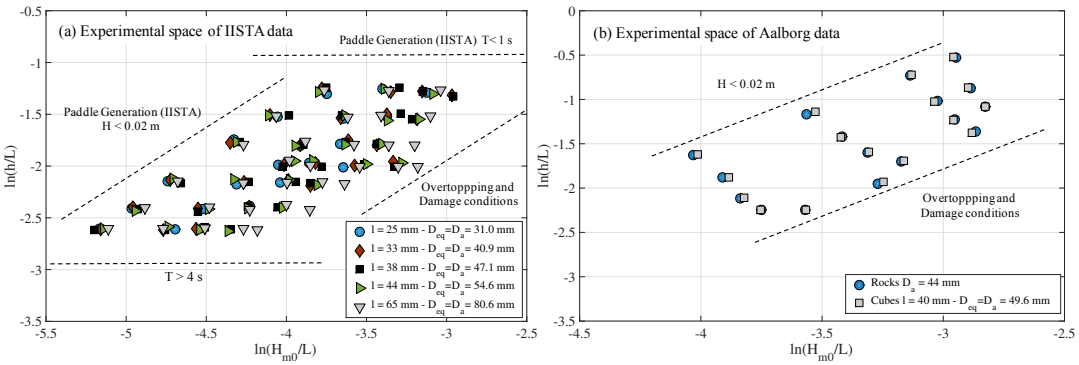

FIGURE 6.3: The log-experimental space [$\ln(h/L)$, $\ln(H_{m0}/L)$] of (a) IISTA - University of Granada, and (b) Aalborg University. The experimental limits for wave generation in the laboratory and the non-overtopping and non-damage conditions are marked.

Figure 6.3 presents the experimental space of the logarithmic transform as the pairs of values of h/L, H_{m0}/L. In this graphical representation, it is easily see how the space is filled with the experimental data and, also, how the experiment is performed. In the case of the experimental data from IISTA-UGR (Figure 6.3-a) the period is kept constant and the wave height is increased in each run. The experimental points are aligned in constant values of h/L and are ordered from left to right when increasing H_{m0}/L. In the case of the experimental data from Aalborg University (Figure 6.3-b), the target values of each experiment were selected to keep the steepness constant and, in each run, the wave height and period were simultaneously increased. Due to the multiple generation controls (Aalborg University, 2007b), the values actually generated did not keep the steepness constant in each run. The values of h/L and H_{m0}/L of Aalborg determine a corresponding parallelepiped displacement up and to the right with greater h/L and H_{m0}/L than the parallelepiped of IISTA-UGR.

6.3 Results

Figure 6.4-a shows the sample space with the experimental data of IISTA-UGR and the best fit lines based on the H_{m0}/D_a value. In addition, the tendency (blue arrows) of evolution of the most likely breaker type of irregular wave train is indicated following the constant H_{m0}/D_a isolines. Following Figure 6.4-a, for the lower values of $H_{m0}/D_a = 0.7$, the breaker type moves from surging to strong plunging, as both the relative water depth, h/L, and the steepness of the wave incident train H_{m0}/L increase. For the higher isoline $H_{m0}/D_a = 2$, the breaker type evolves from weak bore to weak plunging, as both the relative water depth, h/L,

and the wave steepness of the wave incident train H_{m0}/L increase. Moving in a diagonal of the parallelepiped, with a specific way of increasing h/L and H_{m0}/L, the break type evolves from surging to weak-plunging. Note that, since the different cube sizes tested have the same density, H_{m0}/D_a is proportional to their Stability Number, N_s.

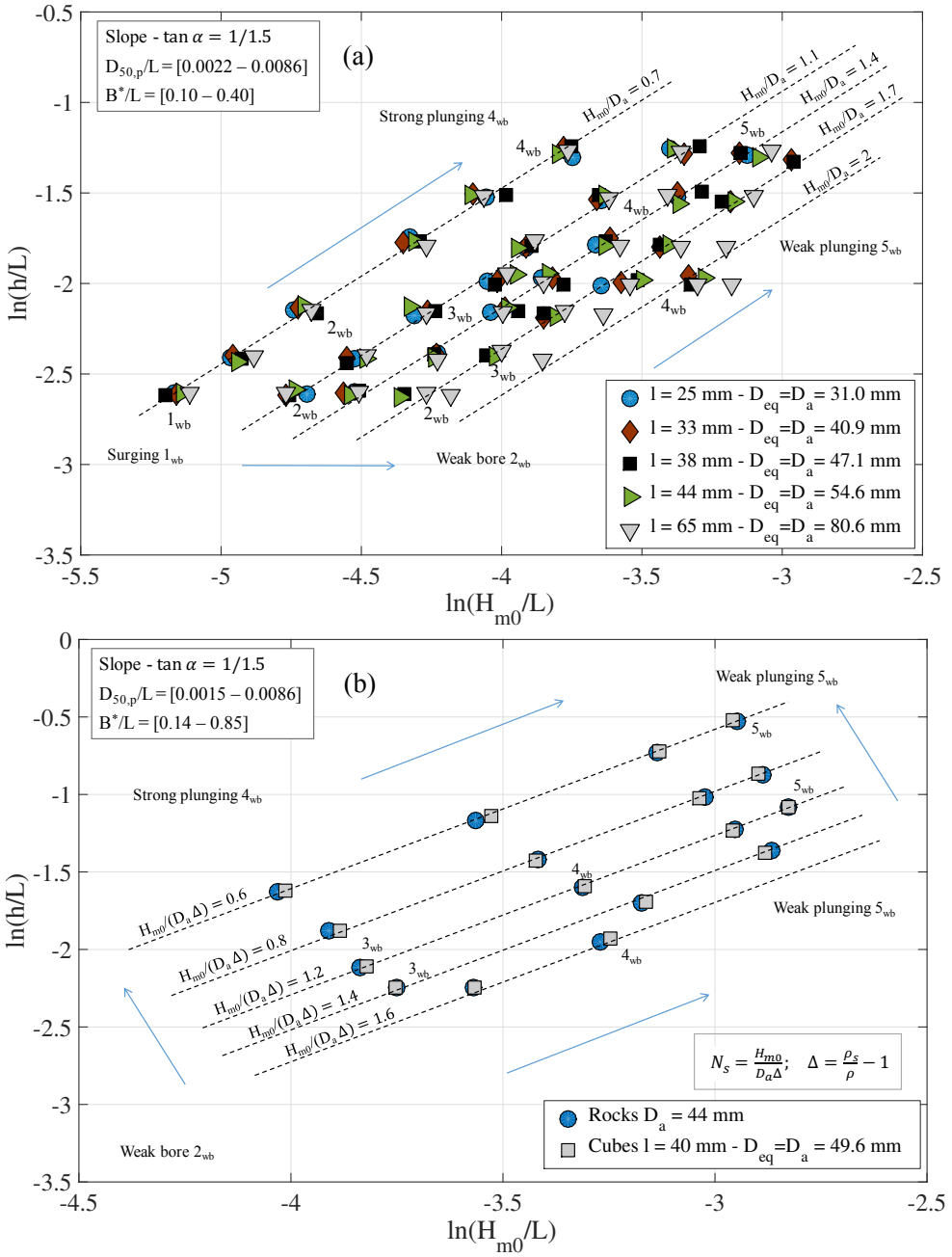

FIGURE 6.4: The log-experimental space $[\ln(h/L), \ln(H_{m0}/L)]$ of the experimental results obtained from (a) IISTA - University of Granada, and (b) Aalborg University. The dash line represents the best fit of H_{m0}/D_a and $H_{m0}/(\Delta D_a)$ for the data of IISTA-UGR and Aalborg University, respectively. The trajectory and the breaker type of some tests are also included.

The same behavior is observed in the experimental space of Aalborg data (Figure 6.4-b). The tests have been performed along approximately perpendicular lines at constant values of the Stability Number. It is observed that by including the submerged relative density, the data of the main armor composed by two layer of rocks is combined with the data of cubes. The most likely breaker type, with the same average Stability Number value, evolves as both h/L

and H_{m0}/L increase. However, the number of tests is smaller than those performed in the UGR wave flume, the experimental data are located in a smaller parallelepiped and, consequently, not all possible types of wave-breaking are observed.

6.3.1 Relative bulk dissipation in the main layer

Figure 6.5 shows the results of the bulk dissipation, D^*, for two sizes of cubes tested in the wave flume of IISTA-UGR. The x-axis represents the logarithmic transformation of the product $(h/L)(H_{m0}/L)$ to facilitate the visualization of the data. It is observed that the points are ordered according to isolines of H_{m0}/D_a. The curves are the result of a fit using splines. At very small water depths and very small wave steepness, the dissipation on the breakwater must be negligible. Hence, the dashed lines represent the estimated values of D^* taking into account that, when the product of $(h/L)(H_{m0}/L)$ decreases, the dissipation should asymptotically tend to negligible values.

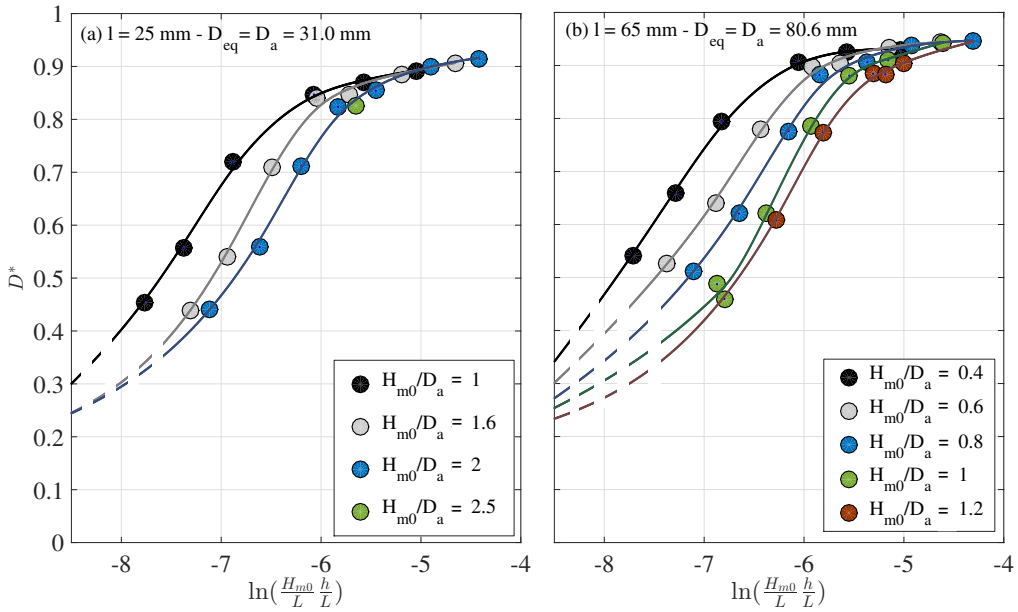

FIGURE 6.5: The bulk dissipation results against the log-transformation of the product $(h/L)(H_{m0}/L)$ for two sizes of cubes tested in the wave flume of IISTA-UGR: (a) Size of $l = 25$ mm and $D_{eq} = D_a = 31.0$ mm, (b) Size of $l = 65$ mm and $D_{eq} = D_a = 80.6$ mm. The results are grouped according to isolines of H_{m0}/D_a. The solid lines represent the fit spline curve and the dashed lines marks the estimated values of bulk dissipation for a small values of $\ln[(h/L)(H_{m0}/L)]$.

The three regions of wave energy transformation described in previous chapters are also identified. Isolines converge in the dissipation-dominated, regardless of H_{m0}/D_a value, and the most likely breaker type is strong or weak plunging. The dissipative process is essentially dominated by the wave evolution and eventually wave-breaking on the free surface of the slope. For small values of $(h/L)(H_{m0}/L)$, the curves converge to negligible dissipation values, and the reflection in the slope and in the porous core is the main process of wave energy transformation. In this reflected-dominated region, the most likely breaker types are surging and weak bore. The transition region extends between the two domains (reflective and dissipative). In it, the bulk dissipation decreases significantly in a small range of $(h/L)(H_{m0}/L)$, and this decreasing is greater with greater values of H_{m0}/D_a. In this regime the most likely types of wave-breaking move from weak bore to strong plunging.

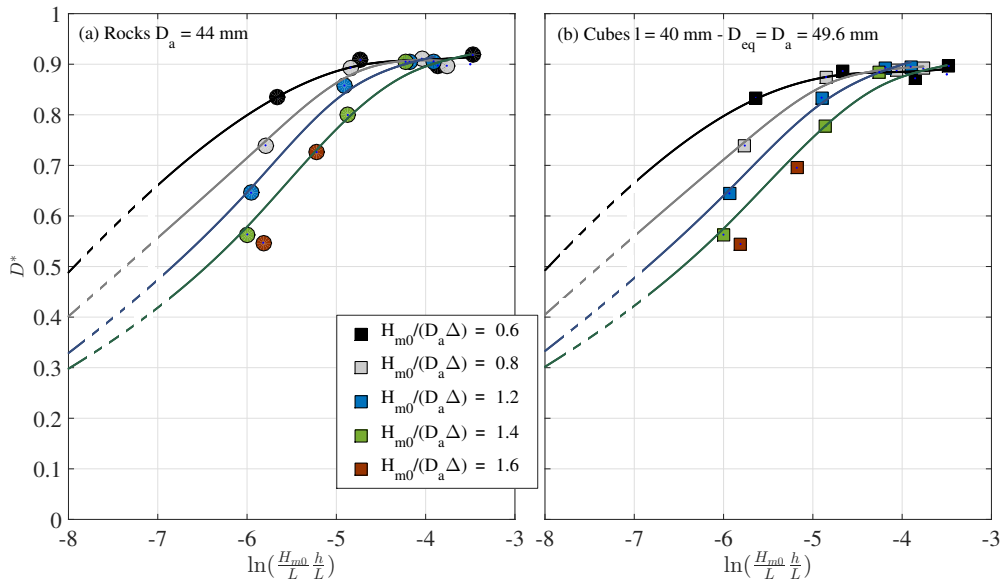

FIGURE 6.6: The bulk dissipation results against the log-transformation of the product $(h/L)(H_{m0}/L)$ for two types of unit pieces tested in the wave flume of Aalborg University: (a) Rocks $D_a = 44$ mm, (b) Cubes $l = 40$ mm and $D_{eq} = D_a = 49.6$ mm. The results are grouped according to isolines of the Stability Number, $N_s = H_{m0}/(\Delta D_a)$. The solid lines represent the fit spline curve and the dashed lines marks the estimated values of bulk dissipation for a small values of $\ln[(h/L)(H_{m0}/L)]$.

Figure 6.6 shows the results of the bulk dissipation, D^*, for the two types of unit pieces tested in the wave flume of Aalborg University. As for the experimental results of IISTA-UGR, the bulk dissipation is ordered according to isolines of the Stability Number, N_s. The three regions of wave energy dissipation are also identified with the same tendency of breaker types. In the transition region, the bulk dissipation decreases significantly in a small range of $(h/L)(H_{m0}/L)$, and this decreasing is greater with greater values of N_s.

Figures 6.7 and 6.8 represents the bulk dissipation difference between breakwaters with different size or type of unit pieces for the main armor layer. According to Equation 6.3, this result can be associated with the different dissipation that the same wave train experiences in each main armor layer. For the experimental results of the main armor composed by two layer of cubes (IISTA-UGR, five different sizes), the dissipation differences between the armor constructed with the larger size, $l = 65$ mm, and the other four sizes of cubes is calculated (Figure 6.7). The dissipation difference in the armor of cubes is negligible in the dissipation-dominated and reflection-dominated regions and it is maximum in the transition region. This maximum occurs in approximately the same values of $(h/L)(H_{m0}/L)$ in both Figures 6.7-a and 6.7-b , but its value depends on H_{m0}/D_a.

In the case of Aalborg data, the difference between the two main armor tested, two layers of rocks and cubes, has been calculated for $N_s = 0.6$ (Figure 6.8-a) and $N_s = 0.8$ (Figure 6.8-b). The experimental data is overlapped on the same isoline of the Stability Number. Therefore, a main armor constructed with rock of $D_a = 44$ mm and another with cubes of $D_a = D_{eq} = 49.6$ mm dissipate the same amount of incident energy for the entire range of $(h/L)(H_{m0}/L)$.

6.4 Discussion

In this Chapter 6, the energy dissipation processes of the incident wave train when it interacts with a mound breakwater with slope angle 1:1.5 is analyzed and, in particular, the process

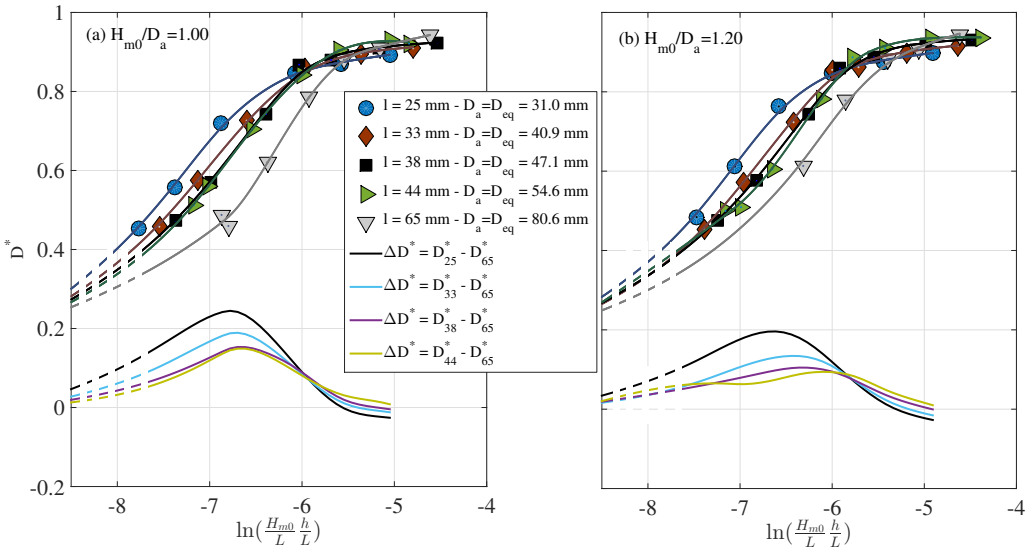

FIGURE 6.7: The bulk dissipation results against the log-transformation of the product $(h/L)(H_{m0}/L)$ for all the cubes tested in the wave flume of IISTA-UGR according to (a) isolines of $H_{m0}/D_a = 1.00$, (b) isolines of $H_{m0}/D_a = 1.20$. The solid lines represent the fit spline curve and the dashed lines marks the estimated values of bulk dissipation for a small values of $\ln[(h/L)(H_{m0}/L)]$. The solid lines with values of $D^* < 0.3$ represent the dissipation difference between the armor constructed with the larger size, $l = 65$ mm, and the other four sizes of cubes.

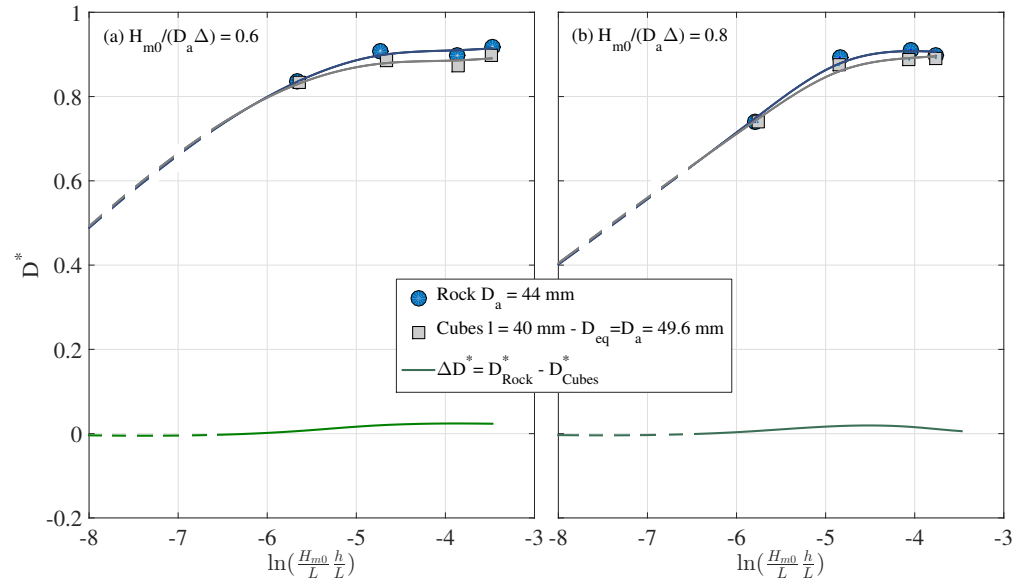

FIGURE 6.8: The bulk dissipation results against the log-transformation of the product $(h/L)(H_{m0}/L)$ for cubes and rocks tested in the wave flume of Aalborg University according to (a) isolines of $N_s = H_{m0}/(\Delta D_a) = 0.6$, (b) isolines of $N_s = H_{m0}/(\Delta D_a) = 0.8$. The solid lines represent the fit spline curve and the dashed lines marks the estimated values of bulk dissipation for a small values of $\ln[(h/L)(H_{m0}/L)]$. The green solid line represents the dissipation difference between the rocks and the cubes.

related to the interaction with the main armor layer and the dependence of type, shape and size of the unit piece has been quantified. This section discusses the aspects of the experimental results related with (1) the evolution of the type of wave-breaking in the sample space of h/L and H_{m0}/L, (2) the relevance of the roughness parameter of the main armor layer, and (3) the connection between the dissipation and the stability parameter of the piece.

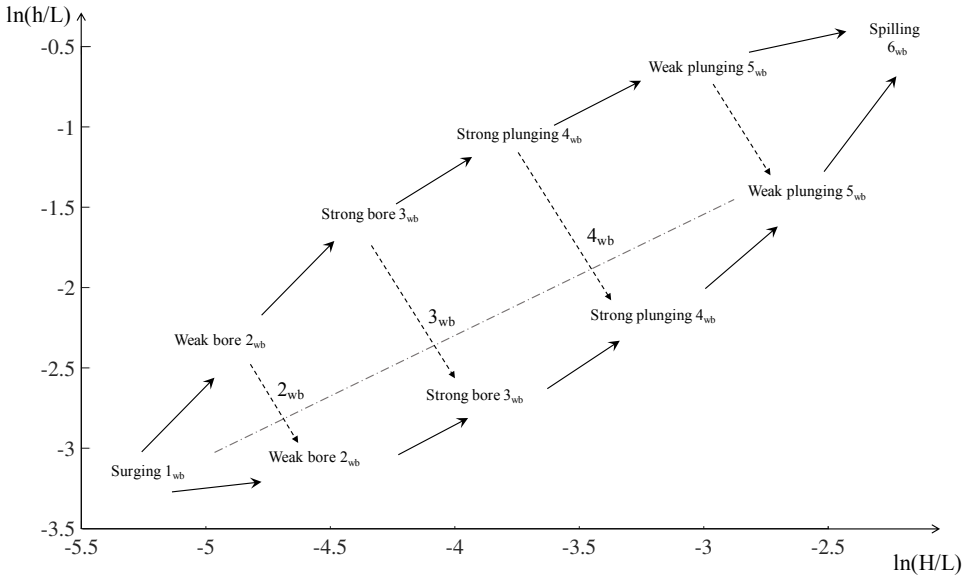

FIGURE 6.9: Scheme of the evolution of the most probable breaker types observed in a mound breakwater. The breaker types are represented in a theoretical log-transformation experimental space [$\ln(h/L)$, $\ln(H_{m0}/L)$] within the ranges of values corresponding to wind waves. The solid arrow follows the isolines of H_{m0}/D_a; the dashed arrows follows the isolines of same breaker type; and the dash-dotted line represents a "determined" relation of h/L and H_{m0}/L.

Figure 6.9 shows, in the log-transformation experimental space [$\ln(h/L)$, $\ln(H_{m0}/L)$], a scheme of the evolution of the most probable types of wave-breaking that can be observed in mound breakwater. As the dimensional analysis indicates, as well as the experimental results of the previous chapter, this scheme depends on the geometric characteristics of the core, mainly width and core diameter (B^*, $D_{50,p}$). The evolution (trajectory) of the breaker type depends on how the "progress" is made in the log-transformation experimental space. Among the many possible options, Figure indicates 6.9 three that are relevant in the behavior of breakwaters:

Case (a): To advance simultaneously increasing h/L and H_{m0}/L but keeping H_{m0}/D_a constant. These trajectories are the sides of the parallelepiped (Figures 6.4-a and 6.4-b). Depending on the start value of $[h/L, H_{m0}/L]_0$, it is possible to traverse all the breaker types, that is: surging $\rightarrow$ weak bore $\rightarrow$ strong bore $\rightarrow$ strong plunging $\rightarrow$ weak plunging and, eventually (only with slopes very stretched), spilling. The higher H_{m0}/D_a value, the lower the possibility of observing the entire spectrum of wave-breaking.

Case (b): To advance with a given relationship, monotonic increasing values, of h/L and H_{m0}/L, for example a diagonal of the parallelepiped. This is the usual trajectory when laboratory tests are performed to study the stability of the armor pieces or the flux on the slope (run-up and run-down) (Moragues et al., 2019c).

Case (c): To advance with a certain relation, decreasing value of h/L and increasing vale of H_{m0}/L, so that the breaker type does not change. If H_{m0}/L remains constant, that is, the Iribarren number is preserved, the trajectory is parallel to the y-axis (h/L). Depending on the

starting point, it is possible to observe a single type of breaker, or several of them. To collect, in this particular case, the dependence on H_{m0}/D_a, (type of piece of the main armor), it is necessary to vary H_{m0}, and consequently L to keep the wave steepness. If the water depth in the laboratory test is constant, the observable breaker types is defined a priori.

It is interesting from an engineering point of view to compare the behavior of a breakwater tested with a "reference breakwater". In the case of dissipation due to the evolution of the free surface on the slope and the interaction with the main armor, a reference breakwater is the impermeable and smooth mound breakwater with the same slope as the one tested. Figure 6.10 shows the isolines of N_s constant for the main armor layer composed by two layer of cubes tested in Aalborg University. The curve splines of two impermeable slopes, with slope angle 1:2 (numerical results showed in 4) and 1:1.5, which, theoretically, correspond to values of $D_a/H \approx 0$, are also included. The dissipation spectrum develops in a very small range of $(h/L)(H_{m0}/L)$ with all the possible breaker types. Outside this range of variability, the impermeable slope only offers perfect reflection or total dissipation. It is evident that the presence of the main armor and the porous core provides greater flexibility to transform the incident wave energy and to control the mass water flow and the forces on the wall.

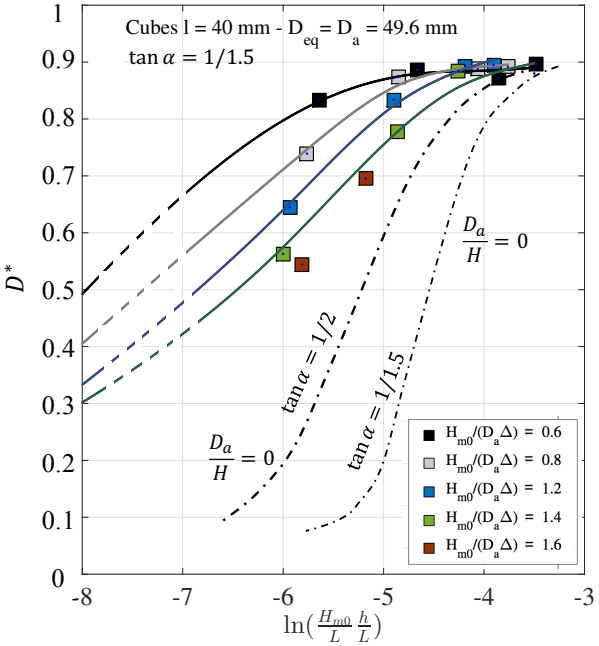

FIGURE 6.10: The bulk dissipation results of Aalborg University against the log-transformation of the product $(h/L)(H_{m0}/L)$ for the main armor layer composed by cubes of $l = 40$ mm and $D_{eq} = D_a = 49.6$ mm. The solid lines represent the fit spline curve according to isolines of the Stability Number, $N_s = H_{m0}/(\Delta D_a)$. The dash-dotted lines marks the tendency of the curve spline for two impermeable mound breakwaters with slopes 1:1.5 and 1:2, following the isoline of $D_a/H = 0$.

Dimensional analysis provides a functional relationship between dimensionless variables without indicating its shape. In this work it has been shown that (Equation 6.7) there is a relationship between the bulk dissipation and the stability number of the piece as follows:

$$D^* = \Psi\left(\frac{h}{L}, \frac{H_I}{L}, \frac{D_{50,p}}{L}, \frac{B^*}{L}, \frac{e}{L}, R_{e,D_a}, N_s\right)$$

This relationship depends on the experimental space $[h/L, H_{m0}/L]$ and is modulated by the characteristics of the core and the main armor: number of layers, shape and placement

criterion that determine, among others, the porosity of the main armor. Bagnold (1946) assumed that the dynamic transport rate is related primarily to the available fluid power, as in all other modes of transport. Then, Losada and Desire (1985) related the dissipation rate of energy on the bottom boundary layer to the length and velocity scales of the large-scale turbulence to obtain a relationship for the initiation of motion of sediments on a horizontal bed under oscillatory motion. The result of the dimensional analysis recovers the Bagnold's model and also indicates the dimensionless variables.

By increasing H_{m0}/D_a and using unit pieces that are placed very compacted, the behavior of the breakwater is close to the behavior of an impermeable slope with a very small transition region, namely small range of $(h/L)(H_{m0}/L)$ (e.g. the acropods type of unit). On the contrary, by reducing H_{m0}/D_a, the behavior of the breakwater widens and more if the porosity of the main armor is greater. In this case, it is advisable not to forget the experience with large-scale of breakwater composed by "dolos" that generate tensile stresses incompatible with the material of the construction.

6.5 Conclusions

In this chapter a further step is taken in the study of the sources of dissipation in the main armor layer of the mound breakwater, and the biunivocal correspondence between the value of I_r, and the breaker type is discussed. For this, the dimensional analysis is reviewed to construct the complete set of independent variables. In addition, the Π-Buckingham theorem is applied in order to properly construct groups of dimensionless variables taking into account those that remain constant in an experiment, a group or in all experiments. Moreover, this work is supported by two series of data obtained experimentally in the wave flume of Aalborg University and also in the wave flume of IISTA - University of Granada. These experimental data allowed calculating the bulk wave dissipation of different sizes and type of pieces for the main armor layer. The experimental technique of Aalborg University is analogous to that followed in the IISTA and the analysis of the records adapts to the methods implemented by that laboratory (Aalborg University, 2007b). In the case of the IISTA-UGR each experiment is performed with a constant period and varying the wave height in each run. In the case of Aalborg, the tests are executed trying to keep the wave steepness of incident wave train (Iribarren number) constant.

The following conclusion can be derived from this study:

1. In the case of the experimental tests performed in the wave flume of IISTA-UGR, the experimental space are organized around lines parallel to the x-axis based on a constant h/L value. The constant H_{m0}/D_a lines relate the tests that satisfy that condition by varying h/L and H_{m0}/L monotonically.

2. The constant H_{m0}/D_a lines determine an evolution of the breaker type in the sense of surging to weak plunging. The spectrum of breaker types is complete, partial or with a single type, depending on the start and end points of the test defined by h/L and H_{m0}/L. Lower values of H_{m0}/D_a offer a higher probability to observe all the breaker types.

3. The experimental technique of Aalborg University of keeping constant the Iribarren number is represented in the experimental space by trajectories parallel to the y-axis, that is, $\ln(h/L)$. The starting point determines the breaker types that can be observed. In addition, the physical limitations of the generation system and its control, make it difficult to comply with the constant Iribarren number requirement, so it cannot be assured that the experimentation collects all types of wave-breaking.

4. The dissipation of the incident energy in the main armor with different sizes of cubes is relevant at specific intervals of $(h/L)(H_{m0}/L)$, related to the transition region and the breaker type, from weak bore to strong plunging. The difference is negligible in the reflective and dissipative domains.

5. The dissipation of the incident wave train in the main armor composed by rocks and in the main armor with cubes, both tested in Aalborg University, have in practice, the same bulk dissipation over the entire range of $(h/L)(H_{m0}/L)$.

6. The number of stability of the piece (rocks or cubes) and the dissipation in the main armor are functionally related and its relation depends on h/L, H_{m0}/L, the characteristics of the porous core, B^*, $D_{50,p}$, and the slope angle of the breakwater.

Conclusions and future research lines

Conclusions

The overall objective of this thesis is to improve the theoretical analysis and characterization of the hydraulic performance of mound breakwaters and its interaction with wind-waves and the seabed. Part of the complexity in modeling and characterizing the wave-breakwater-seabed interaction, is due to the fact that both wave-breakwater interaction and wave-seabed interaction are not still completely characterized. Consequently, to achieve this overall objective, a general framework was defined that allowed studying each part of the wave-breakwater-seabed interaction separately, namely: (Part I) on the breakwater seabed, (Part II) on the breakwater performance. The first part encompasses a theoretical study based on a review and analysis of the processes that arise around the seabed under the sea oscillatory regime action and its impacts on breakwaters. The second part is focused on the improvement of hydraulic performance of breakwaters under wind-waves action from an analytical approach combined with numerical and physical experimentation. Based on the results derived from each specific objective, the following main conclusions are drawn:

- Objective 1: *To review and describe the behavior and geotechnical problems of soft soils against wind-waves action and to propose practical recommendations for the design and experimentation of breakwaters on soft seabeds.*

  A review of the properties and rheological models that arise in the wave-seabed interaction is presented in this study. Although these models have a high degree of uncertainty, it is possible to classify, depending on the soil compaction degree, that non-cohesive or partially cohesive soft soils behave according to a pore-elastic or pore-elastoplastic model. For soft cohesive soils, the best model that suits the behavior of the soil under wave action is the visco-elastic model.

  The geotechnical failures modes on seabeds under the excess pore pressure due to the wave action and the presence of the breakwater are the liquefaction or fluidization phenomenons. The surface erosion is also an important failure mode which is one of the most frequent problems in coastal areas and in the vicinity of the breakwaters.

  Some recommendations are also included in this chapter to propose practical guidelines for the design and maintenance of breakwaters on soft seabeds. Seabed with 40% or more clay content is the threshold to considered inadmissible the seabed as a foundation of breakwaters and should be dredged and filled by other materials. On the other hand, for seabeds with less than 40% clay content, it is advisable and necessary to always carry out a treatment according to the maximum probability of failure by surface erosion and/or liquefaction and fluidization.

- Objective 2: *To deepen in the behavior of dynamic marine-seabed interaction from improving the modeling of sediment transport, cohesive and non-cohesive, under the action of sea oscillations.*

A model is proposed to determine the sediment transport rate generated by the combined action of sea waves and tidal currents, the latter being modeled as a sequence of steady currents because of the large values of the Keulegan-Carpenter number of the tidal flows, which allow neglecting inertial effects in their modeling. The sediment behavior under wave-current interaction is described by means of an integrated numerical model that includes both a hydrodynamic module and a sediment transport module. The hydrodynamic module solves Reynolds-averaged momentum equations by introducing the turbulence model of Menter et al. (2003), which solves the problem from the sea bottom up to the free-surface including the buffer layer and the viscous sublayer, when the bottom behaves like a smooth wall. Hence, the turbulence model of Menter et al. (2003) appears to properly describe the structure of turbulence flow within the boundary layer generated by propagating sea waves, both close to the bed and far from it, and the evaluation of the velocity profile in the near-bed region turns out to be accurate. The sediment transport module determines the sediment concentration and sediment transport for a mixture of non-cohesive and cohesive sediments.

The model is validated with laboratory measurements and field data collected over rippled beds at two different tidal estuaries. Moreover, it is applied for values of the parameters chosen to mimic a site close to Punta Umbría (Huelva, Spain) and considering different hydrodynamic conditions and different sediment mixtures. The influence of the waves on the suspended sediment concentration is lower for the cohesive fraction than for the non-cohesive fraction. For all the sediment mixtures, it turns out that the cohesive fraction is well mixed over the whole water depth, meanwhile the concentration of the non-cohesive fraction has significant values only near the bottom. The latter shows that an accurate description of turbulence dynamics in the buffer layer and viscous sublayer (if it exists) is important to quantify the sediment transport rate.

- Objective 3: *To apply dimensional analysis for studying the physical processes that dominate the wave energy transformation on mound breakwater, impermeable and permeable.*

  The dimensional analysis is applied to determine the functional relations between the dimensionless independent quantities and dependent quantities of the first and second kind. Linear theory provides the freedom (not arbitrary) necessary to apply the dimensional analysis, which involves the following four stages: (1) identification of a complete set of n independent quantities; (2) selection of a complete subset of k_π dimensionally independent quantities; (3) definition of $(n-k_\pi)$ independent quantities, based on the power products of the k_π quantities selected; and (4) application of the Π-Buckingham theorem to express dependent quantities as a function of the $(n-k_\pi)$ independent quantities.

  In this work, the first kind of dependent variables are the total reflected wave energy per unit horizontal surface, E_R, and (if the breakwater is permeable) the total transmitted wave energy per unit horizontal surface, E_T. The second kind is the total dissipation rate, D^*, which is obtained from the first kind quantities by the energy conservation equation. The complete subset of dimensionless independent quantities is $\{\rho, g, L\}$ ($k_\pi = 3$) and the remaining independent variables of the set to obtain the similarity equation depend on the composition of the slope. In the case of an impermeable slope, the application of dimensional analysis resulted in the independent variables: the relative water depth, h/L, the wave steepness, H_I/L, and the Reynolds number in the water column, $R_{e,w}$. In the case of a permeable slope composed only by a porous core, in addition to $\{h/L$, H_I/L, $R_{e,w}\}$, the experimental design includes: the relative granular core diameter,

$D_{50,p}/L$, the relative characteristic width, B^*/L, and the grain Reynolds number, R_{ep}. If the permeable slope is composed by a main armor layer and a core, to the previous sets of independent variables is added: the relative diameter of the main armor, D_a/L, the relative thickness expressed by $e = n_l D_a/L$, and the armor Reynolds number, R_{e,D_a}. The slope angle is considered as an identificative parameter of the problem.

- Objectives 4: *To collate the dependence of the experimental results of wave energy transformation and wave-breaking with Iribarren number.*

  The physical and numerical results of wave energy transformation modes, (K_R^2, K_T^2,D^*) obtained for the impermeable slope and the permeable slope with main armor are compared with the Iribarren number calculated with the incident wave height, $I_{r,I}$. For the impermeable slope, the variability of each slope angle tested is significant with slight changes in the value of $I_{r,I}$. This variation partially stems from small variations in the incident wave height H_I. Nevertheless, local scattering for $I_{r,I}$ intervals did not decrease when the set of wave trains corresponding to a value of $I_{rtarget}$ was repeated. Since the slope is impermeable, this local scattering suggests that, the behavior of the K_R^2 values depends on breaker type, and it seems that Iribarren number does not capture this process. For the permeable slope with main armor, similar to behavior of the impermeable slope, the experimental scattering increases with $I_{r,I}$ and is significant with slight changes in the value of $I_{r,I}$. The same value of the Iribarren number have different energy transformation modes and, consequently, the potential breaker types. Since the slope is permeable, this local scattering can be attributed to: (i) wave-breaking on the slope, (ii) wave interaction with the main armor layer, and (iii) wave propagation through the porous core.

  The results for the permeable and impermeable slopes show that the transformation of incident energy on an undefined slope roughly depends on I_r, with a great dispersion of the experimental data. This variability grows when the reflection is relevant in the wave transformation process on the slope. Small variations in the wave height causes significant variation in the breaker type. This variability in the energy transformation mode and breaker type can occur with a constant wave steepness value, in other words, when the Iribarren number remains constant. Hence, there is not a biunivocal relationship between I_r and the type of breaker, except in the dissipation-dominated region, with weak plunging and spilling breakers.

- Objectives 5: *To analyze the experimental variability and study the influence of the physical variables that characterize the hydraulic performance of mound breakwaters.*

  From the dimensional analysis, the independent variable chosen, which represents the incident wave train and allows fitting a similar sigmoid curve, is: $(h/L)(H_I/L)$. For the impermeable slope, the reflected energy coefficient, K_R^2, and the dissipation rate, D^* can be expressed by a similar sigmoid function for each slope tested, whose variable shows values of $(h/L)(H_I/L)$ that identify three regions: (i) a reflection-dominated region; (ii) a dissipation-dominated region; (iii) a transition region between the two, in which reflection and dissipation processes compete with each other. When a value of $(h/L)(H_I/L)$ is selected in the reflection-dominated region, the breaker type can move in both directions between weak bore and surging. If the value is in the dissipation-dominated region, the move is between weak plunging and spilling. Finally, if the value is in the transition region, the local scattering increases and the breaker types move between strong plunging and strong bore.

For the permeable slope with a main armor layer and a porous core, when these results are compared with those for an impermeable slope with the same angle, significant changes are identified. The energy transformation regions are located in smaller intervals of $(h/L)(H_I/L)$ values, and in each region, the value of the reflected energy coefficient, K_R^2, is lower. The sigmoid functions, above all in the transition region, have different trajectories, depending on the relative width B^*/L and stone diameter $D_{50,p}/L$, with a greater scattering than in the reflected-dominated and dissipation-dominated regions. When a value of $(h/L)(H_I/L)$ is selected in the transition region, K_R^2 increases since the value of B^*/L decreases (when $D_{50,p}$ is constant, there was a simultaneous decreases in $D_{50,p}/L$) and there is a variation in the corresponding breaker type: weak bore, strong bore and strong plunging.

The results of the wave energy transformation modes and breaker types obtained for the homogeneous permeable slope were according to the previous ones and also allowed analyzing the influence of the geometrical variables in the hydraulic performance. The relative characteristic width keeps the hydraulic performance of the breakwater (regions and breaker types), namely the range of B^*/L values are grouped in the same intervals of $(h/L)(H_I/L)$ for the breakwater models tested with different width. As we expected, the slope angle is an identificative parameter which ordered the hydraulic performance of breakwater with similar curves for each slope tested. In the dissipation-dominated region, the saturation of the breakwater in laboratory is reached and the physical models dissipate and reflect practically the same. When the granular core diameter is very different between models, the range of $D_{50,p}/L$ values has a horizontal displacement for the breakwater with lower core diameter and higher width. For each region delimited by values of $(h/L)(H_I/L)$, the reflected energy and the dissipation rate increases and decreases, respectively, as B^*/L and $D_{50,p}/L$ decreases, and much more for the breakwater with lower core diameter and higher width. The latter spatial variation on the values of $(h/L)(H_I/L)$ and on the energy transformation modes could be explained by the variability of the flow regime inside the porous medium and the evolution of the breaker type.

- Objectives 6: *To propose a design methodology for its application in laboratory that identifies the wave generation requirements and the number of wave conditions to quantify the energy transformation on the breakwater.*

  The experimental design significantly improves when the experimental space was defined by taking logarithms of h/L and H_I/L. In this transformed design space, it is possible to identify the wave generation requirements in laboratory and the relevant points where there was a change of behavior in the wave train. The application of the log-experimental space $[\ln(h/L), \ln(H/L)]$ for the laboratory test of a conventional homogeneous permeable mound breakwater allowed designing experimental tests whose wave conditions (i) optimized the number of laboratory tests, (ii) fulfilled the design criteria between model-prototype and the wave generation requirements, and (iii) allowed identifying the regions of wave energy transformation and breaker types for intervals of $(h/L)(H_I/L)$.

- Objectives 7: *To describe the sources of wave energy dissipation on the main armor layer of mound breakwaters.*

  A further step is achieved with the study of the sources of dissipation in the main armor layer of mound breakwater, and with the discussion of the biunivocal correspondence between the value of Iribarren and the breaker type on the slope. For this, the dimensional analysis developed in the previous chapters is reviewed and a new complete set

of independent variables is constructed. In addition, the Π-Buckingham theorem is applied to properly group the dimensionless variables taking into account those that remain constant in an experiment, a group or in all the experiments. In addiction, this work is supported by two series of data obtained experimentally in the wave flume of Aalborg University and also in the wave flume of IISTA - University of Granada. These experimental data allowed calculating the bulk wave dissipation of different sizes and type of pieces for the main armor layer under irregular waves conditions. The experimental technique of Aalborg University is analogous to that followed in the IISTA and the analysis of the records adapts to the methods implemented by that laboratory. In the case of the IISTA-UGR each experiment is performed with a constant period and varying the wave height in each run. In the case of Aalborg, the tests are executed trying to keep the wave steepness of incident wave train (Iribarren number) constant.

The experimental results show that the dissipation of the incident energy in the main armor with different sizes of cubes is relevant at specific intervals of $(h/L)(H_{m0}/L)$, related to the transition region and breaker type, from weak bore to strong plunging. The dissipation difference is negligible in the reflected-dominated and dissipation-dominated regions. Finally, it is shown that the number of stability of the piece (rock or cube) and the dissipation in the main armor are functionally related and its relationship depends on h/L, H_{m0}/L, the characteristics of the core and slope of the breakwater. This result is relevant because it joins the design of the breakwater, clarifies and complements the role of the Iribarren number as the main variable, and helps to reduce the variability and uncertainty of the usual calculation formulas.

Future research lines

A set of lines of research that arise from various aspects addressed during the development of this thesis and that have been left open are presented below. These are related to the main parts in which this work has been structured.

Part I. On the breakwater seabed

- To implement a relatively simple analytical solution of the wave-structure-seabed interaction in numerical models, such as OPEN-FOAM, with direct application in the research and in the design project of the breakwater.
- To perform laboratory tests that properly characterize the wave-structure-seabed interaction, whose results could be validated with numerical models, as well as to serve as the feedback of current results.

Part II. On the breakwater performance

- To calculate analytically and with experimentation the local dissipation associated to: (i) wave-breaking on the slope, and (ii) wave interaction with the main armor layer.
- To study the failure mode “stability of armor unit” based on a dimensional analysis, which includes a relation with the Stability Number, N_S. The loss of stability will be mainly related with the breaker type on the slope and also with the interaction, friction and circulation, between the incident wave train and the main armor.
- To applied the proposed experimental design of the log-transformation space [$\ln(h/L)$, $\ln(H/L)$] to more physical models of breakwater with different slopes, diameters (core and armor) and widths. Irregular wave conditions will be applied to these laboratory

tests and the probability function of the breaker type associated to each irregular test will be calculated.

- To include the climate change projections in the experimental laboratory design and also in the dimensional analysis with the inclusion of scenarios of sea level rise in order to analyze future impacts on maritime structures. In this regard, the *Environmental Fluid Dynamics Group* of the University of Granada is actually working in this topic with the International Project, PROTOCOL (2020), and proceedings in National and International Congresses (Moragues et al., 2018; Díaz-Carrasco et al., 2018; Del-Rosal-Salido et al., 2019; Moragues et al., 2019b).

Appendix A

Analytical expressions for the sediment characterization

A.1 Empirical formulas for the sediment transport

Settling velocity

For non-cohesive sediment fraction, the settling velocity is affected by the value of the sediment concentration (hindering settling)

$$w^*_{s,nc} = \begin{cases} w^*_{s0,nc} & \text{if } c_{nc} < n_s \\ w^*_{s0,nc}\left(1 - \frac{c_{nc}}{c_{\max}}\right)^5 & \text{if } c_{nc} > n_s \end{cases} \tag{A.1}$$

where $w^*_{s0,nc}$ is the fall velocity for a single particle following Soulsby (1997) formulas; n_s is the sediment porosity; and $c_{\max}$ is the maximum volume concentration of suspended sediment. A value of $c_{\max} = 0.65$ is commonly used for a packed porous bed (Fredsoe and Deigaard, 1992).

For the cohesive sediment fraction, which includes mud particles and part of the silt fraction, the settling velocity is concentration-dependent and increases with the concentration because of the flocculation phenomenon. However, when the sediment concentration becomes larger ($c^*_c > 10$ g/l), in-situ measurements (Van Rijn, 1993; Chai et al., 2002; Winterwerp, 2002) confirms the decrease of the cohesive settling velocity because of the hindered effects. Therefore, in order to get an expression for practical applications, the cohesive settling velocity is assumed to be:

$$w^*_{s,c} = \begin{cases} k^*_m \left(c_{nd}\right)^{\gamma_{ws}} \left(1 - \frac{\tau^*_w}{\tau^*_{cr,e}}\right) \left[1 - \tanh(a\, c_{nd})\right] & \text{if } \tau^*_w < \tau^*_{cr,e} \\ 0 & \text{if } \tau^*_w \geq \tau^*_{cr,e} \end{cases} \tag{A.2}$$

where k^*_m (m/s), γ_{ws} and a are empirical constant, $c_{nd} = c_c \rho^*_s / c^*_{un}$ is the dimensionless concentration of cohesive sediment with c^*_{un} = 1 kg/m^3 (Stanev et al., 2007).

1. The expression $k^*_m \left(c_{nd}\right)^{\gamma_{ws}}$ is an empirical formulation proposed by several researchers (Stanev et al., 2007), and it represents the increase of the settling velocity because of the flocculation phenomenon.

2. The expression $\left(1 - \frac{\tau^*_w}{\tau^*_{cr,e}}\right)$ takes into account the sediment erosion ($\tau^*_w > \tau^*_{cr,e}$), which involves flocs-breaking by the flow, thus, no deposition of the sediment, and also verifies the continuity concentration equation at the bottom.

3. The expression $[1 - \tanh(a\, c_{nd})]$ is important for high concentrations and confirms the decrease of the settling velocity because of hindered effects.

Reference concentration

For a flat bed, the reference concentration c_a and the reference level y_a^* are computed, following Zyserman and Fredsoe (1994a) and Zyserman and Fredsoe (1994b), as:

$$c_a = \frac{0.331\,(\theta - \theta_{cr})^{1.75}}{1 + \frac{0.331}{0.32}\,(\theta - \theta_{cr})^{1.75}} \tag{A.3}$$

$$y_a^* = 2d_{nc}^* \tag{A.4}$$

where d_{nc}^* is the representative diameter of the non-cohesive sediment.

On the other hand, for a rippled bed, following Van Rijn, 1984b, we assume

$$c_a = 0.015 \frac{d_{nc}^*}{y_a^* R_p^{0.2}} \left(\frac{\theta - \theta_{cr}}{\theta_{cr}} \right)^{1.5} \tag{A.5}$$

$$y_a^* = \frac{\eta_r^*}{2} \text{ or } y_a^* = k_s^* \tag{A.6}$$

where $R_p = \frac{\sqrt{(s-1)g^* d_{nc}^{*3}}}{\nu^*}$ is the sediment Reynolds number; $s = \rho_s^*/\rho^*$ ($s = 0.65$) is the ratio between the sediment and water densities; η_r^* is the ripple height; θ is the Shields parameter and θ_{cr} is its critical value for the inception of the bed load (Soulsby, 1997).

Shields parameter

The general expression of the Shields parameter is:

$$\theta = \frac{\tau^*}{(s-1)g^* d_{nc}^*} \tag{A.7}$$

In this work, θ is calculated either by considering only the steady-current (θ_c) or the combined action of waves and the steady-current (θ). The bottom boundary conditions depend on the critical value of the shear stresses that, in the numerical solution, are computed with the following critical Shields parameters.

The suspended load can be empirically assumed to take place when the fall velocity of the sediment particles is smaller than the upward component of the turbulent fluctuations, which are supposed to be proportional to the shear velocity u_τ^* . The critical condition for the inception of the suspended load is thus

$$u_{\tau,cr}^* = w_{s0,nc}^*$$

Following the last critical condition, Van Rijn (1984b) suggests that the non-cohesive sediment is put into suspension when the shields parameter is higher than the following critical shields:

$$\theta_{cr,susp} = 0.4^2 \left(\frac{w_{s0,nc}^*}{\sqrt{(s-1)g^* d_{nc}^*}} \right)^2 ;\ R_p > 31.62$$

$$\theta_{cr,susp} = 16 R_p^{-4/3} \left(\frac{w_{s0,nc}^*}{\sqrt{(s-1)g^* d_{nc}^*}} \right)^2 ;\ R_p \leq 31.62$$

For the bed load, there are a lot of empirical expression for critical shields parameter. The predictors of the critical value of the Shields parameter are affected by a large uncertainty. In

this work, we use the formulation of Soulsby (1997), which provides similar results as the formulation of Van Rijn (1984a).

$$\theta_{cr} = \frac{0.3}{1+1.2R_p^{3/2}} + 0.055\left(1-\exp(-0.02R_p^{3/2})\right) \tag{A.8}$$

A.2 Menter turbulence model

Menter's turbulence model is not intrinsically better than other turbulence models but it can be easily applied to the region closest to the bottom in such a way that the no-slip condition and the vanishing of the turbulent kinetic energy can be enforced at the bottom. Indeed, Menter's turbulence model is based on Wilcox's model (Wilcox, 1988) in the bottom region and gradually shifts to the $k-\varepsilon$ model far from it. Therefore, it fairly describes turbulence dynamics in the whole water column without the need to introduce damping functions, as usually made in the "low-Reynolds $k-\varepsilon$" models. Incidentally, different "low-Reynolds $k-\varepsilon$" models exist to deal with the smooth bottom case but, to the authors' knowledge, the only "low-Reynolds $k-\varepsilon$" model able to deal with rough walls is that proposed by Foti and Scandura (2004). The use of such a model might provide data for a better parametrization of the sediment transport rate generated by the simultaneous presence of waves and currents when the bottom is made by both non-cohesive and cohesive sediments.

The model constants σ_k, σ_ω, $\sigma_{\omega 2}$, β_ω, β_k and γ are obtained by simple linear superposition of their values for the $k-\omega$ and $k-\varepsilon$ models (see Table A.1).

Turbulence model	σ_w	σ_k	β_ω	β_k	γ
Wilcox model (ψ_1)	0.5	0.85	0.075	0.9	0.556
$k-\varepsilon$ model (ψ_2)	0.856	1	0.0828	0.9	0.44
Menter model (ψ)	$= F_1\psi_1 + (1-F_1)\psi_2$				

TABLE A.1: Parameters set up for $k-\omega$ turbulence model of Menter et al., 2003.

Let us consider the generic constant and let us denote with ψ_1 its value in the $k-\omega$ model and with ψ_2 its value in the $k-\varepsilon$ model. The corresponding value of ψ in the Menter's model is provided by

$$\psi = F_1\psi_1 + (1-F_1)\psi_2 \tag{A.9}$$

The blending function F_1 is defined as

$$F_1 = \tanh[(\arg_1)^4] \tag{A.10}$$

where

$$\arg_1 = \min\left[\max\left(\frac{\sqrt{k}}{0.09\omega y}; \frac{500}{y^2\omega R_\delta}\right), \frac{4\sigma_{\omega 2}k}{CD_{k\omega}y^2}\right] \tag{A.11}$$

$$CD_{k\omega} = \max\left(2\sigma_{\omega 2}\frac{1}{\omega}\frac{\partial k}{\partial y}\frac{\partial \omega}{\partial y}, \frac{10^{-9}}{R_\delta^2}\right) \tag{A.12}$$

Moreover, the production terms P_k and P_ω in Equations 2.5 and 2.6 are given by

$$P_k = \min\left(\frac{1}{2}\nu_T\left(\frac{\partial U}{\partial y}\right)^2, \frac{1}{2}0.9\omega k R_\delta\right) \tag{A.13}$$

$$P_\omega = \min\left(\frac{1}{2}\left(\frac{\partial U}{\partial y}\right)^2, \frac{1}{2}0.9\frac{\omega}{XG}\right) \tag{A.14}$$

where

$$XG = \frac{\nu_T}{R_\delta k} = \min\left(\frac{1}{\omega}, \frac{a_1}{\left|\frac{\partial U}{\partial y}\right| F_2}\right) \tag{A.15}$$

$$a_1 = 0.31$$

$$F_2 = \tanh[(\arg_2)^2] \tag{A.16}$$

$$\arg_2 = \max\left(\frac{2\sqrt{k}}{0.09\omega y}, \frac{500}{y^2\omega R_\delta}\right) \tag{A.17}$$

Appendix B

Wave-breaking by wave-structure interaction

B.1 Wave-breaking on an impermeable slope

Battjes (1974) established the dependence of the reflection coefficient on an impermeable slope with the Iribarren number and justified the classification, amply accepted, of the following breaker types in terms of this parameter:

- Spilling ($I_r < 0.5$): the wave energy dissipation on the slope is gradual. It is common in very gentle slopes. This type of breaker was not observed in the physical and numerical experimental tests of this study.
- Plunging ($0.5 < I_r < 2.5$): this breaker type is characterized by the asymmetry that acquires the crest of the wave and the curls that occur in it. The front of the crest first becomes almost vertical, then the crest advances to the front and finally falls with great turbulence. Much of the energy dissipates in this process and another part is used to form a "new wave" (jet).
- Bore (collapsing) ($2.5 < I_r < 3.5$): the front of the wave that advances over the slope tends to get vertical, but it loses stability and its bottom face collapses.
- Surging ($3.5 < I_r$): the base of the wave moves fast and does not allow the crest to evolve. As a result, the wave almost does not break and there is very low wave dissipation.

In the last 20 years, some numerical studies of wave-breaking on a smooth impermeable slope by means identified, in the interval $1.5 < I_r < 3.5$, four breaker types: weak plunging and strong plunging (Lakehal and Liovic, 2011) and weak bore and strong bore (Zhang and Liu, 2008). For the results and discussion of our work, the following aspects are relevant:

- A strong plunging breaker (as opposed to a weak plunging one) is characterized by an overturning jet, in which the front face of the wave becomes vertical and the crest curls over and plunges into the water ahead. The turbulence thus occupies the entire water column and dissipates in each wave cycle (Ting and Kirby, 1996).
- In a strong bore, the front face of the wave curls and collapses at some point between the crest and the trough. It then curls over and traps air, thus forming a wedge, which slows the collapse of the wave (Zhang and Liu, 2008).
- In a weak bore, the front face of the wave has a "D-shape". The collapse of the wave generates a tongue of water that goes up the slope. During this process, there is only a little turbulence and the movement of the water mass is more or less parallel to the slope.
- The run-up and run-down in a strong plunging breaker and a strong bore are similar, but those of a strong plunging breaker are usually of larger amplitude.

As we mentioned in Chapter 4, to analyze the possible breaker types in each wave transformation region, we adopt the expanded list that subdivides the breakers into weak and strong types of plunging breaker and bore (or collapsing). Figure B.1, shows the breaker sequence: spilling, weak plunging, strong plunging, strong bore, weak bore, and surging. These results provide a detailed picture of the spatial-temporal evolution of the wave on the slope and help to clarify the origin of the variability and experimental scattering of the results obtained in the experiments.

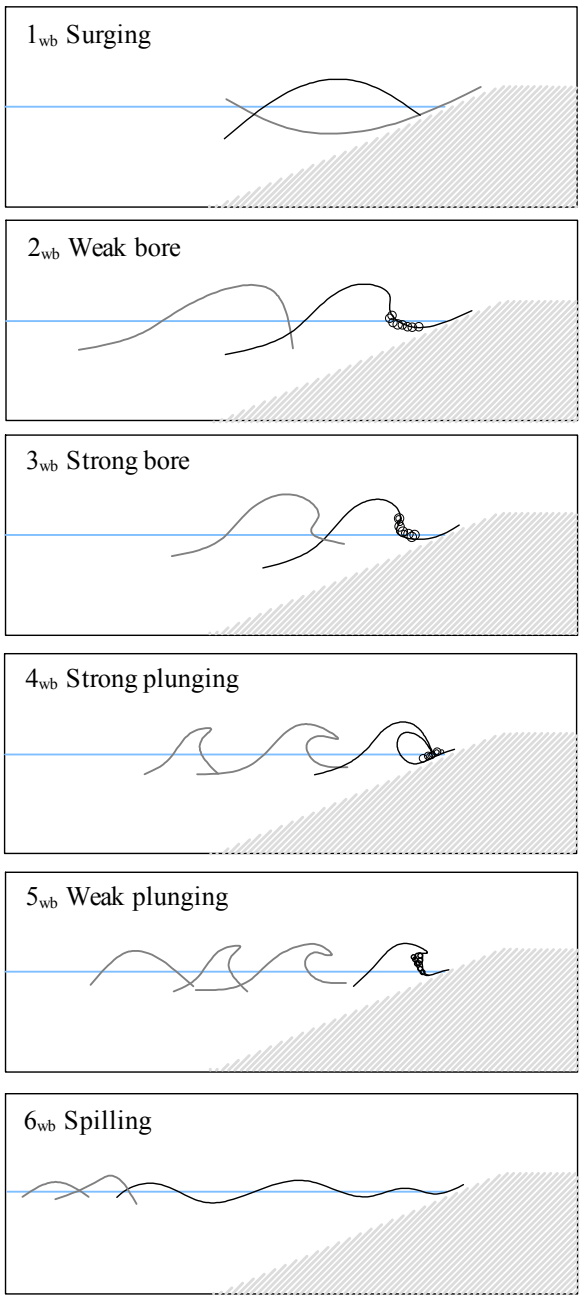

FIGURE B.1: Sequence of wave breaker type: spilling, weak plunging, strong plunging, strong bore, weak bore, and surging, The number j_{wb} ($j = 1 : 5$) identifies the wave breaker types on the slope marked in Figures 4.7, 4.9 and 4.13.

B.2 Wave-breaking in experimental tests

The breaker type on the slope is an essentially non-linear process (Battjes, 1974), and depends on how the test is specified, maintaining H and varying T or vice versa. The transition from one breaker type to another can be sudden or gradual, and can occur with different value pairs of H_I/L and h/L, and also with the same wave steepness (constant I_r). Hence, as we analyzed in Chapter 4, there is not a biunivocal relationship between I_r and the type of breaker.

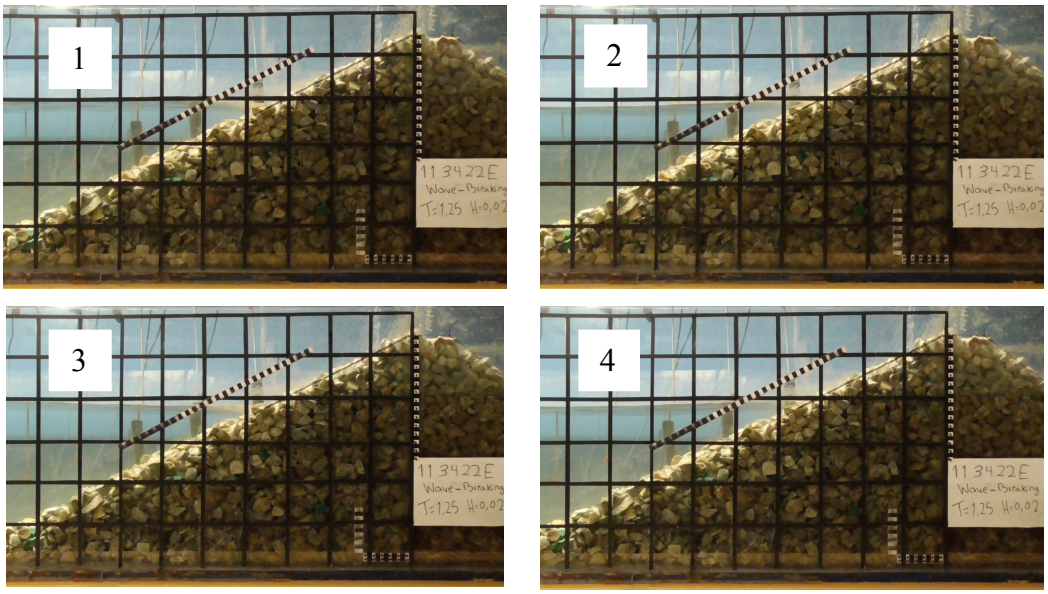

FIGURE B.2: Surging breaker type (1_{wb}) with $T_{target} = 1.25$ s and $H_{target} = 0.02$ m.

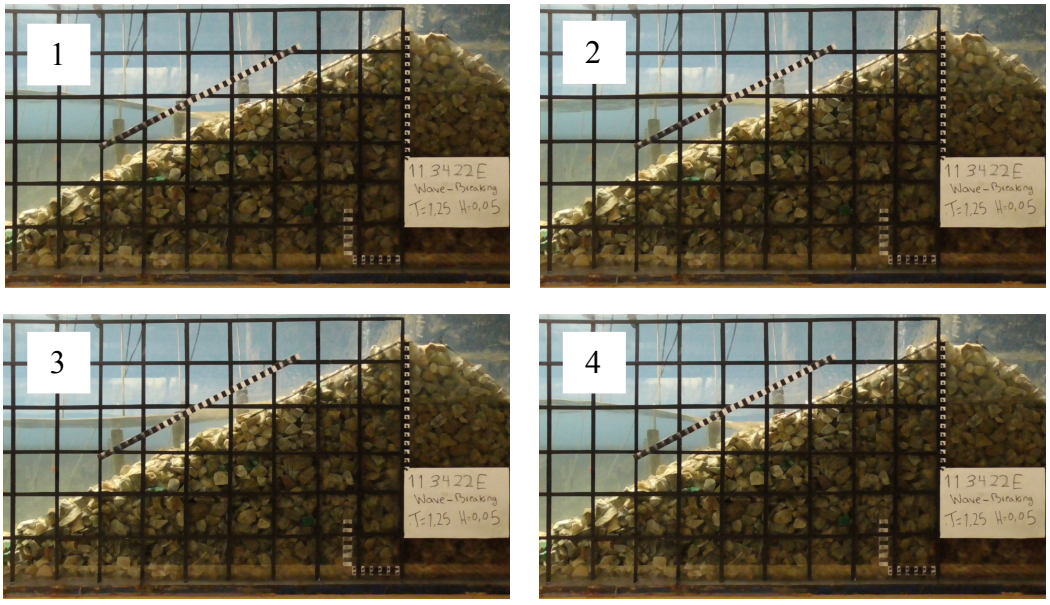

FIGURE B.3: Weak bore breaker type (2_{wb}) with $T_{target} = 1.25$ s and $H_{target} = 0.05$ m.

Chapter 4 and Chapter 5 gather several figures in which the breaker type of some experimental results is indicated. This appendix collects the pictures of the breaker types recorded in laboratory; in particular, Figures B.2, B.3, B.4 and B.5 pretends to show how small changes in the wave height provoke substantially differences in the type of breaker.

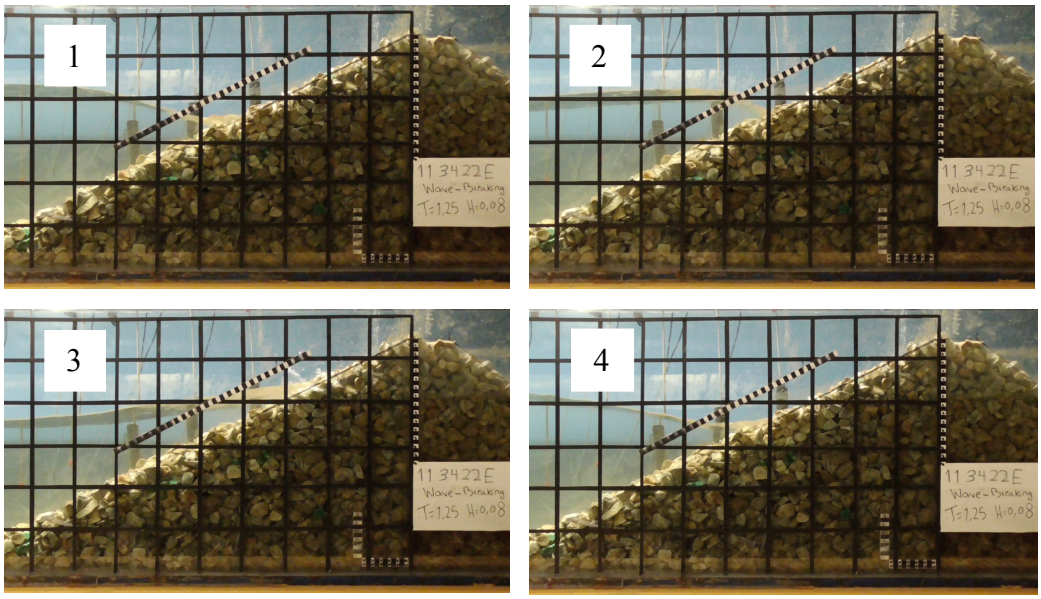

FIGURE B.4: Strong bore breaker type (3_{wb}) with $T_{target} = 1.25$ s and $H_{target} = 0.08$ m.

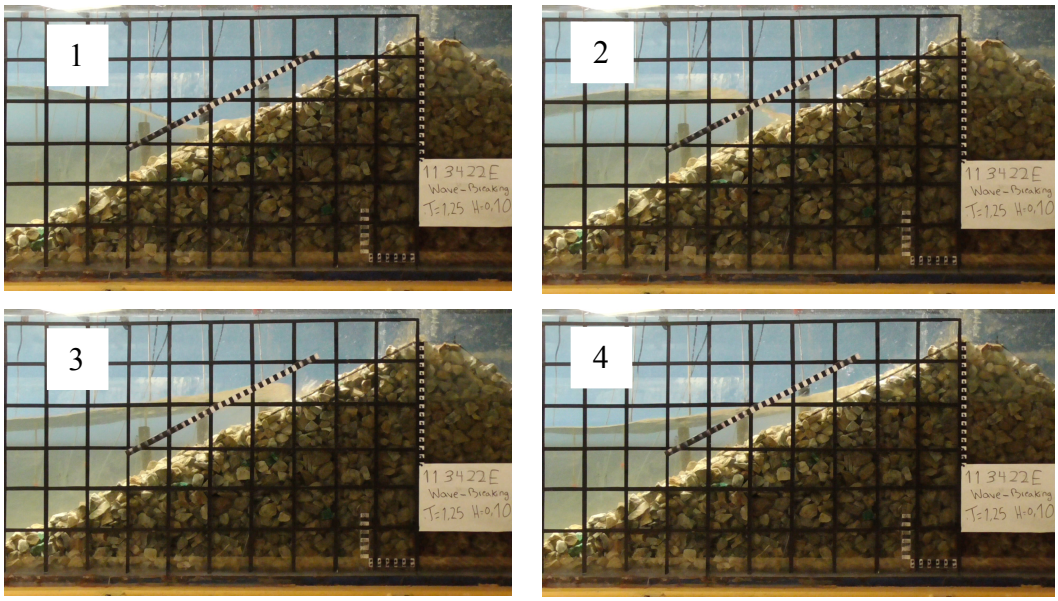

FIGURE B.5: Strong bore breaker type (4_{wb}) with $T_{target} = 1.25$ s and $H_{target} = 0.10$ m.

Likewise, as H_{target} increases and T_{target} is varied (in laboratory) for that large and constant H_{target}, more breaker types are observed (see Figure B.6)

To clarify the wave-breaking on the slope and, specifically, the new four breaker types defined by Lakehal and Liovic (2011) and Zhang and Liu (2008), and used in this study, Figures B.7 and B.8 gather pictures for the permeable slope with main armor to distinguish between weak-strong bore, and weak-strong plunging.

The breaker type for irregular waves depends on the sequence of the wave height. In the same record, several wave-breaking types were observed, although the main breaker was around the breaker that would be for the same case in regular waves $H_{target} = H_{m0}$ and $T_{target} = T_p$. To properly specify the breaker type associated to a irregular wave train, the

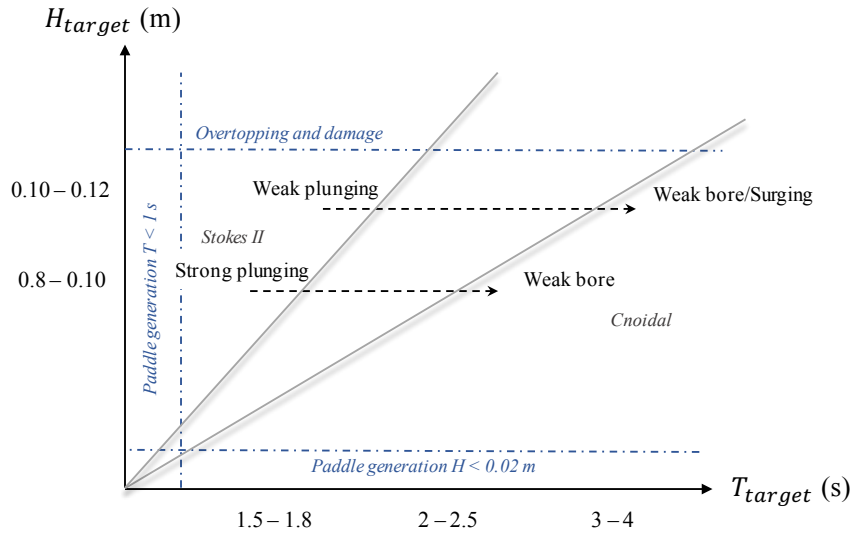

FIGURE B.6: Scheme of the possible breaker types observed with a constant large H_{target} and varying T_{target}.

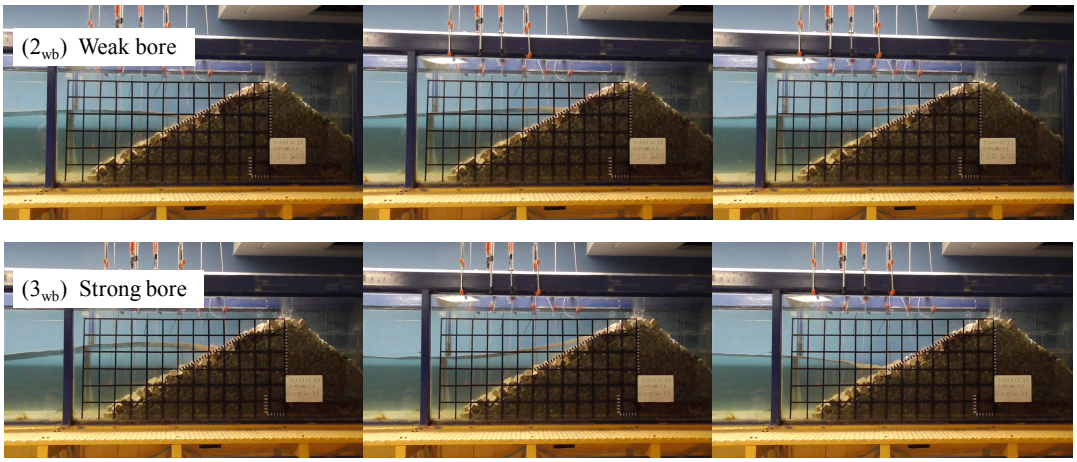

FIGURE B.7: (2_{wb}) Weak bore, (3_{wb}) strong bore breaker types obtained from regular waves conditions of the permeable mound breakwater with main armor layer.

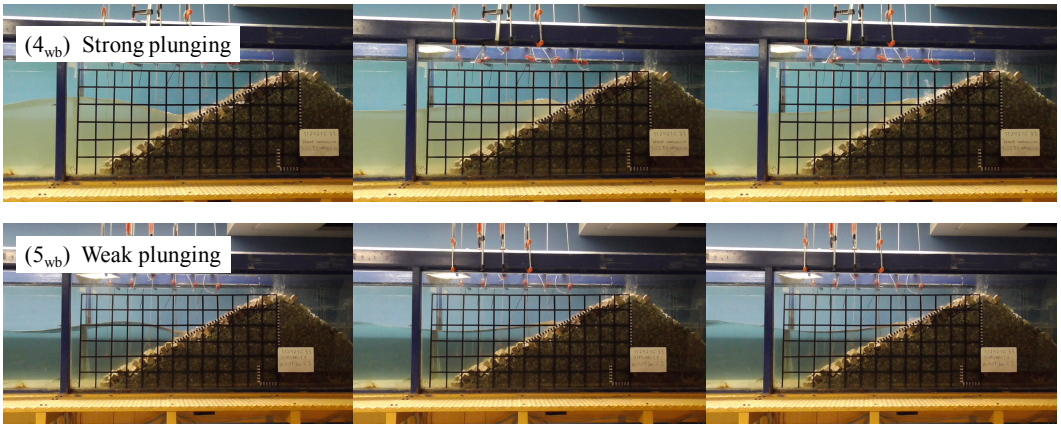

FIGURE B.8: (4_{wb}) Strong plunging, (5_{wb}) weak plunging breaker types obtained from regular waves conditions of the permeable mound breakwater with main armor layer.

frequency of each breaker type within a test should be recorded and adjusted a probability function according to H_{m0} and T_p simulated (future research line).

Appendix C

Experimental scattering: generation and separation method

The technical limitations of the wave-current flume of the Andalusian InterUniversity Institute for Earth System Research (University of Granada), and its adaptive solutions, are described in detail in Pérez-Romero (2008)'thesis, which addresses: (a) wave reflection on the wall of the flume, (b) wave reflection absorbed by the paddle, (c) transversal waves in the wave flume; and (d) the long waves. Therefore, this appendix focuses on the laboratory experimentation, in particular the wave generation and separation method used in this research. In Vílchez et al. (2016b), the reader can find a detailed description of the calibration and validation of the IH-2VOF numerical model.

The relative depth at the toe of the breakwater includes a wide range of intermediate depths, $0.09 < h/L < 0.027$. With one exception, the wave train steepness is too small ($H_I/L < 0.04$) to be able to describe oscillatory movement by means of linear wave theory (Section 3.3.4, Figure 3.4). In these conditions, it is reasonable to assume that the wave energy transformation is largely due to its interaction with the breakwater slope (and when applicable, its main armor layer and porous core). Likewise, the energy content of the reflected and transmitted wave trains on the face of the breakwater is located in their propagation mode, whose frequency is the same as that of the wave generation.

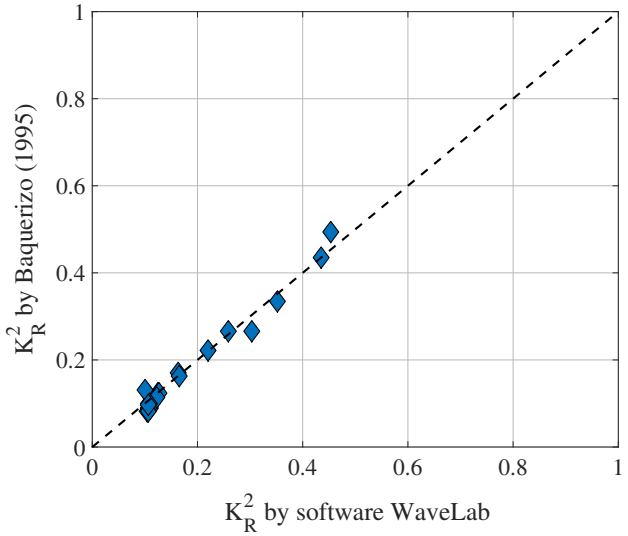

FIGURE C.1: Comparison of Baquerizo (1995) method with WaveLab – Aalborg University (Frigaard, P. and Andersen, T.L., 2014) to obtain the reflected energy coefficient K_R^2. The diagram shows some of the experimental physical results tested in the wave flume of Aalborg University (Díaz-Carrasco et al., 2019).

The separation of the incident and reflected wave trains was performed with the method of Baquerizo (1995), which also provided the phase of the reflected wave train. In order

to contrast this method, Figure C.1 shows the K_R^2 values of experimental tests carried out at Aalborg University (Díaz-Carrasco et al., 2019), analyzed by the software of WaveLab Aalborg University (Frigaard, P. and Andersen, T.L., 2014) and by the Baquerizo's method. In both cases, the modulus values of the reflected energy are very similar.

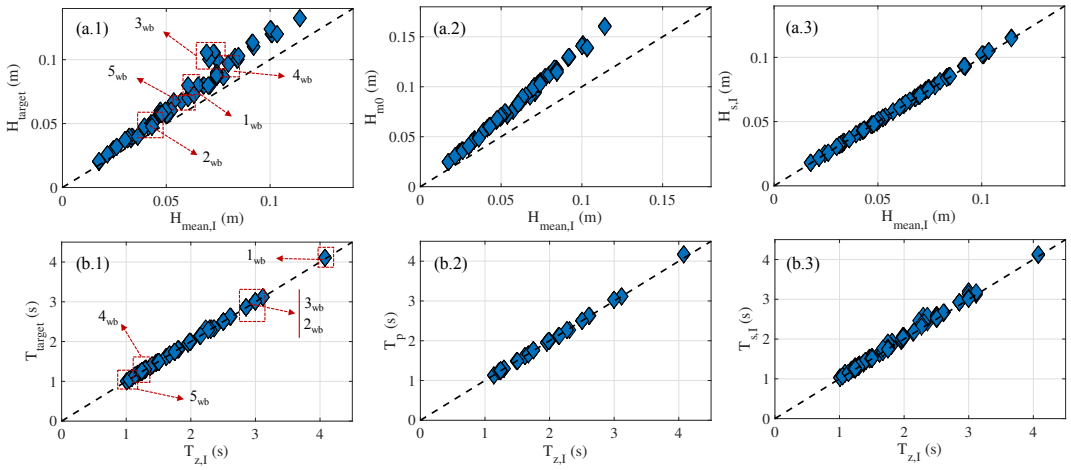

FIGURE C.2: Permeable mound breakwater with main armor layer. Correlation of the descriptors of the (a) wave height and (b) wave period of the incident regular wave train, spectrally and statistically obtained from the time series in the laboratory. The number j_{wb} $(j = 1:5)$ identifies the wave breaker types on the slope: 1_{wb} – surging, 2_{wb} – weak bore, 3_{wb} – strong bore, 4_{wb} – strong plunging, 5_{wb} – weak plunging.

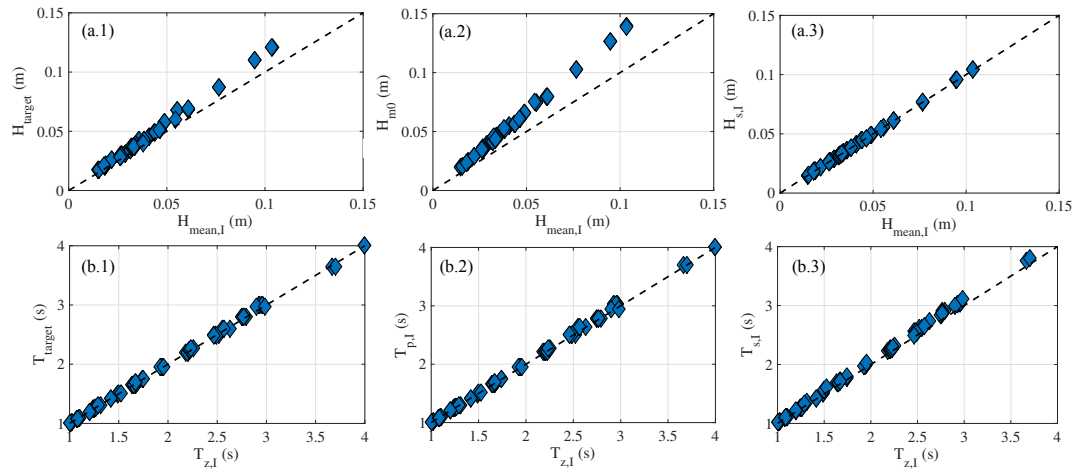

FIGURE C.3: Homogeneous permeable mound breakwater. Correlation of the descriptors of the (a) wave height and (b) wave period of the incident regular wave train, spectrally and statistically obtained from the time series in the laboratory.

The separation method provided the time series of the vertical displacement of the free surface of the incident and reflected wave trains. This confirmed their Gaussian nature. The statistical descriptors of the incident wave height and period H_I, $T_{z,I}$ and the reflected wave height and period H_R, $T_{z,R}$ were also calculated. In all cases, it was found that $H_i \approxeq H_{mean,i} \approxeq H_{phase-averaged,i} \approxeq H_{s,i}$. The same was true for the wave period. Figure C.2 shows the linear relation of the spectral and statistical descriptors of the incident wave train. The tests were repeated at least three times. Figure C.2-a.1 and C.2-b.1 also includes, the types of breaker observed in some specific runs. The images were recorded with video camera. Each red box includes experimental data of repeated runs. Notice, that small changes in the characteristics of

the incident wave (height and/or period) provoke substantially differences in the type (shape) of breaker, particularly in the interval strong plunging - strong bore - weak bore (see Appendix B). In summary, there is not a biunivocal relationship between I_r and the type of breaker.

Figure C.3 shows the statistical parameters obtained from the regular wave conditions tested for the homogeneous permeable mound breakwater with $B_b = 0.24$ m and $\tan(\alpha) = 1/2$. As for the physical model with main armor, regular time series are characterized by: $H_i \approxeq H_{mean,i} \approxeq H_{phase-averaged,i} \approxeq H_{s,i}$, and the same for the wave period.

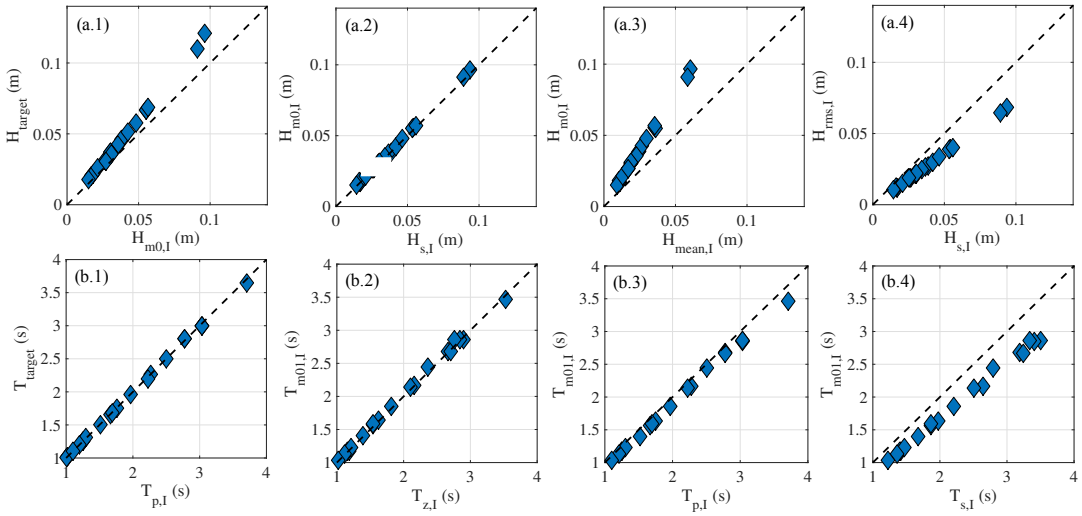

FIGURE C.4: Homogeneous permeable mound breakwater. Correlation of the descriptors of the (a) wave height and (b) wave period of the incident irregular wave train, spectrally and statistically obtained from the time series in the laboratory.

Figure C.4 gathers the statistical parameters obtained from the irregular wave conditions tested for the homogeneous permeable mound breakwater with $B_b = 0.24$ m and $\tan(\alpha) = 1/2$. In this study, the incident irregular wave train was characterized by H_{m0} and T_p. Although the general behavior of the wave train is better represented with the spectral mean period, T_{m01}, we choose the peak period, since we analyze the energy transformation and T_p is the parameter associated with the maximum energy.

For irregular waves, the waves are generated following a Jonswap spectrum (narrow-band spectrum) with a Raleigh distribution of wave heights and a maximum value at the peak period, which implies: $H_{m0} \approx H_{s,I}$ and $T_{z,I} \approx T_{m01} \approx T_p$ (Figures C.4-a.2 and C.4-b.3).

Bibliography

Aalborg University (2007). *AwaSys 5 homepage*. http://www.hydrosoft.civil.auc.dk/ AwaSys.

— (2007b). *WaveLab 2 homepage*. http://www.hydrosoft.civil.auc.dk/ wavelab.

— (2015). *Wave Data Acquisition and Analysis Software - WaveLab 3, Aalborg University. Department of Civil Engineering*. http://www.hydrosoft.civil.aau.dk/wavelab/).

Ahrens, J.P. and B.L. McCartney (1975). "Wave period effect on the stability of rip-rap". In: *3rd Civil Engineering in the Oceans Conference* 2, 1019–1034.

Akhavan, R., R.D. Kamm, and A.H. Shapiro (1991). "An investigation of transition to turbulence in bounded oscillatory Stokes flows Part 1. Experiments". In: *Journal of Fluid Mechanics* 225, 395–422.

Albrecht, M.C., C.J. Nachtsheim, T. Albrecht, and R.D. Cook (2013). "Experimental Design for Engineering Dimensional Analysis". In: *Technometrics* 55 (3).

Alexander, M.P., E.A. Pérez-Agreda, and N.M. Pinyol (2010). *Geomechanics of Failures*. Springer Science y Business Media.

Allsop, N.W.H. and A.R. Channell (1989). "Wave reflections in harbours: reflection performance of rock armoured slopes in random waves". In: *Technical Report OD 102. Hydraulics Research, Wallingford*.

Amoudry, L. and P. L. F. Liu (2010). "Parameterization of near-bed processes under collinear wave and current flows from a two-phase sheet flow model". In: *Continental Shelf Research* 30, 1403–1416.

Andersen, T.L., M.R. Eldrup, and P. Frigaard (2017). "Estimation of incident and reflected components in highly nonlinear regular waves". In: *Coastal Engineering* 119, 51–64.

AREDIS (2015). *Diseño de adecuaciones para robustecer la estabilidad de diques en suelos fangosos (143095)*. Convocatoria Conjunta de Proyectos de Investigación, Desarrollo Tecnológico e Innovación Bilaterales México-España 2010.

Bagnold, R.A. (1946). "Motion of waves in shallow water. Interaction between waves and sand bottoms". In: *Proceedings of the Royal Society of London* 187.A, 1–18.

Baquerizo, A. (1995). "Reflexión del oleaje en playas. Métodos de evaluación y de predicción". PhD thesis. University of Cantabria (Spain).

Battjes, J.A. (1974). "Surf Similarity". In: *Proceedings of 14th International Conference on Coastal Engineering. ASCE, pp. 466-480*.

Belde J.and Reuning, L. and S. Back (2017). "Bottom currents and sediment waves on a shallow carbonate shelf, Northern Carnarvon Basin, Australia". In: *Continental Shelf Research* 138, 142–153.

Benedicto, M.I. (2004). "Comportamiento y evolución de la avería de los diques de abrigo frente a la acción del oleaje". PhD thesis. University of Granada (Spain).

Biot, M.A. (1901). "General Theory of Three-Dimensional". In: *Journal of Applied Physics* 12, 155–164.

Blondeaux, P. (2012). "Sediment mixtures, coastal bedforms and grain sorting phenomena: An overview of the theoretical analyses". In: *Advances in Water Resources* 48, 113–124.

Blondeaux, P. and G. Vittori (1999). "Boundary layer and sediment dynamics under sea waves". In: *Advances in Coastal and Ocean Engineering* 4, 133–190.

Boroomand, B. and O.C. Zienkiewicz (1998). "Recovery procedures in error estimation and adaptivity: Adaptivity in non-linear problems of elasto-plasticity behaviour". In: *Studies in Applied Mechanics* 47, 383–410.

Bruun, P. and A.R. Günbak (1976). "New design principles for rubble mound structures". In: *Proceedings of the 15th International Conference of Coastal Engineering*. Honolulu, Hawaii.

Burcharth, H.F. and O.K. Andersen (1995). "On the one-dimensional steady and unsteady porous flow equations". In: *Coastal Engineering* 24, 233–257.

— (2010). "Stability of Cubipod Armoured Roundheads in Short Crested Waves". In: *Proceedings of the 32nd International Conference of Coastal Engineering*. Shanghai, China.

Chai, J. C., S. Hayashi, and H. Yamanishi (2002). "Effect of SUBMERGED DIKE/LIFTED AREA ON SEABED MUD TRANSPORT". In: *Proceeding of the International Symposium on Lowland Technology, Saga University*.

Chávez, V. (2013). "Comportamiento de los suelos marinos bajo la acción del oleaje". PhD thesis. National Autonomous University of Mexico (Mexico).

Chávez, V., E. Mendoza, R. Silva, A. Silva, and M.A. Losada (2017). "An experimental method to verify the failure of coastal structures by wave induced liquefaction of clayey soils". In: *Coastal Engineering* 123, 1–10.

Chen, D., Y. Wang, B. Melville, M. ASCE, H. Huang, and W. Zhang (2018). "Unified Formula for Critical Shear Stress for Erosion of Sand, Mud, and Sand- Mud Mixtures". In: *Journal of Hydraulic Engineering. ISSN 0733-9429*.

Cheng, Z., X. Yu, T. J. Hsu, C. E. Ozdemir, and S. Balachandar (2015). "On the transport modes of fine sediment in the wave boundary layer due to resuspension/deposition: A turbulence-resolving numerical investigation". In: *Journal of Geophysical Research: Oceans* 120, 1918–1936.

Christensen, E.D. and R. Deigaard (2001). "Large eddy simulation of breaking waves". In: *Coastal Engineering* 42, 53–86.

Churchill, S.W. and R. Usagi (1972). "A general expression for the correlation of rates of transfer and other phenomena". In: *AICHE J.* 18, 11221–1128.

CIRIA, CUR, and CETMEF (2007). "The Rock Manual: The Use of Rock in Hydraulic Engineering". In: *CIRIA, London, p. C683*.

Clavero, M. (2007). "Comportamiento de los diques en talud frente a la acción del oleaje y criterios para el reparto de la probabilidad conjunta de fallo en la vida útil". PhD thesis. Granada.

Clavero, M., P. Folgueras, P. Díaz-Carrasco, M. Ortega-Sánchez, and M.A. Losada (2018). "A similarity parameter for breakwaters: the modified Iribarren number". In: *Proceedings of 36th International Conference on Coastal Engineering*. Baltimore, Maryland (USA).

Cortés, C.D., A.J.J. García, and G. Gómez (2004). "Modelo de elementos finitos para el análisis lineal de un material poroelástico transversalemente isótropo in non-linear problems of elasto-plasticity behaviour". In: *DYNA* 145, 45–56.

Cyril, J. and J.R. Galvin (1968). "Break type classification on the three laboratory beaches". In: *Journal of Geophysical Research* 73, 13651–3659.

Dai, Y.B. and A.M. Kamer (1969). "Scale Effect Tests for Rubble Mound Breakwaters". In: *U. S. Army Engineer Waterway Experiment Station, Corps of Engineers, Vicksburg, Mississippi, Research Report H-69-2*.

Dale, J., H.M. Burgess, D.J. Nash, and A.B. Cundy (2018). "Hydrodynamics and sedimentary processes in the main drainage channel of a large open coast managed realignment site". In: *Estuarine, Coastal and Shelf Science* 215, 100–111.

Dalrymple, R.A. and R.G. Dean (1991). *Water wave mechanics for engineers and scientists*. Advanced Series on Ocean Engineering. Prentice-Hall.

Dalrymple, R.A. and P.L.F. Liu (1987). "Waves over Soft Muds: A Two-Layer Fluid Model". In: *Journal of Physical Oceanography* 8, 1121–1131.

Dalrymple, R.A., M.A. Losada, and P.A. Martin (1991). "Reflection and transmission from porous structures under oblique wave attack". In: *Journal of Fluid Mechanics* 224, 625–644.

Davidson, M.A., P.A.D. Bird, G.N. Bullock, and D.A. Huntley (1996). "A new non-dimensional number for the analysis of wave reflection from rubble mound breakwaters". In: *Coastal Engineering Proceedings* 28, 93–120.

Del-Rosal-Salido, J., P. Díaz-Carrasco, M. Magaña P. Clavero, A. López-Ruiz, M.A. Losada, A. Moñino, M.G. Neves, R. Silva, E. Mendoza, S. Solari, M. Contreras, and M. Ortega-Sánchez (2019). "Addressing the challenge of flooding risk indiced by global warming: PROTOCOL Project". In: *Proceedings of the 38th International Association for Hydro-Environment Engineering and Research World Congress*. Panama City, Panama.

Díaz-Carrasco, P., M. Vílchez, and M. Ortega-Sánchez (2014). "Metodología de mejora para el diseño de los diques en talud: corrección del efecto escala". PhD thesis. Bachelor Thesis, University of Granada (Spain). DOI: `http://hdl.handle.net/10481/32743`.

Díaz-Carrasco, P., M. Ortega-Sánchez, and M.A. Losada (2015). "Recomendaciones para caracterizar y describir la interacción de la dinámica marina con diques de gravedad en suelos blandos". PhD thesis. Master Program in Environmental Hydraulics, University of Granada (Spain): Master Program in Environmental Hydraulics.

Díaz-Carrasco, P., M.V. Moragues, M. Clavero, M. Ortega-Sánchez, and M.A Losada (2017). "Wave overtopping on mixed breakwaters and design curves". In: *Proceedings of the 8th International Short Course/Conference on Applied Coastal Research*. Santander, Spain.

Díaz-Carrasco, P., M.V. Moragues, M. Clavero, M. Ortega-Sánchez, and Losada M.A. (2018). "Efecto de la subida del nivel del mar en la estabilidad de los diques de abrigo". In: *III Jornadas de Investigadores en Formación Fomentado la Interdisciplinariedad. I Congreso Nacional*. Granada, Spain.

Díaz-Carrasco, P., M.V. Moragues, M. Clavero, M. Ortega-Sánchez, and M.A Losada (2018). "Similarity on rubble mound breakwaters tests: analysis and discussion". In: *Proceedings of the 7th International Conference of the Application of Physical Modelling in Coastal and Port Engineering and Science*. Santander, Spain.

Díaz-Carrasco, P., M.R. Eldrup, and T.L. Andersen (2019). "Wave-Breakwater interaction: Test Program in the Flume of Aalborg University". In: *Technical documentation, Department of Civil Engineering, Aalborg University*.

Díaz-Carrasco, P., G. Vittori, P. Blondeaux, and M. Ortega-Sánchez (2019a). "Non-cohesive and cohesive sediment transport due to tidal currents and sea waves: A case study". In: *Continental Shelf Research* 183, 87–102. DOI: `https://doi.org/10.1016/j.csr.2019.06.008`.

Díaz-Carrasco, P., M.V. Moragues, M. Clavero, and M.Á Losada (2019b). "Sobre el mínimo de estabilidad en los diques rompeolas". In: *Proceedings of the 15th National Conference of Jornadas Españolas de Puertos y Costas*. Málaga, Spain.

Díaz-Carrasco, P., M.V. Moragues, M. Clavero, and M.A. Losada (2019c). "2D water-wave interaction with permeable and impermeable slopes: dimensional analysis and experimental overview". In: *Coastal engineering* (Under review).

Dohmen-Janssen, C. M. (1999). "Grain size influence on sediment transport in oscillatory sheetflow: Phase-lags and mobile-bed effects". PhD thesis. Delft University of Technology: Delft University of Technology.

Eldrup, M.R. and T.L. Andersen (2019). "Estimation of incident and reflected wave trains in highly nonlinear tho dimensional irregular waves". In: *Journal of Waterway, Port, Coastal, and Ocean Engineering* 145, Issue 1.

Eldrup, M.R., T.L. Andersen, and H.F. Burcharth (2019). "Stability of rubble mound breakwaters-A study of the notional permeability factor, based on physical model tests". In: *Water (Switzerland)* 11.5, 934.

Elsafti, H. and H. Oumeraci (2017). "Analysis and classification of stepwise failure of monolithic breakwaters". In: *Coastal Engineering* 121, 221 –239.

EurOtop (2018). *Manual on wave overtopping of sea defences and related structures. An overtopping manual largely based on European research, but for worldwide application*. Van der Meer, J.W. et al.

Foda, M.A. and S.Y. Tzang (1994). "Resonant fluidization of silty soil by water waves". In: *Journal of Geophysical Research* 99, 463–475.

Foda, M.A., J.R. Hunt, and H.T. Chou (1993). "A nonlinear model for the fluidization of marine mud by waves". In: *Journal of Geophysical Research* 98, 7039–7046.

Forsberg, P.L., V.B. Ernstsen, T.J. Andersen, C. Winter, M. Becker, and A. Kroon (2018). "The effect of successive storm events and seagrass coverage on sediment suspension in a coastal lagoon". In: *Estuarine, Coastal and Shelf Science* 212, 329–340.

Foti, E. and P. Scandura (2004). "A low Reynolds number k - ε model validated for oscillatory flows over smooth and rough wall". In: *Coastal Engineering* 2, 173–184.

Franco, L. (1994). "Vertical breakwaters: the Italian experience". In: *Coastal Engineering* 22, 31 –55.

Franz, G., M.T. Delpey, D. Brito, L. Pinto, P. Leitão, and R. Neves (2017). "Modelling of sediment transport and morphological evolution under the combined action of waves and currents". In: *Ocean Science* 13, 673–690.

Fredsoe, J. and R. Deigaard (1992). *Mechanics of Coastal Sediment Transport*. 3rd ed. World Scientific, Singapore.

Frigaard, P. and M. Brirsen (1995). "A time-domain method for separating incident and reflected waves." In: *Coastal Engineering*.

Frigaard, P. and Andersen, T.L. (2014). *Wave Data Acquisition and Analysis Software - WaveLab 3*. Aalborg University. Department of Civil Engineering.

Gíslason, K., J. Fredsoe, R. Deigaard, and B.M. Sumer (2009). "Flow under standing waves: Part 1. Shear stress distribution, energy flux and steady streaming". In: *Coastal Engineering* 56, 341–362.

Gómez-Martín, M.E. and J.R. Medina (2014). "Heterogeneous Packing and Hydraulic Stability of Cube and Cubipod Armour Units". In: *Journal of Waterway, Port, Coastal and Ocean Engineering* 140, 100–108.

Grant, W.D. and O.S. Madsen (1979). "Combined wave and current interaction with a rough bottom". In: *Journal of Geophysical Research* 84, 1797–1808.

Gu, Z. and H. Wang (1991). "Gravity waves over porous bottom." In: *Coastal Engineering* 15, 497–524.

Guillén, P.M. (2008). "Large breakwaters in deep water in northern Spain". In: *Proceedings of the Institution of Civil Engineers: Maritime Engineering* 161, 175–186.

Harlow, E.H. (1980). "Large rubble-mound breakwater failures." In: *Journal of the Waterway, Port, Coastal and Ocean Division, ASCE, Proc.* 106, 275–278.

Higuera, P., J.L. Lara, and I.J. Losada (2014). "Three-dimensional interaction of waves and porous coastal structures using OpenFOAM Part II: Application". In: *Coastal Engineering* 83, 259–270.

Hinkel, J., D. Lincke, A.T. Vafeidis, M. Perrette, R.J. Nicholls, R.S. Tol, B. Marzeion, X. Fettweis, C. Lonescu, and A. Levermann (2014). "Coastal flood damage and adaptation costs under 21st century sea-level rise". In: *Proceedings of the National Academy of Sciences of the United States of America* 111, 3292–3297.

Hogarth, P. (2014). "Preliminary analysis of acceleration of sea level rise through the twentieth century using extended tide gauge data sets (August 2014)". In: *Journal of Geophysical Research: Oceans* 119.11, 7645–7659.

Hsu, T., T. Sakakiyama, and P. Liu (2002). "A numerical model for wave motions and turbulence flows in front of a composite breakwater". In: *Coastal Engineering* 46, 25–50.

Hsu, W.Y., H.H. Hwung, T.J. Hsu, A. Torres-Freyermuth, and R.Y. Yang (2013). "An experimental and numerical investigation on wave-mud interactions". In: *Journal of Geophysical Research: Oceans* 118, 1126–1141.

Hudson, R.Y. (1959). "Laboratory investigation of rubble –mound breakwaters". In: *ournal of Waterway, Port, Coastal and Ocean Division* 85, 93–121.

Hughes, S.A. and J.E. Fowler (1995). "Estimating wave-induced kinematics at sloping structures". In: *Journal of Waterway Port Coastal and Ocean Engineering*, 209–215.

Iribarren, C.R. and C Nogales (1949). "Protection des Ports, paper presented at 17th International Navigation Congress, Permanent Int". In: *Association of Navigation Congress. Lisbon, Portugal*.

Iversen, H.W. (1952). "Gravity Waves". In: *Laboratory study of breakers. Natl. Bur. Standards, Circular* 521, 9–32.

Jeng, D.S., J.H. Ye, J.S. Zhang, and P.L.F. Liu (2012). "An integrated model for the wave-induced seabed response around marine structures: Model verifications and applications". In: *Coastal Engineering* 72, 1–19.

Jensen, B.L., B.M. Sumer, and J. Fredsoe (1989). "Turbulent oscillatory boundary layers at high reynolds numbers". In: *Journal of Fluid Mechanics* 206, 265–297.

Jensen, B.L., E.D. Christensen, and B.M. Sumer (2014a). "Pressure-induced forces and shear stresses on rubble mound breakwater armour layers in regular waves". In: *Coastal Engineering* 91, 60–75.

Jensen, B.L., N.D. Jacobsen, and E.D. Christensen (2014b). "Investigations on the porous media equations and resistance coefficients for coastal structures". In: *Coastal Engineering* 84, 56–72.

Jones, W.P. and B.E. Launder (1972). "The prediction of laminarization with a two-equation model of turbulence". In: *International Journal of Heat and Mass Transfer* 15, 301–314.

Kessel, T. van (1998). "Rheology of cohesive sediments: comparison between a natural and an artificial mud". In: *Journal of Hidraulic Research* 36, 591–612.

Kessel, T. van and C. Kranenburg (1998). "Wave-induced liquefaction and flow of subaqueous mud layers". In: *Journal of Coastal Engineering* 34, 109–127.

Kobayashi, N. and A. Wurjanto (1992). "Irregular Wave Interaction with Permeable Slopes". In: *Proceedings of the 23rd International Conference of Coastal Engineering. ASCE, 118, pp. 368-386*. Venice, Italy.

Kortenhaus, A. and H. Oumeraci (1998). "Classification of wave loading on monolithic coastal structures". In: *Coastal Engineering* 26, 867–880.

Kumagai, T. and M.A. Foda (2002). "Analytical Model for Response of Seabed beneath Composite Breakwater to Wave". In: *Journal of Waterway, Port, Coastal and Ocean Engineering*, 62–71.

Lakehal, D. and P. Liovic (2011). "Turbulence structure and interaction with steep breaking waves". In: *Journal of Fluid Mechanics* 674, 522–577.

Lambe, T.W. and V.R. Whitman (1991). *Mecánica de suelos*. Editorial Limusa, S.A.

Lara, J.L., I.J. Losada, and P.L.F. Liu (2006). "Breaking waves over a mild gravel slope: Experimental and numerical analysis". In: *Journal of Geophysical Research Atmospheres* 11, C11019.

Lara, J.L., I.J. Losada, and R. Guanche (2008). "Wave interaction with low-mound breakwaters using a RANS model". In: *Ocean Engineering* 35, 1388–1400.

Lee, G. and W.B. Dade (2004). "Examination of reference concentration under waves and currents on the inner shelf". In: *Journal of Geophysical Research* 109, C02021.

Liao, Chencong, Dagui Tong, and Lihong Chen (2018). "Pore pressure distribution and momentary liquefaction in vicinity of impermeable slope-type breakwater head". In: *Applied Ocean Research* 78, 290 –306.

LIMAS (2004). *Liquefaction around marine structures (EVK3-CT-2000-00038)*. FP5-EESD - Programme for research, technological development, demonstration on "Energy, environment, and sustainable development, 1998-2001".

Lindenberg, J., L.C. van Rijn, and J.C. Winterwerp (1989). "Some Experiments on Wave-induced Liquefaction of Soft Cohesive Soils". In: *Journal of Coastal Research* 5, 127–137.

Losada, I.J., M.A. Losada, and A. Baquerizo (1993). "An analytical method to evaluate the efficiency of porous screens as wave dampers". In: *Applied Ocean Research* 15.4, 207–215.

Losada, I.J., M.D. Patterson, and M.A. Losada (1997). "Harmonic generation past a submerged porous step". In: *Coastal Engineering* 31, 287–304.

Losada, M., P. Martin, and R. Dalrymple (1991). "Reflection and transmission from porous structures under oblique wave attack". In: *Journal of Fluid Mechanics* 224, 625–644.

Losada, M.A. and J.M. Desire (1985). "Incipient motion on a horizontal granular bed in non-breaking water waves". In: *Coastal Engineering* 9, 357–370.

Losada, M.A. and L. A. Giménez-Curto (1979). "The joint effect of the wave height and period on the stability number of rubble mound breakwaters using Iribarren's number". In: *Coastal Engineering* 3.77-96.

— (1981). "Flow characteristics on rough, permeable slopes under wave action". In: *Coastal Engineering* 4.187-206.

Losada, M.A., P. Díaz-Carrasco, M.V. Moragues, and M. Clavero (2019). "Variabilidad intrínseca en el comportamiento de los diques rompeolas". In: *Proceedings of the 15th National Conference of Jornadas Españolas de Puertos y Costas*. Málaga, Spain.

Lu, J., X.H. Wang, A.V. Babanin, S. Aijaz, Y. Sun, Y. Teng, K.T. Jung, and F. Qiao (2017). "Modeling of suspended sediment concentrations under combined wave-current flow over rippled bed". In: *Estuarine, Coastal and Shelf Science* 199, 59–73.

Lu, Y., S. Li, L. Zuo, H. Lio, and J.A. Roelvink (2015). "Advances in sediment transport under combined action of waves and currents". In: *International Journal of Sediment Research* 30, 351–360.

Maa, P.Y. (1986). *Erosion of soft muds by waves*. Gainesville.

Maa, P.Y. and A.J. Mehta (1987). "Mud erosion by waves: a laboratory study". In: *Continental Shelf Research* 7, 1269–1284.

Madsen, P.A. and D.R. Fuhrman (2008). "Run-up of tsunamis and long waves in terms of surf-similarity". In: *Coastal Engineering* 55, 209–223.

Magaña, P., R.J. Bergillos, Del-Rosal-Salido J., M.A. Reyes-Merlo, P. Díaz-Carrasco, and M. Ortega-Sánchez (2018). "Integrating complex numerical approaches into a user-friendly application for the management of coastal environments". In: *Science of the Total Environment* 624, 979–990. DOI: https://doi.org/10.1016/j.scitotenv.2017.12.154.

Mansard, E.P.D. and E.R. Funke (1987). "On the reflection analysis of irregular waves". In: *Natl. Res. Counc. Rev. Can. Hydraulics Laboratory Technical Report, TR-HY-O17*.

Martin, F.L., M.A. Losada, and R. Medina (1999). "Wave loads on rubble mound breakwater crown walls". In: *Coastal Engineering* 37, 149–174.

Masselink, G. and M.G.. Hughes (2003). *Introduction to Coastal Processes and Geomorphology.* Arnold, Hodder Headline Group.

McAnally, W.H., C. Friedrichs, D. Hamilton, E. Hayter, P. Shrestha, H. Rodriguez, A. Sheremet, and A. Teeter (2007). "Management of Fluid Mud in Estuaries, Bays, and

Lakes. I: Present State of Understanding on Character and Behavior". In: *Journal of Hydraulic Engineering* 133, 9–22.

McDougal, W.G., Y.T. Tsai, and C.K. Sollit (1990). "Response of Finite Depth Seabed to Waves and Caisson Motion". In: *Journal of Waterway, Port, Coastal and Ocean Engineering* 116, 1–20.

Mehta, A.J. (2013). *An Introduction to Hydraulics of Sediment Transport*. World Scientific Publishing.

Mei, C.C. and M.A. Foda (1981). "Wave-induced response in a fluid-filed poro-elastic solid with a free surface-a boundary layer theory". In: *Geophy. J.R. Astro. Soc.* 66, 597–637.

MEIPOR-16 (2016). *Revisión y Actualización del Método de Evaluación de Inversiones Portuarias (MEIPOR)*. In Spanish. Puertos del Estado.

Méndez, F.J., I.J. Losada, R.A. Dalrymple, and M.A. Losada (1998). "Effects of wave reflection and dissipation on wave-induced second order magnitudes". In: *Proceedings of the 26th International Conference on Coastal Engineering, pp.537-550*. Copenhagen, Denmark.

Mentaschi, L., M.I. Vousdoukas, E. Voukouvalas, A. Dosio, and L. Feyen (2017). "Global changes of extreme coastal wave energy fluxes triggered by intensified teleconnection patterns". In: *Geophysical Research Letters* 44.5, 2416–2426.

Menter, F.R. (1994). "Two-equation eddy-viscosity turbulence models for engineering applications". In: *American Institute of Aeronautics and Astronautics Journal* 32, 1598–1605.

Menter, F.R., M. Kuntz, and R. Langtry (2003). "Ten Years of Industrial Experience with the SST Turbulence Model". In: *Turbulence, Heat and Mass Transfer* 4, 1–8.

Moraes, C.C. (1998). "Experiments of Wave Reflexion on Impermeable slopes". In: *Proceedings of the 12th International Conference on Coastal Engineering, 1, pp. 509-521*. Washington D.C., USA.

Moragues, M.V., P. Díaz-Carrasco, M. Clavero, Ortega-Sánchez M., and M.A. Losada (2018). "Análisis sobre el rebase en diques de abrigo". In: *III Congreso transfronterizo sobre el Cambio Climático y Litoral - UHINAK*. Bilbao, Spain.

Moragues, M.V., P. Díaz-Carrasco, M. Clavero, and M.Á Losada (2019a). "Sobre el máximo remonte y rebase potencial en los diques rompeolas". In: *Proceedings of the 15th National Conference of Jornadas Españolas de Puertos y Costas*. Málaga, Spain.

Moragues, M.V., P. Díaz-Carrasco, M. Clavero, Ortega-Sánchez M., and M.A. Losada (2019b). "Climate change impact on the hydraulic performance of breakwaters". In: *Proceedings of the 38th International Association for Hydro-Environment Engineering and Research World Congress*. Panama City, Panama.

Moragues, M.V., M. Clavero, and M.A. Losada (2019c). "Flow characteristics on impermeable and permeable slopes: a synthesis for design". In: *Coastal Engineering* (submitted).

Mostafa, A.M., N. Mizutani, and K. Iwata (1999). "Nonlienar Wave, Composite Breakwater, and Seabed Dynamic Interaction". In: *Waterway, Port, Coastal, Ocean Engineering* 125, 88–97.

Mozahedy, A.B.M.K. (2016). "A methodology to decrease the sinking phenomenon in breakwaters constructed in sandy bottom". PhD thesis. University of Cádiz (Spain).

Muñoz-Pérez, J.J., A.B.M. Khan-Mozahedy, M.G. Neves, B. Tejedor, and G. Gómez-Piña (2015). "Sinking of concrete modules into a sandy seabed: A case study". In: *Journal Coastal Engineering* 99, 26–37.

Myrhaug, D., M. C. Ong, and L. E. Holmedal (2015). "Suspended sediments due to random waves including effects of second order wave asymmetry and boundary layer streaming". In: *Ocean Engineering* 104, 414–421.

Ni, J.R. and G.Q. Wang (1991). "Vertical Sediment Distribution". In: *Journal of Hydraulic Engineering* 117, 1184–1194.

Oumeraci, H. (1994). “Review and analysis of vertical breakwater failures — lessons learned”. In: *Coastal Engineering* 22, 3 –29.

Park, E. and E.M. Latrubesse (2014). “Modeling suspended sediment distribution patterns of the Amazon River using MODIS data”. In: *Remote Sensing of Environment* 147, 232–242.

Partheniades, E. (1965). “Physical dynamics of the estuarine suspended sediments”. In: *Marine Geology* 40, 1–14.

Pérez-Romero, D. (2008). “Procesos Hidrodinámicos en diques mixtos y efectos de escala”. PhD thesis. University of Granada (Spain).

Pérez-Romero, D.M., M. Ortega-Sánchez, A. Moñino, and M.A. Losada (2009). “Characteristic friction coefficent and scale effects in oscillatory flow”. In: *Coastal Engineering* 56, 931–939.

Pope, S.B. (2000). *Turbulent Flows*. Cambridge University Press. DOI: 10.1017/CBO9780511840531.

PROTOCOL (2020). *Protection of coastal urban fronts against global warming (917PTE0538)*. CYTED - Programa Iberoamericano de Ciencia y Tecnología para el Desarrollo.

Requejo, S., C. Vidal, and I.J. Losada (2002). “Modeling of wave loads and hydraulic performance of vertical permeable structures”. In: *Coastal Engineering* 46, 249–276.

Reyes-Merlo, M.A., A. Tintore-Parra, M. Díez-Minguito, M Ortega-Sánchez, and M.A. Losada (2015). “Morphodynamic evolution and influence of dredging activities in small-scale mesotidal estuaries: the case of Punta Umbría (southwestern Spain)”. In: *Proceedings of the 36th IAHR-International Association for Hydro-environment Engineering and Research World Congress.*

Reyes-Merlo, M.A., M. Ortega-Sánchez, M. Díez-Minguito, and M. Á. Losada (2017). “Efficient dredging strategy in a tidal inlet based on an energetic approach”. In: *Ocean & Coastal Management* 146, 157–169.

ROM 0.0-01 (2001). *ROM 0.0. General Procedure and Requirements in the Design of Harbor and Maritime Structures*. Puertos del Estado, p. 218.

ROM 0.5 (2005). *ROM 0.5. Recomendaciones Geotécnicas en las Obras Marítimas*. Puertos del Estado.

ROM 1.0-09 (2009). *ROM 1.0. Recommendations for the Project Design and Construction of Breakwaters (Part I: Calculation and Project Factors. Climatic Agents)*. Puertos del Estado.

ROM 1.1-18 (2018). *ROM 1.1. Recommendations for Breakwater Construction Projects*. Puertos del Estado.

Rose, C.P. and P.D. Thorne (2001). “Measurements of suspended sediment transport parameters in a tidal estuary”. In: *Continental Shelf Research* 21, 1551–1575.

Rouse, H. (1937). “Modern concepts of the mechanics of turbulence”. In: *Transactions of the American Society of Civil Engineers* 102, 463–543.

Ruju, A., J.L. Lara, and I.J. Losada (2014). “Numerical analysis of run-up oscillations under dissipative conditions”. In: *Coastal Engineering* 86, 45–56.

Sanford, L.P. (2008). “Modelling a dynamically varying mixed sediment bed with erosion, deposition, bioturbation, consolidation, and armoring”. In: *Computational Geosciences* 34, 1261–1283.

Santoro, P., M. Fossati, P. Tassi, N. Huybrechts, D. P. van Bang, and I. Piedra-Cueva (2017). “A coupled wave-current-sediment transport model for an estuarine system: Application to the Río de la Plata and Montevideo Bay”. In: *Applied Mathematical Modelling* 52, 107–130.

Sayol, J. M. and M. Marcos (2018). “Assessing Flood Risk Under Sea Level Rise and Extreme Sea Levels Scenarios: Application to the Ebro Delta (Spain)”. In: *Journal of Geophysical Research: Oceans* 123.2, 794–811.

Scarcella, D., M. Benedicto, A. Moñino, and M.A. Losada (2007). "Scale effects in rubble mound breakwaters considering wave energy balance". In: *Proceedings of the 30th Coastal Engineering Conference, pp. 4410-4416*. California, USA.

Schumer, R., D.A. Benson, M.M. Meerschaert, and S.W. Wheatcraft (2001). "Eulerian derivation of the fractional advection-dispersion equation". In: *Journal of Contaminant Hydrology* 48, 69–88.

Seeling, W.N. and J.P. Ahrens (1981). "Estimation of wave reflection and energy dissipation coefficients for beaches, revetments and breakwaters". In: *CERC Technical paper 81-1, Fort Belvoir, U.S.A.C.E. MS, Vicksburg*.

Silvester, R. and J.R.C. Hsu (1989). "Sines revisited". In: *Journal of Waterway, Port, Coastal and Ocean Engineering* 115, 327–344.

Sollitt, C.K. and R.H. Cross (1972). "Wave transmission through permeable breakwaters". In: *Proceedings of the 13th International Conference on Coastal Engineering*. Vol. 3. Vancouver, Canada, pp. 1827–1846.

Sorenson, T. (1992). "Breakwater failure brings lessons (ltr)". In: *Civil Engineering, ASCE* 62.9, 37–38.

Soulsby, R. (1997). *Dynamics of Marine Sands: a manual for practical applications*. 1st ed. Thomas Telford, London.

Soulsby, Richard L and Richard JS Whitehouse (2005). *Prediction of ripple properties in shelf seas-Mark 2 predictor for time evolution-Final technical report*. Tech. rep.

Stanev, E.V., G. Brink-Spalink, and J.O. Wolff (2007). "Sediment dynamics in tidally dominated environments controlled by transport and turbulence: A case study for the East Frisian Wadden Sea". In: *Journal of Geophysical Research* 112, C04018.

Sutherland, J. and T. O'Donoghue (1998). "Wave phase shift at coastal structures". In: *Journal of Waterway, Port, Coastal and Ocean Engineering* 124.2, 90–98.

Tang, J., Y. Lyu, Y. Shen, M. Zhang, and M. Su (2017). "Numerical study on influences of breakwater layout on coastal waves, wave-induced currents, sediment transport and beach morphological evolution". In: *Ocean Engineering* 141, 375–387.

Ting, F.C.K. and J.T. Kirby (1996). "Dynamics of surf-zone turbulence in a spilling breaker". In: *Coastal Engineering* 27.3-4, 131–160.

Tzang, S.Y. (1998). "Unfluidized soil responses of a silty seabed to monochromatic waves". In: *Journal Coastal Engineering* 35, 283–301.

Tzang, S.Y. and S.H. Ou (2006). "Laboratory flume studies on monochromatic wave-fine sandy bed interactions. Part 1. Soil fluidization". In: *Journal Coastal Engineering* 52, 965–982.

Tzang, S.Y., S.H. Ou, and T.W. Hsu (2009). "Laboratory flume studies on monochromatic wave-fine sandy bed interactions. Part 2: Sediment suspensions". In: *Journal Coastal Engineering* 56, 230–243.

Van der Meer, J. W. (1988). "Rock Slope and gravel Beaches Under Wave Attack". PhD thesis. Delft University.

Van der Meer, J.W. (1992). "Conceptual design of rubble mound breakwaters". In: *Proceeding of a short course on the design and reliability of coastal structures, attached to 23rd Conference of Coastal Engineering. Tecnoprint, 447-510*. Venice, Italy.

— (2011). "Design aspects of breakwaters and sea defences". In: *Proceedings of the 5th International Short Course/Conference on Applied Coastal Research*. Santander, Spain.

Van der Meer, J.W., M.R.A. Van Gent, G. Wolters, and D. Heineke (2018). "New Design Guidance for Underlayers and Filter Layers for Rock Armour under Wave Attack". In: *ICE Publishing: London, UK*.

Van Gent, M.R. (1995). "Wave Interaction with Permeable Coastal Structures". PhD thesis. Delft University.

Van Gent, M.R (2013). “Rock stability of rubble mound breakwaters with a berm”. In: *Coastal Engineering* 78, 35–45.

Van Gent, M.R and I.M. Van der Werf (2014). “Rock toe stability of rubble mound breakwaters”. In: *Coastal Engineering* 83, 166–176.

Van Ledder, M., Z.B. Wang, H. Winterwerp, and H. De Vriend (2006). “Modelling sand-mud morphodynamics in the Friesche Zeegat”. In: *Ocean Dynamics* 56, 248–265.

Van Rijn, L.C. (1984a). “Sediment Transport, Part I: Bed Load Transport”. In: *Journal of Hydraulic Engineering* 110, 1431–1465.

— (1984b). “Sediment Transport, Part II: Suspended Load Transport”. In: *Journal of Hydraulic Engineering* 110, 1613–1641.

— (1991). “Sediment transport in combined waves and currents”. In: *Proceedings of Euromech*, 3–15.

— (1993). *Principles of Sediment Transport in Rivers, Estuaries and Coastal Seas*. 1st ed. Aqua Publications, The Netherlands.

Van Rijn, L.C., H. Van Rossum, and P. Termes (1990). “Field Verification of 2-D and 3-D Suspended-sediment Models”. In: *Journal of Hydraulic Engineering* 116, 1270–1288.

Vanneste, D. and P. Troch (2015). “2D numerical simulation of large-scale physical model tests of wave interaction with a rubble-mound breakwater”. In: *Coastal Engineering* 103, 22–41.

Vílchez, M. (2016). “An unified design method of maritime works against waves”. PhD thesis. University of Granada (Spain).

Vílchez, M., M. Clavero, and M.A. Losada (2016a). “Hydraulic performance of different non-overtopped breakwater types under 2D wave attack”. In: *Coastal Engineering* 107, 34–52.

Vílchez, M., M. Clavero, J.L. Lara, and M.A. Losada (2016b). “A characteristic friction diagram for the numerical quantification of the hydraulic performance of different breakwater types”. In: *Coastal Engineering* 114, 86–98.

Vílchez, M., P. Díaz-Carrasco, M. Clavero, and M.A. Losada (2016c). “Verification of the crown wall stability taking into account the hydraulic performance curves”. In: *Proceedings of 35th International Conference on Coastal Engineering*. Estambul, Turkia.

Vílchez, M., M. Clavero, A. Baquerizo, and M.A. Losada (2017). “An approximation to the statistical characteristics of wind waves in front and from the toe of the structure to the toe of the crown of non-overtopped breakwaters”. In: *Coastal Engineering* 59, 1–28.

Vittori, G. (2003). “Sediment suspension due to waves”. In: *Journal of Geophysical Research* 108 (C6), 3173.

VIVALDI (2019). *Integrated verification of the hydrodynamical and structural behavior of a breakwater and its implications on the investment project (BIA2015-65598-P)*. Spanish Ministry of Economy and Competitiveness.

Vousdoukas, M. I., L. Mentaschi, E. Voukouvalas, M. Verlaan, and L. Feyen (2017). “Extreme sea levels on the rise along Europe’s coasts”. In: *Earth’s Future* 5.3, 304–323.

Vreugdenhil, C.B. (2013). *Numerical methods for shallow-water flow*. Vol. 13. Springer Science & Business Media.

Waeles, B., P.L. Hir, and P. Lesueur (2008). “A 3D Morphodynamics Process-based Modelling of a Mixed Sand/Mud Coastal Eenvironment: the Seine Estuary”. In: *France* 8, 477–498.

Wang, Z.B. (1989). “Mathematical modelling of morphological processes in estuaries”. In: *Ph.D. Thesis. Delft, The Netherlands: Delft University of Technology*.

Wellens, P. and M.R. Van Gent (2012). “Wave-induced setup inside permeable structures.” In: *Proceedings of the 33rd International Conference of Coastal Engineering, 43*. Santander, Spain.

Wilcox, D.C. (1988). “Reassessment of the scale-determining equation for advanced turbulent models”. In: *American Institute of Aeronautics and Astronautics Journal* 26, 1299–1310.

Winterwerp, J. C. (2002). "On the flocculation and settling velocity of estuarine mud". In: *Continental Shelf Research* 22, 1339–1360.

Wit, P.J. and C. Kranenburg (1997). "The Wave-induced Liquefaction of Cohesive Sediment Beds". In: *Estuarine, Coastal and Shelf Science* 45, 261–271.

Xu, T. and X. You (2017). "Numerical simulation of suspended sediment concentration by 3D coupled wave-current model in the Oujiang River Estuary, China". In: *Continental Shelf Research* 137, 13–24.

Yamamoto, T. and S. Takahashi (1985). "Wave damping by soil motion". In: *Journal of Waterway, Port, Coastal and Ocean Engineering* 111, 62–77.

Yao, B. and Q. Liu (2018). "Characteristics and influencing factors of sediment deposition-scour in the Sanhuhekou-Toudaoguai Reach of the upper Yellow River, China". In: *International Journal of Sediment Research* (In press).

Ye, J., D. Jeng, R. Wang, and C. Zhu (2013). "Validation of a 2-D semi-coupled numerical model for fluid-structure-seabed interaction". In: *Jouernal of Fluids and Structures* 42, 333–357.

Ye, J., Y. Zhang, R. Wang, and C. Zhu (2014). "Nonlinear interaction between wave, breakwater and its loose seabed foundation: A small- scale case". In: *Ocean Engineering* 91, 300–315.

Yu, X., T.J. Hsu, and D.M. Hanes (2010). "Sediment transport under wave groups: relative importance between nonlinear wave shape and nonlinear boundary layer streaming". In: *Journal of Geophysical Research* 115, 102–113.

Zanuttigh, B. and J.W. Van der Meer (2008). "Wave reflection from coastal structures in design conditions". In: *Coastal Engineering* 55, 771–779.

Zhang, C., J.H. Zheng, Y.G. Wang, M.T. Zhang, D.S. Jeng, and J.S. Zhang (2011). "A process-based model for sediment transport under various wave and current conditions". In: *International Journal of Sediment Research* 26, 498–512.

Zhang, F. and Z. Ge (1996). "A study on some causes of rubble mound breakwater failure". In: *China Ocean Engineering* 10, 473–481.

Zhang, Q. and P.L.F. Liu (2006). "A numerical study of bore runup a slope". In: *Advance in Engineering Mechanics - Reflection and Outlooks*.

— (2008). "A numerical study of swash flows generated by bores". In: *Coastal Engineering* 55, 1113–1134.

Zhang, Q., S. Drapper, L. Cheng, and H. An (2016). "Effect of limited sediment supply on sedimentation and the onset of tunnel scour below subsea pipelines". In: *Coastal Engineering* 116, 103–117.

Zhao, H.-Y. and D.-S. Jeng (2015). "Numerical study of wave-induced soil response in a sloping seabed in the vicinity of a breakwater". In: *Applied Ocean Research* 51, 204 –221.

Zyserman, J.A. and J. Fredsoe (1994a). "Data analysis of bed concentration of suspended sediment". In: *Journal of Hydraulic Engineering* 120, 1021–1042.

— (1994b). "Bed concentration of suspended sediment and total load transport in asymmetric oscillatory flow". In: *Book of Abstracts Overall Workshop MAST, Gregynog, Wales*.